Combcrack Generation in PVD Coated Hardmetal Milling Inserts

Dipl.-Ing. Tamara Teppernegg

Being a thesis in partial fulfilment of the requirements for the degree of a

Doktor der montanistischen Wissenschaften (Dr. mont.)

at the Montanuniversität Leoben

Leoben, October 2016

Eidesstattliche Erklärung

Ich erkläre an Eides statt, dass ich diese Arbeit selbständig verfasst, andere als die angegebenen Quellen und Hilfsmittel nicht benutzt und mich auch sonst keiner unerlaubten Hilfsmittel bedient habe.

Affidavit

I declare in lieu of oath, that I wrote this thesis and performed the associated research myself, using only literature cited in this volume.

Leoben, October 2016

Tamara Teppernegg

gewidmet meiner Oma

Zäzilia Teppernegg

(*23.04.1926 - †02.08.2016)

Damit das Mögliche entstehen kann,

muss immer wieder das Unmögliche versucht werden.

(Hermann Hesse)

Acknowledgements

Man kann es kaum in Worten fassen, wie groß mein Dank an Christoph Czettl ist, welcher mich vor 8 Jahren in die Welt der Beschichtungen und Hartmetalle hat eintauchen lassen, die mich auch in Zukunft nicht mehr loslassen wird. Ohne dein ansteckendes Feuer zum Themengebiet hätte ich nie dieses Projekt begonnen und ohne die anregenden Diskussionen wäre diese Arbeit nicht in dieser Qualität vorhanden.

Ein großes Dankeschön an alle Mitarbeiter des Material Centers Leoben, dass mir die Möglichkeit gab, diese Arbeit in der passenden Umgebung zu verfassen. Ausgewählte Personen möchte ich hier ins Besondere erwähnen:

Ich danke Thomas Klünsner für deinen Einsatz, die unermüdliche und geduldige Zusammenarbeit und Betreuung. Du bist im Wesen ein wahrer Wissenschaftler-Experte in Hartmetallfragen und der beste Englischlehrer, den ich je hatte!

Ich danke auch dir, Christian Tritremmel, für dein ausgeglichenes Wesen, wenn die Diskussionen gar „heiß“ wurden. Ich danke dir für die vielen Ideen zur Probenpräparation.

Die komplizierte Welt der Eigenspannungsmessung erklärte mir Paul Angerer. Einen großen Dank für die vielen Stunden an Diskussionen und Beantwortung der Fragen. Ohne dich wäre ein Großteil meiner Veröffentlichungen nicht möglich gewesen.

Od srca bih se rado mom kolegi Ivanu Kranijovic zahvalila, koji je moj rad sa FE-Simulacijama podrzavao.

Danke, Michael Tkadletz für deine Unterstützung in der Beantwortung der Fragen über die thermischen Eigenschaften der Beschichtungen.

Ich danke auch Andreas Bubnik, der mit viel Geduld und Liebe zum genauen Messen mich bei den Eigenspannungsuntersuchungen unterstützte. Des Weiteren gilt auch mein Dank Kevin Tobisch, ohne seine Ausdauerfähigkeit beim Spulenbau wäre keine Hochtemperatur Fließkurvenbestimmung möglich gewesen. Ich danke auch allen Mitgliedern des Umformtechnik Instituts, insbesondere meinem Studienkollegen Roland Kasberger, die an der Idee des Probeneinschrumpfens geglaubt und mich unterstützt hatten.

Ich möchte auch Prof. Jozef Keckes und Prof. Reinhard Pippan danken, die mir sowohl die Synchrotron- als auch die Bruchzähigkeits- „Welt“ näher gebracht habt und immer ein offenes Ohr für meine Fragen hatten.

Ich hatte auch das unendliche Glück einen der besten studentischen Mitarbeiter zu betreuen. Danke Clemens Kremsner, ohne dich wären die Hochtemperatur K_{IC} Versuche nie so zu Stande gekommen.

Ich danke meinen Jungs im Büro: Uwe Oßberger, Hiasi Jonke, Phippo Thomma, Ändi Keplinger und Luki Pritz. Ihr habt mir erlaubt die männliche Psyche besser zu verstehen, und

andererseits danke ich auch den Mädls Marina Gruber und Annika Vieweg. Ihr alle habt mir geholfen meine technischen Probleme aus einem anderen Blickwinkel zu betrachten. Ich habe die Zeit bei euch sehr genossen!

Auch in Tirol bei Ceratizit Austria GmbH arbeiteten viele Leute im Hintergrund, ohne die das Projekt niemals so erfolgreich gewesen wäre; ein großes Dankeschön an alle Mitarbeiter der F&E Carbides and Coatings insbesondere Christa Bader und Christian Jäger, die den kühlen Überblick über meine Vielzahl an Proben bewahrten. Des Weiteren danke ich Angelika Strobl für die Durchführung der Strahlversuche. Auch dem Team der F&E Tooling Academy und hier in Besonderem Markus Lorenz danke ich für die geduldige Durchführung der Frästests, welche essentiell für diese Arbeit waren. Einen großen Dank auch an dir, Ingo Pirker, für deinen Einsatz bei der Planung und Fertigung der Versuchsproben für die HT-Druckversuche. Auch möchte ich Peter Schoderböck danken für die Durchführung der Tests an Laser Flash und Dilatometer.

Es ist wichtig Personen im Hintergrund zu haben, die einem die nötige Stütze geben um an sein eigenes Wesen zu glauben. Ich danke meinen Mädls July Pachlhofer, Leni Mühlbacher Marion Werinos und Rebekka Stadler. Ich danke dir, Sarah Kettner, die in den dunkelsten Momenten einfach da war. Ich danke Marion und Dietmar Pachlhofer, die mir den Start in Tirol um so vieles erleichtert haben. Ich danke meinen Geschwister Georg, Griseldis und Simon, und meinem Vater. Ohne euch alle wäre ich nur ein halber Mensch.

Financial support by Austrian Federal Government (in particular from Bundesministerium für Verkehr, Innovation und Technologie and Bundesministerium für Wirtschaft, Familie und Jugend) represented by Österreichische Forschungsförderungsgesellschaft mbH and the Styrian and the Tyrolean Provincial Government, represented by Steirische Wirtschaftsförderungsgesellschaft mbH and Standortagentur Tirol, within the framework of the COMET Funding Programme is gratefully acknowledged.

Content

1 Introduction

Machining of iron based workpiece materials is a widely used production method in several industries like automotive industry, mechanical engineering and energy generation. Therefore, milling is a frequently applied method for material removement. The milling application is identified by rotating the tool and moving it relative to a fixed workpiece material, which leads to non-constant cutting conditions. Due to this intermittent cutting, alternating mechanical and thermal loads are acting on the tool during cutting and idle period [1]. To meet the increasing demands in metal cutting, most of the tools are made of hardmetal based on a hard phase mainly consisting of WC and a soft binder phase, most frequently Co. The whole tool can consist completely of hardmetal (solid carbide drills, endmills, reamers) or smaller inserts can be fixed on a steel holder. This depends on the application and the price of the hardmetal [1]. Most of the hardmetal tools are coated with a hard coating to enhance the service life in metal cutting. These hard coatings are produced either by physical vapour deposition (PVD) or by chemical vapour deposition (CVD) [2].

State of the art in milling application for steels are inserts consisting of hardmetal grades with varied Co content from 6 to 13 wt.% Co and coatings based on PVD Ti-Al-N or Cr-Al-N, as well as CVD TiCN-Al2O3. Additional post treatments of the coating, e.g. dry blasting process, showed an enhanced performance in cutting application [3].

For further improvements of hardmetal substrates and hard coatings, it is necessary to expand the knowledge of damage evolution during the milling application.

In milling the damage is identified by abrasive wear marks [1],[4] and thermal fatigue in form of characteristic cracks [5], which were often referred to combcracks in literature.

An introduction of tensile residual stresses parallel to the cutting edge due to cyclic thermal and mechanical loads foster the nucleation and growth of [5]. Either cyclic thermo-shock due to the alternating temperature loads between heating upon cutting and cooling upon idle period [5],[6], or localized plastic deformation, induced by mechanical loading and the increased temperature during cutting, introduce these residual stresses [7].

In open literature the location of these residual stresses in the milling inserts and their evolution in the hardmetal substrate as well as in the coating within the cutting process are not well documented.

Thus, the aim of this thesis is to enhance the understanding of the main damage mechanisms wear and thermal fatigue, and the evolution of residual stresses in coated milling inserts over the complete lifetime.

Therefore the location, magnitude and evolution of residual stresses and the corresponding damage state in the substrate as well as in the coating were determined till the end of

service life. Special emphasis was laid in investigations of combcracks, their location, and their appearance shown in cross sections as well as their enlargement in the volume of an insert. Additionally, a dry blasting process and the influence of the blasting time on residual stress evolution in the hardmetal at early stages in milling application were investigated.

The cutting temperature has a crucial influence on the flow behavior and wear resistance of the coating and the hardmetal substrate and consequently on the lifetime of an insert. Therefore the apparent temperatures were determined on the insert's surface outside of the contact zone between insert and workpiece.

The finite element (FE) simulation is a further important tool to estimate the cutting temperatures and cutting forces during application [8]. To provide reliable material models, it is necessary to determine thermo-physical and thermo-mechanical data of the substrate material as well as that of the coating. Within this work these material data of the used hardmetal grade were determined at elevated temperatures.

The calculated cutting temperatures and stresses were validated with the results of the residual stress and temperature measurements, which were apparent during the milling experiment and showed good agreement.

The generated methods and materials data are a powerful tool to enhance the understanding of the wear behaviour and thus to increase the lifetime of tools in milling operation.

2 Theoretical background

In the following sections the reader is introduced to the production of a coated hardmetal milling insert. Special emphasis is put on the coating synthesis and their structure properties. An overview of milling applications, their apparent cutting forces and temperatures, which act on a milling insert during application, is also shown in this chapter. A particular part of this thesis is devoted to the apparent main damage mechanisms wear and thermal fatigue during the milling application and the creation of combcracks which determine the insert's lifetime.

2.1 Production of hardmetals

Most of the milling inserts used in metal cutting applications are based on hardmetal. Hardmetal is produced via powder metallurgy route. Hardmetal consists of a hard phase, which is mainly tungsten carbide (WC) and a soft binder phase, which is most commonly cobalt. Some amount of other carbides, e.g. titanium, tantalum, niobium, zirconium and vanadium carbides can be added [9]. Fig. 1 shows the manufacturing process of a coated hardmetal cutting insert from weighing the raw materials for producing granulate, pressing it into shape, sintering and coating the inserts.

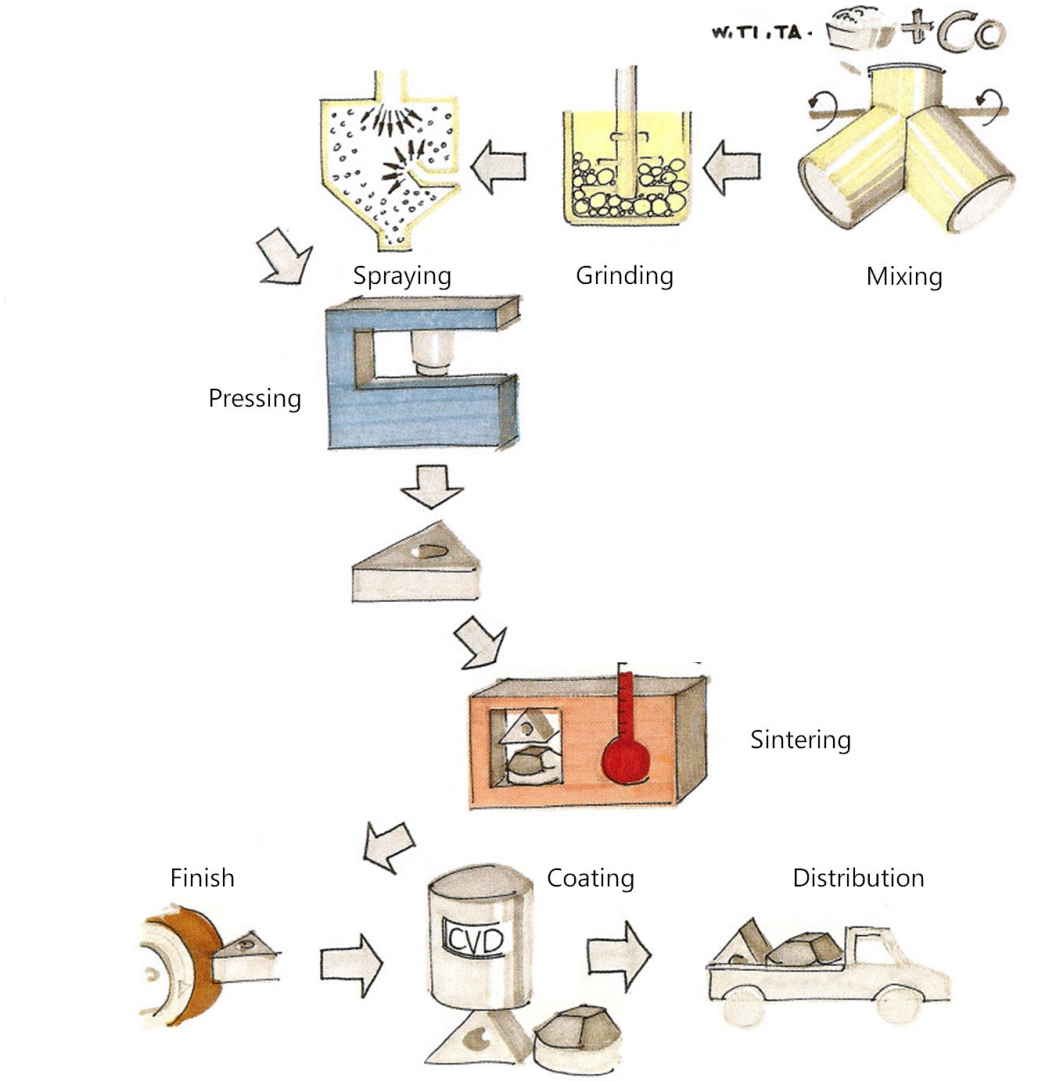

Fig. 1: Schematic production line of a coated hardmetal based milling insert [9]

After weighing the raw material powders, all ingredients are mixed and ground in an attritor, see step two in Fig. 1. The attritor may be filled up with raw material powder, WC balls and with benzoin or alcohol or acetone [9],[10], but within this work the powder was mixed with water [11]. After the grinding step a plastifying agent, paraffin wax, is added to the water-powder emulsion. This waxing step is important for the latter direct pressing step [9]. To produce a hardmetal granulate, the dissolver has to be removed from the emulsion by a spay-drying process (c.f. Fig. 1).

The dried granulate should exhibit narrow size distribution which results in good free-flow properties, necessary for the pressing process. To achieve suitable size distribution the dried agglomerate hardmetal powder has to be sieved.

The hardmetal granulate is commonly uniaxially pressed to form the green body of cutting inserts, because of its high productivity [12]. The pressure between the top and the bottom punch can reach a value between 100 and 300 MPa [9], which corresponds to a green

density from 20 to 60 % of the theoretical density [12]. The right compaction pressure and consequently the green density are important for reaching a good sintering result. On the one hand, a too low pressing pressure results in pores at the finished sintered milling insert. On the other hand, a too high pressing pressure has a negative influence on the green tool itself, which may result in cracks and swelling in the green parts [12].

To reach a theoretical density of 100 % of the finished inserts, the green parts have to be sintered. During heating up to the sintering temperature, there is a previous dewaxing step at temperatures between 300 and 600 °C. Here, the heating velocity is reduced [9]. In this temperature range the paraffin wax is removed in form of CO or CO_2 as long as the pores of the green parts are open. Sintering without the dewaxing step results in pores filled with gas in the finished part [9]. During sintering under vacuum at temperatures above 1300 °C the Co phase is liquid, and parts of the WC grains skeleton are dissolved. At the sinter temperature approximately 15 % of the specimen volume is in the liquid phase. This liquid Co phase wets the WC grains and closes all pores. During cooling the WC grains are resolved again [9]. The finished sintered milling insert exhibits 50 % less volume compared with the green part.

After sintering process the inserts have to be grinded and edge honed. Most of the cutting inserts are coated. These hard coatings can be produced either by chemical (CVD) or physical vapor deposition (PVD) [2].

2.2 PVD Ti-Al-N based coating systems and cathodic arc evaporation

Milling inserts coated with a hard coating show an enhanced service life during the application due to improvements in hardness, wear resistance and thermal resistance. For more than 35 years TiN was one of the most widely used hard coatings on the hardmetal substrates. TiN is characterized by a high hardness of 2300 HV 0.05 and good toughness [9], but there is limitation in oxidation resistance at temperatures above 500 °C [2]. To improve the oxidation resistance TiN can be alloyed with Al. The metastable ternary system Ti-Al-N shows a high oxidation resistance, a low thermal conductivity and a high hardness [13], and was introduced in 1998 as tool coating. The increase of hardness can be explained by the increasing lattice distortion with increasing Al content in the TiN lattice [14],[15] (see Fig. 2).

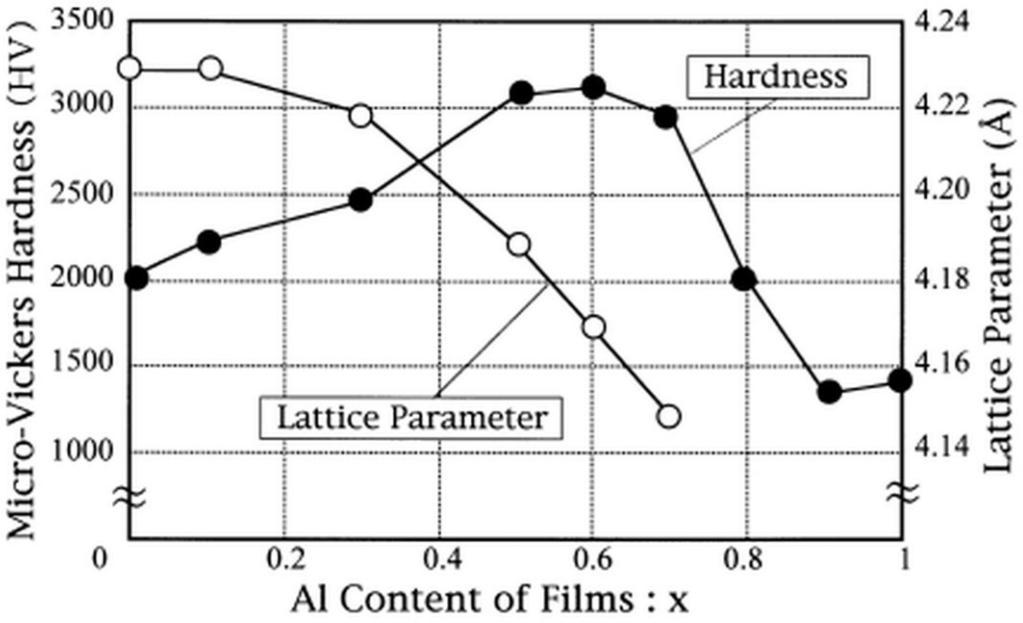

Fig. 2: Hardness and lattice parameter in dependence on the Al/(Al+Ti) ratio in the $Ti_{1-X}Al_XN$ system [15].

Depending on the Al content, Ti-Al-N coatings can crystallize in different crystallographic structures. For lower Al content they consist of a single-phase face centered cubic (fcc) solid solution. The area of existence of the fcc $Ti_xAl_{1-x}N$ varies in the literature form 55 mol% to 67 mol% AlN [13]. The Al atom is smaller than the Ti atom resulting in a decrease of the lattice parameter in the fcc lattice, see Fig. 2. The coating can also crystallize in the dual phase of the fcc and hexagonal closed-packed modification (hcp). A higher Al content fosters the hcp modification, which shows inferior mechanical properties than the fcc modification [14], e.g. decreasing hardness, see Fig. 2. Within this work used Ti-Al-Ta-N coating with 61 mol% AlN exhibits a pure fcc crystallographic structure, which was determined by X-ray diffraction [16]. The addition of Tantalum in the Ti-Al-N structure also distorts the lattice cell and reduces of the crystallite size resulting in a further increase of hardness [17].

In the cutting application temperatures up to 1000 °C can be apparent. Therefore a high thermal stability is important. Ti-Al-N based coatings show a decomposition resulting in hardness increase due to age hardening in a temperature range from 600 to 950 °[18]. Fig. 3 shows the four exothermic reactions in two Ti-Al-N coatings with different amount of Al content, which were detected via differential scanning calometry (DSC) [18].

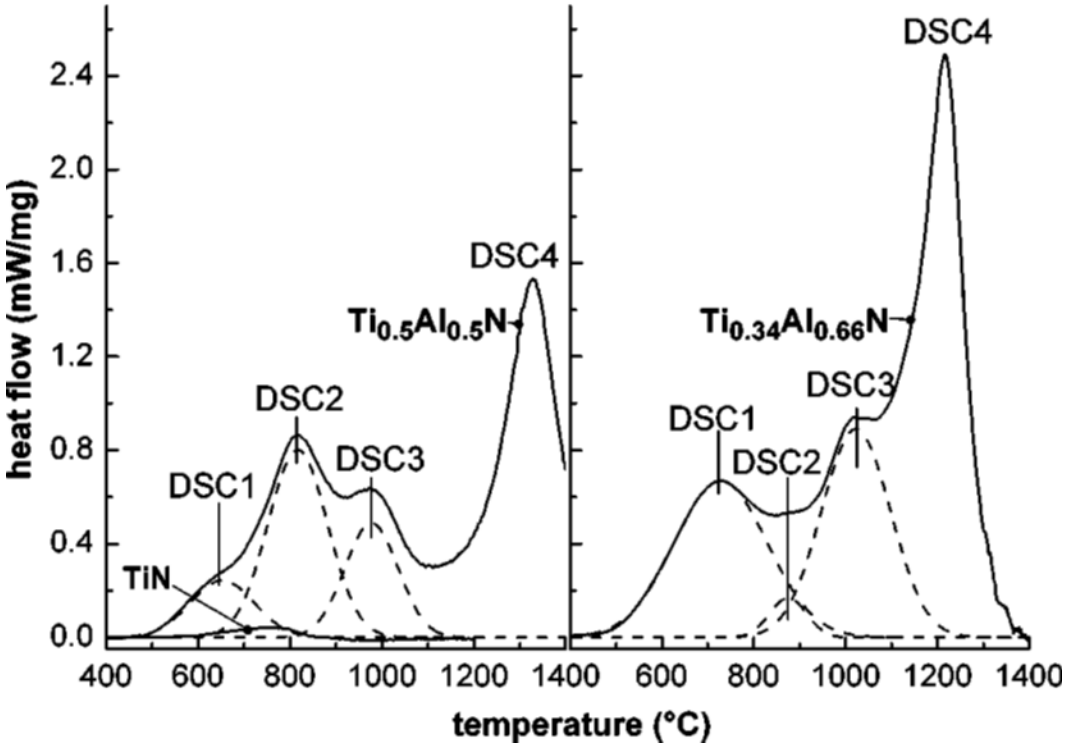

Fig. 3: DSC measurements of two different Ti-Al-N coating systems [18].

The first reaction (DSC1, see in Fig. 3) starts from 500 to 800 °C and is a recovery process. During the second reaction (DSC2) some Ti-Al-N domains are enriched with fcc AlN, which increases the hardness due to the formed coherent strains. At ~900 °C the third reaction (DSC3) starts and the coating now consists of three different phases. Within the fcc Ti-Al-N matrix there are fcc AlN and fcc TiN apparent. The fourth reaction (DSC4) at ~1300 °C completes the decomposition process, in which the fcc AlN phase is transformed into the hcp structure [18].

Most of the industrial coatings for cutting inserts (e.g. Ti-Al-N coatings) are deposited by cathodic arc evaporation (CAE) process. CAE is often used in industrial application because the technique is fast and efficient compared with a sputter process [2]. The cathode is vaporized under arcing conditions whereas the substrates, which can be cutting tools, as well as the wall of the chamber, are the anode [2],[18]. The process runs with several cathodes and the cutting tools are fixed on rotating rods. This rotation is needed for homogenous deposition. A vacuum with pressure below $1\text{-}10^{-5}$ Pa (10^{-2}-10^{-7} mbar) is necessary to reduce collisions of particles during transport between substrate and targets [19]. Due to the roughness of the target surface and consequently the limited size of surface asperities, field emission is fostered, which creates an arc. This arc is concentrated on one point of the target, it has a diameter between 1 and 20 µm and exists for 5 to 40 ns [2],[20]. The target material evaporates immediately and the ions are accelerated to the substrate due to the applied negative bias voltage between target and substrate. The

localized removal of the cathode material creates a crater. The field electron emission decreases and the arc does extinguish. At the edge of the crater a new surface peak is created and a new arc starts. The process is repeated again [21],[22]. Molten particles with a diameter of several µm can also be created during the evaporation. These particles are also partly transported with the particle stream towards the substrate and cause defects in the coating. These defects are typical in CAE coatings and they are called droplets. These droplets influence the coating properties negatively due to the increasing inhomogeneity of the structure and composition, for instance the hardness is decreased [21],[22].

2.3 Milling

Milling is a cutting process which is identified by a rotating tool that cuts a fixed workpiece material (see Fig. 4). Due to the intermittent cut, alternating mechanical and thermal loads act on the tool during the milling process. A further characteristic of the milling application is the production of chips with non-constant chip thicknesses [1],[23].

The milling process can be distinguished into plain-, face-, profile- and plunge milling [23],[24]. Plunge milling is used for creation of notches and profile milling is chosen to form threads. For preparing flat surface areas, plain and face milling are the preferred milling arrangements. Plain milling is used for small areas. Face milling is the favorite milling application to reach good surface quality on large areas.

Within this work, the face milling is in the main focus, which is schematically shown in Fig. 4. Most of the face milling operations was done using milling inserts in a milling tool holder [23]. Coated hardmetal based milling inserts are the preferred material to mill steel materials [1],[25].

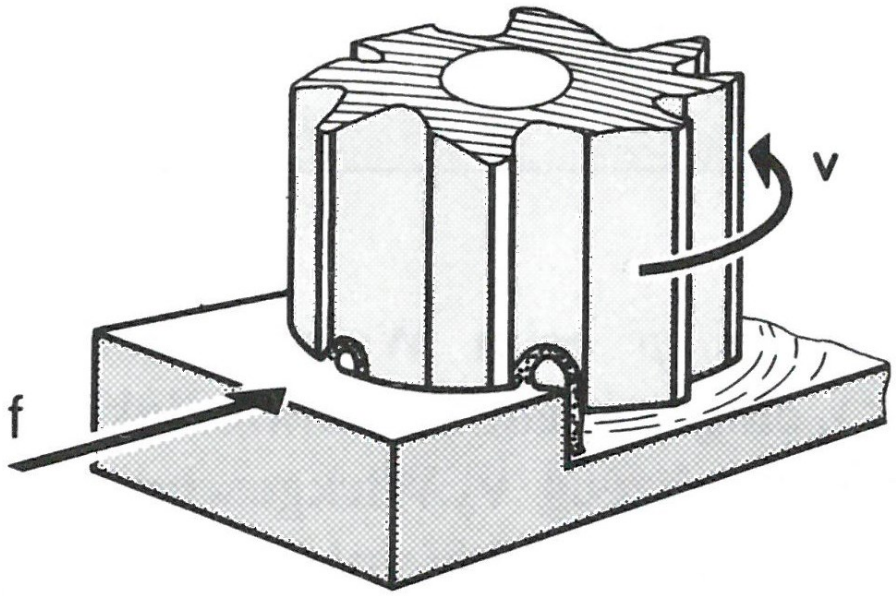

Fig. 4: Scheme of a face milling arrangement, in which the milling tool is fixed perpendicular to the workpiece surface [23].

Face milling is identified by milling tool holder, which is perpendicular fixed to the surface, which has to be cut, see Fig. 4. Within this face milling the inserts' cutting edges have contact along the front and the peripheral cutting edges [23].
The rotation direction of the milling tool determines milling in climb-cut or up-cut milling arrangement, which is illustrated in Fig. 5.

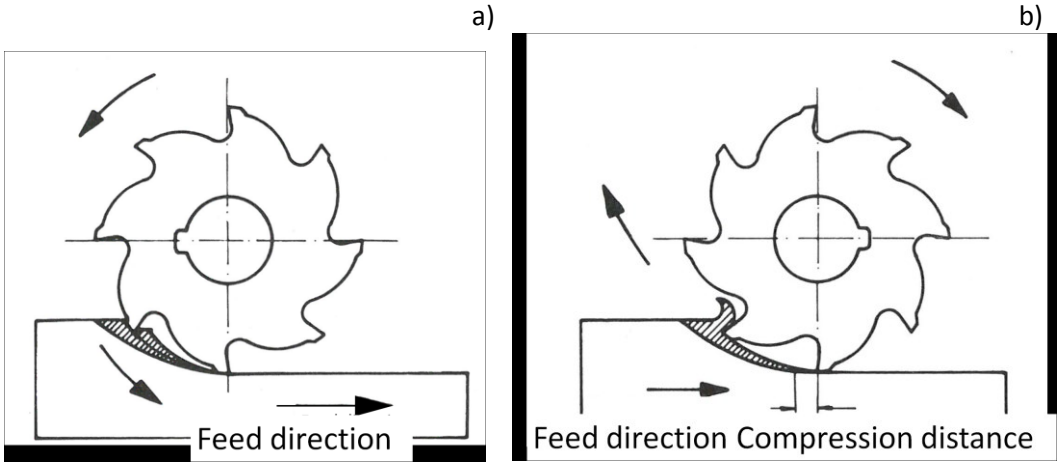

Fig. 5: Scheme of the a) climb-cut and b) up-cut milling [23].

In the climb-cut milling arrangement the rotation direction of the milling tool is the same as the feed direction. Cutting under climb-cut mode is indicated by high chip thickness at the beginning of a contact and decreasing chip thickness to zero to the end of the cut. This

milling arrangement induces many vibrations and consequently the milling inserts and the milling holder have to be rigid [23]. In this case high contact pressures at the cutting edge are apparent at the beginning of the cut till the chip formation takes place [24],[26]. In contrast, the up-cut mode is indicated by a contrary rotation direction of the milling tool and the feed direction. Here, the chip thickness is low at the beginning of the contact and it increases with increasing duration of the cut [23],[24],[26]. In this case the milling inserts have to slip a specific distance along the workpiece without a significant cutting, see Fig. 5b). Depending on the slip distance, some amount of heat is induced into the insert due to friction [23],[24],[26].

The face milling arrangement also gives the opportunity to mill in climb-cut as well as in up-cut mode within one contact with the workpiece, referred to symmetric milling, shown in Fig. 6.

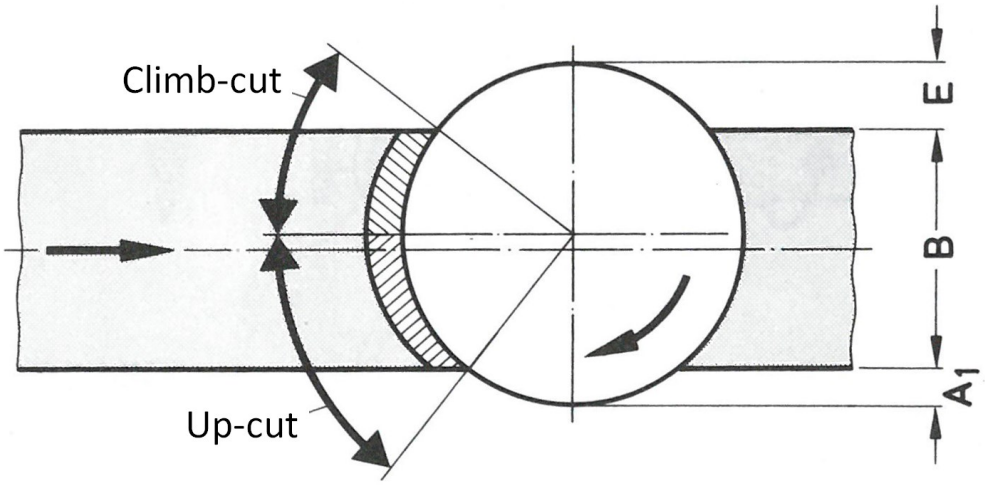

Fig. 6: Symmetric cutting where milling in climb-cut as well as in the up-cut mode is apparent during one cut [23].

For milling in this combined mode the ratio between radius of the milling tool and cutting broadness (indicated as *B* in Fig. 6.) has to be higher than 50 %. Cutting under this combined mode gives the opportunity to increase the efficiency of the milling process because the apparent cutting forces are well-balanced over the whole cut [23].

For designing new cutting materials and new cutting geometries the knowledge of the occurring cutting forces and temperatures (see details in chapt. 2.4) are important. In milling experiments they are often determined by a force dynamometer in which inside 3-component piezoelectric force sensors are mounted [27]-[29]. The force parallel to the feed direction, normal to the feed direction and the normal force can be determined [29],[30]

and increase with increasing feed rate, cutting depth and strength of the workpiece material. The detected data can be used in FE simulations to calculate the apparent stresses, which act at the cutting edge [31]. Bouzakis et al. calculated the resulting von Mises stresses in the coating material at the cutting edge [32]. With increasing cutting edge radius the maximum Mises stress decreases.

2.4 Cutting temperature in milling

The design of new cutting materials and new cutting geometries needs the knowledge of apparent temperature on the insert's surface within and outside of the chip contact zone [33]. The FE simulation is a powerful tool to calculate strains, stresses and temperatures. For validation the FE simulation requires temperature measurements in cutting experiments. Therefore, real temperature measurements are the preferred choice [34]. A short overview of apparent methods of temperature measurements and the general hypothesis of cutting temperature in milling are given within this chapter.

2.4.1 Methods of cutting temperature determination

Using thermocouples for temperature measurements is a common method in metal cutting [33]. The advantages of this method are the accurate time resolution, the wide range of temperature detection and the price. The physical principle of the thermocouples is based on the Seebeck effect, where a voltage is created due to the temperature difference between the beginning and the end of a metal conductor [35]. In most of the cases these thermocouples were positioned inside of the inserts or in the tool holder. To fix the element very close to the contact zone, a hole has to be drilled and the thermocouples are positioned inside [33]. Three facts influences negatively the correct temperature measurement in hard metal based inserts in milling application:

(a) Due to the low thermal conductivity of hard coating the temperature gradient is very steep and the region of apparent highest temperatures are small, in a range of µm², and concentrated at the surface [33]. The smallest conventional thermocouples exhibit diameters down to 0.22 mm [36]. Temperature measurements via thermocouples can only determine a mean temperature underneath the contact zone [33].

(b) Lower temperatures can be detected as in reality due to thermal resistance of the contact conditions between thermocouple and surface of the hardmetal. In milling application the tool rotates and the thermocouples have to be fixed with glue, which exhibits metal particles, e.g. Silver. The roughness of the drilled hole and the glue create a temperature difference between the surface of the thermocouples and the surface of the hardmetal within the hole [33].

(c) Especially in climb-cut milling, the beginning of a cut is determined by high cutting forces. The hole with the thermocouples has to be located closely to the cutting edge. This weakens the cutting edge and increases the risk of catastrophic failure of the insert [33].

The temperature measurement via a thermal resistor is based on the knowledge of the temperature dependent electric resistance of the materials [35]. The area of temperature measurement is limited to 850 °C [36]. The handling of temperature resistor is similar as for the thermocouples. Thermal resistors exhibit a diameter from 1.6 to 6.0 mm [36]. Due to the comparable handling with the thermocouples, this system has the same disadvantages in milling application as described before.

There are opportunities to measure contactless the temperature during cutting via thermo camera or pyrometer. The temperature calculation of both methods is based on the Plank's law [37] and Wien's displacement law [38]. The advantage of both methods is the wide range of temperature measurement and no loss of temperature information due to the wrong contact conditions, which thermocouples and –resistor might have.

Fig. 7 shows a test setup using a pyrometer in a turning operation. Using a pyrometer for temperature measurement is characterized by recording frequency of 1000 Hz [39].

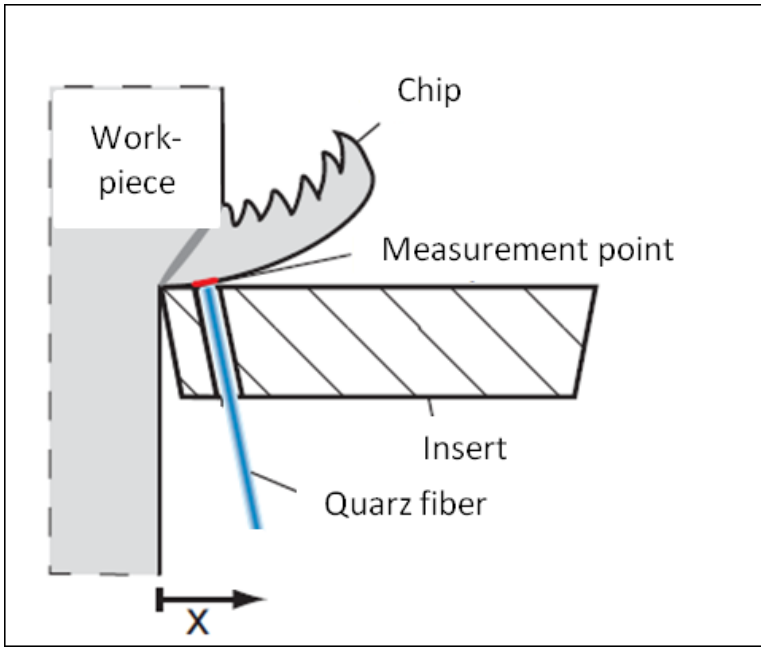

Fig. 7: Schematic view of a test setup for temperature measurement during a turning process using a quarz fiber pyrometer [39].

To measure the temperature in the contact zone, an insert prepared with a hole is necessary [39]. Also here, the danger of catastrophic failure is high in climb-cut milling [33].

All discussed measurement methods determine the temperature at one position. Position resolved temperature measurements are hardly possible because it requires several drilled holes within the insert [33].

The temperature measurement via thermo camera gives the opportunity to measure temperature mappings outside of the contact zone on the surface of the insert during application [33]. But, this advantage decreases the recording frequency. The highest recording frequency is 250 Hz, which results in a loss of information during the cutting especially in milling applications [33]. There, cut duration can be in the same time range. Additionally in a milling test setup, the thermo camera has to be protected from flying chips, which were produced after each contact with the workpiece. This protection is necessary because the equipment is more cost intensive [40] than other measurement methods. Further, this method is limited to dry cutting operations.

Detection of areal temperatures can also be done by thermo paint and thermo chalks [41]. The costs of the thermo paints and chalks are very low [42] and the inserts can be prepared easily [41]. Both, the thermo paint and the thermo chalk exhibit a specific color at RT. After heating up of an insert's surface area to a specific temperature, there is a color change, which is irreversible [41]. Some thermo chalks exhibit temperature levels for color change of one temperature up to four temperatures. The use of thermo chalks is limited to temperatures up to 600 °C. Whereas the thermo paints exhibit a wide temperature range of application and can be used from RT to 1200 °C. They have many temperature levels with step size from 30 to 150 °C, where the color change can take place [42].

The reaction time of thermo paints and chalks is a disadvantage. When the specific temperature is effective, the thermo paints need 10 min and the thermo chalk needs 2 s to react and convert into another color [42]. If the apparent temperatures are higher than the needed specific temperature for color change, the reaction time is shorter. Only the mean temperatures on the surface can be determined [42].

Due to their time and cost efficiency thermo chalks were the favorite choice for temperature measurement within this work. They are used for the validation of FE simulation in cutting experiments [34].

2.4.2 Temperature evolution in milling

During milling application, the temperature as function of time is indicated by a period of exponential temperature increase during the insert-workpiece contact and an exponential temperature decrease during the idle time. At the beginning of the milling process the mean insert temperature increases linearly with the number of cutting cycles [5],[43]. The variation of the tool temperature during milling is illustrated in Fig. 8.

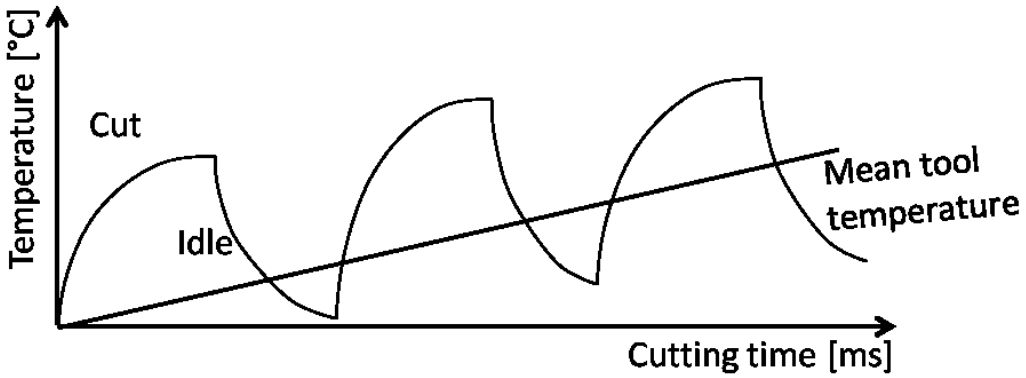

Fig. 8: Cutting temperature evolution of an insert during milling [43].

There are no explicit statements in the literature about the exact cutting temperatures. Many authors assume that the insert reaches temperatures between 800 and 900 °C within the contact zone during cutting and the temperatures decrease to values between 250 and 300 °C in the idle period [4],[5],[44]. Bouzakis et al. argue that the cutting temperature has to be the same or lower than the deposition temperature of the coating, which corresponds to a temperature of ≤ 500 °C. They assume that there is a strong impact of this fact on coating failure and wear evolution when the cutting temperatures are higher and the danger of premature failure before 5×10^4 cycles is increased [32].

2.5 Combcrack formation in milling tools

The dominant damage mechanisms in milling are abrasive wear and thermal fatigue [5]. Abrasive wear in form of flank wear or crater wear is indicated by a removal of coating material from the tool surface [1],[4]. It strongly increases when debris in the form of hardmetal and coating fragments are formed by the shattering of exposed surface features such as combcrack flanks [5].

The key factor influencing thermal fatigue is the temperature difference between maximum temperature after heating and minimum temperature at the end of cooling in idle period [5],[6]. After certain numbers of tool-workpiece contacts, characteristic cracks appear with propagation planes perpendicular to the cutting edge of a milling tool [5],[6]. These characteristic cracks will be referred to combcracks within this thesis. Both damage mechanisms can be seen on the rake and flank face of an uncoated milling insert at the end of lifetime in Fig. 9.

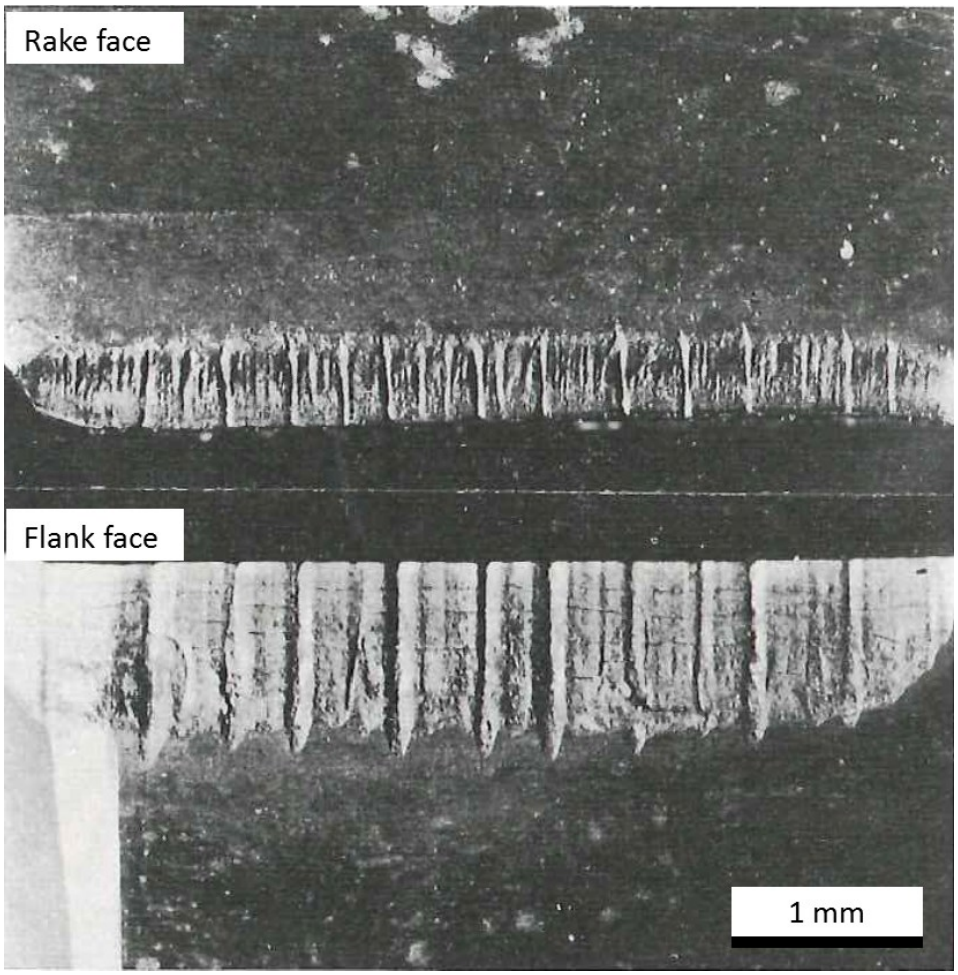

Fig. 9: Rake and flank face of a milling insert at the end of lifetime. During cutting the workpiece material slips from the cutting edge over the rake face, the plane perpendicular to the rake face is indicated as flank face. Combcracks propagate perpendicular to the cutting edge. Adhesive and abrasive wear marks are visible [5].

Cyclic thermo-shock can foster combcrack formation [5],[6]. During the idle period, when high cooling rates are effective and the surface temperature falls below the mean temperature (see Fig. 8), the creation and evolution of tensile residual stresses are to be expected, if the substrate is deformed plastically during the heating period [5],[6]. Combcracks can be apparent in milling under dry conditions as well as in milling using lubricants. After the creation of the first combcracks, the crater wear increases disproportionally because the edges of the combcracks are shattered which increases the amount of debris of hardmetal and coating fragments [43].

Opitz and Lehewald [5] expected that residual stresses are oriented parallel to the cutting edge. It is apparent that these residual stresses promote crack initiation and growth. Yellowley and Barrow [7] described that combcracking is induced by a compressive yielding of the surface layer of an insert in the heating cycle and the tensile residual stresses in the

cooling. Cyclic mechanical loads in form of alternating contact pressure between chip and tool may also introduce local plastic deformation close to the cutting edge [7].

This local plastic deformation is introduced by thermal stress amplitudes induced by frictional heating, which appears in a small area close to the cutting edge [7]. The combination of high cutting forces and high temperatures may exceed the flow stress of a tool material due to the combination of current thermal stresses and sufficiently high mechanical load stresses during cutting. Plastic deformation may be apparent in a localized region during cutting. During cooling, the material of this region is prevented on contraction. These loads can trigger the build-up and evolution of tensile residual stresses in the cutting edge of milling inserts [7].

Ekemar et al. assumed that the hottest point on the surface of the rake face is the site of crack initiation [6]. Dependent on cutting edge geometry the location of this site varies within distances of several hundred micrometers from the cutting edge [6]. The use of liquid cooling agents in milling leads to higher thermal shocks which fosters the creation of combcracks [43]. Combcrack formation in milling inserts can be suppressed by lowering the temperature amplitudes acting localized at the tool edge, e.g. by heating the inserts [5].

Another hypothesis on the combcrack formation is the high difference of the linear thermal expansion coefficient between WC and the Co binder phase in the hardmetal substrate. The difference induces residual stresses during cooling due to the higher contraction of the Co phase which results in tensile residual stresses in the Co phase and compressive stresses in the WC phase [45].

Bathia et al. described a combination of process parameters under which no tool failure induced by combcracks occurs in interrupted cutting of mild steel plates (S275JR, 1.0044, R_m~ 470-630 MPa [46]) due to subcritical thermal or mechanical loading [47]. The feed rate and the cutting speed have to be lower than 0.1 mm/revolution and 90 m/min, respectively. The machine parameter intervals for the described process field of thermal fatigue tool failure are also influenced by the radius of the tool's cutting edge. A milling insert with a large cutting edge radius widens the machine parameter field in which wear rather than fracture determines tool life [47].

3 Experimental background and test procedure

The milling inserts were tested in two different test setups. Details of the testing parameters, the used workpiece grade and the test matrix are given in this section (see details in 3.5, 3.6, 3.7). Within this work the inserts are based on an 8 wt.% Co hardmetal grade and a PVD Ti-Al-N based hard coating. Details concerning the insert geometry, the microstructure of the hardmetal grade, and the material properties of hardmetal as well as the hard coating are shown in chapters 3.1, 3.2 and 3.4.

To document the influence of a dry blasting process and the blasting time on the residual stress in the substrate and the damage evolution in milling application, selected inserts were post treated. The used blasting media and blasting time are described in chapt. 3.3.

After the milling experiments, the damage and the residual stress evolution over the complete lifetime of the milling inserts were determined. The applied methods are presented in the sections 3.9 and 3.10.

The understanding of loads and temperatures being situated at the cutting edge during application is rare in the current literature. Within this work, an estimation of the cutting temperature by investigation of microstructure changes of the workpiece, using thermo chalks on the milling inserts and the use of FE simulation [34] was conducted (see chapt. 3.8). The FE method is also a powerful tool to estimate mechanical tool loads [48]. The realistic simulation of temperatures and loads in the WC-Co substrate during cutting [34] requires detailed knowledge of the mechanical, thermo-mechanical and -physical properties. In cutting application elevated temperatures are apparent and these material data are rather rare in the open literature. This chapter also discusses the used testing method for determination of thermal diffusivity and – conductivity, heat capacity and thermal expansion coefficient, elastic material properties, compressive yield strength and fracture toughness at elevated temperature (see details in chapt. 3.11).

3.1 Hardmetal properties and microstructure

Within this work, one specific hardmetal grade was used in the milling inserts as substrate material. The chemical composition, density, magnetic saturation, coercivity and hardness of the hardmetal grade are shown in Tab. 1. The density of the hardmetal was determined by means of the principle of Archimedes according to ISO 3369 [49]. The magnetic saturation was determined by a Helmholz coil and the coercivity was detected by a Koerzimat according to standard ASTM B886 [50].

Tab. 1: Chemical composition, density, magnetic saturation, coercivity and Vickers hardness of the used substrate material.

WC [wt.%]	Co [wt.%]	Mixed carbide (TaC, NbC) [wt.%]	Density, ρ [g/cm³]	Magnetic saturation, $4\pi\sigma$ [T×m³/kg]	Coercivity, H_c [A/m]	Hardness *HV30* [-]
90.4	8.0	1.6	14.68±0.05	153±8	11857±1194	1414±50

The microstructure of the hardmetal is visualized via scanning electron microscopy (SEM) in Fig. 10. The polyangular shaped light grey phases represent the WC phase and the black regions correspond to the positions of the Co phase. The darker gray phases characterize the mixed carbides. The surface was ground and polished using a diamond paste to remove the surface damages. In addition, the samples were polished using a colloidal silica suspension (OP-S suspension). OP-S polishing enables the visualization of WC grain boundaries by removing the softer Co binder phase [51]. The WC grain size of the investigated hardmetal grade is about 0.704 ± 0.006 µm. The perimeter of the WC grains was observed using the electron backscatter diffraction (EBSD) method. The samples were tilted with an angel of 60° in the scanning electron microscope (SEM, Crossbeam field emission gun, Zeiss Auriga) and the DigiView IV EBSD detector was used. The WC grain size is an average value of about 400 detected WC grains.

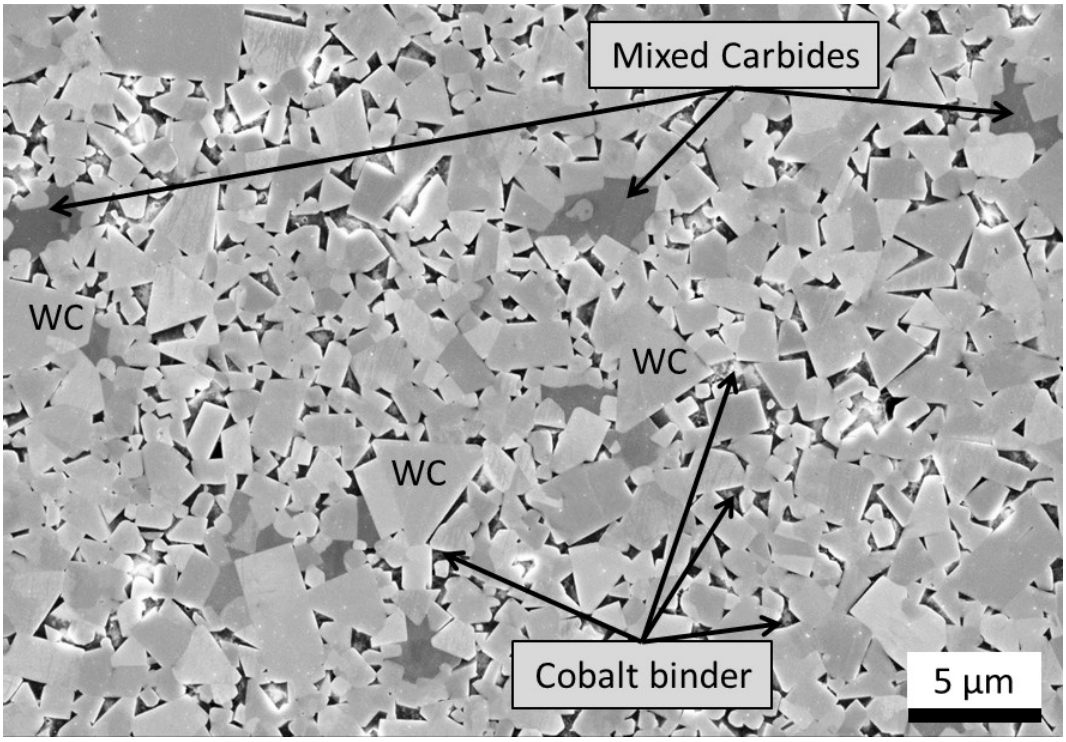

Fig. 10: SEM micrograph of the microstructure of the hardmetal grade. Grey shaped grains are the WC phase and the darker grey grains are the mixed carbides. The black/ dark areas around the WC grains are the areas of the Co binder phase.

3.2 Ti-Al-N based hard coating

All milling inserts were coated with an 8 µm thick Ti-Al-Ta-N film via PVD using CAE process in an industrial scale PVD device [2]. The chemical composition of the coating was determined via glow discharge optical emission spectroscopy (GDOES) and is summarized in Tab. 2 and [16].

Tab. 2: Chemical composition of the Ti-Al-N coating [16].

Ti [at.%]	Al [at.%]	Ta [at.%]	N [at.%)
18.5	30.8	0.7	50.0

The Ti-Al-Ta-N coating used within this work exhibited a hardness of about 30.8 ± 1.1 GPa and a Young's modulus of about 499.3 ± 13.3 GPa. Both values were determined by the method of Oliver and Pharr [52] using nanoindentation (CSM nanoindenter) with a Berkovic diamond tip and test load of 30 mN [16]. To reach a statistically relevant hardness value, 16 indents were averaged.

The fracture toughness values of this coating are hardly available in the open literature. But, the fracture toughness of a Ti-Al-N based hard coating is known and about 3.8 MPa√m [53].

The thermo-physical properties of the Ti-Al-Ta-N coating were determined by Tkadletz et al. [54]. The coating exhibits a heat conductivity of about 5.8 ± 0.6 $Wm^{-1}K^{-1}$, which was determined by time-domain thermo reflectance method [54]. The thermal expansion coefficient of the coating was determined up to 700 °C by high temperature X-ray powder diffraction. The Ti-Al-Ta-N coating exhibits a thermal expansion coefficient of 5.64×10^{-6} K^{-1} [54].

3.3 Post treatments

After deposition selected inserts were post-treated via a dry blasting process. An injector blasting facility was applied using a blasting pressure of 3 bars. Spherical particles composed of zirconia, silica and alumina with grain sizes ranging from 125 µm to 250 µm and three different blasting times were chosen. After 168, 252 and 336 seconds the blasting process was stopped, see details in own publication IV [55].

3.4 Milling insert

In all milling experiments the same milling insert geometry was used. The schematic view of the milling insert and the cross section of the cutting edge are shown in Fig. 11 as a light optical microscope (LOM) image. The top side is referred to rake face and the flank face is located perpendicular to the rake face, see Fig. 11a). When a milling insert cuts a workpiece, the produced chip moves along the chamfered cutting edge of the rake face (see Fig. 11b)). The chamfer has an angle of about 10° to the rake face and the width is about 0.3 mm. The choice of this geometry for this work possesses two advantages. Firstly, the cutting edge geometry exhibits plane faces, which are necessary for reliable residual stress measurements and to reduce their uncertainty. Secondly, the danger of sudden failure of the cutting edge is lower because the cutting edge is not sharp. Additionally all faces of the cutting inserts were grinded to guarantee a similar surface quality.

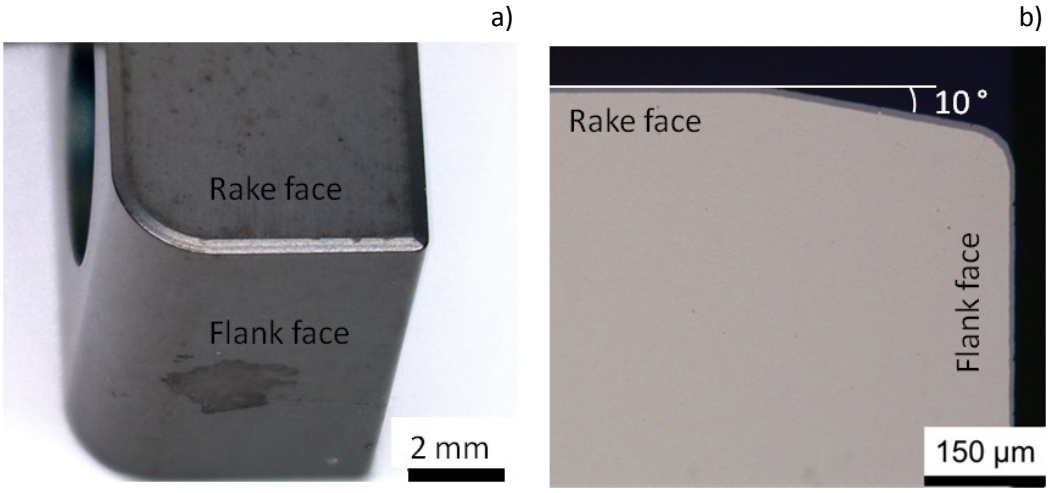

Fig. 11: a) Schematic illustration of the milling insert, b) LOM image of the cross section of the chamfered cutting edge.

The tool dimensions were 6.35 × 11.4 × 10 mm³. All inserts consisted of the same hardmetal grade with 8 wt.% Co and an average WC grain size of 0.7 µm (see details in chapt. 3.1.) and they were coated with a Ti-Al-Ta-N film having a thickness of about 8 µm (details in chapt. 3.2.).

3.5 Workpiece material

For all experiments a 42CrMo4 (1.7225) steel of the same production lot was used. The chemical composition and the mechanical properties are presented in Tab. 3 [56].

Tab. 3: Chemical composition, yield strength ($R_{p0.2}$), ultimate tensile strength (R_m), elongation (A_5) and Brinell hardness (*HB30*) of the workpiece material, a 42CrMo4 steel in normalized condition [56].

C [%]	Mn [%]	Si [%]	P [%]	S [%]	Cr [%]	N [%]	Cu [%]	Al [%]	N [%]	V [%]	Ti [%]	Mo [%]
0.43	0.66	0.2	0.013	0.005	0.99	0.06	0.06	0.028	0.005	0.01	0.002	0.22

$R_{p0.2}$ [N/mm²]	R_m [N/mm²]	A_5 [%]	HB30 [-]
435	760	15	226

The workpiece dimension was 800 × 96 × 200 mm³. The microstructure of the workpiece material is shown in Fig. 12.

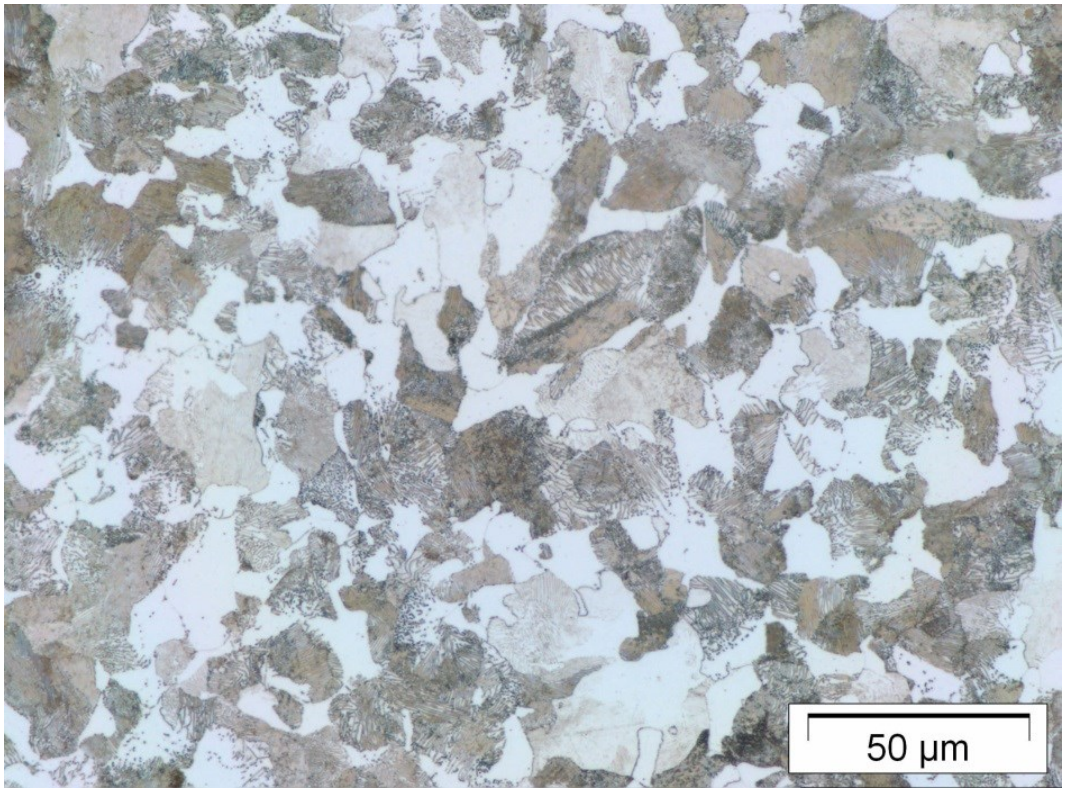

Fig. 12: LOM image of the microstructure of a 42CrMo4 (1.7225) steel in a normalized condition.

The main components of the microstructure are ferrite and pearlite grains.

3.6 Milling experiments

Within this work, milling experiments were carried out in two different milling test setups A [57] and B [58], which are illustrated in Fig. 13. The milling insert was fixed in a special milling tool, which exhibits a diameter of 125 mm. This tool is shown in Fig. 13 referred as tool [57],[58]. In both test setups, the same workpiece material, a normalized 42CrMo4 (1.7225) with a hardness of 226 *HB30* (see Tab. 3) was used, see details in chapter 3.5. [57],[58].

All experiments in both test setups were done in a single edge climb-up milling arrangement using a cutting speed v_c of 220 m/min and depth of cut a_p of 4 mm in dry conditions [57],[58].

Experiments in test setup A were carried out using a feed rate f_z of 0.4 [57] whereas inserts tested under test setup B conditions f_z of 0.5 mm/tooth was applied [58]. The cut segment length is equal to the length of the workpiece, in which the tool had to move in feed rate direction, see Fig. 13. After cutting a cut segment, the tool had to move from the end position to the start position. In test setup A [57], the cut segment length was about 800 mm whereas in test setup B, this cut segment length was shorter and about 96 mm, see Fig. 13b) [58]. In the test setup A arrangement the milling insert can perform 1,900 contacts within one cut segment length. Milling tests with a higher number of cuts required the movement of the milling tool to the start position to cut a new segment [57]. This test setup A is characterized by less frequent tool movements from end to start than in test setup B [57],[58]. For example a tool with one insert, that cuts 3800 times under test setup A conditions, had to be removed two times whereas inserts tested under test setup B conditions had to be removed 13 times.

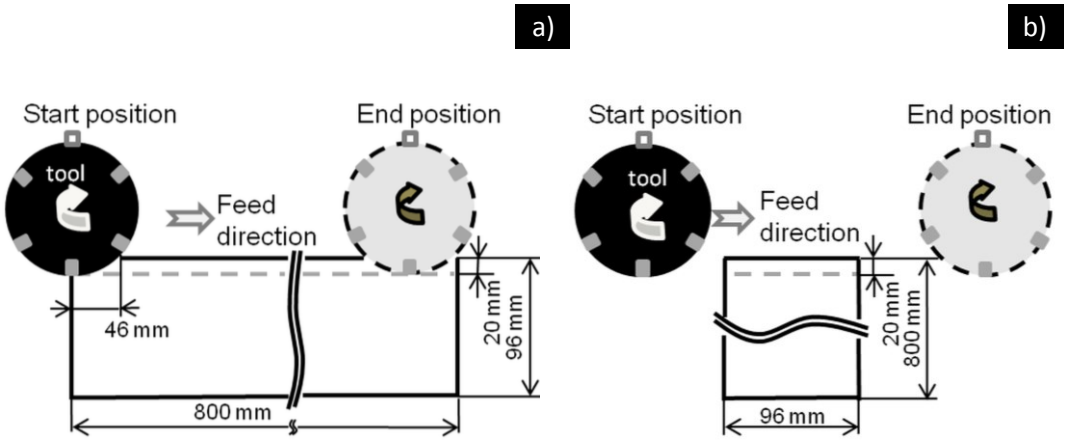

Fig. 13: Scheme of applied milling test setups A and B with different cut segment lengths and feed rates of a) 96 mm and 0.5 mm/tooth referred to as test setup A, and b) 800 mm and 0.4 mm/tooth referred to as test setup B. Only one of six milling inserts was mounted in the tool holder [57],[58].

In test setup A a dummy insert removed previously a length of about 46 mm at the beginning and the end of each cut segment [57]. Therefore the start and end position between test setup A and B was different (see Fig. 13). Fig. 14 shows the workpiece, in which a dummy insert had removed the beginning of a cut segment. In test setup A it was ensured a constant tool-workpiece contact length (TWCL) at each cut. Milling inserts, tested under test setup A conditions, always cuts the same TWCL of about 51.44 mm at each contact with the workpiece. Under constant cutting conditions, one contact took 14 ms to cut this TWCL of 51.44 mm. The idle time was 96 ms [57].

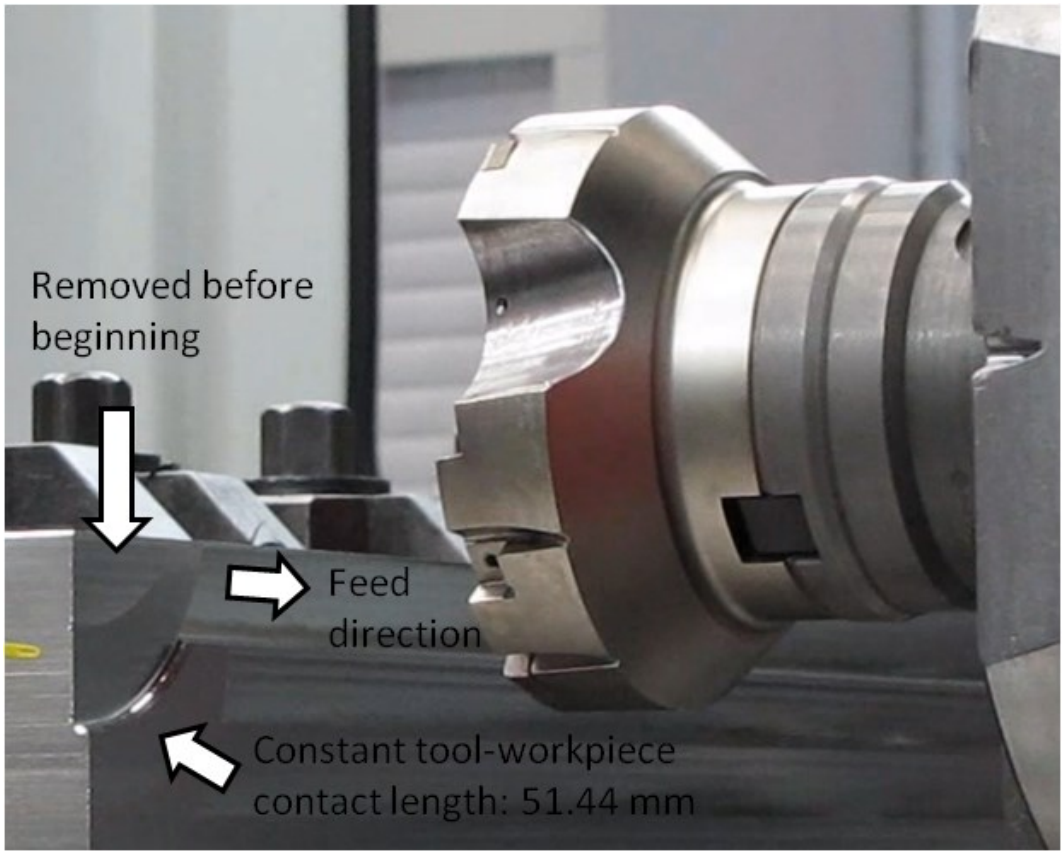

Fig. 14: Start position of tool in test setup A. Workpiece exhibits a removed beginning of a cut segment [57].

The milling inserts in test setup B experienced non-constant TWCL at the beginning and at the end of each cut segment because of the entry and exit of the tool (see Fig. 13b) [58]. During the entry the TWCL increases with increasing number of cuts from nearly 0 to 51.44 mm after 92 contacts with the workpiece material. Until TWCL reaches the constant value of 51.44 mm after 92 cuts, the insert has to cut 2.5 m accumulated tool-workpiece contact length (aTWCL) under non-constant cutting conditions [58]. In the test setup B the milling inserts can carry out 100 cuts under constant cutting conditions with a constant TWCL of 51.44 mm within one cut segment. After these 100 contacts the TWCL decreases

again because of the exit of the tool. A milling insert, tested under test setup B conditions, performs 100 cuts under constant and 184 cuts under non-constant cutting conditions within one cut segment, respectively [58]. To compare the residuals stress and damage state in milling inserts tested in both test setups, the tool-workpiece contact length (TWCL) were accumulated, which is referred to accumulated tool-workpiece contact length (aTWCL) within this work.

3.7 Overview of milling experiments

All milling inserts were tested either under test setup A or B conditions, see testing details in previous chapter 3.6. Tab. 4 shows an overview of all milling tests, which were done and stopped after a selected accumulated tool-workpiece contact length (aTWCL).

Tab. 4: Overview of the milling experiments conducted within this thesis. Red coloured columns indicate the milling tests in both test setups, which were done to enlarge the knowledge of the residual stress and damage evolution in inserts over their complete lifetime [57],[58]. The blue colored columns indicate the tests under test setup B conditions for estimation of the influence of the post treatment and blasting time on residual stresses and damage [55]. Two additional milling tests with the same aTWCL were done to estimate the cutting temperature (indicated by a star).

Test setup A	**Test setup B**			
Determination of residual stress and damage in inserts over the complete lifetime		**Influence of dry blasting on residual stress and damage**		
		Blasting duration 162 s	Blasting duration 252 s	Blasting duration 336 s
Milling stop after after accumulated tool-workpiece contact length (aTWCL) [m]	Milling stop after aTWCL [m]	Milling stop after aTWCL [m]	Milling stop after aTWCL [m]	Milling stop after aTWCL [m]
0.102	2.50	36.00	36.00	36.00
0.51	36.00	407.81	407.81	407.81
2.57	407.80	815.60	815.60	815.60
15.12*	611.70	1223.46	1223.46	1223.46
25.72	2854.70	1631.28	1631.28	1631.28
52.44		2039.1	2039.1	2039.1
288.06		2446.92	2446.92	2446.92
493.82				
673.86				
910.49				
1203.70				
1347.73				

To enlarge the knowledge of the residual stress and damage evolution over the complete lifetime of milling inserts in two different milling arrangements, twelve and five milling tests were done under test setup A and B conditions, respectively. The detailed cut length of aTWCL are indicated in the red colored cells in Tab. 4 [57],[58].

Selected milling inserts were post treated with different blasting time of 168, 252 and 336 s. To document the influence of post-treatment and its durations on the emergence of residual stress and damage, the milling tests were done under test setup B conditions. Independent

of the blasting time, all inserts had to cut the same amount of aTWCL, which is shown in the blue marked cells in Tab. 4 [55].
Two milling tests, cutting the same aTWCL of 15.12 m (indicated by a star in Tab. 4), were performed to estimate the cutting temperature using thermo colors, see experimental details in next chapter 3.8.
Four additional milling tests (see Tab. 5) were performed to document the influence the mechanical impact on the hardmetal substrate, which may foster the combcrack formation. This was applied by varying the feed rate and speed.

Tab. 5: Cutting parameter of four additional milling tests, in which speed and feed rate was varied in test setup A arrangement.

Test setup A arrangement **Influence of varied speed and feed rate on damage state**		
f_z [mm/tooth]	v_c [m/min]	Milling stop after aTWCL [m]
0.4	220	1923.86
0.5	220	1241.14
0.6	220	285.59
0.6	250	64.60

Under test setup A conditions, the feed rate f_z is increased from 0.4 to 0.6 mm/tooth. Additionally, one milling test was done in which the f_z was constant at 0.6 mm/tooth and the speed was increased from 220 to 250 m/min. The other machining parameters were the same as used in test setup A.

3.8 Indirect cutting temperature determination

The cutting temperature was estimated in two different ways. First, after a cut the microstructure of the steel chips of the workpiece material was investigated. A change of the steel microstructure gives the opportunity to estimate the cutting temperature. This was done using LOM and SEM. Second, the temperature in the areas close to the wear marks can be directly determined on the rake and the flank face of the milling insert using thermo chalks (FA Kager Industrie Produkte GmbH). An orange colored thermo chalk changes the color to grey at a temperature higher than 245 °C, to black at 335 °C and to white when the temperature reaches 505 °C, respectively. The green one has the colour change at 600 °C. The temperatures have to be reached and stayed longer than two seconds to activate this

colour change. Within this work, the cutting duration only lasted 14 ms. Despite the short cutting duration, the colour change of the thermo chalks can be activated, when the apparent temperatures are higher. Secondly, the mean temperature (see Fig. 8) on rake faces can reach this magnitude and the color change can be activated within 15.12 m aTWCL. The colored inserts were investigated after milling 15.12 m aTWCL.

3.9 Damage investigation

The rake face's surface topography of all milling inserts was investigated by scanning electron microscopy (SEM, Crossbeam field emission gun, Zeiss Auriga). Cross sections of selected milling inserts were prepared by means of focused ion beam technique (FIB, Orsay Physics Cobra Z-05 FIB extension) to document the damage state after application. The cross sections had a depth of 15 µm. Position resolved detection of the chemical elements within the cross sections was performed by means of X-ray emission spectroscopy (EDX, EDAX Apollo 40+).

For documentation of the shape of the first combcrack of the milling insert with 611.7 m aTWCL in test setup B, the scanning acoustic microscopy (SAM, SAM 400, PVATePla) with a sound frequency of 75 MHz in reflection mode was used. A cross section of the sample was prepared. Fig. 15a) presents a schematic view of the milling insert. Dashed lines in Fig. 15a) show the position of the cross section (see Fig. 15b)), in which the acoustic waves were induced in milling insert.

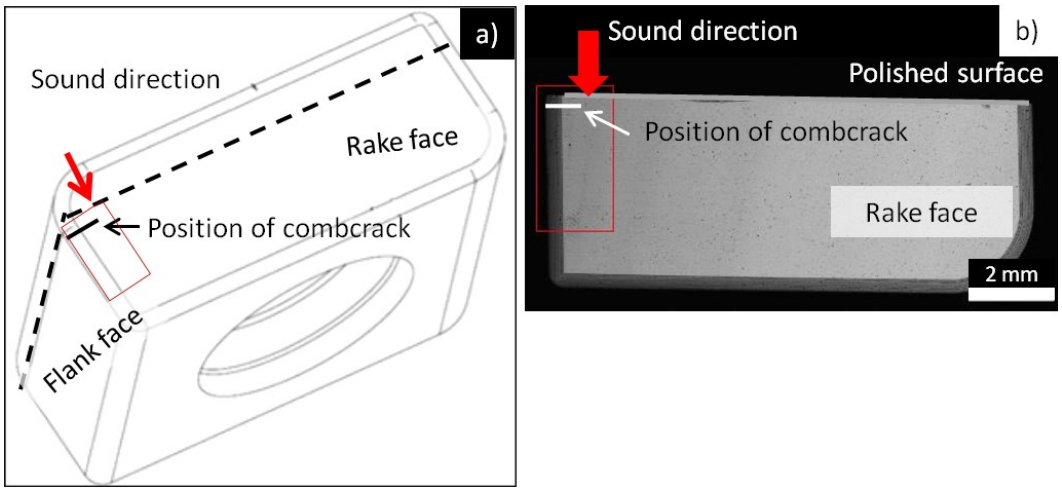

Fig. 15: a) Schematic view of milling insert, dashed lines indicates position of prepared, polished cross section. b) Prepared milling insert, which cuts 611.7 m aTWCl and exhibits first combcrack. Position of combcrack, indicated with a white line, is about 500 µm in depth and away from cross section's surface, in which the sound was induced.

The surface of the specimen's cross section was previously prepared and polished to avoid reflexion of the sound due the surface roughness.
Each inhomogeneity, e.g. sample hole, appeared very brightly grey in the SAM image due to acoustic wave reflection within the sample. In the area of detailed investigations (see red rectangle in Fig. 15b)) the radius of the sample had to be removed to avoid undesired reflections. Using this sample preparation, the acoustic waves were only reflected by the crack flanks of the combcrack. The combcrack was positioned about 500 µm away from the polished surface, in which the sound was induced (see white line in Fig. 15b)).

3.10 Position resolved residual stress measurement

3.10.1 Residual stresses in WC phase determined via synchrotron X-ray diffraction

The residual stress maps of selected inserts were determined using a synchrotron X-ray diffraction method. The early stages of milling application under test setup A conditions were investigated, in which milling experiments of the investigated inserts were stopped after cutting 0.201, 0.51 and 51.44 m aTWCL (see red colored cells in Tab. 4), which corresponds to two, ten and thousand cuts [59]. Additionally, the as-deposited milling insert without any tool-workpiece contacts, so-called virgin insert, was also characterized as reference material at the G3 beamline of the Hasylab synchrotron source in Hamburg. A 4-circle diffractometer using monochromatic synchrotron X-rays with energy of 10 keV was used. The residual stress states in the direction parallel and normal to the straight portion of the cutting edge were measured using a position sensitive charge-couple device (CCD) detector with fiber optics (see Fig. 16a)). It is possible to determine position resolved results by facilitating thousands of diffractograms with this so called MAXIM system [60]. The side inclination method was used [61] (see Fig. 16b)). The data relates to the mean penetration depth up to which a fraction of $(e - 1)/e$ = 63 % of the incident radiation is absorbed [59]. In the mean penetration depth of about 1.3 µm below the interface between coating and hardmetal substrate, the residual stresses were determined in the tungsten carbide phase.

a) b)

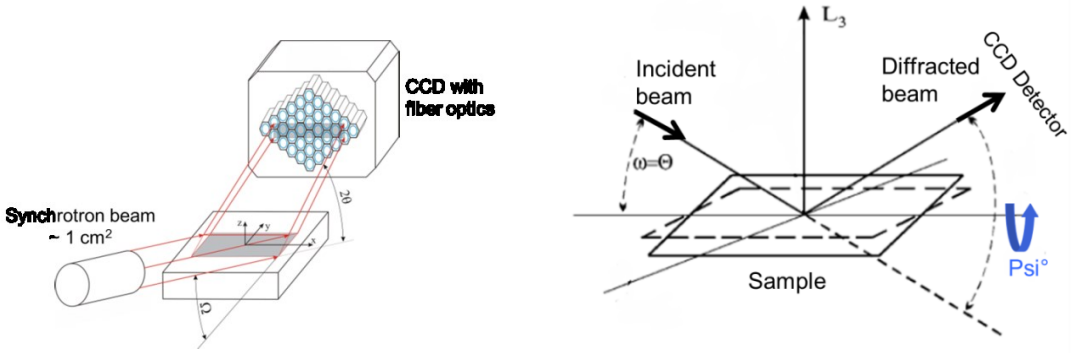

Fig. 16: Scheme of a) applied G3 beamline synchrotron source [60] and b) side inclination method [mod.[62].

The white rectangle in Fig. 17 indicates the position of the synchrotron measurements on the milling insert's rake face.

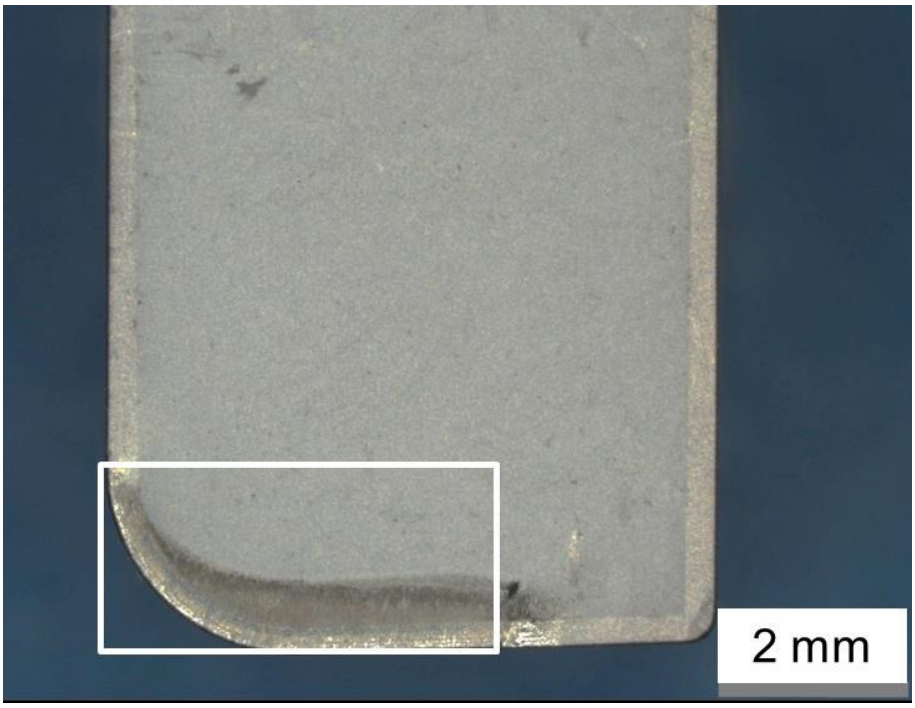

Fig. 17: Top view of a milling insert after cutting 51.44 m aTWCL (accumulated tool-workpiece contact length corresponding 1000 tool-workpiece contacts) under test setup A conditions. The white square indicates the area of residual stress measurements [59]**.**

The used diffraction peak was at a 2Θ angle of 86°, which corresponds to the (211) plane of the WC phase [59]. The uncertainty associated with the residual stress measurements was in the order of the magnitude of the determined values and was influenced by two aspects. On the one hand, the diffraction intensity is strongly affected by the low number of illuminated WC grains. On the other hand, the lateral resolution of the measurement is decreased due to

the necessary distortion correction procedure resulting in a lateral resolution of 100 µm² [59],[60].

3.10.2 Residual stress in WC phase determined X-ray diffraction

To determine the evolution of residual stresses in the substrate material on the rake face of the milling insert in both milling test setups, selected milling inserts were investigated by X-ray diffraction. The residual stress state in the substrate was determined in inserts over the complete lifetime, which were tested under test setup A [57], as well as under test setup B conditions [58]. The detailed lengths of aTWCL are documented in Tab. 4, see in red cells.
The influence of the blasting time of post treated inserts on the residual stress state was also investigated at early stages of application. The residual stresses in inserts, which had cut 3.6 m aTWCL under test setup B conditions, and in inserts, which were post-treated but without any workpiece contact were determined [55].
An X-ray diffractometer (XRD, Brucker AXS D8 Discover) in parallel beam geometry was used, which was equipped with a Sol-X energy dispersive detector, an open (90°) Eulerian cradle and a polycapillary collimator. Detailed description of the method is given in [57],[58]. For determination of residual stresses in the WC phase of the substrate, Cu K_α radiation was used. A current of 35 mA and a voltage of 40 kV were applied [57].
The ω-method was selected to determine the residual stress states in the WC and TiN phase [62] (see Fig. 18)). Using the ω-method, the samples were tilt along the ψ angle.

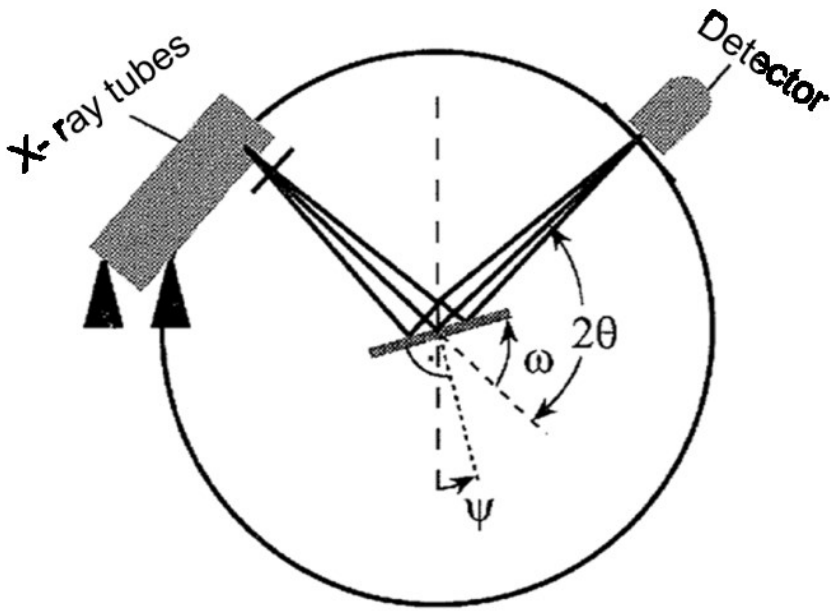

Fig. 18: Graphical illustration of the ω- method [63]. For residual stress determination, the sample was tilted along the ψ angle.

The residual stresses in the WC phase were determined at a diffraction peak at a 2Θ angle of 117.3°, which corresponds to the same (211) plane as used in the synchrotron investigations (see chapt. 3.10.1) [57]-[59]. The mean penetration depth was ranging from the interface between coating and hardmetal substrate to 5 µm below this interface. The measurement values refer to the mean penetration depth up to which a fraction of $(e - 1)/e$ = 63 % of the incident radiation is absorbed [58].

To realize the position resolved residual stress measurements, a covering method was used, in which areas outside of the region of interest (ROI) were covered by a self-fixed brass foil with a thickness of 34 µm, shown in Fig. 19. This ROI did exhibit a size of 0.3 × 1.6 mm² and was located 0.3 mm away from cutting edge. Brass was chosen as a cover material to avoid an overlapping of the diffraction peak (211) originating from the WC phase in the sample and the cover material [57]. For stress determination in the WC phase, diffraction intensity was recorded in a diffraction angle range 2θ from 114.6 to 119.1° and sample tilt angle ψ up to 35° [57].

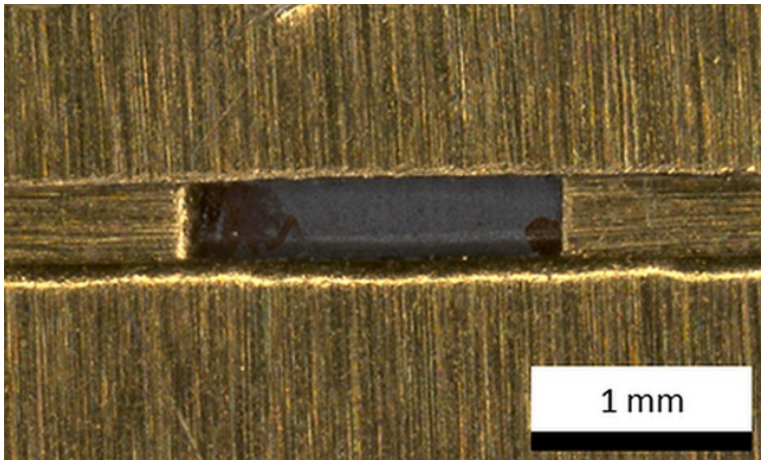

Fig. 19: Light optical microscopy image of the rake face of a milling insert, which is prepared for position resolved X-ray diffraction in the region of interest (1.6 × 0.3 mm²). Areas outside of this region were covered by brass for determination residual stresses in the WC phase [57],[58].

In all measurements, a stress component parallel to the straight portion of the milling insert's cutting edge was determined. Diffraction geometry with incident and diffracted beam parallel to this direction was chosen. These beams penetrate the investigated phase parallel to the long axis (1.6 mm) of the uncovered area to minimize shadowing effects caused by the covering brass foil. Otherwise, the shadowed fraction of the rectangular region with a long axis a (1.6 mm) and a short axis b (0.3 mm) would be larger by a factor of five at the same incidence angle θ if symmetric incident and diffracted beams are assumed and no sample tilt is considered (ψ = 0). The effect would be larger at tilted samples ($\psi \neq 0$, see Fig. 18 [57].

The determination of the diffraction angle of the measured peak was done by the software Topas 4.2 (Brucker AXS, Germany). For each specimen the residual stress component parallel to the surface and parallel to the straight portion of the cutting edge was then deduced from the slope determined by linear regression in the $\sin^2\psi$-plot according to the formalism described in [63]. Using elastic constants of Young's Modulus (660 GPa [10]) and Poisson's ration (0.23 [10]) from literature were taken to calculate the residual stress values.

3.10.3 Residual stresses in Ti-Al-N based coating determined by X-ray diffraction

The evolution of residual stresses in the coating was also determined with the same X-ray diffraction equipment using the ω-methods explained in the previous chapter 3.10.2. Cr K_α radiation with a current and voltage of 40 mA and 40 kV, respectively, was used [64]. For the residual stress determination of the coating, the diffraction peak of cubic TiN phase at 2Θ angle of 66.8°, which corresponds to the (100) plane, was chosen. The diffraction intensity of the TiN phase was recorded of a 2Θ angle from 64.2° to 69° and the sample tilt angle ψ was up to 20°. Al and Ta are dissolved in the cubic TiN phase, details are shown in chapt 2.2.

The residual stresses were detected in the virgin insert and in the milling inserts, which had cut 51.44, 493.82 and 1923.8 m aTWCL under test set up A conditions and 36, 407.8 and 611.7 m aTWCL under test setup B conditions (see details in red coloured cells in Tab. 4) [64].

The residual stresses were determined localized using the cover method. For investigations of the coating, a lead foil with a thickness of 16 µm as cover material was chosen.

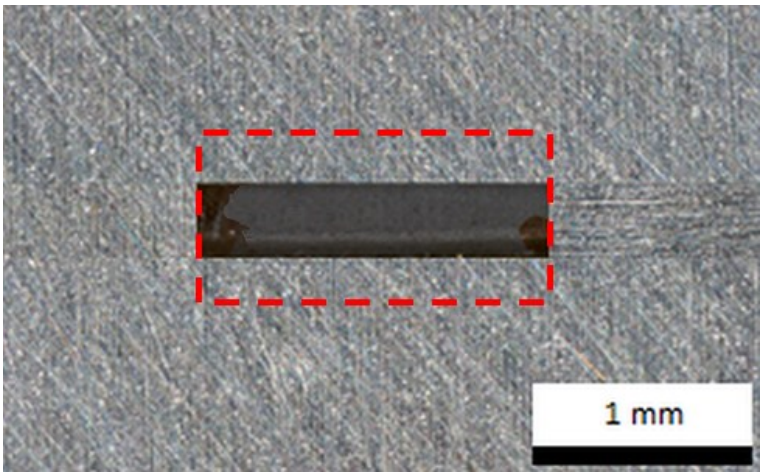

Fig. 20: Light optical microscopy image of the rake face of a milling insert, which is prepared for position resolved X-ray diffraction via cover method using a lead foil as cover material. The red rectangle indicates position and size of the location without a covering by lead foils for one measurement with enlarged region of interest in vertical direction (1.6 × 0.6 mm²), see details elsewhere [64].

In this case brass as cover foil could not be used due to the overlapping of the diffraction peak (100) originating from the TiN phase in the coating and brass. The lead foil was fixed by a double-face adhesive tape, which had a thickness of 30 µm. The summarized thickness of the lead foil and the double-face adhesive tape of 46 µm is higher than the thickness of the brass foil [57],[64].

During the residual stress determination of the coating, the shadowed area is higher, which increases the measurement uncertainty. A background correction was done to improve intensity between the diffraction maxima of the TiN phase and the background signal of the lead foil. This decreased the measurement uncertainty. For that, a lead foil sample was measured with the same measurement parameters as the actual stress measurements. For each diffraction angle 2Θ and for each tilt angle ψ the observed diffraction intensity I_{sample} was corrected according to the relation $I_{corr}(\Theta,\psi) = I_{sample}(\Theta,\psi) - I_{Pb}(\Theta,\psi)$. The subsequent data reduction was performed using the corrected diffraction intensity [64]. The values of residual stresses of the TiN phase were generated from the surface to a depth region of about 4 µm below the surface [64].

An open point in the literature is the localization and size of region, in which tensile residual stresses may be effective, in the hard coating. To verify the size of this region, residual stresses were determined in an enlarged region (1.6 × 0.6 mm²) in vertical direction (see red dashed rectangle in Fig. 20). The horizontal distance of 1.6 mm of the region is the same. The residual stresses in the enlarged region were detected in the coating of the milling insert with an aTWCL of 407.8 m, tested under test setup B conditions.

3.11 Thermo-physical and -mechanical tests

The FE method is a powerful tool for estimation of mechanical and thermal tool loads [48]. The realistic simulation of temperatures apparent during cutting requires detailed knowledge of the thermo-physical and mechanical properties [8], in particular thermal diffusivity (*a)*, the thermal conductivity (*λ*), heat capacity (c_p), thermal expansion coefficient, Young's modulus (*E*) and shear modulus (*G*), Poisson's ratio (*v*), yield strength ($R_{p0.2}$), fracture toughness (K_{IC}). These determined material data were used as input data for FE simulation [34].

3.11.1 Thermo-physical tests

The thermal diffusivity (*a)* and the heat capacity (c_p) were directly detected by means of the laser flash method, according the method described in [65]. The used laser flash equipment was a Netzsch LFA 457 MicroFlash. Details concerning the used measurement method are described in [65],[66]. A rectangular hardmetal specimen with a size of 10 × 10 × 3.5 mm³ was heated up with a short laser beam impulse. The introduced amount of heat was distributed over the whole sample. The emitted infrared rays from the opposite specimen side (see Fig. 21a)) were collected by a detector.
The thermal diffusivity of the testing material was calculated according to Equation 1.

Equation 1: Thermal diffusivity *a* [mm²/s], sample thickness *d* [mm] and and soaking time $t_{1/2}$ [s] which is defined as the duration, in which the specimen side that is not irradiated by the laser reaches half of maximum temperature rise, see Fig. 21b) [66].

$$a = 0.1338 * \frac{d^2}{t_{1/2}} \qquad \text{Equ.1}$$

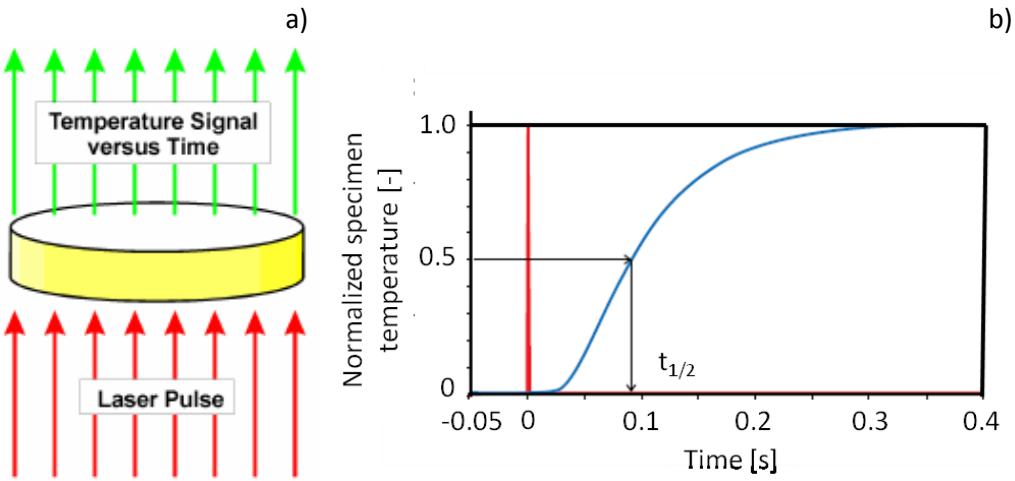

Fig. 21: a) Schematic illustration of heating up the specimen by a laser pulse and the emitted infrared rays. b) Definition of the soaking time $t_{1/2}$. Emission of laser pulse (red line) and the temperature of the sample's non-irradiated side (blue curve) as a function of the time [66].

The c_p of the hardmetal was determined using comparative measurement with a molybdenum specimen as reference material. The ratio between the c_p and the energy of the emitted rays of the molybdenum was used to calculate the heat capacity of the hardmetal using the measured energy of the emitted rays, according to [65].

All samples were coated with a thin graphite coating before testing and therefore the samples can be considered as a black body, which exhibits an emission coefficient of 1 and which results in an almost complete storage of the laser energy in the specimen's temperature reservoir. The temperature difference (ΔT) is determined directly by the detector.

The thermal conductivity was calculated according to Equation 2 using the density and the determined thermal diffusivity and heat capacity.

Equation 2: Thermal conductivity λ [$Wm^{-1}K^{-1}$]

$$\lambda = \rho * c_p * a \qquad \text{Equ. 2}$$

The measurement inaccuracy of the laserflash equipment for ρ, a, c_p and λ are 2 %, 3 %, 5 % and 9 %, respectively [67]. The density of the hardmetal was determined at RT. The thermo-physical data were measured as a function of temperature up to 1000 °C.

The thermal expansion coefficient (α) was determined by a dilatometer (Netzsch DIL 402 E/7) for temperatures up to 1300 °C. Cylindrical samples with a diameter of 5 mm and a length L_0 of 25 mm were used. The increase of the specimen length with increasing temperature was detected and the thermal expansion coefficient was calculated according to Equation 3. ΔL and $\Delta L_{at\ 25\ °C}$ corresponds the difference between the lengths, which are

detected at testing temperature (*T*) and at room temperature 25 °C, and the reference length L_0.

Equation 3: Linear thermal expansion coefficient α [K^{-1}]:

$$\alpha = \frac{\frac{\Delta L}{L_0} - \frac{\Delta L_{at\ 25\,°C}}{L_0}}{(T - 25°C)} \qquad \text{Equ. 3}$$

The measurement error connected with the value of α is approximately 5 %. At temperatures below 100 °C thermal expansion coefficients determined at temperatures below 100 °C are not accurate because the dilatometer can only resolve changes in length greater than 10 µm.

3.11.2 Thermo-mechanical tests

The temperature dependent Young's- and the shear modulus was determined for the hardmetal grade via resonant ultrasound spectroscopy in a heating device. A rectangular bar specimen with dimensions of 45 × 4 × 3 mm³ was used. The bar was induced to oscillate, the Eigenfrequency of the hardmetal bar was determined and the Young's (*E*) – and shear (*G)* moduli were calculated according to [68]. The Poisson's ratio (*v*) was determined according to Equation 4. The Young's modulus was determined for the temperature range from room temperature (RT) to 1100 °C, *G* and *v* from RT up to 700 °C.

Equation 4: Poisson's ratio ν [-]

$$\nu = \frac{E}{2*G} - 1 \qquad \text{Equ. 4}$$

The measurement error for *E, G* and v using this test setup are 2 %, 6 % and 9 % respectively. For determination of the compressive flow strength, static uniaxial tests under compression loading conditions were done using a servo hydraulic testing machine type Instron 8803. The experiments were carried out under ambient atmosphere at temperatures of 400, 600 and 800 °C. All hardmetal samples (see Fig. 22) were heated inductively. Strain measurements were done contactless via a laser extensometer P- 2S- 50 / 400 Hz (Fiedler Optoelectronic GmbH) with a class of accuracy of 0.2 and resolution of 0.1 µm.

The accuracy class describes the possible deviation of the measured elongation from the correct elongation. The definition can be found in [69]. The value 0.2 corresponds to the maximum deviation of ± 0.2 %.

The strain values were determined experimentally at a measurement length of 8 mm. This means that the absolute error made when measuring the strain, reaches 7.5 % at strain values of 0.01 % and 75 % at strain values of 0.001 %. The specimens for uniaxial testing did

not have a constant cross section within the measurement length of 8 mm with a minimum diameter of d_{min} = 5.5 mm. The detected strain values need to be corrected by means of finite element simulation. The detailed theoretical description of this correction can be found in [70].

Fig. 22: Image of the uniaxial test sample shape.

The compressive yield strength $R_{p0.2}$ at a plastic strain of 0.2 % was determined using the stress-strain curves attained under compressive loading conditions.

High temperature (HT) fracture toughness (K_{IC}) was determined using single edge notched bending specimens (see Fig. 23) according to the standard ASTM E399 [71]. Rectangular hardmetal specimens with a size of 36 × 7 × 4 mm³ (L × W× B) were used. The notch was induced by a slicing machine and refined using a razor blade and a fatigue crack. The fatigue crack was initiated by cyclic compression at a stress ratio of 10 with a stepwise increase of applied stress intensity factor range ΔK until detection of a fatigue crack. The fatigue crack lengths within the specimens were between 30 and 100 µm. The complete lengths of the refined notches (a) were between 0.45 to 0.55 times of the specimen width (W) [71].

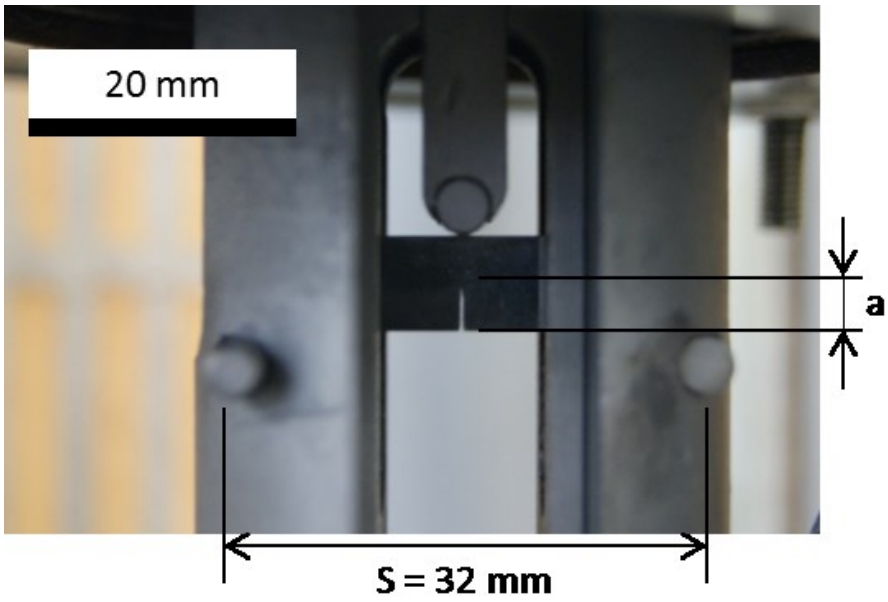

Fig. 23: Image of a single notched bending test setup with the notched hardmetal specimen. *S* corresponds to the distance of 32 mm between the supports and length *a* identifies the length of refined notch.

The K_{IC} is calculated according to Equation 5. The empirical factor *f(λ)* is based on the ratio between length *a* and *W* and calculated according to equations, which are described in standard ASTM E399 [71].

Equation 5: Fracture toughness K_{IC} [MPa√m]. P_{tat} corresponds to the maximum load during the bending test. Factor *S* indicates the distance between the supports, see Fig. 23.

$$K_{IC} = \frac{P_{tat} * S * f(\lambda)}{B * W^{1.5}} \qquad \text{Equ. 5}$$

The experiments were done using a spindle drive testing facility (Zwick) at temperatures from RT up to 800 °C. The tests at RT and 300 °C were carried out at ambient atmosphere whereas experiments at 500, 700 and 800 °C were done under vacuum conditions to avoid oxidation at crack flanks.

4 Results

4.1 Damage investigations of milling inserts

The following chapters illustrate the dominant damage mechanisms in milling experiments of test setup A and B. The contact lengths at early stages, the wear damage and the thermal fatigue in form of combcracks are shown. More details about the scanning electron microscope investigations including the focused ion beam preparations are described in publications I – III, see [57]-[59].

4.1.1 Test setup A

The contact length of this chip on the rake face can be determined via length measurements on the wear marks at insert's rake face. These wear marks are not clearly pronounced at very early stages of application. Therefore, platinum as soft metal was previously deposited as a layer on the rake face of a virgin milling insert, which is illustrated in Fig. 24a). Platinum is removed during chip formation. Due to the contrast in the SEM image between the bright apparent platinum layers and the dark apparent Ti-Al-Ta-N coating, the contact length can be determined easily. The SEM micrograph of the same milling insert after 2 cuts, which corresponds to an accumulated tool-workpiece contact length (aTWCL) of 0.103 m under test setup A conditions, is shown in Fig. 24b). The platinum layer on the surface was partially removed.

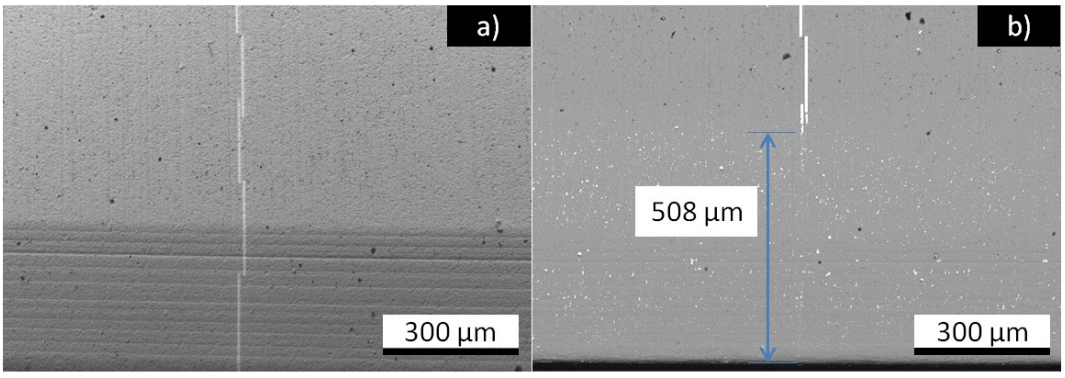

Fig. 24: SEM micrographs of rake face of a) a virgin insert, and b) of the same insert after two cuts tested under test setup A conditions, corresponding an aTWCL of about 0.103 m. The brighter lines are platinum layers, deposited on insert's rake face. After two cuts these layers are partially removed due to chip forming.

The contact length of the chip on the rake face was 508 µm because of the removement of the previously deposited platinum layer along this distance. The contact length increased with increasing cutting duration. In inserts at the end of lifetime the contact length was about 860 µm (see Fig. 28a) for test setup A.

To document the damage state of the used cutting edges tested under test setup A conditions, the flank and rake faces of selected milling inserts with 51.440 and 900.200 m aTWCL and at the end of lifetime after about 1,923.856 m aTWCL (see red cells in Tab. 4) were investigated by SEM [57].

Fig. 25 shows SEM flank face surfaces of the milling inserts, which cut 51.44 m, 910.49 m aTWCL and the insert at end of lifetime (1923.86 m).

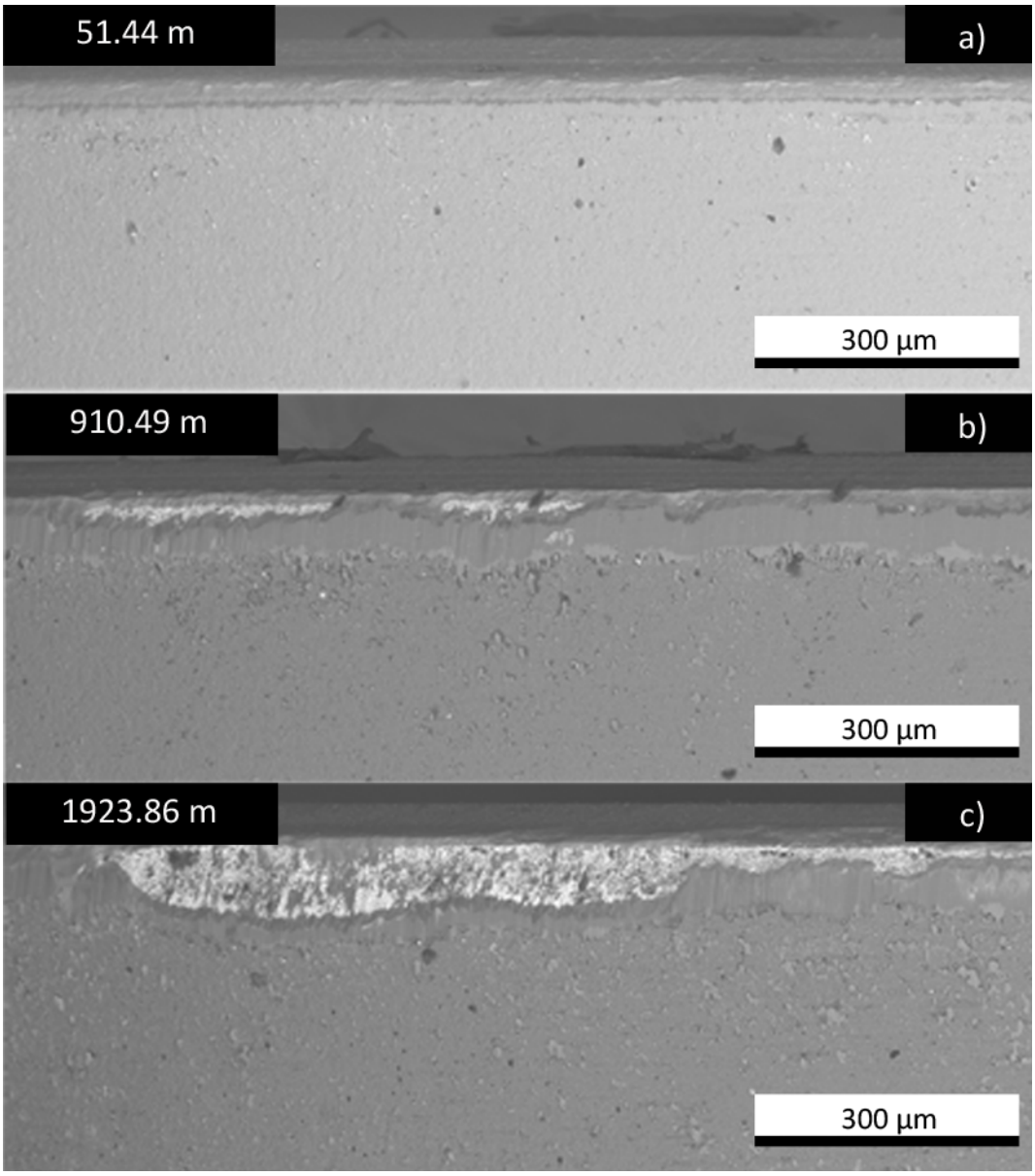

Fig. 25: SEM images of the flank face of inserts (rake faces are shown in Fig. 26a), Fig. 27a) and Fig. **28**a)) after a) 51.440, b) 900.200 m aTWCL and c) end of lifetime (1,923.856 m aTWCL) tested under test setup A conditions [57].

During application the coating at the cutting edge and flank face is removed. Wear damage is increased without the protection of the coating, see Fig. 25c). At end of lifetime the coating on the tool's flank face is removed up to a distance of about 100 µm from the cutting edge (see Fig. 25c)) and the whole cutting edge was disintegrated. A continued use of the worn tool after 1,923.856 m aTWCL would raise the risk of complete fracture of the cutting edge [57].

To document the surface topography and damage state at the rake face, the same selected milling inserts (see length of aTWCL specified in red cells in Tab. 4) were investigated by SEM [57].

Fig. 26a) shows an overview of the rake face, which cut 51.55 m aTWCL, and the small red coloured square indicates the location of surface image with higher magnification positioned at the upper edge of the chamfer as shown in Fig. 26b). A FIB cross section is illustrated in Fig. 26c); the respective position is indicated by a red line in Fig. 26b). Platinum layers were deposited on all specimens prior to FIB cutting to produce a smooth FIB cut. These platinum layers appear as a bright film on top of the grey coloured hard coating on the hardmetal substrate [57].

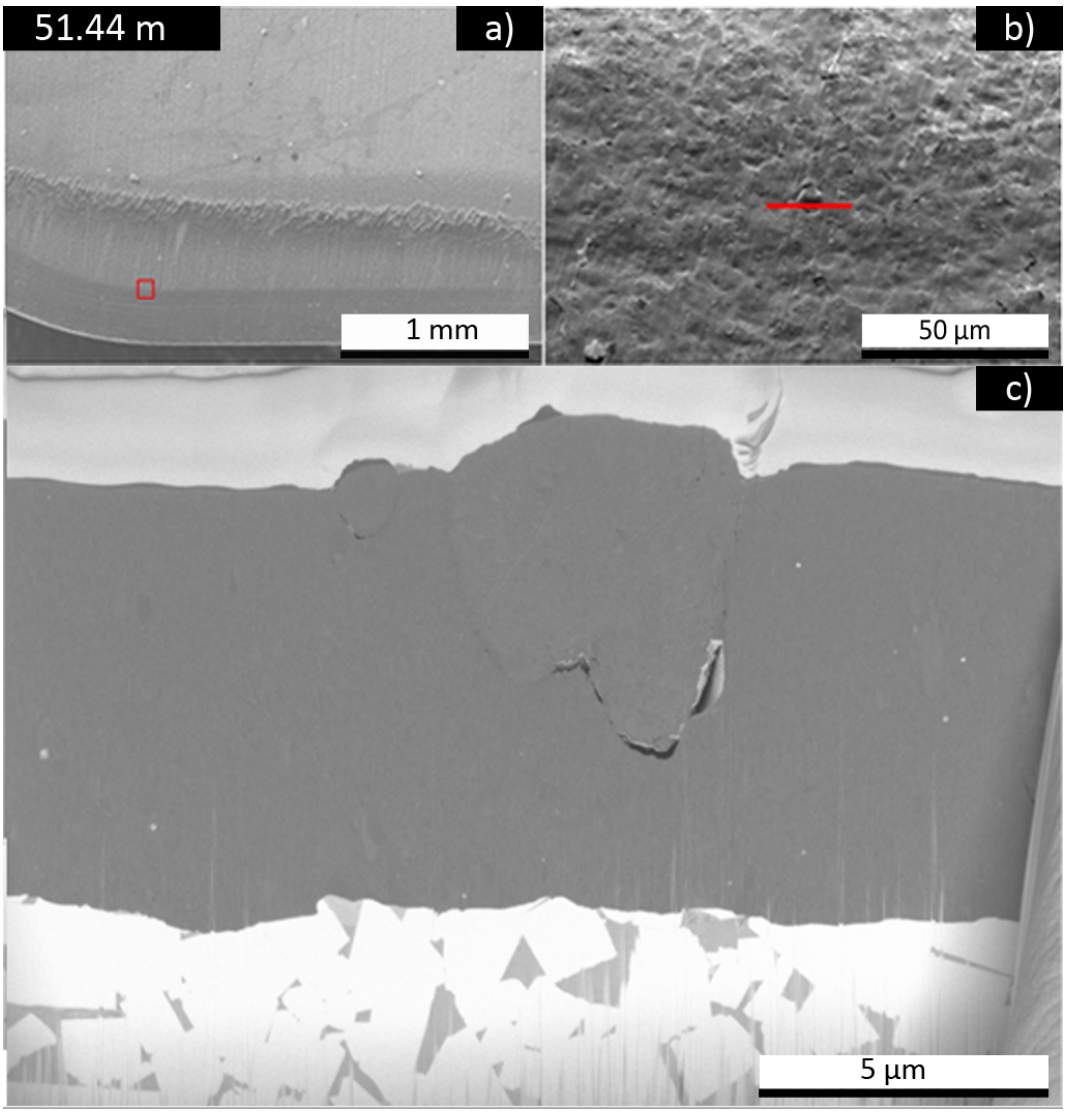

Fig. 26: a) SEM micrograph of the rake face of used milling inserts after 51.44 m aTWCL, tested under test setup A arrangement. Red frame in a) indicates the location of detailed surface investigations shown in b) with higher magnification. Red line in b) indicates the position of FIB cross section illustrated in c). Bright top layers on top of the FIB cross sections represent protective platinum layers [57].

Abrasive wear marks, which look like grooves, are visible on the rake face of the insert that cut 51.44 m aTWCL. Droplets were detected in the cross section of the coating, see Fig. 26c). Some pores were found around of one droplet, which are typical in CAE deposited coatings [22].

The rake face of a used milling insert, which had cut 910.49 m, is shown in Fig. 27a). The small red coloured square in this overview image indicates the location of surface image with higher magnification positioned at the upper edge of the chamfer as shown in Fig. 27b). Fig. 27c) illustrates the FIB cross section with its respective position indicated by red line in Fig. 27b) [57].

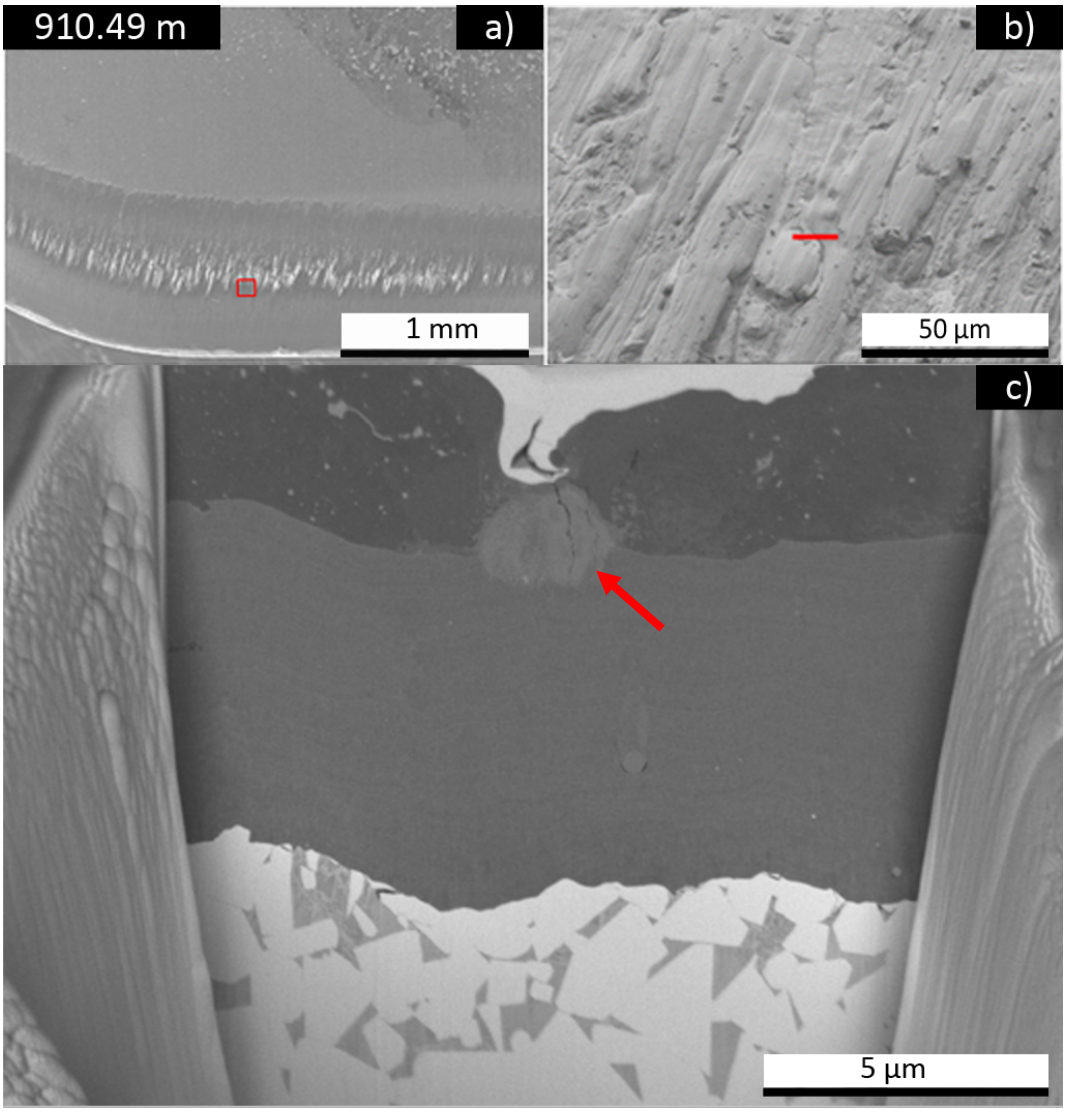

Fig. 27: a) SEM micrograph of the rake face of used milling inserts after 910.49 m aTWCL, tested under test setup A conditions. Red frame in a) indicates the location of detailed surface investigations shown in b) with higher magnification. Red line in b) indicates the position of FIB cross section illustrated in c). Bright top layers on top of the FIB cross sections represent protective platinum layers [57]. The positions of a detected crack within the adhesive workpiece layer in c) are indicated by a red arrow.

Fig. 28a) shows the cutting edge at end of lifetime, tested 1923.86 m aTWCL under test setup A conditions. The small red coloured square indicates the location of the surface image with higher magnification positioned at the upper edge of the chamfer as shown in Fig. 28b). The FIB cross section is illustrated in Fig. 28c); the respective position is indicated by a red line in Fig. 28b).

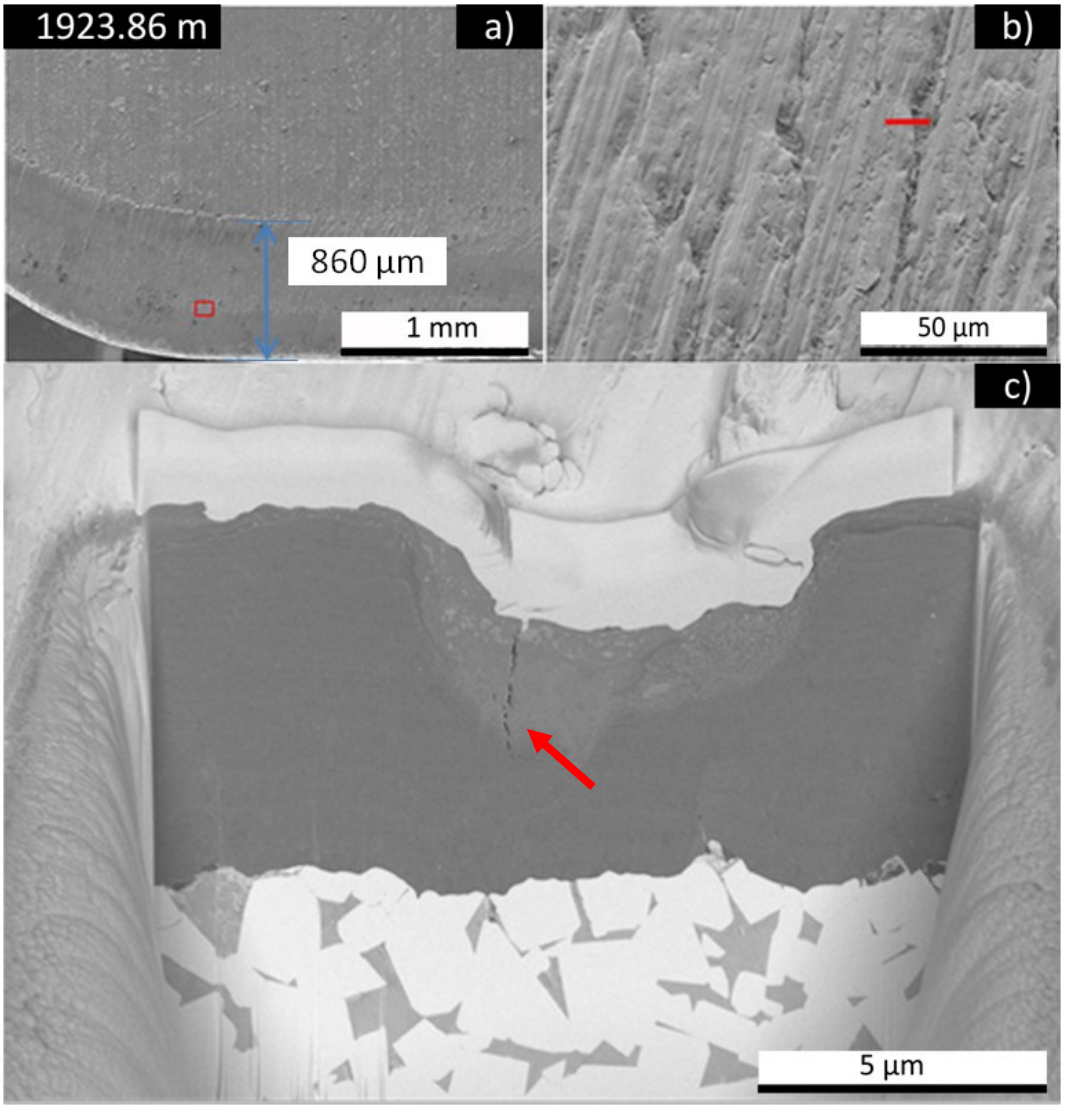

Fig. 28: a) SEM micrograph of the rake face of used milling insert at the end of lifetime after 1923.86 m aTWCL tested in test setup A arrangement. Red frame in a) indicates the location of detailed surface investigations shown in b) with higher magnification. Red line in b) indicates the position of FIB cross section illustrated in c). Bright top layers on top of the FIB cross sections represent protective platinum layers [57]. The crack is detected within the adhesive workpiece layer and not in the coating in c), which is indicated by a red arrow.

Adhesive wear marks and abrasive wear, which look like grooves, were detected on milling inserts, which cut more than 51.440 m aTWCL, e.g. see Fig. 27b), c) and Fig. 28b), c). The grooves are apparent either in the adhered workpiece layer (see Fig. 27c)) or in the coating (cf. Fig. 28c)). The width and depth of the grooves seem to increase with increasing number of cuts, see FIB cross sections in Fig. 27c) and Fig. 28c). During cutting application the adhered workpiece layer tends to be removed and re-created. The milling insert, which cut 910.49 m aTWCL, exhibits a workpiece layer thickness of about 4 µm (see dark grey layer

below the platin layer in Fig. 27c)) whereas the insert at the end of lifetime has a much lower layer thickness of workpiece material with a thickness of about 0.3 µm, see in Fig. 28c). Workpiece material completely fills up the grooves, which were induced by abrasive wear, as seen in the FIB cross sections in Fig. 28c). Along these filled grooves, cracks were found perpendicular to the surface and in normal direction to the cutting edge. This crack growth started from the surface and stopped when the crack reached the workpiece material/coating interface, as indicated in the FIB cross sections by red arrows in Fig. 27c) and Fig. 28c) [57]. Some authors also determined this kind of wear damage dominated by grooves on their milling inserts [72],[73].

In this test setup, neither macroscopic nor microscopic combcracks were determined in the coating or hardmetal substrate [57]. This result is not characteristic for most of the milling experiments documented in literature [5],[6],[43]. Usually thermal fatigue in form of combcracks was observed, independent of feed rate, the cutting speed and the depth of cut [5],[44],[45]. Only Bathia et al. described a combination of process parameters for a certain test setup under which no tool failure induced by combcracks occurred due to subcritical thermal or mechanical tool loading [47]. Here, the feed rate and the cutting speed had to be lower than 0.1 mm/revolution and 1.5 m/s, respectively. In test setup A, see chapt. 3.6. [57], following machine parameter were used; feed rate of 0.4 mm/revolution and cutting speed of 220 m/min (3.6 m/s). Despite of the use of higher feed rate and cutting speed, only wear damage limited the tool lifetime and no combcracks appeared [57]. The machine parameter intervals for the described process field of tool failure in form of combcracks were also dependent on the radius of the cutting edge [32]. The combination of protective hard coatings with a chamfered cutting edge reduces the sharpness of the edge. This leads to an enlargement of the process parameter field and no tool failure induced by cracks appears effectively. Bathia et al. mentioned that a milling insert with enlarged cutting edge radius widened the process parameter field in which wear before fracture occurs [47].

4.1.2 Test setup B

The damage state of the cutting edge tested in test setup B was documented via SEM investigations of flank and rake faces of selected milling inserts after milling 36.00, 611.73 m aTWCL and at the end of lifetime after 2854.75 m. Detailed description of the damage state can also be found in publication III.

Flank face surfaces of the milling inserts with 36.00, 611.73 m aTWCL and at end of lifetime after cutting 2854.75 m are illustrated in Fig. 29 [58].

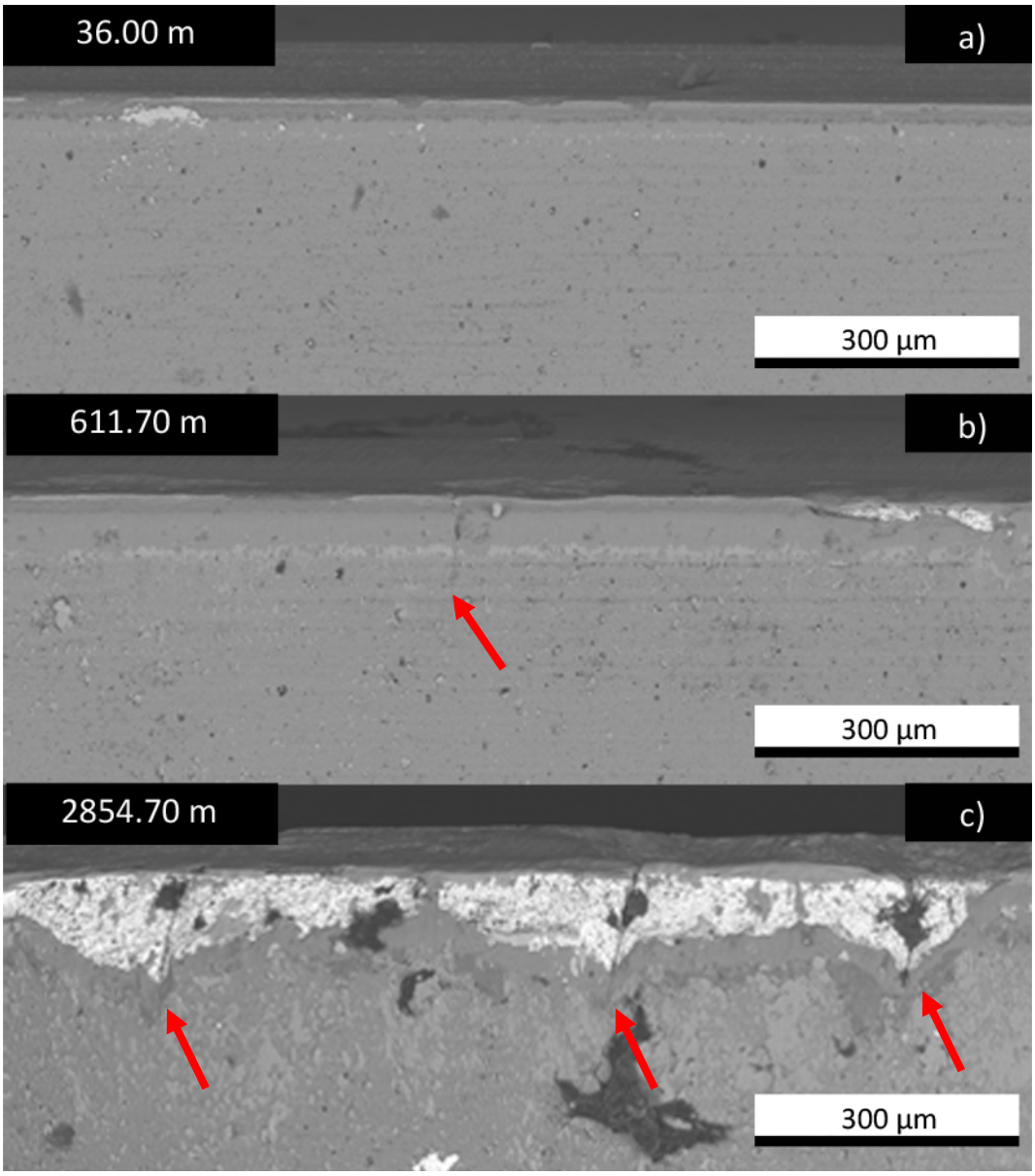

Fig. 29: SEM images of the flank face of inserts tested using setup B after a) 35.99, b) 611.73 m, and c) at end of lifetime 2854.75 m aTWCL. The red arrows in b) and c) indicate detected combcracks.

At early stages of testing crater and flank wear are the dominant damage forms. Some workpiece material sticking at the cutting edge was visible in the insert with 36.00 m aTWCL, see lighter grey area in Fig. 29a) [58]. After cutting 611.73 m aTWCL, the first combcrack was also detectable on the flank face, which is indicated by the red arrow in Fig. 29b). With increasing test duration, the abrasive wear damage increased and the coating was partially removed similar to the inserts tested using test setup A [58]. At the end of lifetime the coating on the tool's flank face was removed up to a distance of about 250 µm off the flank face surface, see Fig. 29c). The wear damage significantly increases after loss of the protective coating [58]. The abrasive wear damage is more pronounced in regions around a

combcrack, see Fig. 29c). A limiting factor regarding lifetime in the current test setup was that the whole cutting edge was disintegrated in a similar extent as in test setup A [58].
The overview image of the rake face of a used insert with an aTWCL of 36.00 m is presented in Fig. 30a). The red square in Fig. 30a) shows the detailed surface investigation in Fig. 30b) and the red line in Fig. 30b) indicates the position of cross section prepared by FIB milling (see Fig. 30c)) [58].

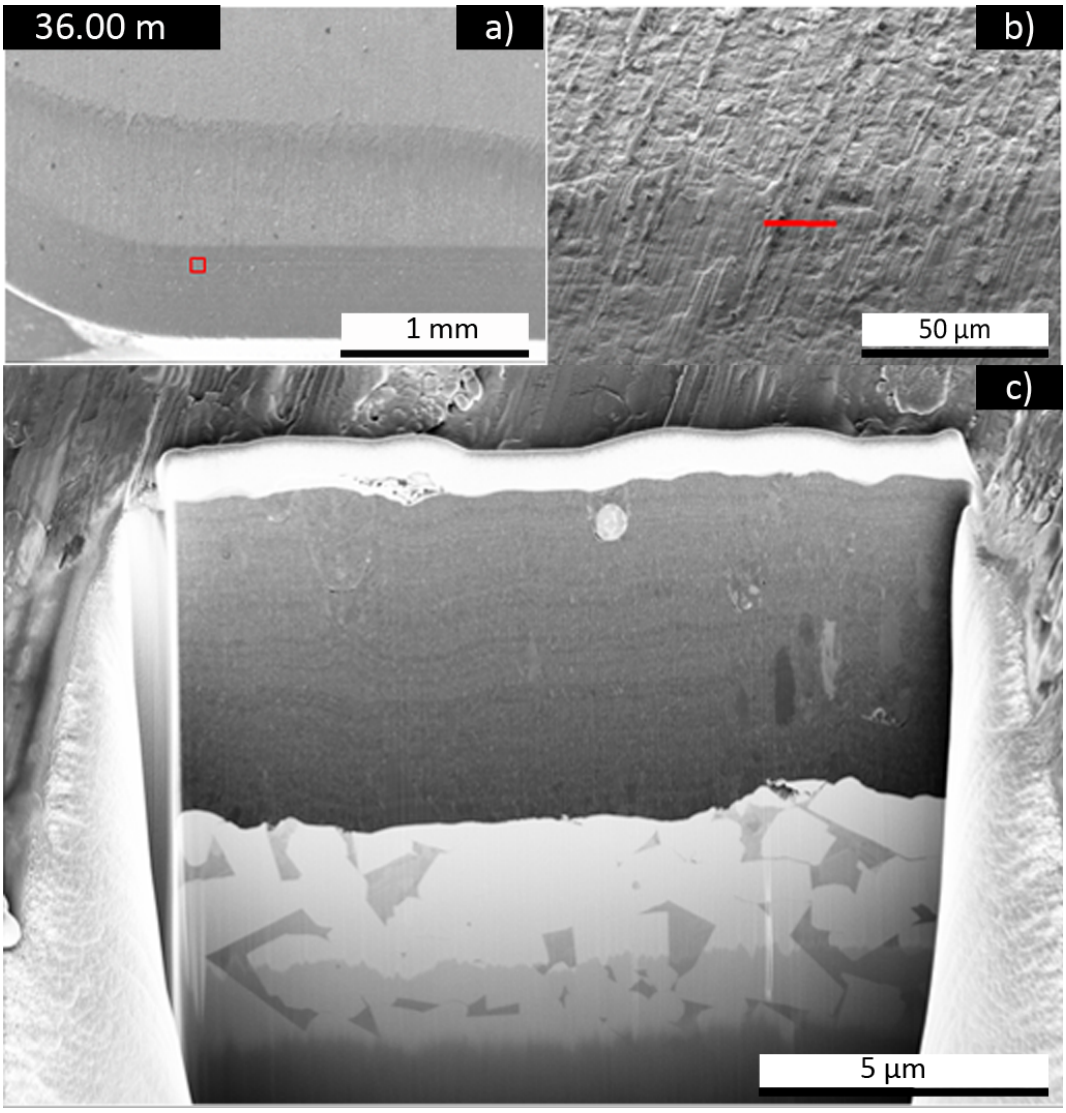

Fig. 30: SEM micrograph of the rake face of milling insert after 36.00 m aTWCL, using test setup B. Red frame in a) indicates the location of detailed surface investigations shown in b) with higher magnification. Red line in b) indicates the position of FIB cross section illustrated in c). Bright top layers on top of the FIB cross sections represent protective platinum layer, which was deposited on rake face prior to FIB cut to produce a smooth FIB cross section.

At early stages of the test wear dominates the damage of the milling inserts. Neither on the surface of the rake face nor in the FIB cross section combcracks were detected in a milling insert with an aTWCL of 36.00 m [58].

Fig. 31a) shows the cutting edge of insert, which had cut 611.73 m aTWCL under test setup B conditions. The red arrows indicate the position of the detected combcracks. The small red square shows the location of surface image with higher magnification positioned at the upper edge of the chamfer as shown in Fig. 31b). The position of the FIB cross section (see Fig. 31c)) of the most pronounced combcrack is illustrated as red line in Fig. 31b).

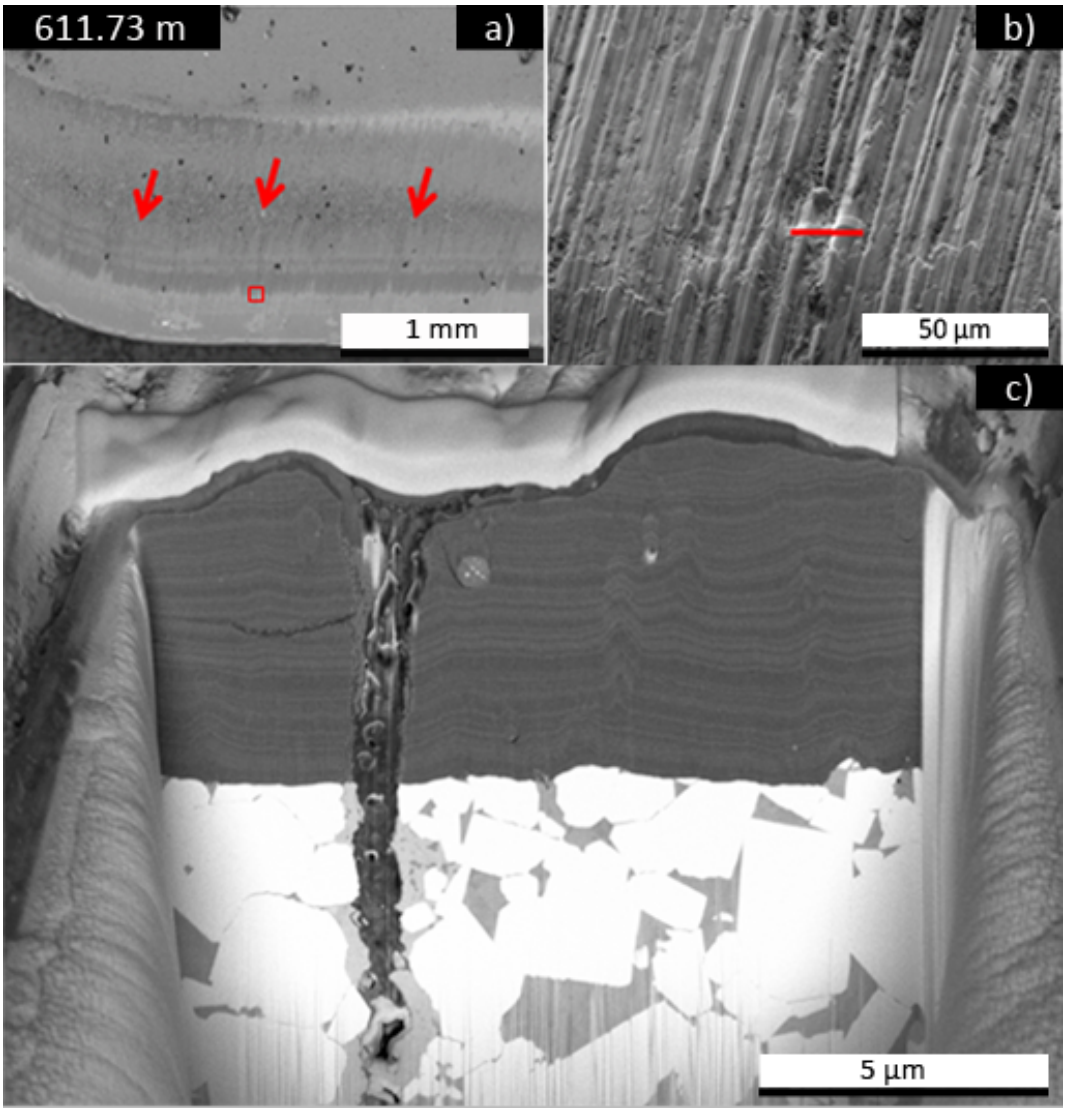

Fig. 31: a) SEM micrograph of the rake face of milling inserts after 611.73 m aTWCL, tested under test setup B conditions. Red arrows in a) indicate the positions of detected combcracks. At the most pronounced combcrack detailed surface investigations were done and the red frame indicates their location shown in b) with higher magnification. Red line in b) indicates the position of FIB cross section illustrated in c). Bright top layer on top of the FIB cross section represents protective platinum layers [58].

The first combcracks appeared in an insert after an aTWCL of 611.7 m [58]. The combcrack, which is positioned in the middle, has the most pronounced shattered crack edges compared to the other cracks edges of the other cracks, which may be an indication for earlier appearance. The other two combcracks are located about 570 and 630 µm away from this distinctive combcrack. In an used milling insert with an aTWCL of 407.8 m, tested under test setup B conditions, also a crack around a droplet was detected, see ref. [58]. Cracks which appear around droplets were possibly created upon tool loading. Tkadletz et al. [74] found a similar damage formation in an arc evaporated Ti-Al-Ta-N coating after a ball on disc test.

The rake face of a used milling insert at the end of lifetime after cutting 2854.75 m aTWCL is shown in Fig. 32a). The red square in this overview image indicates the location of the surface image with higher magnification positioned at the upper edge of the chamfer as shown in Fig. 32b). Red arrows indicate the location of the detected combcracks. Fig. 32c) illustrates the cross section prepared by FIB milling with their respective positions indicated by red lines in Fig. 32b) [58]. The end of lifetime was caused by the appearance of a crack, which grew parallel to the cutting edge and connected two combcracks. That consequently increases the risk of complete fracture, see black arrows in Fig. 32a). The dashed red line indicates the position of an additional FIB cross section (see Fig. 33) of one crack, which grew parallel to the cutting edge [58].

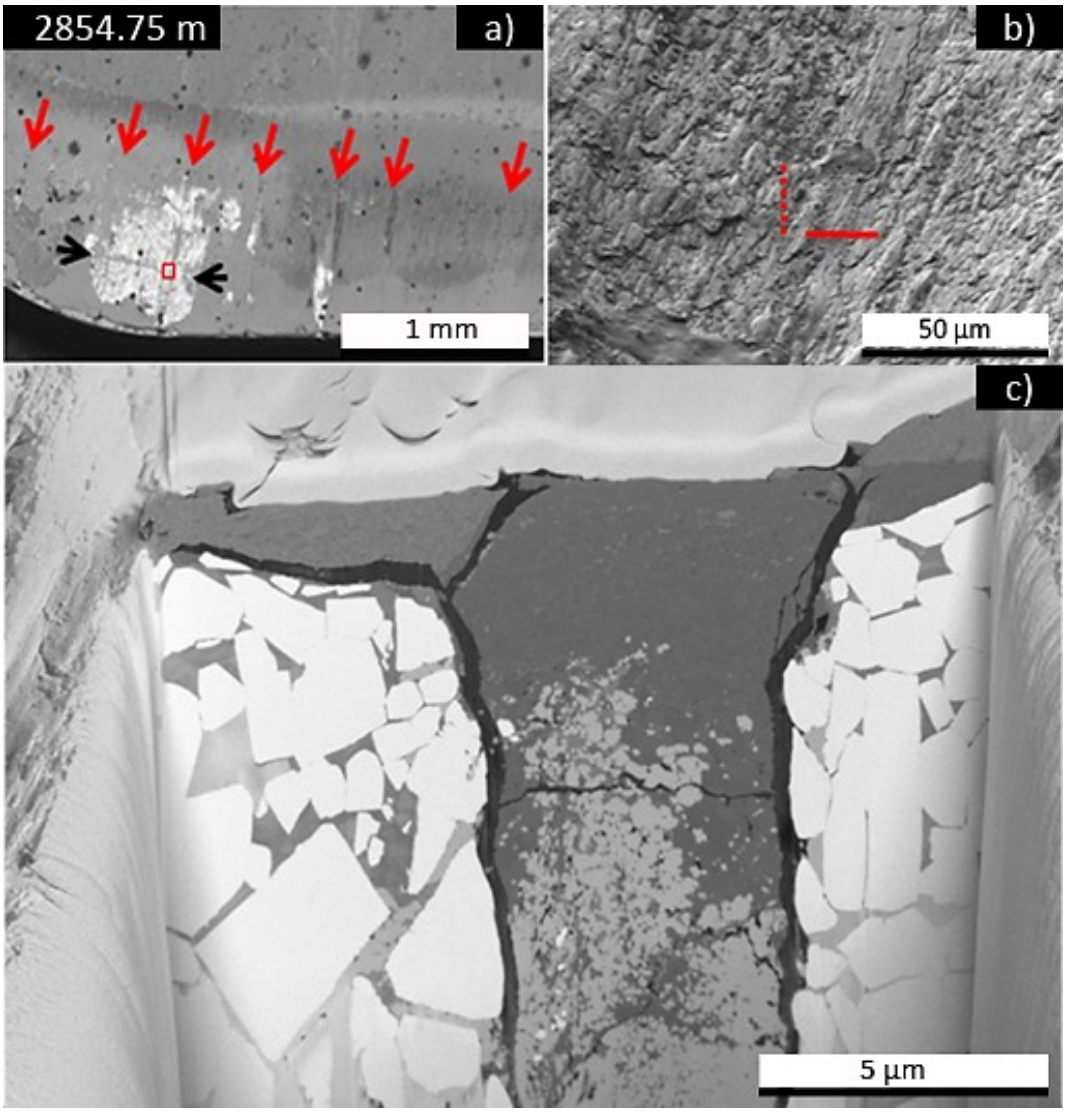

Fig. 32: a) SEM micrographs showing the damage state of rake face of an used milling insert tested under test setup B conditions at end of lifetime (2854.75 m aTWCL). Red square in a) indicates the location of b) detailed surface investigations with higher magnification. Red lines in b) indicate the positions of FIB cross sections shown in c). Bright top layers on top of cross sections represent platinum layers. The dashed red line in b) shows the position of an additional FIB cut, which is illustrated in Fig. 33. Red arrows in a) indicate the position of detected combcracks perpendicular to the cutting edge. The black arrows in a) show the position of a crack growing parallel to the cutting edge that is connecting two combcracks [58].

All investigated combcracks already penetrated in coating and hardmetal substrate, no earlier stage could be found. The width of the combcrack was about 1 µm at the surface and the end of the crack is not visible; consequently its length is greater than 15 µm, see FIB cross section Fig. 32c). With increasing aTWCL the number of combcracks increased and at the end of lifetime the insert showed seven combcracks, illustrated Fig. 32a). The FIB cross section of the most pronounced combcrack shows that both crack flanks and edges were

shattered and the detected crack opening at the surface was about 6 µm [58]. The mean distance between the combcracks is about 350 µm, which is much shorter as the distances in the early stage. It seems that new combcracks were created between two already existing combcracks. This result is comparable with the findings of Raninger et al. [75]. However, the end of lifetime was determined by the partial removal of the coating from the surface in an area of about 500 x 500 µm² (see Fig. 32a)) followed by formation of cracks with growth planes parallel to the cutting edge (see location in Fig. 32a) indicated by black arrows). This kind of cracks connecting two combcracks increases the danger of cutting edge breakage. One of these parallel cracks is shown in Fig. 33 in more detail.

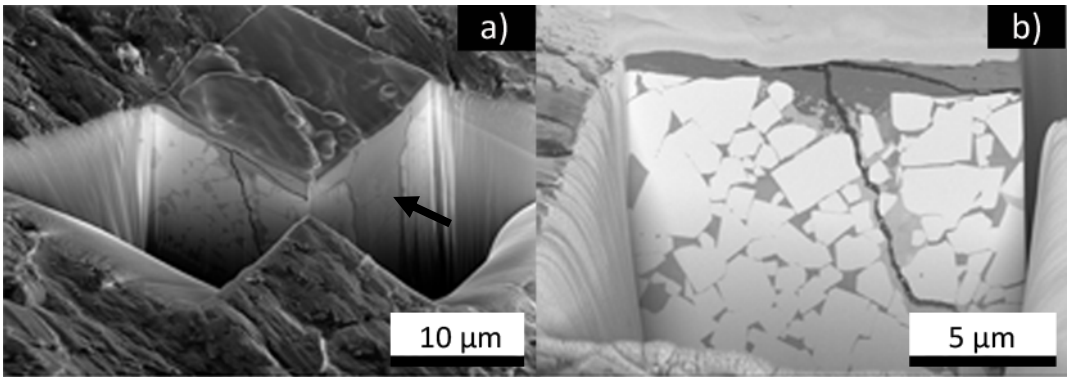

Fig. 33 a) SEM image of an overview of two positions of FIB cross sections on the milling insert at end of lifetime (2854.75 m aTWCL). In the cross section at the right side (indicated by a black arrow) the most pronounced combcrack is visible, see Fig. 32a). The left cross section illustrates a crack, which grew parallel to the cutting edge. b) The left cross section shows a crack with growth direction parallel to the cutting edge at higher magnification.

The width of the parallel crack was less than one micron and its length was greater than 10 µm. Opitz et al. postulated that these sorts of cracks were induced by pure mechanical fatigue. Milling experiments using heated inserts were applied and no thermal fatigue damage in form of combcracks but these characteristic parallel cracks appeared at latter state of application [5].

In another milling insert at the end of lifetime (4057.600 m aTWCL) tested with the same parameters, EDX mapping was done in FIB cross sections, see Fig. 34.

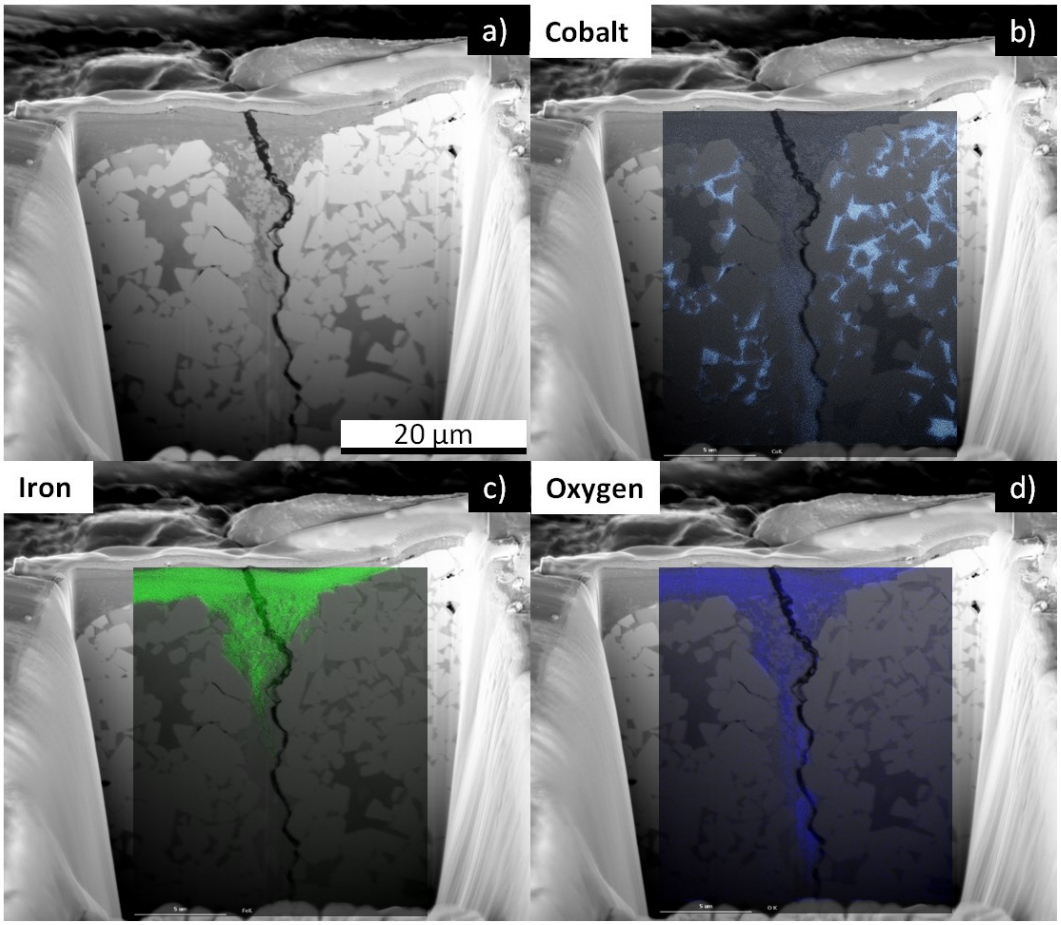

Fig. 34: a) SEM micrograph of a combcrack in a milling insert tested under test setup B conditions at end of lifetime after 4057.600 m aTWCL. Determination of the elements b) cobalt within in the binder phase, c) iron and d) oxygen at the same position as in a).

The dark layer at the hardmetal surface was identified as workpiece material (see Fig. 32c, Fig. 33b) and Fig. 34c)). The workpiece material is pressed into the combcrack during cutting. Iron was detected up to a depth of 15 µm (see Fig. 34c) and oxygen in the whole crack. The crack flanks and edges were shattered due to alternating opening and closing of the crack during the milling operation. In the crack also cobalt (see Fig. 34d) and tungsten carbide fragments were identified up to high depths.

The scanning acoustic microscopy (SAM) image of the combcrack dimension in the insert's volume is illustrated in Fig. 35a). The dashed yellow lines indicate the extension of the combcrack. The dimensions of the combcrack in the SAM image were compared with the SEM images of the rake (see Fig. 35b)) and the flank (see Fig. 35c)) face of the milling insert.

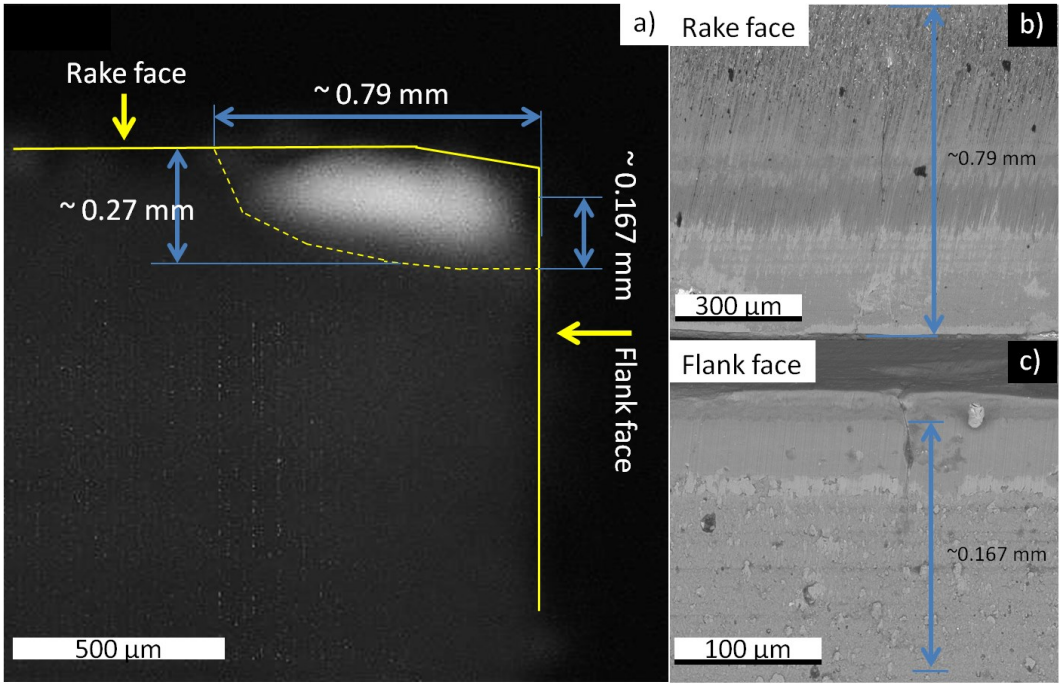

Fig. 35: a) Scanning accoustic microscope image of the combcrack within the milling insert, which had cut 611.7 m aTWCL under test setup B conditions and in which the first combcrack appeared. b) SEM image of the rake face including the dimension of the first combcrack, and c) SEM image of the flank face with the dimension of the first combcrack.

This comparison shows excellent agreement between the crack extension at the surface and the ultrasonic image. From those findings, it can be concluded that the combcrack has a shape to a quarter of an ellipse, see Fig. 35b,c). The total combcrack has reached a depth of about 0.27 mm from the rake face into the volume. Opitz et al. investigated the dimension of the combcracks in an uncoated hardmetal milling insert for specific milling [5]. An insert, which exhibited a high number of combcracks, was divided into two parts via electric discharge and the cross section was investigated. Due to the high temperatures during sample preparation, induced by electric discharge, the WC grains on the crack flanks were oxidized and the dimensions of the combcrack were visible. The shape and extension of the combcracks found in this work are similar to the dimensions of the investigated combcracks by Opitz et al. [5].

4.1.3 Evolution of damage in post treated milling inserts

Dry blasted post treated milling inserts were tested under test setup B conditions. Details concerning blasting parameters were shown in chapt. 3.3.

The inserts show the same damage mechanism and evolution as previously described in chapt 4.1.2. The detailed SEM investigations of the surface topography of the rake face can

be found in the own publication, see [55]. The number of combcracks observed in the SEM as function of aTWCL is illustrated in Fig. 36.

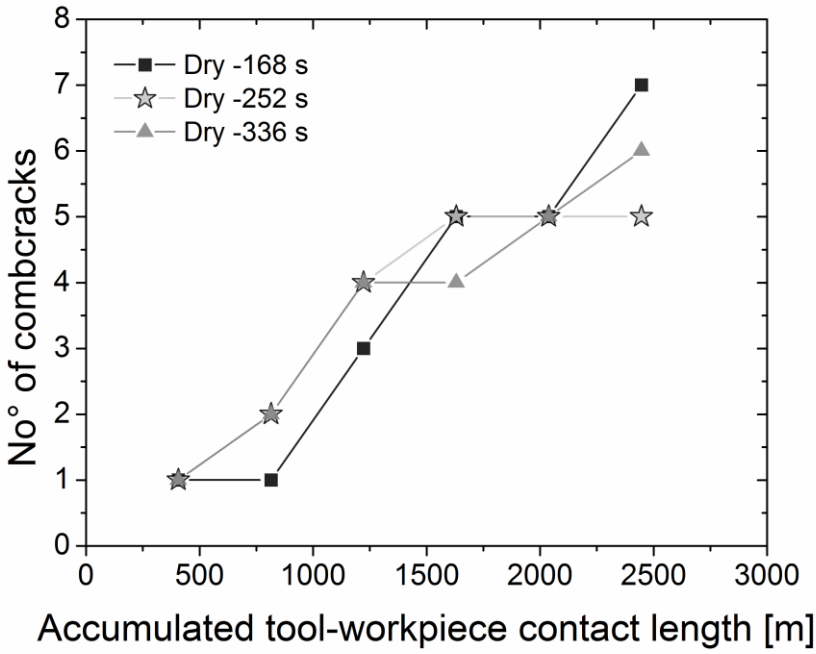

Fig. 36: Number of combcracks apparent in post treated milling inserts as function of milled accumulated tool-workpiece contact length. The three different symbols indicate the different blasting times of 168, 252 and 336 s which was used to post treat the milling inserts [55].

After cutting of 407 m aTWCL, the first combcrack was visible in all inserts independent of their blasting time. The number of combcracks increased with increasing length of aTWCL in inserts which were post treated for 252 s and 336 s. In contrast, the insert with the lowest blasting time developed its second combcrack between 815 m and 1220 m aTWCL [55].
After cutting 2446 m aTWCL all inserts reached the end of lifetime. The blasting duration had no significant influence on the lifetime. Parallel cracks, which have a growth direction parallel to the cutting edge (see Fig. 33), were apparent in all milling inserts at end of lifetime. The insert at end of lifetime, which was blasted for 168, 252 and 336 s, did exhibit seven, five and six combcracks, respectively [55].

4.1.4 Variation of feed rate and cutting speed

The mechanical and thermal loads are influenced by cutting speed and feed rate. A rise of the feed rate increases the volume (V = TWCL × cutting depth × feed rate) of workpiece which has to be cut per contact. Increasing the feed rate from 0.4 to 0.6 mm/tooth, the cut volume increases per contact from 41 to 62 mm^3, respectively. With increasing cut volume the mechanical loads increase. SEM images of the rake faces of milling inserts, which were

tested under test set up A conditions in variation of the feed rate are illustrated in Fig. 37. The red arrows in Fig. 37b,c) indicate the positions of the apparent combcracks.

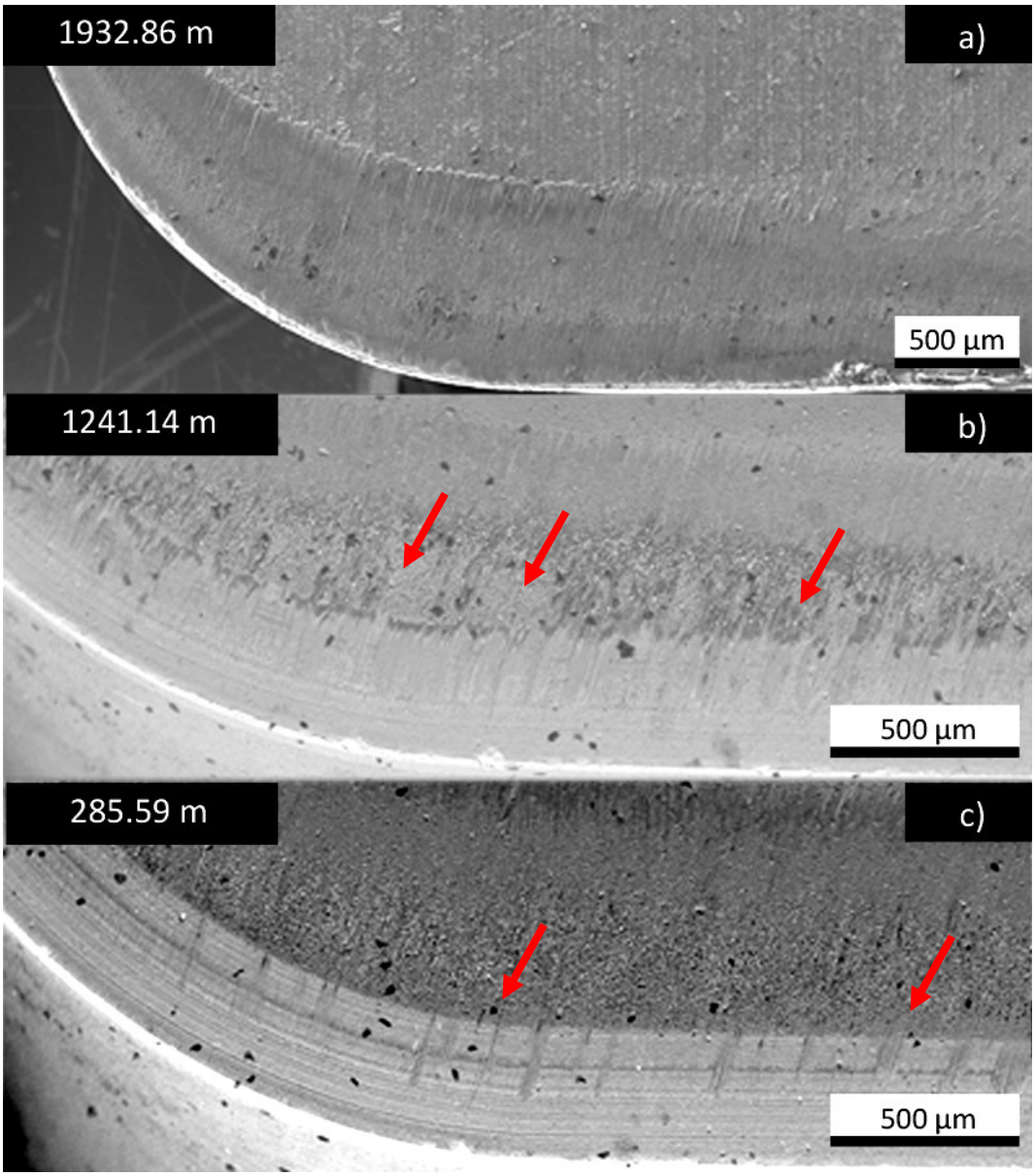

Fig. 37: SEM micrographs of rake faces of used milling inserts tested under the setup A conditions with increasing feed rate a) 0.4, b) 0.5 and c) 0.6 mm/tooth. Milling tests were stopped either after appearance of first combcracks (e.g. in b) and c)) or after reaching a critical magnitude of wear damage (e.g. a)).

No combcracks were found at the end of lifetime in inserts tested under test setup A conditions, when a feed rate of 0.4 mm/tooth was used. With increasing feed rate, combcracks appeared before end of lifetime. The milling insert, which was tested with a feed rate of 0.5 mm/tooth, showed three combcracks after cutting an aTWCL of 1241.14 m. Using a feed rate of 0.6 mm/tooth fostered the combcrack formation and the first combcracks

were detected in the insert with 285.59 m aTWCL. These results are comparable with literature. Bathia et al. described a combination of process parameters with feed rate lower than 0.1 mm/tooth and 1.5 m/s under which no tool failure induced by combcracks was observed. An increase of the machine parameters, feed rate and speed, resulted in combcrack formation [47]. Melo et al. assumed that thermal stresses were more generated when higher feed rates are used due to the increase of the temperature difference [43].
The influence of the cutting speed at a constant feed rate of 0.6 mm/tooth is illustrated in SEM images of milling inserts, which were tested with 220 (Fig. 38a) and 250 m/min (Fig. 38b).

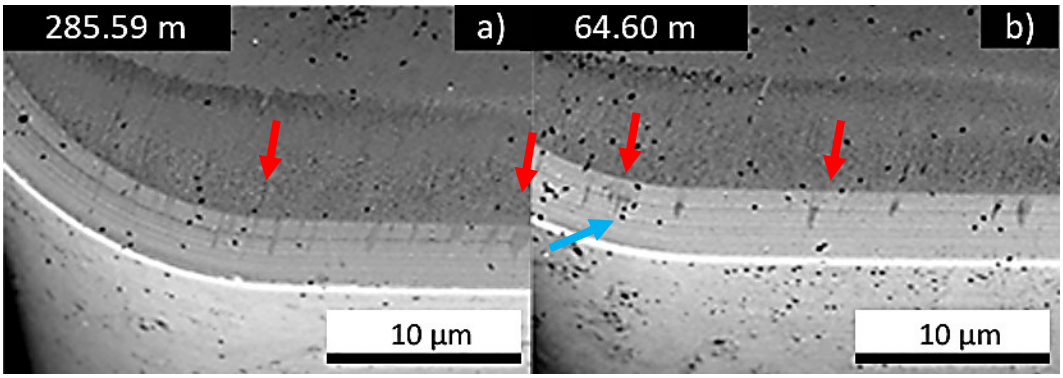

Fig. 38: SEM images of cutting edges of milling inserts cutting edge tested under test setup A conditions using a constant feed rate of 0.6 mm/tooth and a varied cutting speed of a) 220 m/min and b) 250 m/min. Red arrows indicate the position of the combcracks. Milling tests were stopped after appearance of first combcracks. In b) a combcrack was detected, which did not reach the cutting edge, indicated by the blue arrow.

First combcracks were observed after 285.59 m aTWCL in the inserts, tested with a cutting speed of 220 m/min whereas in the inserts, tested with a speed of 250 m/min the first combcracks were already detected after 64.60 m aTWCL. An increase of the cutting speed thus fostered the combcrack formation. These results correspond well with the findings in literature [43],[47]. The milling insert, which was tested with a speed of 250 m/min, did exhibit two combcracks including one, which did not reach the cutting edge, see red arrows within the rake face in Fig. 38b). As assumed it seems that the combcracks start at the rake face some distance away from the cutting edge and grow into the depth and towards the cutting edge perpendicular to the rake face. Some authors in the literature also assume that the site of crack initiation is located at the hottest point on the rake face [5],[43] followed by growth towards the cutting edge [5],[43],[76].

4.2 Residual stress evolution in substrate and in coating

In the following sections the position resolved residual stress evolution of the WC phase and of the Ti-Al-Ta-N coating as function of the accumulated tool-workpiece contact length (aTWCL) is illustrated. Details regarding the complete residual stresses in the WC phase and Ti-Al-Ta-N coating were described in own publications I-III, V [57]-[59],[64].

4.2.1 Position resolved synchrotron measurements

Residual stresses in the WC phase parallel to the cutting edge of selected milling inserts with zero, 0.102, 0.514 and 51.440 m aTWCL using test setup A were characterized in a position-resolved manner within a rectangular area indicated in Fig. 17 via synchrotron X-ray diffraction [59]. The corresponding two-dimensional distribution of the residual stress component in the direction parallel to the cutting edge is presented in Fig. 39.

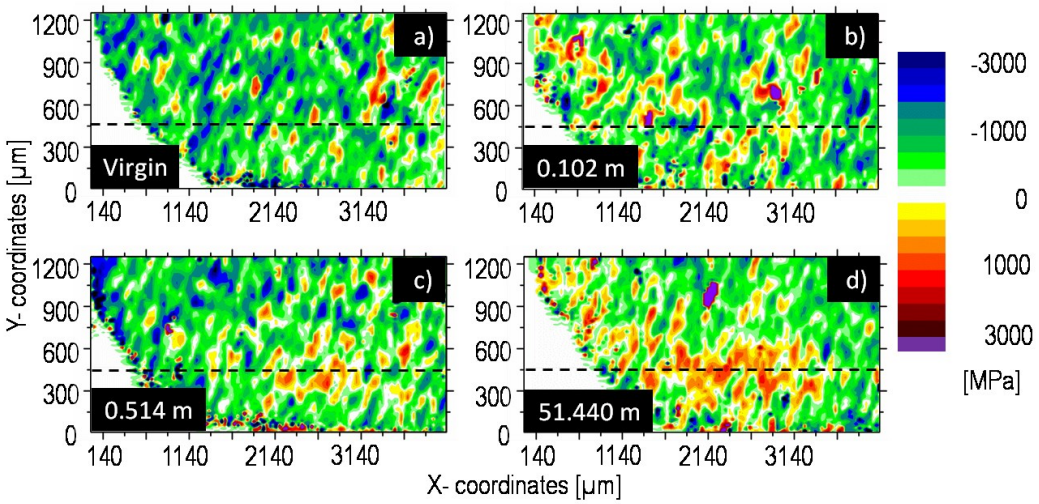

Fig. 39: Residual stress maps of milling inserts in the WC phase in x-direction with a) 0, b) 0.102 m accumulated tool-workpiece contact length (aTWCL), c) 0.514 m and d) 51.440 m aTWCL using milling setup A (see details in chap 3.4). [59]. Black dashed lines indicate the position of the residual stresses profiles in x-direction in Fig. 40.

Predominantly compressive residual stresses were observed in the WC phase of the virgin milling insert (see Fig. 39a)). As seen in Fig. 39b) and c) the residual stress state of milling inserts with 0.102 m aTWCL and 0.514 m aTWCL, which corresponds to two and ten contacts, showed buildup of a tensile residual stress state as indicated by the increased fraction of orange areas [59]. However, after 51.440 m aTWCL (1000 contacts) significant tensile residual stresses developed parallel to the cutting edge in an area of approximately 0.3 mm x 1.6 mm. The center of significant tensile residual stress buildup is located about

0.4 mm away from the straight portion of the cutting edge [59]. The residual stress profiles in x-direction along the black dashed lines parallel to the cutting edge indicated in Fig. 39 are presented in Fig. 40.

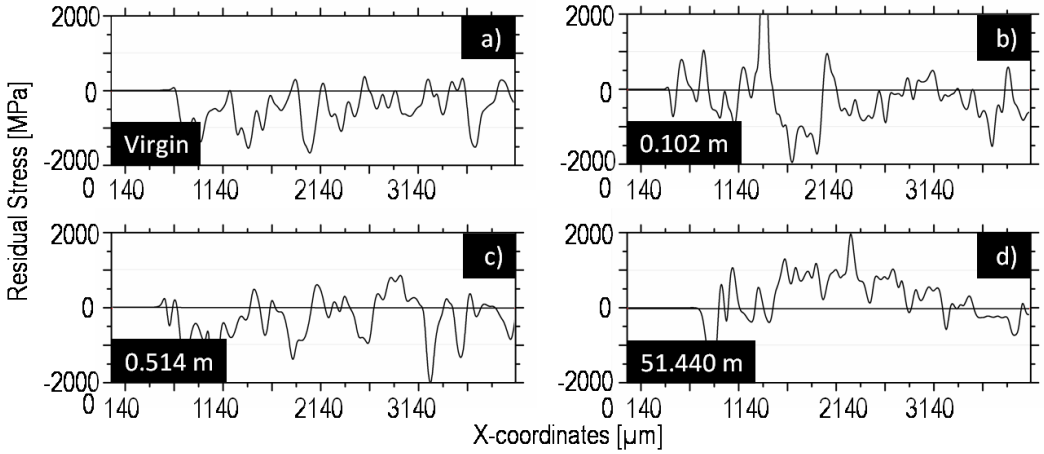

Fig. 40: Residual stress profiles in x-direction obtained from horizontal sections of residual stress maps in milling inserts as indicated by black dashed lines in Fig. 39: (a) 0, (b) 2 cuts (0.102 m aTWCL), (c) 10 cuts (0.514 m aTWCL) and (d) 1000 cuts (51.44 m aTWCL) using milling setup A [59].

The residual stresses in the WC phase of the virgin milling insert were mainly compressive. This result corresponds to findings of neutron diffraction experiments of uncoated hardmetal specimens from literature [77]. There were no significant changes of residual stress state in specimens with 0.102 m (two cuts) and 0.514 m (10 cuts) aTWCL. Most of the detected residual stress values were still mainly compressive (see Fig. 40b) and Fig. 40c)). However, significant tensile residual stresses of about 1000 MPa were observed in the specimen with 51.440 m aTWCL, which corresponds to 1000 cuts, on a length of scale of about 1.6 mm (see Fig. 40d)). Please note that the uncertainty associated with the measured value is about 900 MPa. For testing under test setup A conditions, more than ten tool-workpiece contacts are required to build up significant tensile residual stresses on the rake face of the inserts [59].

The corresponding two-dimensional distribution of the residual stress components oriented normal to the cutting edge for the same inserts at the virgin state and after 0.102, 0.514 and 51.440 m aTWCL is presented in Fig. 41.

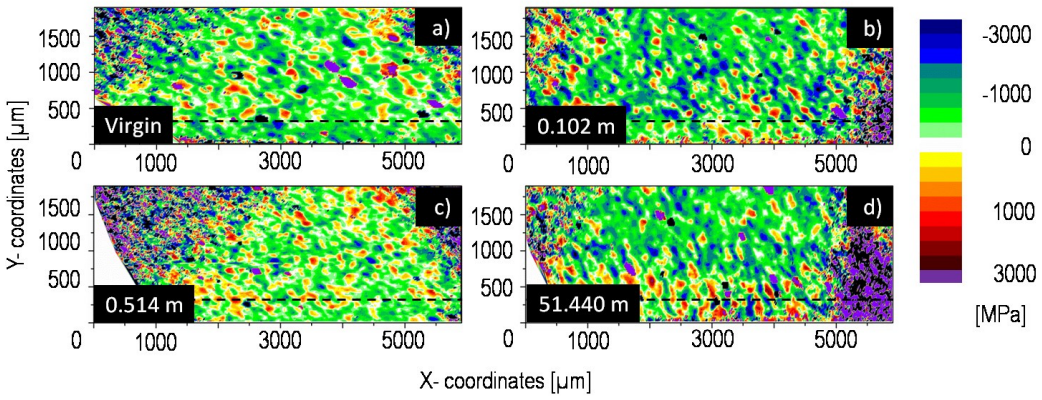

Fig. 41: Position resolved maps of residual stress in the WC phase in direction perpendicular to the cutting edge (y-direction) in milling inserts with a) 0, b) 2 cuts, which corresponds to 0.102 m accumulated tool-workpiece contact length (aTWCL), c) 10 cuts (0.514 m aTWCL) and d) 1000 cuts (51.440 m aTWCL) using milling setup A. The lower boundaries of the stress maps correspond to the straight portions of the cutting edges of the inserts. Black dashed lines indicate position of residual stresses profiles in y-direction in Fig. 42.

The insert at the virgin state exhibited compressive residual stresses acting normal to the cutting edge in the WC phase (see Fig. 41a)). After two, ten and 1000 cuts there was no significant stress change. Most of the fractions were green and blue colored, which indicates a compressive residual stress state. Only a slight increase of the amount of orange fractions in the insert with 51.4 m aTWCL was observed within the ROI (see Fig. 39d).

Some areas of the inserts' surfaces, especially the rims, did exhibit a high amount of violet and black coloured fractions (cf. Fig. 41) which correspond to high tensile and compressive residual stresses at the respective positions. These findings were not trustable and were thus not considered for further interpretations. Using this test setup, at low tilt angles ψ the incident beam penetrated the whole sample area at the same incidence angle θ if symmetric incident and diffracted beam are assumed. At higher tilt angles ψ (see Fig. 16b)) there is a shadowing effect at the rim of the specimens. Calculations of residual stresses resulted in high compressive and tensile stress values with an associated uncertainty higher than 1500 MPa. The local variations of residual stresses acting normal to the cutting edge along the black dashed lines indicated in Fig. 41 are presented in Fig. 42.

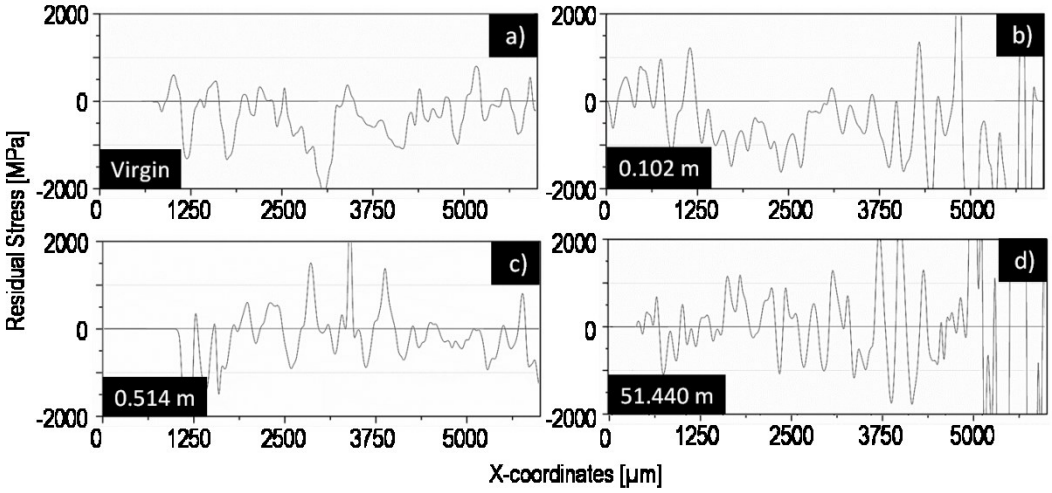

Fig. 42: Profiles of the residual stresses in y- direction in the WC phase obtained from residual stress maps in millings inserts at positions indicated by dashed lines in Fig. 41: a) at the virgin state, and after b) 0.102, c) 0.514 and d) 51.440 m aTWCL using milling setup A.

At early stages the residual stresses in the direction normal to the cutting edge were mainly compressive. No significant increase of residual stresses or a build-up of tensile residual stresses within the ROI was observed with increasing aTWCL up to 51.44 m. These findings by and large confirm the assumption of Opitz et al. [5] that tensile residual stresses act parallel to the cutting edge. The mean compressive residual stress values in inserts with 0, 0.102, 0.514 m aTWCL are comparable with the values of uncoated WC-Co specimen [77]. Please, keep in mind that inserts had cut 0.102 and 51.440 m aTWCL residual stresses, which were coordinated 5500 and 5000 µm in x-direction, respectively were not trustable because of limitations resulting from test setup.

4.2.2 Residual stress in WC and TiAlN phase determined by X-ray diffraction

The evolution of residual stresses in the ROI (see Fig. 39d)) of milling inserts using test setup A is presented in Fig. 43 as function of aTWCL. The test setup for residual stress measurements is described in chapters 3.10.2. and 3.10.3.

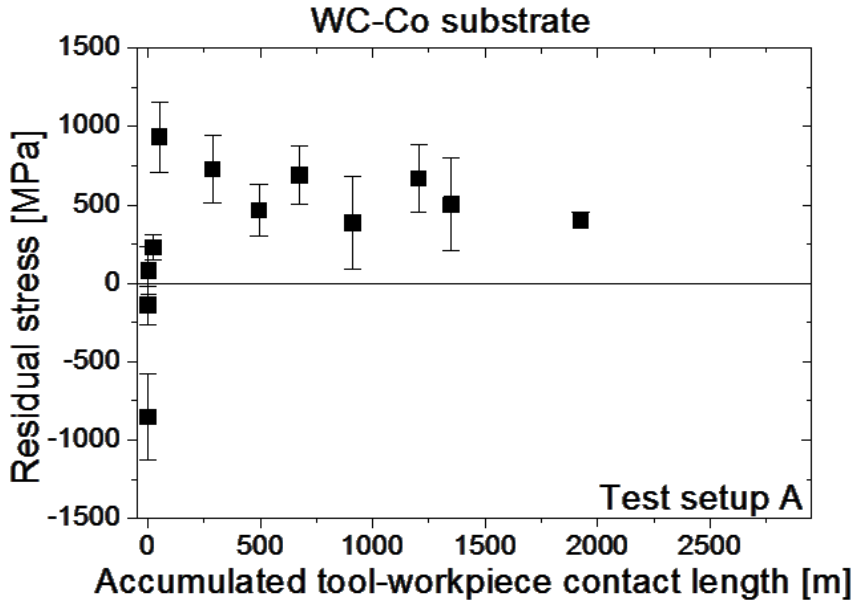

Fig. 43: Residual stress of the WC phase in the direction parallel to the cutting edge of inserts tested under test setup A conditions as function of accumulated tool-workpiece contact length [57].

Compressive residual stresses of -850 ± 270 MPa were detected within the ROI in the virgin milling insert. This corresponds well with the results of synchrotron residual stress measurements in [59] and the results of neutron diffraction experiments of uncoated hardmetal specimens, described in [77].

In the early stages of cutting the residual stresses in the WC phase changes dramatically within the ROI. After an aTWCL of about 0.51 m the compressive residual stresses were reduced to a value of approximately -140 ± 120 MPa. Already after 25.72 m aTWCL, tensile residual stresses of about 300 ± 80 MPa were observed. The highest tensile residual stresses of 930 ± 230 MPa were detected in a milling insert that had 51.44 m aTWCL which corresponds to 1000 contacts. This detected value is comparable with the value of about 1000 MPa found in exactly the same specimen via synchrotron X-ray diffraction [59]. After about 500 m aTWCL the tensile residual stresses were decreased to a plateau value of about 500 MPa which remains constant until the end of tool lifetime [57].

The residual stress states in the Ti-Al-Ta-N coating was calculated according to the modified fundamental relation (see Equation 6) described in [63] from the regression in a diagram strain vs. $\sin^2\psi$. The inserts were tilted along angle ψ. Only the stress component parallel to the cutting edge was considered. In Equation 6 the Young's modulus is indicated as E, σ corresponds to the apparent residual stresses in one direction, and v is the Poisson ratio.

Equation 6: Fundamental relation between strains and stresses acting in one direction [63]. E and σ correspond to the Young's modulus and residual stress in the observed direction and ν is Poisson ratio.

$$E(\psi) = \frac{1+\nu}{E} * \sigma * \sin^2\psi + \frac{1}{E} * [-2 * \nu * \sigma]$$

Equ. 6

The slope σ × (1 + ν) / E in a strain vs. sin2ψ diagram can be interpreted as the residual stress in units of the reciprocal X-ray elastic constant E / (1 + ν). The residual stress in units of reciprocal X-ray elastic constant E / (1 + ν) as function of aTWCL is presented in Fig. 44.

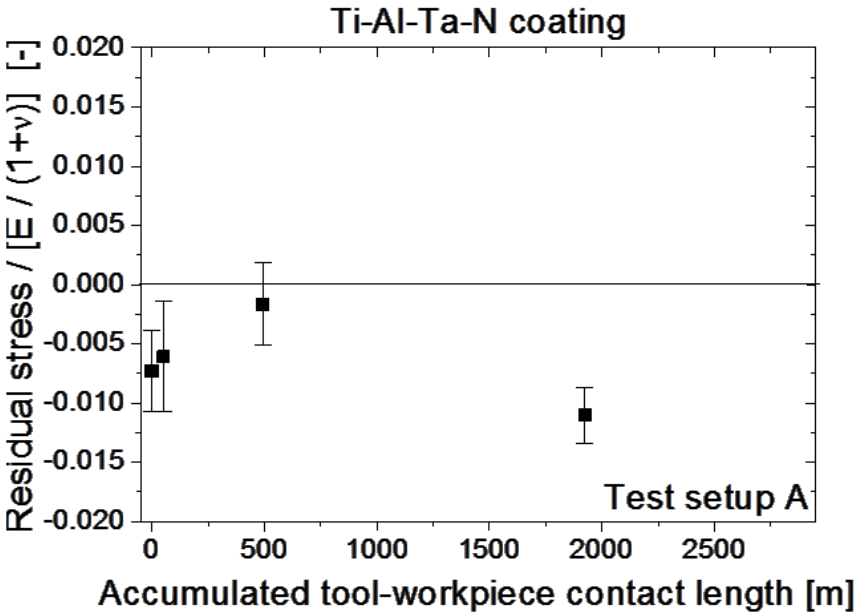

Fig. 44: Residual stresses in the direction parallel to the cutting edge determined in the Ti-Al-Ta-N coating within the ROI on the rake face of milling inserts tested under test setup A conditions. The parallel component of the residual stresses was determined using cover method [57] with lead as cover material [64].

Compressive residual stresses of about $-7.2 \times 10^{-3} \times E / (1 + \nu)$ were found in the virgin specimen. The residual stress value of the virgin insert can be varying between -2 and -3.11 GPa depending on the used elastic constants. A quantitative discussion of the XRD results requires a consideration of the uncertainties resulting from the elastic constants of the coating material, which depend on the exact chemical composition and on the anisotropy (texture) of the coating [63], see details in own publication V [64].

In this test setup, the residual stresses remained in compression in a range from -1.6×10^{-3} to $-11.0 \times 10^{-3} \times E / (1 + \nu)$ throughout the whole tool lifetime.

The evolution of residual stress in the WC phase over the complete tool life of milling inserts tested using test setup B is illustrated in Fig. 45.

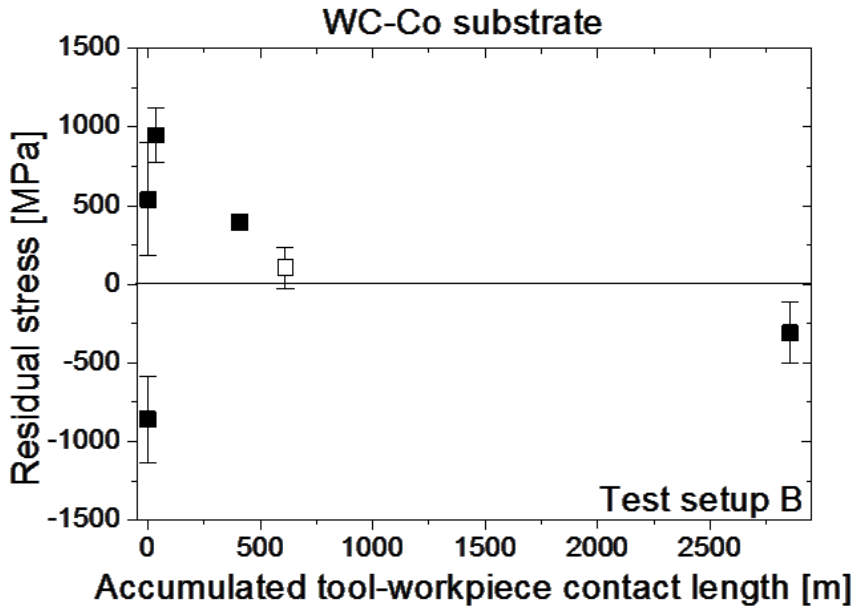

Fig. 45: Residual stresses of the WC phase parallel to the cutting edge within the region of interest (ROI) as function of accumulated tool-workpiece contact length (aTWCL) in inserts tested using test setup B. The open square represents an insert where the first combcracks were observed [57].

At very early stages of testing, the residual stress evolution in the milling inserts, tested in test setup B, is comparable to residual stress evolution of inserts, tested in test setup A. The compressive residual stresses in the virgin insert changed to tensile after a few meters of aTWCL for both conditions. The insert with an aTWCL of 2.4 m tested under test setup B conditions already showed tensile residual stresses of 540 ± 360 MPa (see Fig. 45) [58]. After 1000 tool-workpiece contacts, which correspond to an aTWCL of 36 m the highest tensile residual stresses of about 930 ± 230 MPa were detected.

The measured value corresponds well with the results of synchrotron measurements published in [59] and the residual stress state of insert with aTWCL of 51.4 m, tested under test setup A conditions [57], see Fig. 43. Until 500 m aTWCL the residual stress evolution was comparable in inserts tested using test setup A (see in chap. 4.2.2) and B. A milling insert, which cut 500 m aTWCL, did exhibit tensile residual stresses of about 400 MPa. These values are in the same range as the residual stress plateau value of test setup A (see in chap. 4.2.2). After 611 m aTWCL the first combcracks appeared in the ROI of an insert tested under test setup B conditions (see open circle in Fig. 45). The detected residual stresses decreased significantly to a value of about 100 MPa [58] as a consequence of cracking. At the end of lifetime, the residual stress state is compressive at a value of -310 ± 190 MPa. Thermal

fatigue in form of combcracks determines lifetime. The decrease of tensile residual stresses can be explained by relaxation of tensile stresses around the apparent combcracks [75].

The residual stress evolution of the Ti-Al-Ta-N coating of selected milling inserts, tested under test setup B conditions, in units of reciprocal X-ray elastic constant E / (1 + ν) as function of aTWCL is illustrated in Fig. 46. More details concerning these residual stress measurements of the coating are given in Publication V.

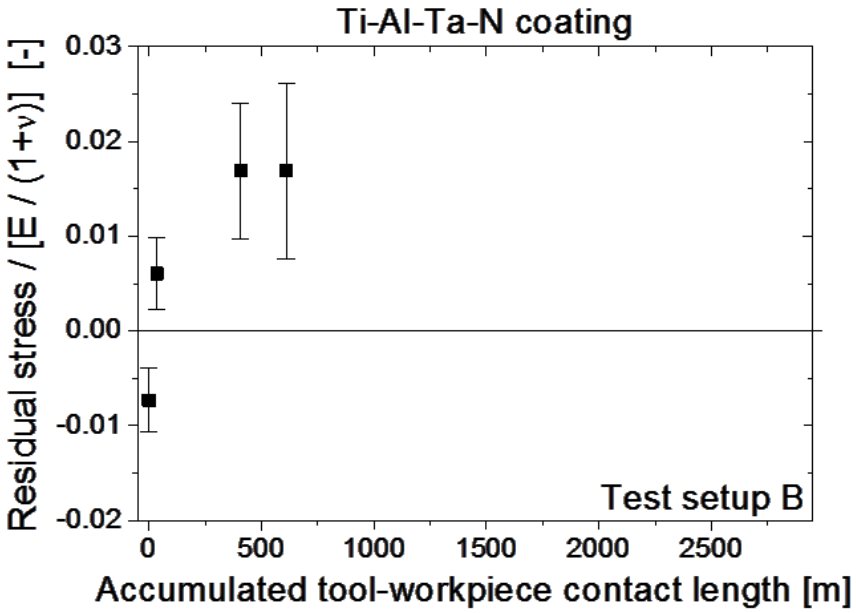

Fig. 46: Residual stress determined in Ti-Al-Ta-N coating parallel to the cutting edge of milling inserts tested using test setup B [64].

The residual stresses in milling inserts, tested using test setup B, changed after cutting of few meters of aTWCL. After 1000 tool-workpiece contacts, which correspond to 36 m of aTWCL, tensile residual stresses of about $6.07 \times 10^{-3} \times E / (1 + \nu)$ were determined. In a specimen, which cut 407.8 m aTWCL, tensile residual stresses were observed to have increased to about $16.9 \times 10^{-3} \times E / (1 + \nu)$. The specimen which contained the first detected combcrack, the residual stress state was found to be in tension. In test setup B, the coating and the WC phase did exhibit tensile residual stresses which possibly promoted the nucleation and growth of combcracks.

In contrast to the evolution of residual stress observed in the WC-Co substrate, the tensile residual stresses in the coating did not decrease when the first combcrack appeared. In the WC phase the found tensile residual stresses decreased and at end of lifetime the residual stress state was compressive [57]. This absence of decrease in tensile stresses after appearance of combcrack may be explained by the existence of inhomogeneities in an arc evaporated coating, e.g. droplets [78]. After a ball on disc test Tkadletz et al. found cracks

around droplets induced by shear stresses [74]. In both test setups, arising cutting forces may foster the introduction of this kind of cracks. However, if they are present in the coating, their orientation, density and / or distance to one another [75] did not lead to decrease the observed residual stresses to zero in both test setups (see Fig. 44 and Fig. 46).

4.2.3 Residual stresses in coating determined in enlarged region of interest

To document the position of the significant tensile residual stresses in the coating at a later point in the test, an additional residual stress measurement was done within an enlarged ROI (0.6 × 1.6 mm²). The result is compared with the results of measurements in ROI (0.3 × 1.6 mm², filled squares in Fig. 47), which were already described in pervious chapter, and it is shown in units of reciprocal X-ray elastic constant E / (1 + ν) indicated as open square in Fig. 47.

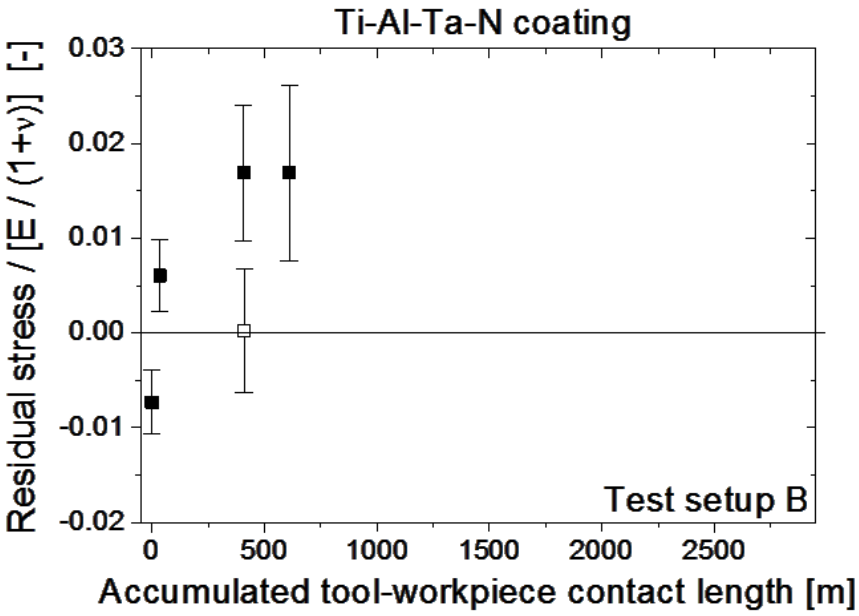

Fig. 47: Residual stress determined in a Ti-Al-Ta-N coating in direction parallel to the cutting edge of milling inserts tested under test setup B conditions. Both, results of residual stress measurements determined within ROI (0.3 × 1.6 mm², filled squares) (see Fig. 46 [64]) as well in the enlarged ROI (0.6 × 1.6 mm², open square) are shown.

By comparing results from the smaller (0.3 × 1.6 mm) and the enlarged ROI (0.6 × 1.6 mm) in one and the same specimen, the residual stresses, determined in the enlarged ROI (see dashed red rectangle in Fig. 19), showed a value close to zero (see open rectangle in Fig. 47). This finding can be interpreted as an averaging of tensile and compressive residual stresses inside and outside of the ROI as it seems to be present in the WC phase based on the

position resolved residual stress measurements using synchrotron radiation (see cf. Fig. 39 in [59]). This result also corresponds well with the positions in the simulation, in which high temperatures and stresses are apparent, see Fig. 59.

4.2.4 Residual stress states of post treated milling inserts at early application

The residual stresses in the WC phase of post treated unused and used inserts, which had cut 36 m aTWCL under test setup B conditions, are illustrated as a function of dry blasting time in Fig. 48. The residual stress state of an insert after coating deposition without additional dry blasting post-treatment is included as reference in Fig. 48 [55]. A detailed description can also be found in own publication IV.

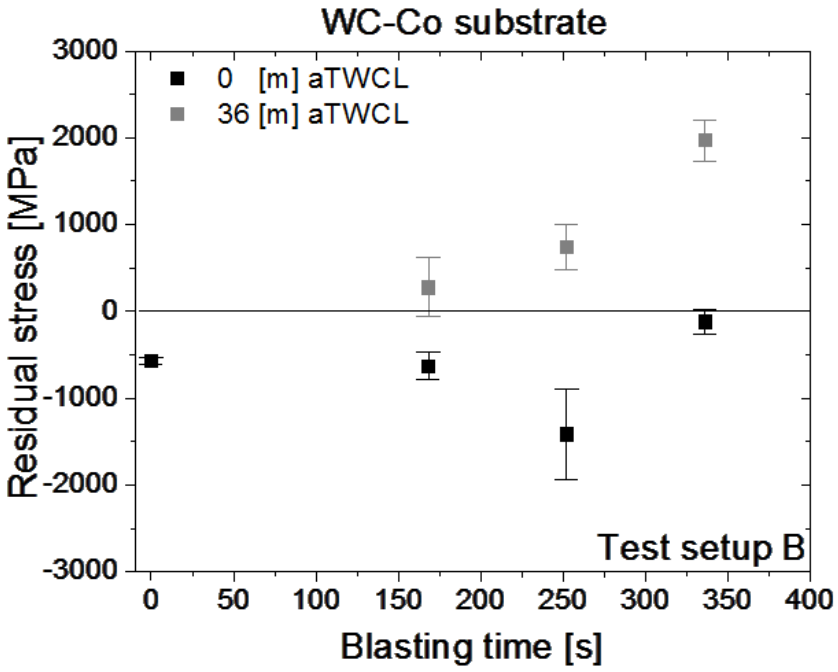

Fig. 48: Residual stress in WC phase as function of dry blasting time: Black squares indicate the residual stress values measured in the ROI of inserts after post-treatment by means of blasting without any tool-workpiece contacts. Grey squares represent results from used inserts with 36 m of accumulated tool-workpiece contact length (aTWCL) [55].

After coating deposition the WC phase of the reference insert without any additional post treatments exhibits compressive residual stresses of about -570 MPa [55]. All post treated inserts in the virgin state show compressive residual stresses [55]. The increasing dry blasting time does not influence significantly the residual stress state of the inserts: A value of residual stress of -600 MPa being very similar to the one from the non-blasted reference was observed in the unused insert with the lowest dry blasting time of 168 s. After 252 s of dry

blasting, a compressive residual stress state in the unused insert of about -1000 MPa was determined. Whereas, the virgin insert with 336 s of dry blasting time exhibits a compressive residual stress state of about -130 MPa [55]. This low compressive residual stress value may be an indication for plastic deformation in the substrate, induced by a too long blasting process. The magnitude and/ or region of plastic deformation have to be small because no cracks or fragmentation of the coating was apparent on the rake face after blasting process. This sort of damage is an indication for plastic deformation in substrate material, see the detailed SEM investigations of the surface topography of the rake face in the own publication IV, see [55].

After cutting 36 m aTWCL, all inserts exhibit tensile residual stresses. This tendency was also observed in inserts without any additional post treatments; see in the previous chapters 4.2.1 and 4.2.2. With increasing blasting time the detected tensile residual stresses increase from 300 MPa to 1900 MPa. It seems that short blasting times decelerate the tensile residual stress build-up after a certain number of tool-workpiece contacts compared to longer blasting times [55].

4.2.5 Discussion of uncertainty in residual stress measurements by X-ray diffraction

The uncertainty of the residual stress measurements arise from several factors: Position and size of ROI, non-linear evolution relationship between strain and sin2ψ and unknown X-ray elastic constants ($1/2\ s_2 = (1 + \nu) / E$) [63].

The position of the uncovered area might have varied 30 µm in horizontal and vertical direction. A deviation of position has influence on the detected residual stress value. The apparent tensile residual stresses are localized in specific areas on insert's rake face, see in chapters. 4.2.1 and details in own publication I [59]. Due to the small size of the ROI, the intensity of the diffracted beam is low. This measurement region is further decreased, when the sample is tilt due to the shadowing effect induced by the use of the metallic foils. This fact is pronounced effective in residual stress determination of the Ti-Al-Ta-N coating. The summarized thickness of the metal foil and the double-face adhesive tape was higher than of the brass foil used for residual stress measurements in the substrate [57],[64]. All detected strains had a linear regression in the diagram strain vs. sin2ψ and the elastic data for calculation of X-ray elastic constant $1/2\ s_2$ of pure WC are well known [9].

The X-ray elastic constants of the Ti-Al-Ta-N coating are unknown in the open literature. In contrast X-ray elastic constants of the pure TiN and AlN phases are well-known [79],[80]. The X-ray elastic constants can be determined experimentally via tension or bending tests, in which loadings in one direction are effective [63]. The data can also be calculated numerically by means of first principle density-functional theory [81]. The influence of the X-

ray elastic constants on the residual stresses are described in own work, see details in publication V.

A possible texture or inhomogeneities in form of microscopic pores in the coating can also influence the regression in a diagram strain vs. $\sin 2\psi$. The residual stresses cannot be calculated according to Equation 6 when the relationship is not linear. Pure Ti-Al-N exhibits a preferred growth direction in the (100) orientation. Alloying with Ta results in a mixed (100)/(111) orientation as preferred growth direction, which Kathrein et. al determined for a similar Ti-Al-Ta-N coating as used within this work [17]. The effect of texture can be negligible for the Ti-Al-Ta-N coating, which was used within this work. The determined linear relationship of all measurements let to the conclusion that the influence of microscopic porosity was not significant.

4.3 Estimation of cutting temperature

The following chapter gives an overview how the insert temperature near to the cutting edge and in an area located some distance away from cutting edge was estimated. The in directed investigation were done via microstructural investigations of a steel chip of the 42CrMo4 (1.7225) steel workpiece and the results of the cutting modeling via finite elements simulation. Additionally, temperatures were directly determined at the areas around the wear track on the tool's rake face by the color change of the used thermo chalk.

4.3.1 Investigations on chips

A longitudinal light optical microscope (LOM) cross section of a steel chip was prepared for microstructure investigation. Fig. 49 shows the top and side view of the chip. The red dashed line Fig. 49 indicates the position of the longitudinal section, see Fig. 50.

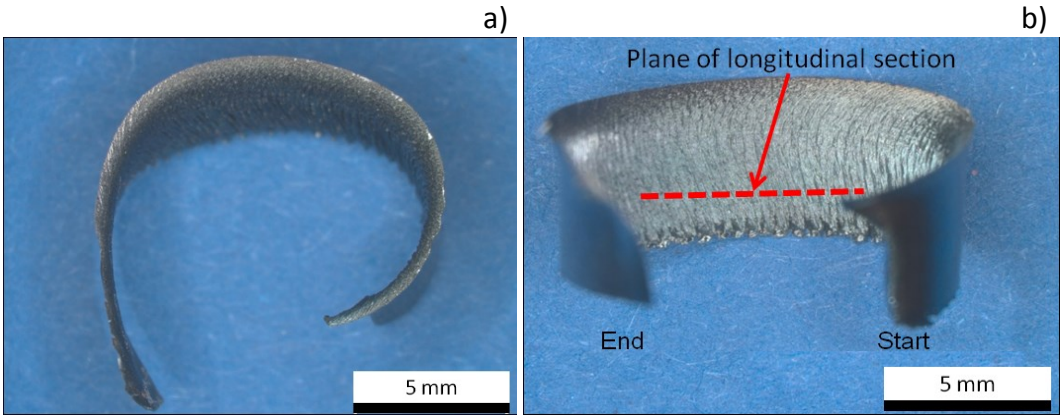

Fig. 49: Images of a 42CrMo4 steel chip, which was created during milling. a) Top view, b) side view - dashed red line indicates position of longitudinal section, presented in Fig. 50.

The chip was partially blue colored and curled. At 300 °C low carbon steel changes the color from silver gray to blue due to oxidation in air [82]. This found color indicated that the chip temperatures have reached at least 300 °C during milling. Probably the temperature is much higher than 300 °C because the chip is rapidly cooled after its generation which results in a very short time for oxide growth.

The used machine parameters within this work (see chapter 3.6) created this specific shape of the 42CrMo4 steel chip. The shape of the chip is influenced by the yield strength of the material and by the machining parameters [83]. Abel [83] showed the influence of the machine parameters on the shape of a Ck45 steel chip. The produced chip has a similar shape as the Ck45 steel chips, described in [83]. There, a feed rate, cutting speed and cutting

depth of 0.53 mm/rev., of 200 m/min and 3 mm, respectively, were used [83]. A Ck45 steel exhibits a minimum $R_{P0.2}$ of ~ 370 MPa according to [84]. These machine parameters were similar as these machine parameter used within this work [83]. A different shape of the chip may be an indication for another insert's geometry and/or inhomogeneities in the workpiece material [83]. The longitudinal section of a chip is shown in Fig. 50. For detailed investigations of the microstructure 5 different positions were chosen, which were indicated by coloured rectangles in Fig. 50.

The chip thickness was not constant because of the change of the feed rate direction angle ϕ during cutting. The chip thickness is dependent on feed rate, feed rate direction angle ϕ, working diameter and engagement [26], which was within this work 20 mm (see Fig. 13). Other machine parameters remained constant during the whole cutting process. Due to the use of climb-cut milling within this work, the chip thickness is very broad at the beginning of the cut (see Pos.1 in Fig. 50). With increasing cut duration the chip thickness decreases.

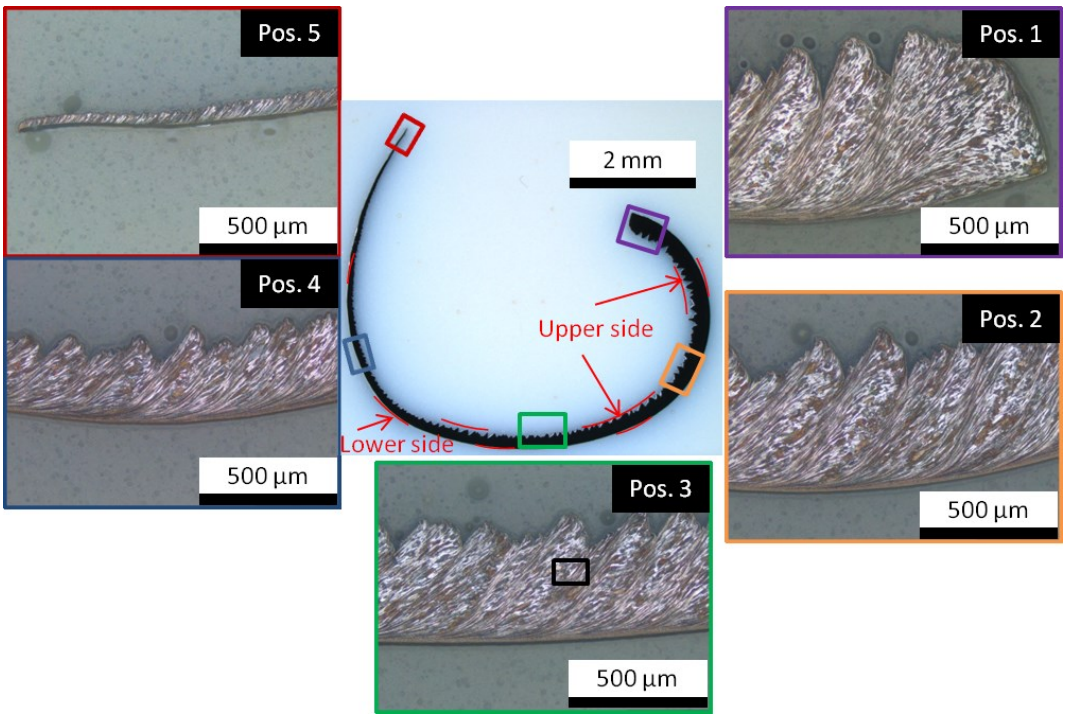

Fig. 50: LOM image of longitudinal section without etching. Red arrows indicate the upper and lower side of the chip for determination of the chip length. Colored rectangles define the different positions of the detailed LOM investigations. For better visualization of the microstructure the areas of detailed investigations were etched by nital solution. The small black rectangle in Pos. 3 indicates the position of the SEM investigation, shown in Fig. 51.

The chip length on the upper and lower side was 31.2 and 25 mm respectively, see Fig. 50. These determined lengths were shorter than the tool-workpiece cutting length of about 51.4 mm, due to compression during the chip formation. Fig. 50, the positions one, two and

three show zones of high deformation, so-called shear zones, in which no original ferrite-pearlite structure was detectable and the workpiece material was deformed [24]. Next to these shear zones there are zones, in which the workpiece material is less deformed and parts of the original microstructure were visible. Shear zones are also detected in positions four and five (see in Fig. 50). At these positions four and five no parts of less deformed ferrite-pearlite microstructure were detected. This result is comparable with findings in literature [72]. Detailed intersection between a shear zone and original microstructure is shown a SEM micrograph in Fig. 51. The position is indicated in Fig. 50 as black rectangle in Pos.3 at the middle of the chip.

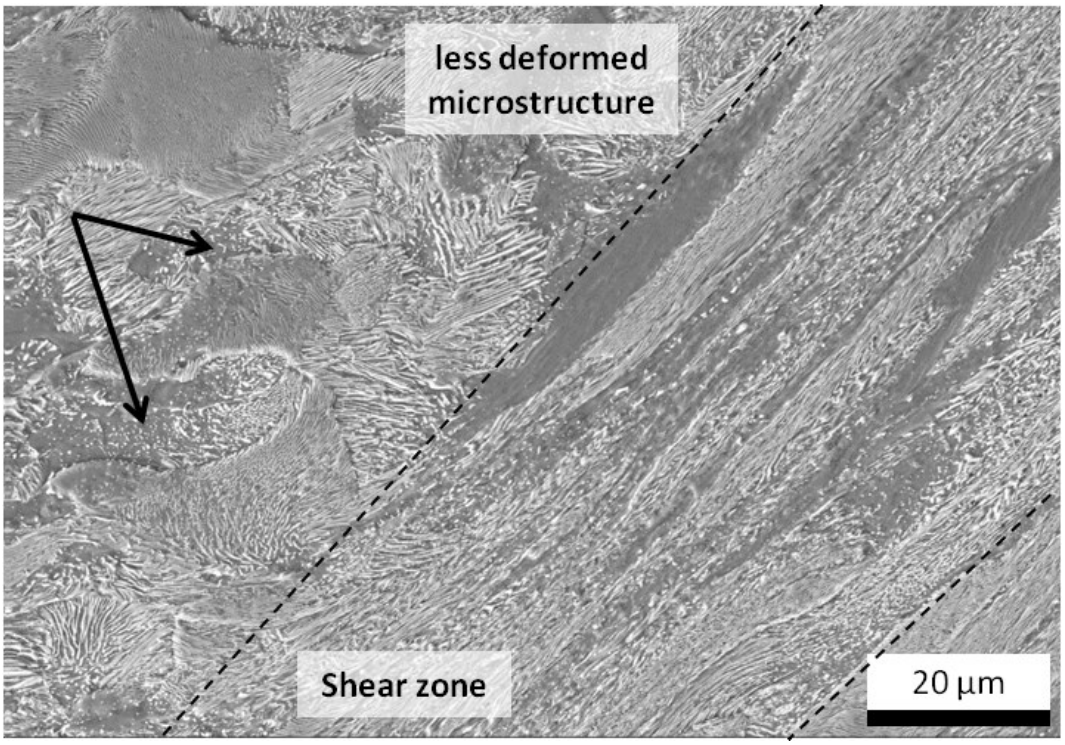

Fig. 51: Detailed SEM micrograph of indicated in Pos. 3 in Fig. 50 in a longitudinal section of the chip. The area between the dashed lines indicates the strong deformed shear zone. Areas outside are characterized by less deformed ferrite-pearlite microstructure. Black arrows indicate position of partially formed spherical perlite structure.

Fig. 51 illustrates a strong deformed shear zone and a less deformed zone, in which original pearlite and ferrite phases are still visible. In the strongly deformed shear zone, the original pearlite and ferrite has changed to strongly elongated structure. Some cementite lamellas of original pearlite structure were partially transformed to spherical shape (see black arrow in Fig. 51). In each position of the longitudinal section no martensitic phase was observed. The absence of martensitic structure may indicate that the temperature of the chip was not

higher than 911 °C and/or not enough time was given to stay at this temperature [85], in which austenite structure can form [72],[85].

4.3.2 Temperature measurements using thermo chalks

Two selected milling inserts were prepared either by an orange or by a green thermo chalk. They cut a distance of 15.12 m aTWCL under test setup A conditions (details see in chapt. 3.6). Temperatures, which are apparent close to the wear mark on rake and flank face, can be determined by the colour change of the thermo chalks at a certain temperature (details see in chapt. 3.8). Fig. 52 illustrates the rake faces of the two milling inserts prepared with orange (Fig. 52a)) and green thermo chalk (Fig. 52b) after cutting. Additionally, the flank face of the orange coloured milling insert is shown in Fig. 52c).

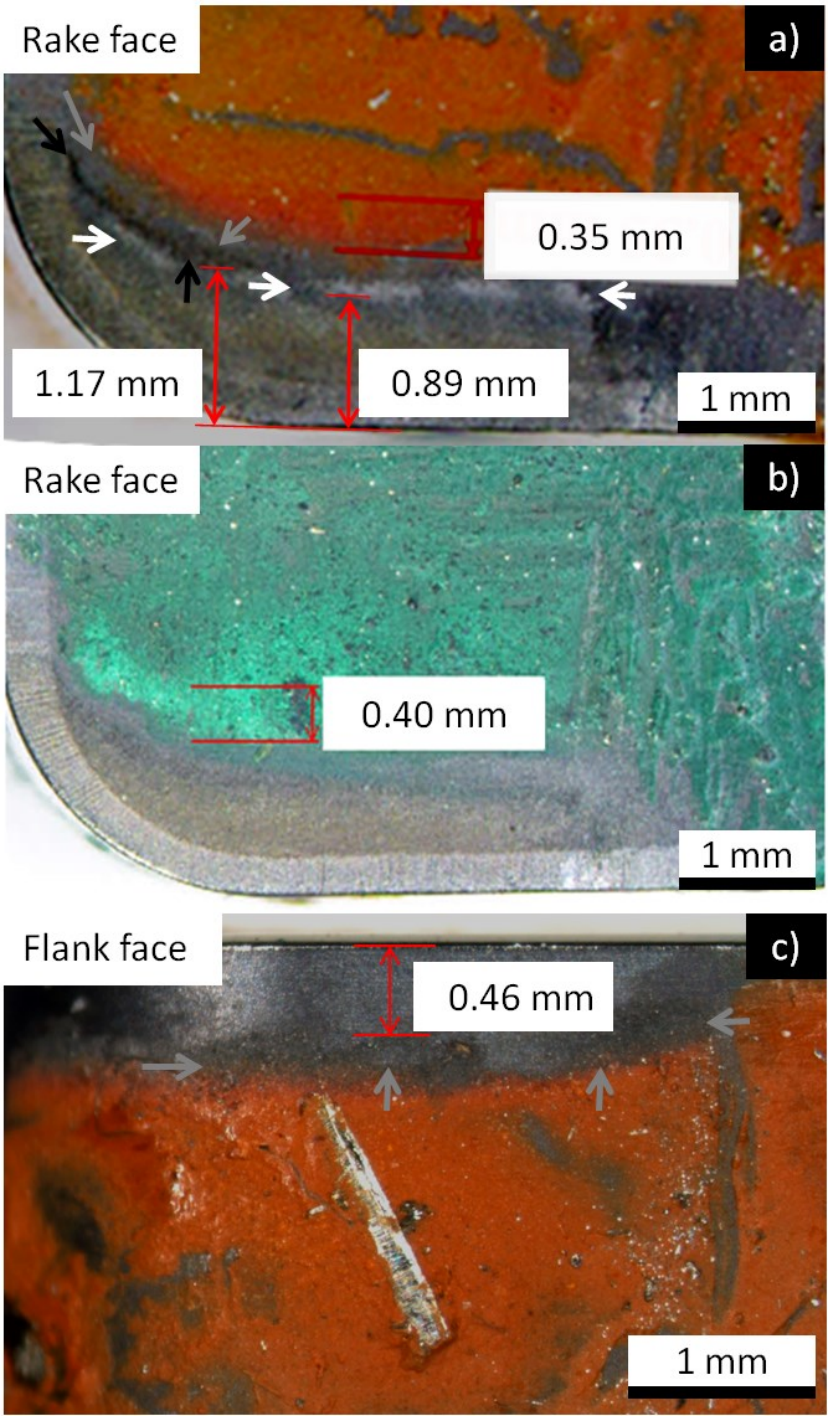

Fig. 52: LOM images of used inserts after cutting of 15.12 m aTWCL, which surfaces were prepared with an orange thermo calk - a) rake face and c) flank face of the insert. White, black and grey arrows in a) and c) indicate regions, in which orange thermo chalk change the colour to white, black and grey, respectively. b) Rake face of a used milling insert prepared by green thermo chalk after cutting of 15.12 m aTWCL.

Due to contact of the workpiece with the milling insert during chip formation, the thermo chalk was removed up to a distance of about 890 µm on the rake face and of about 461 µm on the flank face from the cutting edge, sees Fig. 52a).

The colour change of the thermo chalk documents the apparent mean temperature of cutting of 1.5 cut segments under test setup B conditions (see detail in chapt. 3.6), which lasts 45 s. The mean temperature increases within the first 21 s due to the entry of the tool and milling under constant conditions with a constant cutting duration of 14 ms. Within the next 10 s the mean temperature decreases due to the exit of the tool. After, no heat impact is given for duration of two seconds because the miller moves from end to start position. In the last 10 s of application the mean temperature increases again due to the entry of the tool.

The colour of the chalk changes when the specific temperature is reached and remained for at least two seconds. This reaction can be accelerated when higher temperatures are reached [42]. This may be happened during the contact of the milling insert with the workpiece.

On the rake face of the orange coloured insert a white coloured area was detected, which was located between 0.89 and 1.07 mm from the cutting edge (see Fig. 52a)). The change of the colour from orange to white indicates rake face's surface temperatures higher than 505 °C during cutting. Additionally, on the milling insert's rake face, a black coloured region between 1.07 and 1.17 mm away from cutting edge and a grey coloured area behind located (1.32 mm away from cutting edge) were observed, see Fig. 52a). The black and grey colours indicate apparent temperatures of about 335 °C and 245 °C. On the flank face (see Fig. 52b)), no white areas were observed but a grey coloured area located 0.46 mm away from the cutting edge was detected.

Temperatures higher than 600 °C were not determined via green thermo chalk because a colour change into white was not detected on milling insert's rake face, see Fig. 52c). The exact temperatures at the region in which the insert is in contact with a normalized 42CoMo4 steel workpiece material for milling applications are hardly available in literature. Trent et al. [72] mentioned that temperatures of about 900 °C can appear in TiN coated M34 high speed steel tools.

4.4 Thermo-physical and thermo-mechanical properties of the hardmetal grade

4.4.1 Thermo-physical properties

Within this work, the thermal diffusivity (a) and the thermal conductivity (λ), the linear thermal expansion coefficient (α) and the heat capacity (c_p) were determined and illustrated in Fig. 53 and Fig. 54. The measurement uncertainties are discussed in chapt. 3.11.

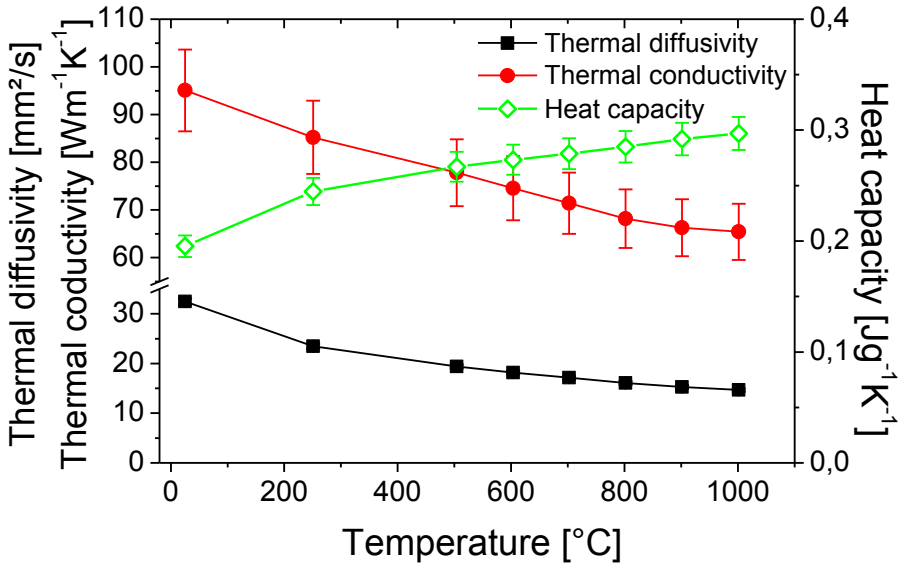

Fig. 53: Thermal diffusivity, thermal conductivity and heat capacity of hardmetal as function of temperature.

Thermal diffusivity and conductivity decrease with increasing temperature whereas the α and c_p increase. The RT values of the a, λ and c_p for hardmetals are available in the open literature [1],[86]. At higher temperatures only data of pure WC and Co were documented.
Within this work the used hardmetal, which exhibits a Co content of 8 wt.%, exhibits an a value of 32.46 ± 0.65 mm²/s, a λ value of 95.07 ± 8.56 W/mK and a c_p value of 0.19 ± 0.01 J/gK, respectively at RT.
This findings correspond well with findings of a hardmetal grade with 6 wt.% Co, where values for a of 32 mm²/s, λ of 105.6 W/mK and c_p of 0.22 J/gK were detected [86]. According to Brooks [10], the λ values of a hardmetal grade with 8 wt.% Co may vary between 75 and 120 W/mK. Other literature sources document the λ range from 70 to 120 W/mK for different hardmetal grades [1],[87]. Brooks et al. determined for hardmetal grades with 8 wt.% Co heat capacity values from 0.20 to 0.22 J/gK at room temperature [10].

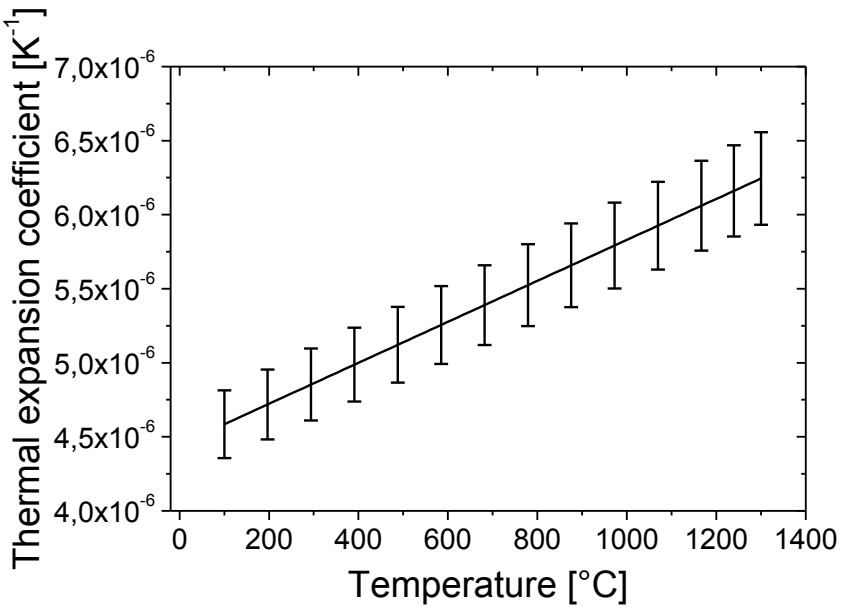

Fig. 54: Linear thermal expansion coefficient of the hardmetal is shown.

In literature the linear thermal expansion coefficient is reported to vary from 5.8 x 10^{-6} K^{-1} for a temperature difference between RT and 800 °C to 5.9 x 10^{-6} K^{-1} for RT and 600 °C for a hardmetal grade with 8 wt.% Co [9],[10]. The detected thermal expansion coefficient values are slightly lower than literature data, see Fig. 54. Between RT and 600 °C the hardmetal grade exhibits an α of about 5.3 x 10-6 K-1, and between RT and 800 °C a value of about 5.5 x 10^{-6} K^{-1}. The used hardmetal exhibits 2 wt.% mixed carbides in form of TaNbC. According to Schedler, an addition of mixed carbides in hardmetal leads to a decrease of the linear expansion coefficient [9].

4.4.2 High temperature elastic properties

The Young's – (*E*) and Shear modulus (*S*) and the Poisson's ratio (*v*) of hardmetal grade are presented as function of the temperature in Fig. 55. The measurement uncertainties are discussed in chapt. 3.11.

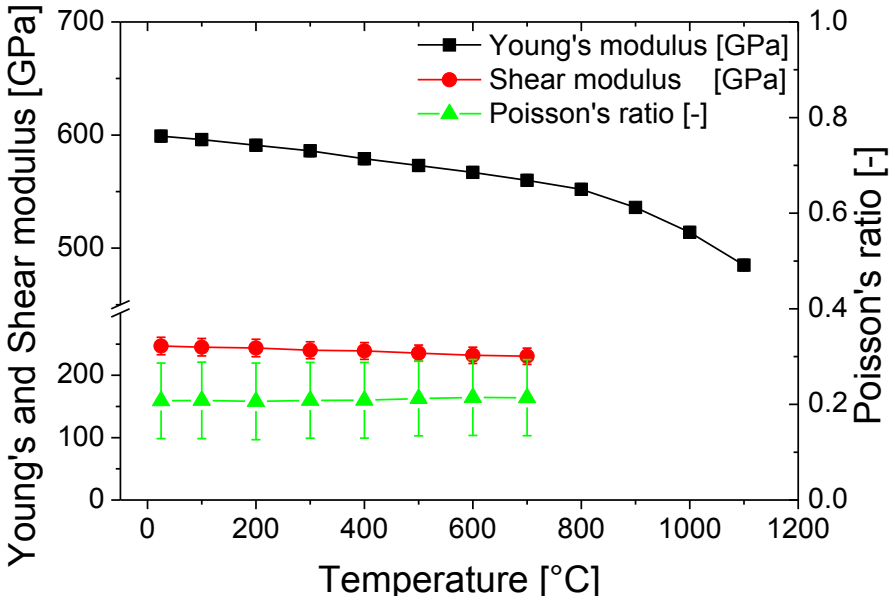

Fig. 55: Young's - and shear modulus and the Poisson's ratio values of the hardmetal with increasing temperature [88].

At room temperature the hardmetal exhibits Young's - and Shear moduli of about 599 and 247 GPa, respectively [88]. The Poisson's ratio of about 0.208 was calculated indirectly using *E* and *G* values [88] according Equation 4. Young's modulus decreases linearly from 599 to 552 GPa at temperatures between room temperature and 800 °C. Above 800 °C, the decrease becomes more pronounced. At temperatures of about 1100 °C the Young's modulus is about 458 GPa [88]. In contrast, *G* decreases accordingly and *v* remains almost constant over the whole temperature range from room temperature to 700 °C. At 700 °C the hardmetal exhibits a *G* of about 230 GPa and a *v* of about 0.214 [88].

The findings correspond well with room temperature values reported in literature [9],[89],[90]. Brooks mentioned in his work *E* and *G* values of about 600 and 230 GPa, respectively, and a *v* of about 0.22 for a hardmetal grade with 8 wt.% Co [10].

Elastic property data at elevated temperatures are rarely available. Blumenthal determined the elastic properties of a hardmetal grade with 9 wt.% Co for temperatures up to 500 °C. The values were slightly lower compared with data of the current work. At 500 °C *E* and *G* are reported to be about 546 and 226 GPa, respectively, and a *v* of about 0.204 [91].

4.4.3 Temperature dependent flow curves

The compressive flow curves and the compressive yield strengths ($R_{P0.2}$) of the selected hardmetal grade were determined at temperatures of 400, 600 and 800 °C in Fig. 56. Please

note that the under used compressive loadings, most samples did not fracture either after having reached the maximum load.

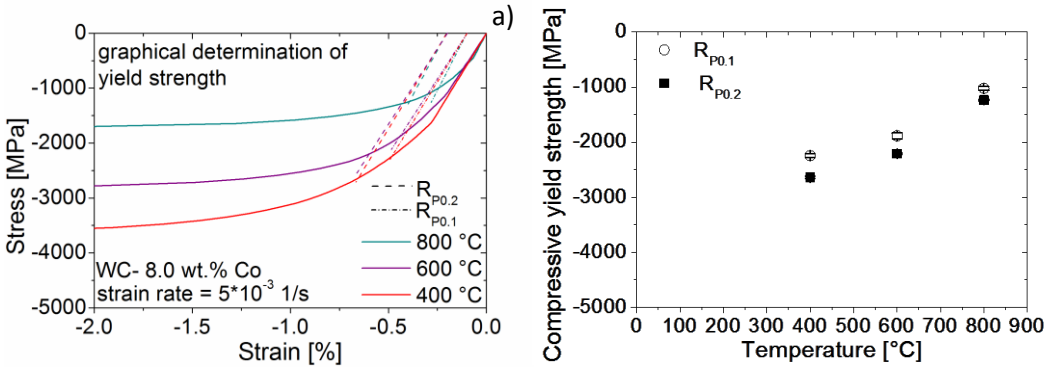

Fig. 56: a) Compressive flow curves of the used hardmetal grade at 400, 600 and 800 °C. b) Compressive yield strength value R_P for 0.1 and 0.2 plastic strain. All experiments were carried out using a strain rate of 5×10^{-3} 1/s.

The hardmetal shows a remarkable strain hardening at all temperatures. Plastic deformation starts at lower stress values at higher temperatures, see in Fig. 56. $R_{P0.2}$ decreases with increasing temperature from -2656 at 400 °C to -1250 MPa at 800 °C. The measurement uncertainties are discussed in chapt. 3.11.

Some authors determined the flow curves via 3 point testing with a strain rate of 1.6×10^{-6} s^{-1} at elevated temperature [92],[93]. They detected flow curves up to a strain value of 0.5 % for a hardmetal grade with 11 wt.% Co at 1000 °C [92]. The stress-strain values are smaller but in a similar range as the determined stress- strain values of the flow curve at 800 °C [92]. Milmann et al. investigated the HT hardness of WC-Co. The temperature dependence of the hardness is similar to that of the flow curves [94].

4.4.4 Fracture toughness as function of temperature

The fracture toughness (K_{IC}) of the hardmetal grade A is presented as function of temperature in Fig. 57.

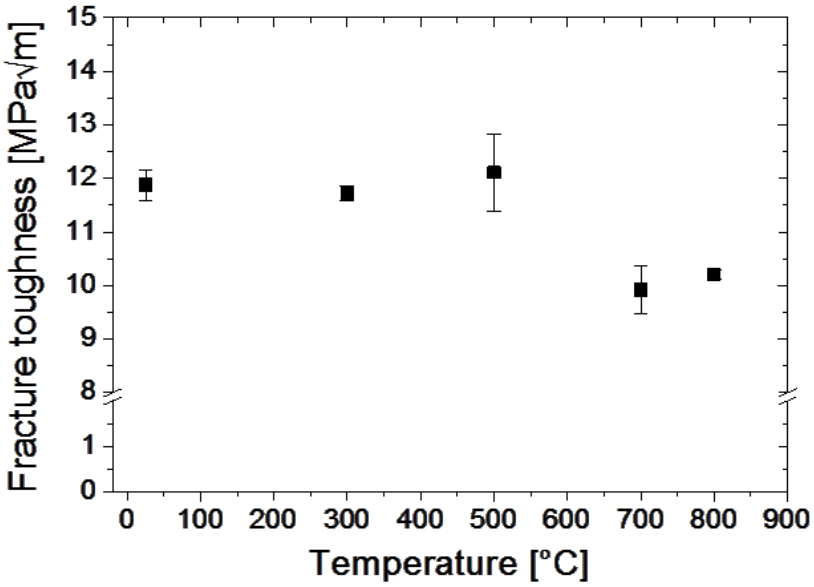

Fig. 57: Fracture toughness of WC 8 % Co - mean values from results of three experiments [88].

K_{IC} remains constant at a value of about 11.5 MPa√m at temperatures from room temperature to 500 °C. Between 500 and 700 °C K_{IC} decreases to about 10 MPa√m (see Fig. 57a)) [88].

At RT the detected K_{IC} values are higher than the value of 9.2 MPa√m of a finer grained hardmetal grade with similar amount of Co binder [95],[96]. According to literature at RT the fracture toughness increases with increasing mean WC grain size, detected for hardmetal grades with mean WC grain size from 0.5 to 9 µm [96]-[98].

At temperatures from 300 to 600 °C the determined K_{IC} values are comparable with results from literature [98]. At higher temperatures the results from this work are comparable with K_{IC} values of hardmetal grades with higher Co content and WC grain size (15 wt.% Co, 1.7 µm) [99].

The mixed carbide content may also influence the K_{IC} values at elevated temperature. A hardmetal grade with 9 wt.% Co and a high mixed carbide content of 35 wt.% exhibited an almost constant K_{IC} up to 1000 °C [99].

4.5 Comparison of measured temperatures and stresses with FE simulation

The thermo-physical and –mechanical data determined in this work were used as input data for FE simulation done by I. Krajinović et al. [34]. This gives the opportunity to estimate the cutting temperature and load evolution at the cutting edge. The results of the simulation are compared in this chapter with the results of the real milling experiment.

Keep in mind, in the simulation model one cut took 8 ms and the idle lasted 96 ms [34]. In the real experiment one cut and idle under constant cutting conditions (equal as in test setup A arrangement) took 11 ms and 96 ms, respectively, see details in chapt. 3.6. The temperature evolution of five cut-idle cycles in six different positions on the rake face (see Fig. 58a)) of the milling insert is presented in Fig. 58b) [34]. The first cut-idle cycle is presented in detail in Fig. 58c). In the simulation the contact length between chip and milling insert is 1370 µm within the first 5 cuts [34]. This modelled contact length is larger than the detected contact length of about 508 µm in the experiment, see details in chapt. 4.1.1.

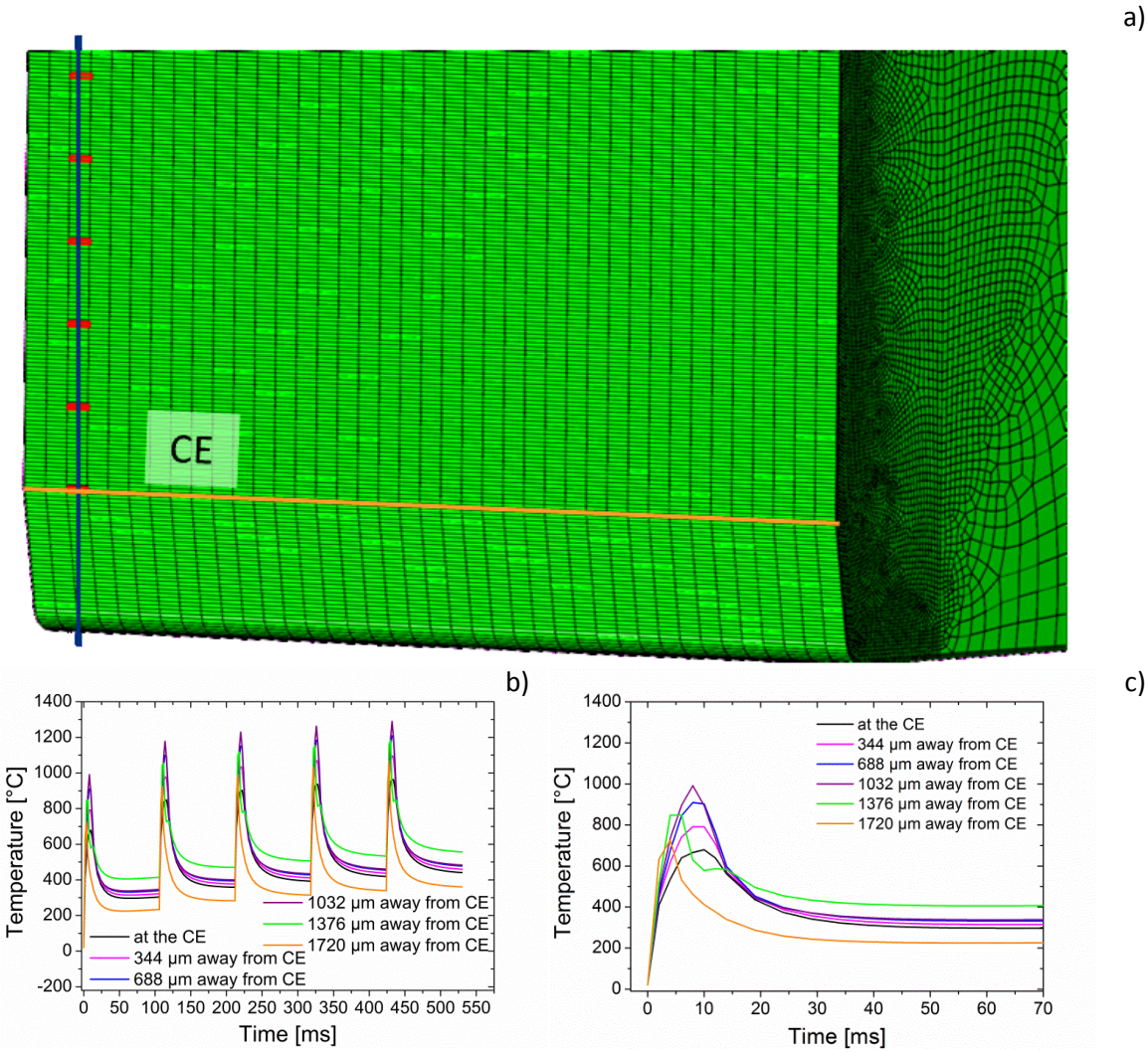

Fig. 58: a) Schematic image of the milling insert used in the finite element simulation- red lines indicate the six positions and/or elements with different distances away from chamfered edge (CE), in which temperature data and stress data were generated via finite elements simulation [34]. Blue line indicates position of cross section, in which stresses in depth are shown in Fig. 60. b) Modelled temperatures for five cut and idle cycles using the material data of the hardmetal (see chap. 4.4) and the Ti-Al-Ta-N coating [100], and c) temperature evolution during the first cut and idle cycle at the six different positions on the rake face [34].

The temperature evolution within the first five cycles is comparable to literature, see Fig. 8 [43].

During cutting, the insert heats up exponentially, after 7 ms the temperature reaches the maximum, and after 8 ms the temperature decreases exponentially because the idle starts. After 40 ms the temperature reaches a plateau value. The next cut starts after 110 ms and the temperature increases again [34]. After 10 ms cutting the maximum temperature of about 990 °C is calculated within first cycle for an element located 1032 µm away from chamfered edge (CE), see Fig. 58c). During idle the temperature decreases to a plateau value

of about 345 °C [34]. Between heating and cooling, the temperature difference on one position of the rake face may become as large as 700 °C. The apparent mean temperatures of about 500 and 300 °C in elements located 1376 µm and 1720 µm away from chamfered edge are in a similar range as the estimated temperatures using thermo chalks. The calculated temperatures increase within these five cut-idle cycles (see Fig. 58b)) [34].
Within the first five cut-idle cycles the evolution of induced stresses, which act parallel to the cutting edge, on the same six positions on the chamfered cutting edge are shown in Fig. 59 [34].

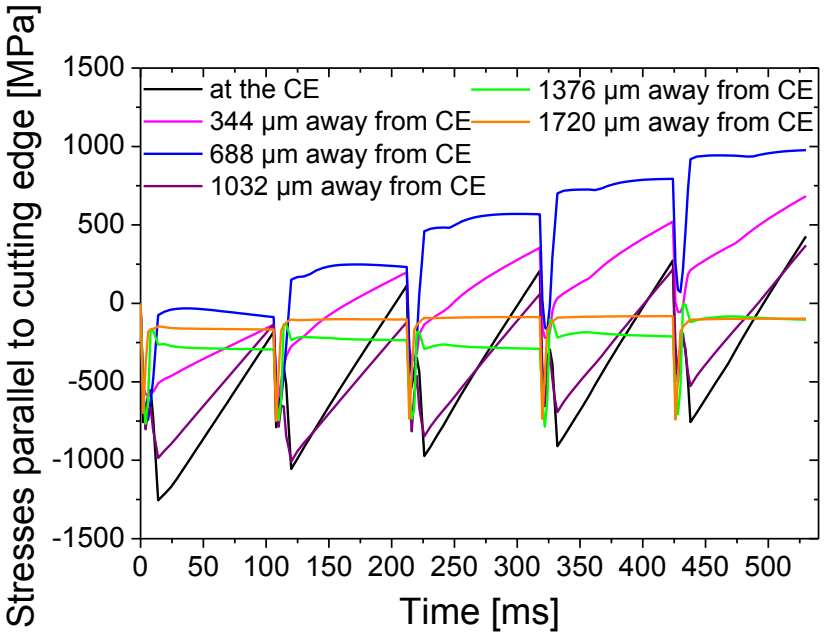

Fig. 59: Induced stresses acting parallel to the cutting edge at six different positons (same position as for temperature evolution, see Fig. 58) on the surface of the coating at the cutting edge for 5 cutting cycles modeled via finite element simulation [34].

Within the first cut the compressive stresses acting parallel to the cutting edge are formed and reach their maximum after 8 ms. The cross section of the rake face shows the stress and their range in the depth after first cut (8 ms), see Fig. 60 [34].

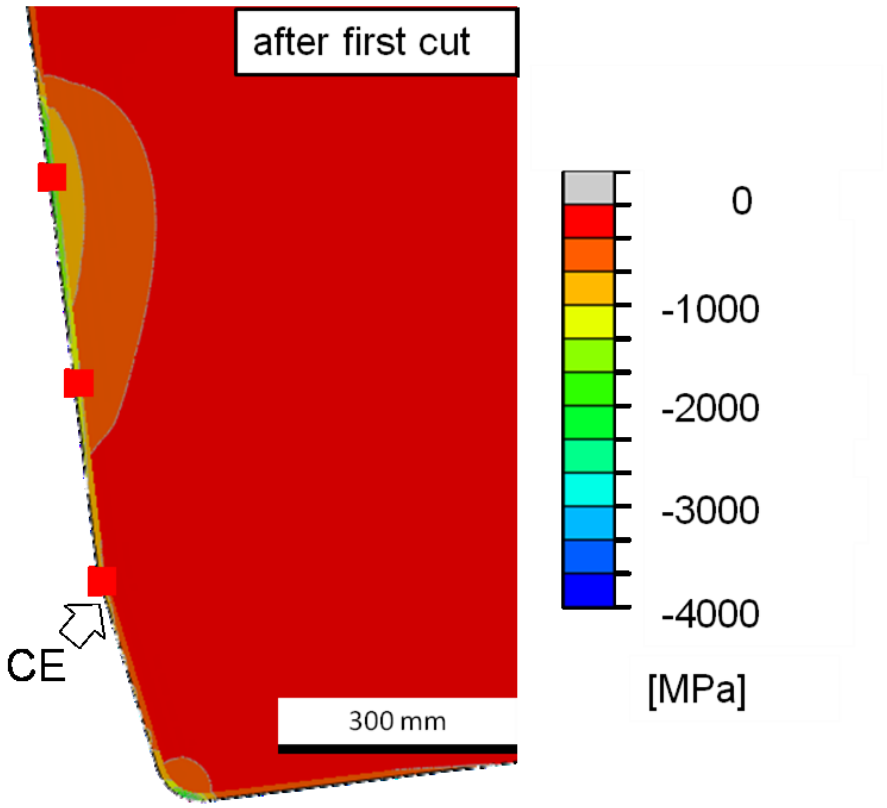

Fig. 60: Stress distribution in the cross section of a milling insert at the end of the first cut (after 8 ms). Coloured areas indicate the effective stresses acting parallel to the cutting edge after first cut. Red squares indicate positions of elements at the chamfered edge (CE), 344 and 688 µm away from CE, which are indicated in Fig. 58 as red rectangles [34].

During the first idle these induced compressive stresses decrease. However, after the first cut-idle cycle the simulated stresses of all position are in compression. During the second cut the compressive stress build up repeats again in all investigated elements on the rake face, see Fig. 59. After the second cut the simulated induced stresses are shifted towards tensile at the end of the second idle period. The stresses in the finite element located 344 µm away from chamfered edge increase linearly with progressive idle time whereas in the element, located 688 µm away from the chamfered edge tensile stress of 240 MPa are effective during the whole idle [34]. During cutting these tensile stresses build up is not observed at a position 1032 µm away from chamfered edge. But, after the fourth cut tensile stresses are present in elements 344 and 688 µm away from the chamfered edge even if the fifth cut starts, see Fig. 59 [34]. During the fifth idle tensile stresses of 670 and 930 MPa are effective in elements 344 and 688 µm away from chamfered edge. No tensile stresses were predicted for the finite elements 1376 and 1720 µm away from chamfered edge within the first cut-idle cycles. At these positions the simulated temperatures are lower than at the positions closer to the cutting edge (see Fig. 58b),c)) [34].

Within the first five cut-cycles, the highest modelled temperature of 1000 °C and mechanical loads in combination are found in element, located 688 µm away from chamfered edge. At the same position in the hardmetal compressive stresses acting parallel to the cutting edge of about 900 MPa are simulated, see yellow area in Fig. 60 [34].

These simulated thermal and mechanical loads may surpass the compressive yield strength ($R_{P0.2}$) of the hardmetal. Within this work the used hardmetal grade exhibits a compressive $R_{P0.2}$ value of 1200 MPa at 800 °C, see Fig. 56b). But, plastic deformation starts at much lower stresses than indicated by the $R_{P0.2}$ value, see Fig. 56b). During cutting the compressive yield strength of the hardmetal might be even lower due to higher apparent temperatures. Within the first cuts, the hardmetal can be plastified most easily in a region 688 µm away from chamfered edge. During unloading during the idle, tensile residual stresses may be induced in this region.

The position of significant tensile residual stresses build-up in hardmetal is comparable with the position, which was found via position resolved residual stress measurements, see chapt. 4.5. According to simulation tensile residual stresses have to be induced within the first cycles. In the position resolved residual stress measurements significant tensile residual stresses were detected after 1000 cuts (51.440 m aTWCL), see Fig. 39. The number cut-idle cycles, which is required to build up significant tensile residual stresses is not comparable with the assumption of the residual stress measurements.

This deviation can be explained by the fact that the exact coefficient of friction can be hardly determined in real experiments. The used friction model in simulation is an estimation of the real situation apparent in experiment. An enlarged coefficient of friction increases the cutting temperature in the simulation [8]. The combination of the apparent loads and lower temperatures during cutting experiment does not surpass the yield strength of the hardmetal grade within the first 5 cut-idle cycles.

5 Discussion

State of the art in milling is the use of inserts based on WC-Co hardmetal substrate coated by Ti-Al-N based films. In milling abrasive wear and thermal fatigue, with the latter inducing characteristic combcracks, dominate the lifetime in these inserts. The combcrack formation was in focus of the investigations in the past. In literature there are three hypotheses of combcrack formation apparent. First, combcracks were induced by pure periodical cyclic thermo shock [4]-[6],[43]. Due to intermittent cut in milling, these authors postulated that the temperature difference between heating upon cutting and cooling upon the idle period in a cutting cycle is the key factor influencing damage [4]-[6],[43]. The second hypothesis deals with the local plastification induced by high cutting forces and thermal stresses due to the apparent high temperatures as trigger for combcrack formation [7]. Both effects may exceed the flow stress of a tool material due to the combination of current thermal stresses and sufficiently high mechanical load stresses during cutting. During cooling, the material is hindered in contraction in region in which plastic deformation was apparent during cutting. These loads can trigger the build-up and evolution of tensile residual stress in the cutting edge of milling inserts [7]. Third hypothesis deals with combcrack formation induced by the different thermal expansion coefficient between WC and Co phases in the hardmetal substrate. Due to higher thermal expansion coefficient of Co, the binder phase contracts more than the WC phase, which results in tensile stresses in the binder phase and compressive stresses in the WC phase [45].

These damage investigations and consequently the developed hypotheses on combcrack formation are based on milling tests with uncoated hardmetal inserts.

The aim of this thesis is to prove the validity of existing damage hypotheses and to enlarge the knowledge on combcrack formation for coated hardmetal milling inserts. The damage state as well the residual stress state in coating as well as in the hardmetal substrate over the complete lifetime were documented in own publications [57]-[59],[64].

Two different milling test setups were used. In the first one (test setup A), the thermal and mechanical impact was subcritical, no combcracks were apparent and wear damage in form of crater wear was responsible for reaching end of lifetime [58]. In the second test setup (test setup B), thermal fatigue in form of combcracks was the dominant damage mechanism. These combcracks exhibited a characteristic growth direction perpendicular to the cutting edge [57].

A new preparation method was developed to perform position resolved residual stress measurements in the milling inserts via X-ray diffraction. The results determined for the

hardmetal substrate were validated with values of residual stress maps of selected milling inserts determined via synchrotron X-ray diffraction.

Additionally, the apparent cutting temperature was estimated using thermo chalks and by investigations of the steel chip microstructure. These results were compared with the results of FE simulation. To develop an adequate material model for FE simulation the knowledge of thermo mechanical and thermo physical properties of the tool material are required. Within this work these data were generated for the relevant temperature range.

Barthia et al. described such a field at the first time, in which no tool failure induced by combcracks occurred due to subcritical thermal or mechanical tool loading. They determined that the feed rate and cutting speed have to be lower than 0.1 mm/rev. and 90 m/min for uncoated milling inserts [47].

Within this work it can be shown that milling inserts coated with Ti-Al-N based films enlarge the field of process parameters under which no tool failure induced by combcracks occurs. In the current work a feed rate of 0.4 mm/rev. and a speed of 220 m/min were applied in test setup A and combcracks were not detected in the substrate or in the coating. An increase of feed rate and speed in the same test setup A causes that the critical loading is reached and fosters the combcrack formation. This behavior corresponds well with findings in literature [43],[47].

It can be shown that an increase of feed rate does have more influence on combcrack formation as detected by Melo et al. for uncoated inserts [43]. In the milling tests with coated inserts it can also be found that the location, where combcrack growth starts, is several hundred micrometer away from the cutting edge and that growth of cracks occurs towards to the cutting edge [6]. In one of the own milling tests, a combcrack was detected on the rake face, which did not reach the cuting edge, see Fig. 38b). This result confirms the findings described in [6].

Based on the results of this work, it can be argued that the second hypothesis describes the combcrack formation in coated milling inserts in the best way [7]. Fig. 61 shows schematically what happens during cut and idle cycles.

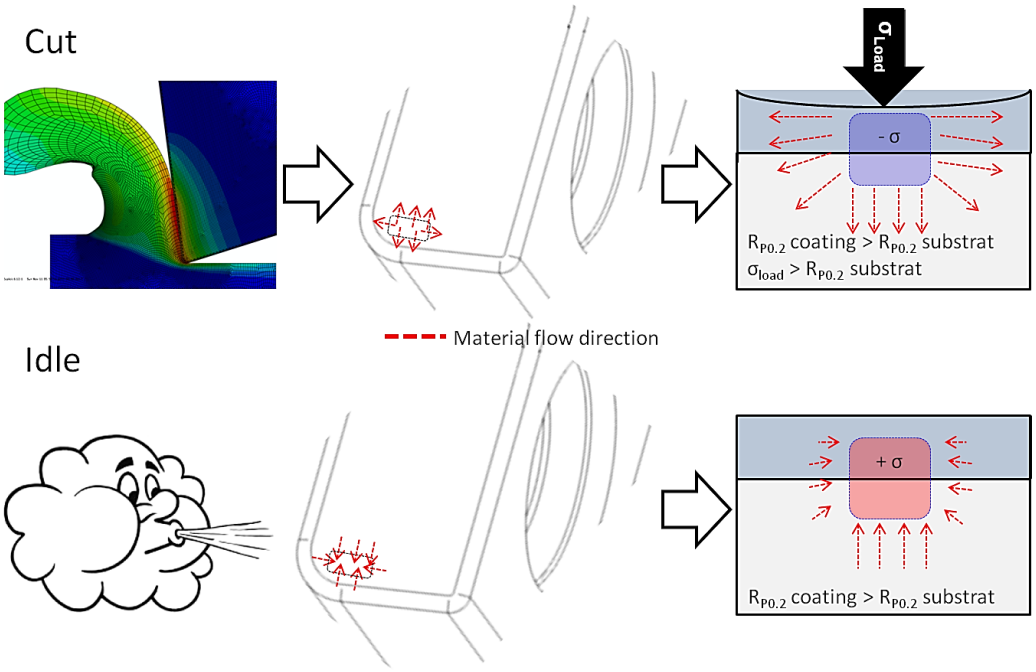

Fig. 61: Schematic view of material flow and formation of stresses due to plastification during a cut and hindered expansion during an idle period.

According to the results of the simulation, the apparent cutting temperatures are higher than 900 °C and the induced compression stresses are about 900 MPa, which act parallel to the cutting edge during chip formation [34]. Due to the thermal and mechanical impact, the insert's material expands in all directions. In direction normal to the cutting edge, this material can expand due to the free surface at the cutting edge. On the other side, in direction parallel to the cutting edge expansion is blocked. Due to this blockage, the yield strength of the substrate is localized reached. In compression tests yield strength of about 1230 MPa was determined for the substrate material at 800 °C [88]. Regarding to the evolution of yield strength as function of temperature, at 900 °C the yield strength of the substrate material is in the same range as the induced stresses during chip forming.

But, plastic deformation starts at much lower stresses than indicated by the yield strength of 1230 MPa, see Fig. 56b). During cutting the compressive yield strength of the substrate material might be even lower due to higher apparent temperatures.

This localized plastic deformation of the substrate material starts at very early stages in a milling operation and generates compressive stresses, which were effective parallel to the cutting edge. The heated and plastically deformed insert's material contracts during the idle period. In the locations, in which plastic deformation is apparent, this material is hindered in contraction. The localized compressive loading stresses convert into tensile residual stresses

[59]. These tensile residual stresses are mainly effective parallel to the cutting edge [59]. After cutting 36 m accumulated tool-workpiece contact length (aTWCL), which corresponds 1000 cuts, for the first time a region of about $1.6 \times 0.3\ mm^2$ was detected by position resolved residual stress measurements via X- ray diffraction by synchrotron sources [59] and confirmed as well by laboratory X-ray sources [57],[58]. This region of interest is located about 0.4 mm away from the cutting edge [59]. The position of the area of significant tensile residual stress build-up in the milling insert corresponds well with the location of the most pronounced combcrack [59]. Fig. 62 shows schematically the residual stress evolution in the coating and substrate material.

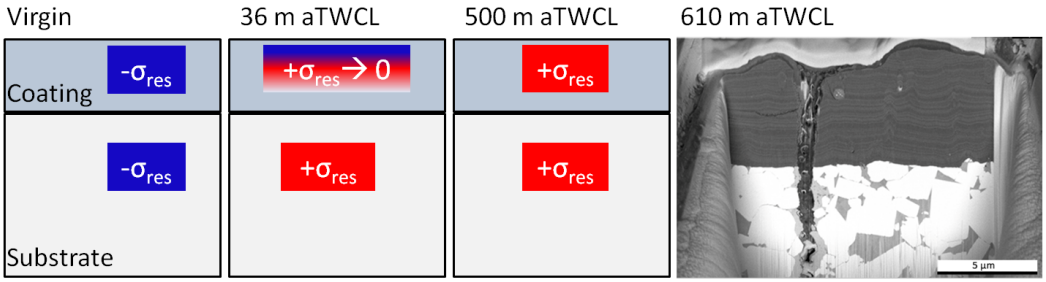

Fig. 62: Residual stress evolution in coating and the WC phase of the substrate of milling inserts tested in test setup B, in which thermal fatigue was dominant and the consequently formed combcrack in coating and substrate after milling 610 m accumulated tool-workpiece contact length (aTWCL) [58],[64].

The Ti-Al-N based coating has an increased resistance against combcrack formation due to protective compressive residual stresses, which were induced during the deposition process [100]. Tensile residual stresses were also detected in the coating in the same region in which tensile residual stresses were also found in the substrate material [59],[64]. It can be assumed that the coating also plastifies or undergoes a volume reduction during the cutting application. Due to the lower thermal conductivity of a factor of ten, the apparent temperatures are higher in the coating than in substrate. Similar as in the substrate material, the yield strength of the coating can be reached during cutting. Additionally, the thermal decomposition can start locally, which also decreases the hardness of the coating.

A more pronounced effect on tensile residual stress formation in the hard coating may be the different thermal expansion coefficient between the coating and the substrate material. In test setup B, in which combcrack formation is dominant, is specified by a higher number of tool movements [58]. This increases the number of thermal shocks, in which the insert nearly cools down to room temperature. The coating exhibits a higher thermal expansion coefficient than substrate material [54], see chapt. 4.4.1. Therefore the coating contracts more than the substrate material during the idle period.

However, the creation and development of tensile residual stresses last longer in the coating than in the substrate material. After cutting 36 m aTWCL under test setup B conditions, first tensile residual stresses in the coating as well in the substrate material were detected but these tensile stresses in the coating were significantly increased after milling 500 m aTWCL [64]. In comparison, in the substrate material the highest tensile residual stresses were already detected after 36 m aTWCL [58]. Without the protective compressive residual stresses in the coating, combcracks can easily nucleate and grow through the coating as well as in the substrate material (see cross section of an insert after milling 611 m aTWCL in test setup B (Fig. 31c)). In comparison, the compressive stresses in the coating are present in inserts till the end of lifetime, in which wear damage was the dominant damage mechanism and no combcracks were apparent [57].

By the appearance of combcracks, the abrasive wear damage increases due to the increase of coating and hardmetal fragments on the surface induced by shattering the crack edges and flanks during chip forming [58]. The number of combcracks increases with increasing number of cuts [43],[58]. The crack opening gets larger with increasing duration of milling operation because of shattering the crack flanks and filling the cracks with workpiece material. End of lifetime of a milling insert is reached when cracks appear, which grow parallel to the cutting edge. These sorts of cracks connect two combcracks. The whole cutting edge gets unstable and the danger of cutting edge breakage is increased [58]. These kinds of cracks are induced by mechanical fatigue [5]. Opitz et al. also detected these parallel cracks in heated inserts without the appearance of combcrack [5]. It seems that the Ti-Al-N based coating decelerate the mechanical fatigue damage due to the compressive stresses in the coating [64]. Because, these parallel cracks are not detected till the end of lifetime in milling arrangements, in which wear damage is dominant and no combcracks are apparent [57].

Fig. 63 summarizes the results of the residual stress measurements and their effect on combcrack formation.

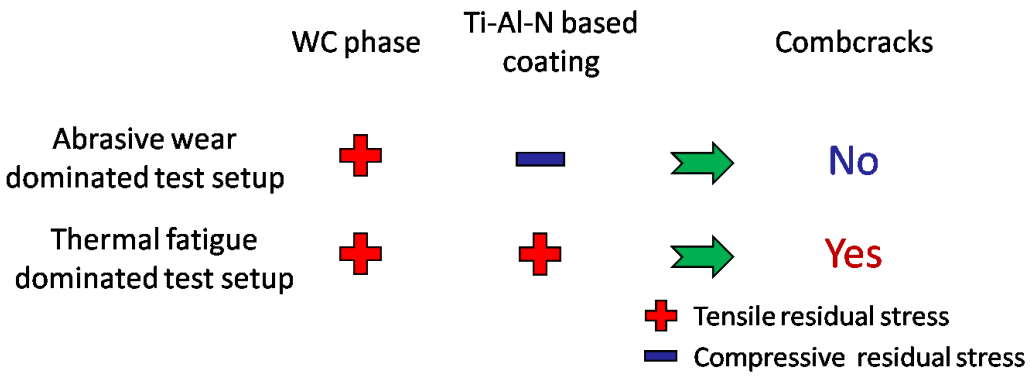

Fig. 63: Residual stress states in the WC and (Ti-Al-N) phase caused by milling operations and the consequence on combcrack formation.

It seems that the residual stress state in the coating as well in the substrate material influences the combcrack formation. Compressive residual stresses delay the combcrack formation. The residual stress state can be modified by post treatments, e.g. a blasting process. Within this work the residual stress and damage evolution was documented in milling inserts, which were post-treated with varied blasting times [55]. These first investigations showed that the blasting duration does not influence significantly the residual stress state in the substrate material. This missing influence can also be found in the cutting performance. All inserts reached a similar lifetime [55].

The results of this work enhance the understanding of damage mechanisms in coated hardmetal milling inserts in milling application. This knowledge of the influence of the residual stress state gives the opportunity to improve and modify in detail the combination of substrate and hard coating.

6 Summary

In milling application the damage and consequently the lifetime is dominated by thermal fatigue in form of combcracks and crater wear. Especially the combcrack formation and residual stress evolution in used coated milling inserts are based on guesses in literature. Therefore the aim of this thesis was to enlarge the knowledge of residual stress evolution in used milling inserts over the complete lifetime and their influence on combcrack formation.

WC-Co hardmetal milling inserts deposited by Ti-Al-N based film were tested in two different milling test setups. The first test setup was dominated by the crater wear damage for reaching end of lifetime. Thermal and mechanical impact was subcritical and no combcracks were apparent [58]. In the second test setup the thermal fatigue in form of combcracks was dominant for reaching end of lifetime.

Within the work it can be shown that Ti-Al-N based film coated hardmetal inserts, enlarge the field of process parameters in which milling without tool failure induced by combcracks occurred.

The apparent combcracks exhibit a characteristic growth direction perpendicular to the cutting edge [57] and start several µm away from the cutting edge, independent of using coated or uncoated inserts. In coated milling inserts the combcrack has a shape similar to a quarter of an ellipse and the crack extension at the surface is in an excellent agreement with the dimension in the volume. During application the combcrack flanks and edges were shattered due the peoridical opening and closing of the crack. The cracks are filled with workpiece material into a depth of 15 µm.

Position resolved residual stress measurements by X-ray diffraction using synchrotron sources on used milling inserts detected significant tensile residual stresses in the WC phase in a region of 1.6 x 0.3 mm². This region is positioned about 0.4 mm away from the cutting edge and is detected at the very early stages of application in a milling insert with 1000 contacts with the workpiece (51.44 m accumulated tool-workpiece contact lenght). The position of this region with significant residual stress buildup corresponds well with the location of the most pronounced combcrack [59].

Own laboratory based X-ray diffraction experiment confirms and completes the position resolved residual stress measurement in region of interest in the substrate material and in the coating of tested milling inserts over their complete lifetime via X-ray diffraction using X-ray sources. In the virgin state milling inserts exhibit compressive residual stress in the substrate as well as in the coating. Already in early stages of application, after 1000 contacts, tensile residual stresses in the WC phase are observed in inserts from both investigated test setups. The results of the X-ray diffraction in the WC phase using synchrotron and laboratory

X-ray sources are in an excellent agreement. Tensile residual stresses in the WC phase are apprarent till end of lifetime in inserts tested in a milling test setup, in which wear dominates lifetime. Contrary, the tensile residual stresses in the WC phase decreased significantly upon apparence of the first combcrack in inserts, which were tested in a milling arrangement, in which thermal fatigue is dominant.

The Ti-Al-N based coating has an increased resistance against combcrack formation due to protective compressive residual stresses, which were induced during the deposition process [101]. These compressive stresses are present in inserts till the end of lifetime, in which wear damage was the dominant damage mechanism and no combcracks were apparent [57]. In contrast, in the same region tensile residual stresses were also detected in the coating of inserts, which were tested in the thermal fatigue dominated test setup [58].

The position of the region of residual stress build up is comparable with the modelled results of the simulation. The simulation also shows that during the chip formation the apparent cutting temperatures are probably higher than 900 °C and the induced compression stresses are about 900 MPa, which act parallel to the cutting edge [34]. At 900 °C the yield strength of the substrate material, which was determined within this work, is in the same range as the induced stresses during chip forming. It seems that the yield strength of the substrate material is surpassed and localized plastic strains occur during cutting. This generates compressive stresses, which were effective parallel to the cutting edge. During the idle period the heated and plastically compressed material contracts and in the locations, in which plastic deformation was apparent, this material is hindered in contraction. The localized compressive loading stresses convert into tensile residual stresses acting parallel to the cutting edge.

First investigations on inserts were done, which were post-treated with varied blasting time [55]. It can be shown that the blasting duration does not significantly influence the residual stress state in the substrate material. This missing influence can also be found in the cutting performance. All inserts reached a similar lifetime [55].

7 Outlook

Based on the knowledge and methods for studying combcrack formation reported within this thesis, there are several opportunities to improve the coating/hardmetal system in milling inserts.

The local plasitification of the substrate as well as of the coating has to be delayed by decreasing the temperatures and cutting forces during milling. The cathodic arc evaporate deposited Ti-Al-N based hard coating can be optimized concerning its thermo-physical properties and friction coefficient. An increased thermal insulation of the coating decreases the apparent temperature in the hardmetal substrate during cutting. The thermal insulation can be achieved by reducing the thermal conductivity of the hard coating material. A lower friction coefficient at the coating's surface also decreases the cutting temperatures. This can be reached by a lower surface roughness of the coating e.g. by removing of the droplets from the surface. Wet and dry blasting processes after CAE deposition remove these droplets and these post treatments show good results in milling application. The dry blasting process used as post treatment of inserts seems to be a promising way to induce additional compressive residual stresses in the coating and in the substrate material within the first microns below the coating/substrate interface. Compressive residual stresses in the coating act protective against combcrack formation. The influence of the shape of the blasting material and the variation of blasting pressure on the residual stress evolution in coating and hardmetal substrate may be significant for tool lifetime and deserve attention in the future.

Improvements in the substrate material can be done using a hard metal substrate with increased yield strength at elevated temperatures. The use of alloying elements, e.g. Cr or Mo, in the Co binder phase and the use of a higher amount of cubic carbides, e.g. TiC, can act as triggers.

The cutting forces as well as the position of the apparent highest temperatures can be influenced by cutting edge geometry [33]. Optimization of cutting edge, their production and their validation in the milling application is very time consuming. The FE simulation is a time-saving tool for designing the cutting edge geometry and to estimate the mechanical and thermal tool loads apparent within a cutting process [8]. The knowledge of the thermo-mechanical and thermo-physical properties of the hard coating as well as in the hardmetal substrate are necessary to develop adequate material models for FE simulation [8]. At RT most of the relevant data are available in the open literature but at elevated temperature these data are very rare. It needs effort in the future to provide these material data up to 1000 °C for the whole range of used coatings as well substrate materials used in several cutting applications.

The results of simulation have to be validated by cutting experiments. A specific topic is the position resolved determination of cutting forces and temperatures during the cutting process. The use of thermo chalks is one way to determine temperature maps outside of the contact zone between workpiece and insert. The position resolved detection of the apparent temperatures and forces within the cutting zone using new sensor techniques are a promising research field for the future.

Within this work a preparation method for position resolved residual stress measurements via X-ray diffraction was developed, which gives the opportunity to validate the calculated strain and stress results of the FE simulation. A missing point in the literature is the position resolved residual stress measurements in other cutting applications. To improve the knowledge of damage and to support the FE simulation in other cutting applications it is necessary to further develop the preparation method for other cutting insert's geometries to estimate these residual stresses. Based on these methods, the understanding of tool wear in several cutting applications using various workpiece materials can be enhanced significantly.

8 Overview of the publications

To enlarge the knowledge on the damage mechanisms in coated hard metal milling inserts during milling operation six publications were published within the framework of this thesis. Here, a short overview of the content and results is given.

The first publication deals with the position resolved residual stress measurements in the hard metal substrate. Tested milling inserts and a virgin insert as reference were investigated by means of synchrotron sources. It could be shown that significant tensile residual stresses are apparent parallel to the cutting edge in a small region of 0.3×1.6 mm² and located 0.3 mm away from the cutting edge in inserts tested at early stages of milling operation. The position of these tensile stresses is comparable with the position of combcracks.

On the basis of publication I, a special covering method was developed to facilitate the position resolved residual stress measurements in this area of interest in hard metal substrate via X-ray diffraction using in-house X-ray sources. Publications II and III deal with the residual stress and damage investigations of milling inserts, which were tested in two different milling test setups. Inserts, tested in the wear dominated test setup, show tensile residual stresses till end of lifetime. Inserts, tested in the thermal fatigue dominated test setup, show a similar residual stress evolution upon appearance of the first combcrack. After the appearance of combcracks the tensile residual stresses decrease significantly and at end of lifetime compressive residual stresses are detected within the region of interest.

The influence of a dry blasting process and especially the blasting duration on the residual stress evolution in the hard metal substrate at early stages of application is demonstrated in publication IV. It is shown that the blasting time has not a significant influence on the residual stress evolution at early stages of application and it does not decelerate the combcrack formation.

Publication V deals with the improvements of the special covering method for residual stress measurements, which gives opportunity for position resolved residual stress measurements in the hard coating. The coatings of the same milling inserts as already shown in publication II and III were investigated. It can be illustrated that tensile residual stresses are apparent in the coating after testing the inserts in the thermal fatigue dominated test setup, whereas compressive residuals stresses are detected in the coatings till end of lifetime of inserts, which were tested in wear dominated test setup. Compressive residual stresses in the coating prevent combcrack formation.

Creation of an adequate material model for FE simulation requires material data as input data of the hard metal substrate. Publication VI summarizes material properties such as Young's and shear modulus, Poisson's ratio, yield strength, fracture toughness as function of temperature, which were determined for hard metals with varied Co content and WC grain size. The Young's modulus, shear modulus and yield strength decrease with increasing temperature and Co content whereas the Poisson's ratio is not influenced either by Co content or WC grain size and temperature. No pronounced influence of Co content and WC grain size on fracture toughness was detected within the investigated parameter range from RT to 700 °C. In contrast at 800 °C all investigated hard metal grades with a Co content higher than 8 wt.% showed a significant increase in fracture toughness. The determined material data was used in publication VII for FE simulation.

9 Publications

9.1 List of included publications

I. Spatial Correlation of Tensile Residual Stress and Thermal Fatigue Damage in Coated Cemented Carbide Milling Inserts
T. Teppernegg, T. Klünsner, C. Tritremmel, C. Czettl, J. Keckes, T. Wroblewski, R. Ebner, R. Pippan
18th Plansee Seminar, International Conference on Refractory Metals and Hard Materials, Reutte (2013) Hard Metal47/ 1- Hard Metal47/10.

II. Residual Stress and Damage in Coated Hard Metal Milling Inserts
T. Teppernegg, T. Klünsner, C. Tritremmel, C. Czettl, J. Keckes, R. Ebner, R. Pippan
Advances in Tungsten, Refractory and Hardmaterials IX - Proceedings of the 9th International Conference on Tungsten, Refractory and Hardmaterials, Orlando (2014) 245-253.

III. Evolution of Residual Stress and Damage in Coated Hard Metal Milling Inserts Over the Complete Tool Life
T. Teppernegg, T. Klünsner, P. Angerer, C. Tritremmel, C. Czettl, J. Keckes, R. Ebner, R. Pippan
International Journal of Refractory Metals and Hard Materials 47 (2014) 80-85.

IV. Residual Stress and Damage in Post-Treated Coated Milling Inserts
T.Teppernegg, T. Klünsner, C. Tritremmel, P. Angerer, C. Czettl, R. Pippan
Proceedings of the Euro PM2014, Salzburg (2014) EP140186 1-6

V. Evolution of Residual Stress in TiAlTaN Coatings on Hard Metal Milling inserts
T. Teppernegg, P. Angerer, T. Klünsner, C. Tritremmel, C. Czettl
International Journal of Refractory Metals and Hard Materials 52 (2015) 171-175.

VI. High Temperature Mechanical Properties of WC-Co Hard Metals
T. Teppernegg, T. Klünsner, C. Kremsner, C. Tritremmel, S. Puchegger, C. Czettl, S. Marsoner, R.Pippan, R. Ebner
International Journal of Refractory Metals and Hard Materials 56 (2016) 139-144.

9.2 Publication related to this work

VII. Finite element study of the influence of hard coatings on hard metal tool loading during milling
I. Krajinović, W. Daves, M. Tkadletz, T. Teppernegg, T. Klünsner, N. Schalk, C. Mitterer, C. Tritremmel, W. Ecker, C. Czettl
Surface and Coatings Technology, 304 (2016) 134-141.

VIII. Arc Evaporated Ti-Al-N / Cr-Al-N Multilayer Systems for Cutting Applications
T. Teppernegg, C. Czettl, C. Michotte, C. Mitterer
Submitted to the 19th Plansee Seminar

9.3 My contribution to the included publications

Publication I

The design of the concept for this publication and the selection of suitable cutting parameters were done by me. The milling experiments were performed by Markus Lorenz in the Ceratizit tooling academy and the residuals stress measurements were conducted by Jörn Donges at the Deutsches Elektronen-Synchrotron (DESY), both under my supervision. I evaluated the measurement data of the residual stress measurements and prepared them to graphical mappings. I investigated the worn milling inserts via SEM with technical assistance by Bernhard Sartory. The manuscript was prepared by myself.

Publication II

Also here, the concept of this manuscript was done by myself. I developed based on publication I the testing parameters for test setup A inclusive the suitable stops of the milling experiments. Similar to the other publications I, III and IV, the milling experiments were conducted by Markus Lorenz under my supervision. I developed a new cover method of preparing milling inserts for residual stress measurements on small areas of interest at the milling inserts via laboratory X-ray diffraction. Next to the preparation of the milling inserts I also performed the residual stress measurements with technical assistance by Andreas Bubnik. I evaluated the calculation of the residual stresses, conducted by Paul Angerer. Similar to publication I,III and IV, the SEM investigations of the worn milling inserts were conducted by Bernhard Sartory under my supervision. I wrote the manuscript.

Publication III

Within this publication, my contribution was the design of the concept as well the choice of suitable cutting parameter of the milling experiments for test setup B. The cutting tests were performed at the Ceratizit tooling academy under my supervision. Similar to publication II, I prepared the milling inserts and conducted the residuals stress measurements with assistance of Andreas Bubnik and Paul Angerer. The results of residuals stress measurements were elevated and interpreted by myself. Both, the results of the residual stress measurements as well of the SEM investigations, which were done by Bernhard Sartory, were included in the manuscript, which was prepared by me.

Publication IV

Also for this publication, the concept of the manuscript was developed by myself. I defined the parameters for the blasting experiments. The blasting experiments and the cutting tests

were conducted at Ceratizit. Preparation of the milling inserts for the residual stress measurements as well the residual stress measurements were done by me, with technical assistance by Andreas Bubnik. These results of residual stress measurements and the results of the SEM analysis, conducted by Bernhard Sartory, were elevated and interpreted by myself and I wrote the manuscript.

Publcation V

The design of the concept was done by myself. For measurement residual stresses in the Ti-Al-N coating at small areas on the milling inserts, I had to adapt the cover method of the publication II. The worn milling inserts of publications I-III were prepared by myself for the residual stress measurement in the Ti-Al-N coating. Under my supervision, Andreas Bubnik conducted the residual stress measurements. I calculated and evaluated the residual stress values in the coating of the milling inserts on my own. The elastic constants of components of the coating were also calculated by myself with assistance of Paul Angerer. With his support the interpretation of the elastic constants was included in the manuscript. The major part of the manuscript was prepared by myself.

Publication VI

Also for the last publication, I developed the concept and prepared all samples. The determination of the elastic properties of the hardmetal grades were performed by Stephan Puchegger at the Technical University Vienna. The Poisson ratio of all hardmetal grades were calculated by me. The compression tests at elevated temperature were done under my supervision by Kevin Tobitsch. Due to the different specimen diameter the attained strain values required correction. A support in creation of the finite element model was given by Stephan Krobarth and Uwe Oßberger. The correction of all determined strain-stress curves was performed by means of a finite element model on my own. Under my supervision, Clemens Kremsner conducted the bending tests at elevated temperature and the SEM analysis with technical assistance by Christian Puschnig. With my support, Clemens Kremsner determined the fracture toughness values. I calculated the CTOD values and plastic size zones of all tested hardmetal grades.
Support in interpretation of the results of the fracture toughness at elevated temperature was given and concluded in the manuscript by Thomas Klünsner. All other results were elevated, interpreted and incorporated in the manuscript by myself.

Summary

The proportion of contribution in percent is summarized in the table below.

	Concept and planning [%]	Experiments [%]	Analysis and interpretation [%]	Manuscript preparation [%]
Publication I	100	100	100	100
Publication II	100	100	100	100
Publication III	100	100	100	100
Publication IV	100	100	100	100
Publication V	100	100	80	80
Publication VI	100	80	90	90

Supervision is not included.

10 References

[1] Emuge Franken, Handbuch der Gewindetechnik und Frästechnik, Publics Coperate Publishing, Erlangen, 2004

[2] K.W. Mertz, H. Jehn, Praxishandbuch moderne Beschichtung, Hanser, Leipzig, 2001

[3] K.-D. Bouzakis, G. Skordaris a, I. Mirisidis, N. Michailidis, G. Mesomeris, E. Pavlidou, G. Erkens, Cutting performance improvement through micro-blasting on well-adherent PVD films on cemented carbide inserts, Surface & Coatings Technology 200 (2005) 1879-1884.

[4] P.C. Pandey, S.M. Bhatia, H.S. Shan, Thermo - Mechanical Failure of Cemented Carbide Tools in Intermittent Cutting, CIRP Annals - Manufacturing Technology 28 (1) (1979) 13-17.

[5] H. Opitz, W. Lehwald, Untersuchungen über den Einsatz von Hartmetallen beim Fräsen, Westdeutscher Verlag, Köln und Opladen, 1963.

[6] C.S. Ekemar, S.A. Iggstrom, G.K. Héden (Ed.), Influence of Some Metallurgical Parameters of Cemented Carbides on the Sensitivity to Thermal Fatigue Cracking at Cutting Edges, 1971.

[7] I. Yellowley, G. Barrow, The influence of thermal cycling on tool life in peripheral milling, International Journal of Machine Tool Design and Research 16 (1) (1976) 1-12.

[8] V.P. Astakhov, Tribology of Metal Cutting, Elsevier, Oxford, 2006.

[9] W. Schedler, Hartmetall für den Praktiker: Aufbau, Herstellung, Eigenschaften und industrielle Anwendung einer modernen Werkstoffgruppe, VDI-Verlag, Düsseldorf, 1988.

[10] K. Brookes, World Directory and Handbook of Hard metals and Hard Materials, International Carbide Data, 1992.

[11] G. Knünz, H. Beirer, A. Lackner, W. Glätzle, E. Hartlmayr, Verfahren zu Herstellung eines Hartmetallansatztes, EU Patent No. EP 1373585B2, Reutte, 2002.

[12] P.K. Mehrotra, 1.07 - Powder Processing and Green Shaping, in: V.K. Sarin (Ed.), Comprehensive Hard Materials, Elsevier, Oxford, 2014, pp. 213-235.

[13] M. Zhou, Y. Makino, M. Noose, K. Nogi, Phase transition and properties of Ti-Al-N thin films prepared by r.f.-plasma assisted magnetron sputtering, Thin Solid Films 339 (1) (2012) 203-208.

[14] K. Kutschej, P.H. Mayrhofer, M. Kathrein, P. Polcik, R. Tessadri, C. Mitterer, Structure, Mechanical and tribological properties of sputtered $Ti_{1-x}Al_xN$ coatings with $0.5 \leq x \leq 0.75$, Surface and Coatings Technology 200 (7) (2005) 2358-2365.

[15] A. Kimura, H. Hasegawa, K. Yamada, T. Suzuki, Effects of Al content on hardness, lattice parameter and microstructure of $Ti_{1-x}Al_xN$ films, Surface and Coating Technologies 120-121 (1999) 438-441.

[16] T. Teppernegg, PVD TiAlN/CrAlN Multilayer Systems for Cutting Application. Diploma Thesis, Leoben, 2012.

[17] M. Kathrein, C. Michotte, M. Penoy, P. Polcik, C. Mitterer, Multifunctional multi-component PVD coatings for cutting tools, Surface and Coatings Technology 200 (5) (2005) 1867-1871.

[18] P.H. Mayrhofer, A. Hörling, L. Karlsson, J. Sjölèn, T. Larsson, C. Mitterer, L. Hultman, Self-organized nanostructures in the Ti-Al-N system, Applied Physic Letters 83 (10) (2003) 2049-2051.

[19] R.F. Bunshah (Ed.), Handbook of Hard Coatings: Deposition Technologies, Properties and Applications, Noyes Publications; William Andrew Pub., Park Ridge, N.J., Norwich, N.Y., 2001.

[20] J.L. Vossen, W. Kern, Thin Film Processes II, Academic Press, San Diego, 1991.

[21] W. Gissler, H. Jehn, Advanced Techniques for Surface Engineering, Kluwer Academic Publishers, Dordrecht, 1992.

[22] B. Rother, J. Vetter, Plasmabeschichtungsverfahren und Hartstoffschichten: mit 19 Tabellen, Dt. Verlag für Grundstoffindustrie, Leipzig, 1992.

[23] H. Tschätsch, Praxis der Zerspanungstechnik, Vieweg, Braunschweig Wiesbaden, 1999.

[24] D.H. Bruins, H.J. Dräger, Werkzeuge und Werkzeugmaschinen für die spanende Metallbearbeitung, Carl Hanser, München Wien, 1975.

[25] Ceratizit, Werkzeug und Wendeplatten zum Fräsen, Ceratizit Austria GmbH, Reutte, 2008.

[26] H.H. Klein, Fräsen, Springer, Hamburg, 1974.

[27] K. Cheng, D. Huo, Micro-Cutting: Fundamentals and Applications, Wiley, West Sussex, 2013.

[28] P. Bhattacharyya, D. Sengupta, S. Mukhopadhyay, Cutting force-based real-time estimation of tool wear in face milling using a combination of signal processing techniques, Mechanical Systems and Signal Processing 21 (6) (2007) 2665-2683.

[29] Ş. Aykut, E. Bagci, A. Kentli, O. Yazıcıoğlu, Experimental observation of tool wear, cutting forces and chip morphology in face milling of cobalt based super-alloy with physical vapour deposition coated and uncoated tool, Materials & Design 28 (6) (2007) 1880-1888.

[30] I. Korkut, M.A. Donertas, The influence of feed rate and cutting speed on the cutting forces, surface roughness and tool–chip contact length during face milling, Materials & Design 28 (1) (2007) 308-312.

[31] B. Denkena, H.K. Tönshoff, Spanen, Springer, Heidelberg, Berlin, 2010.

[32] K.-D. Bouzakis, N. Michailidis, N. Vidakis, K. Efstathiou, T. Leyendecker, G. Erkens, R. Wenke, H.-G. Fuss, Optimization of the cutting edge radius of PVD coated inserts in milling considering film fatigue failure mechanisms, Surface and Coatings Technology 133-134 (2000) 501-507.

[33] M.B. da Silva, J. Wallbank, Cutting temperature: prediction and measurement methods - a review, Processing Technology 88 (1999) 195-202.

[34] I. Krajinović, W. Ecker, W. Daves, Internal Communication: Simulation of Cutting Temperature at the Cutting Edge During Application, Leoben, 2014.

[35] D.D. Pollok, D.M. Rowe (Ed.), CRC Handbook of Thermoelectrics, CRC Press LLC, Boca Raton, (1995) 1-17.

[36] SAB Bröckskes, MTE und MWT Matnetel-Thermoelemente und Mantel-Widerstandthermometer, SAB Bröckskes Produktkatalog, Viersen, 2012.

[37] M. Plank, Über das Gesetz der Energieverteilung im Normalspektrum; Annalen der Physik, 4 (1901) 553-563.

[38] W. Wien, Temperatur und Entropie der Strahlung, Annalen der Physik 52 (2) (1894) 132-165.

[39] B. Müller, Thermische Analyse des Zerspanens metallischer Werkstoffe bei hohen Schnittgeschwindigkeiten, PhD tesis, Aarchen, 2004.
[40] Homepage: http://www.flir.de/science, Stand: 24.01.2014.
[41] B.T. Chao, H.L. Li, Trigger, K.J., An experimental investigation of temperature distribution at tool flank surface, Journal of Engineering for Industry, 109 (1961) 92-99.
[42] Kager Industrieprodukte GmbH, TMC Farbwechsel-Thermometer, Kager Industrieprodukte Produktkatalog, Dietzenbach, 2011.
[43] A.C.A. de Melo, J.C.G. Milan, M.B. da Silva, A.R. Machado, Some Observation on Wear and Damages in Cemented Carbide Tools, Journal of Brazialian Society of Mechanical Sciences & Engineering 28 (3) (2006) 269-277.
[44] H. Chandrasekaran, Fracture of Carbide Tools in Intermittent Cutting, in: R.K. Viswanadham, D.J. Rowcliffe, J. Gurland (Eds.), Science of Hard Materials, Springer; Springer US, Boston, MA, 1983, pp. 735-755.
[45] M. Lagerquist, A Study of the Thermal Fatigue Crack Propagation in WC-Co Cemented Carbide, Powder Metallurgy 18 (35) (1975) 71-87.
[46] Homepage: http://www.salzgitter flachstahl.de/fileadmin/mediadb/szfg/informationsmaterial /produktinformationen/warmgewalzte_produkte/deu/S355JR.pdf, Stand: 31.05.2015.
[47] S.M. Bhatia, P.C. Pandey, H.S. Shan, Failure of cemented carbide tools in intermittent cutting, Precision Engineering 1 (3) (1979) 148-152.
[48] J.S. Strenkowski, J.T. Carroll, A finite element model of orthogonal metal cutting, Journal of Manufacturing Science and Engineering 107 (4) (1985) 349-354.
[49] DIN, Impermeable sintered metal materials and hard metals - Determination of density, Beuth, Berlin, 2010.
[50] Standard Test Method for Determination of Magnetic Saturation (Ms) of Cemented Carbides, ASTM International, West Conshohocken 77.040.20.
[51] Strues GmbH, Über das Schleifen und Polieren, 2014.
[52] W.C. Oliver, P.G.M Pharr, An improved technique for determining hardness and elastic modulus using load and displacement sensing indentation experiments, Journal of Material Research 7 (6) (1992) 1564-1583.
[53] G. Jaeger, I. Endler, M. Heilmaier, K. Bartsch, A. Leonhardt, A new method of determining strength and fracture toughness of thin hard coatings, International Conference on Metallurgic Coatings and Thin Films 377-378 (2000) 382-388.
[54] M. Tkadletz, N. Schalk, C. Mitterer, Internal Communication: Thermal-physical properties of Ti-Al-Ta-N coating, Leoben, 2015.
[55] T. Teppernegg, T. Klünsner, C. Tritremmel, P. Angerer, C. Czettl, R. Pippan, Residual Stress and Damage in Post-Treated Coated Milling Inserts, Proceedings of the Euro PM2014, Salzburg, 2014, pp. EP140186 1-6.
[56] Ilsenburger Grobblech, data specification of 42CrMo4 (1.7225), (2008).

[57] T. Teppernegg, T. Klünsner, P. Angerer, C. Tritremmel, R. Ebner, C. Czettl, J. Keckes, R. Pippan, Residual stress and damage in coated hard metal milling inserts, Advances in Tungsten, Refractory and Hardmaterials IX - Proceedings of the 9th International Conference on Tungsten, Refractory and Hardmaterials (2014).

[58] T. Teppernegg, T. Klünsner, P. Angerer, C. Tritremmel, C. Czettl, J. Keckes, R. Ebner, R. Pippan, Evolution of residual stress and damage in coated hard metal milling inserts over the complete tool life, International Journal of Refractory Metals and Hard Materials 47 (2014) 80-85.

[59] T. Teppernegg, T. Klünsner, C. Tritremmel, C. Czettl, J. Keckes, T. Wroblewski, R. Ebner, R. Pippan, Spatial Correlation of Tensile Residual Stress and Thermal Fatigue Damage in Coated Cemented Carbide Milling Inserts, in: 18th Plansee Seminar: International Conference on Refractory Metals and Hard Materials, Reutte, 2013, pp. Hard Metal47/ 1-Hard Metal47/10.

[60] T. Wroblewski, O. Clauß, H.-A. Crostack, A. Ertel, F. Fandrich, C. Genzel, K. Hradil, W. Ternes, E. Woldt, A new diffractometer for materials science and imaging at HASYLAB beamline G3, Nuclear Instruments and Methods in Physics Research Section A: Accelerators, Spectrometers, Detectors and Associated Equipment 428 (2-3) (1999) 570-582

[61] C. Genzel, C. Stock, W. Reimers, Application of energy-dispersive diffraction to the analysis of multiaxial residual stress fields in the intermediate zone between surface and volume, Materials Science and Engineering: A 372 (1-2) (2004) 28-43.

[62] U. Welzel, J. Ligot, P. Lamparter, A.C. Vermeulen, E.J. Mittemeijer, Stress analysis of polycrystalline thin films and surface regions by X-ray diffraction, Journal of Applied Crystallography 38 (1) (2005) 1–29.

[63] L. Spieß, R. Schwarzer, H. Behnken, G. Teichert, Moderne Röntgenbeugung: Röntgendiffraktometrie für Materialwissenschaftler, Physiker und Chemiker, 1st ed., Teubner, Wiesbaden, 2005.

[64] T. Teppernegg, P. Angerer, T. Kluensner, C. Tritremmel, C. Czettl, Evolution of Residual Stress in TiAlTaN Coatings on Hard Metal Milling Inserts International Journal of Refractory Metals and Hard Materials 52 (2015) 171-175.

[65] Standard Test Method for the Thermal Diffusivity by Flash Method, E1461 ASTM International, West Conshohocken.

[66] W.J. Parker, R.J. Jenkins, C.P. Butler, G.L. Abbott, Flash Method of Determining Thermal Diffusivity, Heat Capacity, and Thermal Conductivity, Journal of Applied Physics 32 (9) (1961) 1679–1684.

[67] LFA 457 MicroFlash, Leading of Thermal Analysis. Netzsch Gerätebau GmbH, Selb, 2012.

[68] W. Lins, G. Kaindl, H. Peterlik, K. Kromp, A novel resonant beam technique to determine the elastic moduli in dependence on orientation and temperature up to 2000 °C, Review of Scientific Instruments 70 (7) (1999) 3052-3058.

[69] DIN EN 10002-4, Verification of extensometers used in uniaxial testing, Beuth, Berlin, 1994.

[70] T. Klünsner, Influence of Microstructure on Material Behaviour of WC-Co Hard Metals under Static and Cycling Loading Conditions. PhD, Leoben, 2011.

[71] Standartd Test Method for Linear Elastic Plain Fracture Toughness K_{IC} of Metallic Materials, E399, ASTM International, West Conshohocken.

[72] E. Trent, P. Wright, Metal Cutting, Butterworth-Heinemann, Woburn, 2000.

[73] M. Nordin, R. Sundström, T.I. Selinder, S. Hogmark, Wear and failure mechanisms of multilayered PVD TiN/TaN coated tools when milling austenitic stainless steel, Surface and Coatings Technology 133-134 (2000) 240-246.

[74] M. Tkadletz, C. Mitterer, B. Sartory, I. Letofsky-Papst, C. Czettl, C. Michotte, The effect of droplets in arc evaporated TiAlTaN hard coatings on the wear behavior, Surface and Coatings Technology 257 (2014) 95-101.

[75] P. Raninger, W. Ecker, T. Antretter, M. Leindl, R. Ebner, Interaction of heat checks in aluminum pressure casting dies and their effect on fatigue life, Key Engineering Materials 488-489 (2012) 626-629.

[76] P.K. Philip, Tool wear and tool life characteristics of unconventional sintered carbides in the intermittent cutting of hardened steel, Wear 47 (1) (1978) 45-60.

[77] D. Mari, A.D. Krawitz, J.W. Richardson, W. Benoit, Residual stress in WC-Co measured by neutron diffraction, Materials Science and Engineering: A 209 (1-2) (1996) 197-205.

[78] D.M. Mattox, Handbook of Physical Vapor Deposition (PVD) Processing, 2nd ed., Elsevier Science, Oxford, 2010.

[79] A.J. Perry, A contribution of the study of poisson's ratios and elastic constants of TiN, ZrN and HfN, Thin Solid Films 193-194 (1) (1990) 463-471.

[80] A.Kampfe, B. Eigenmann, O. Vohringer, D. Lohe, X-Ray and Single Crystal Values of the Elastic Constants and Determination of Machining Residual Stresses in AlN, High Temperature Material Process: An International Quarterly of High-Technology Plasma Processes 2 (3) (1998) 309-326.

[81] F. Tasnádi, I.A. Abrikosov, L. Rogström, J. Almer, M.P. Johansson, M. Odén, Significant elastic anisotropy in $Ti_{1-x}Al_xN$ alloys, Applied Physics Letters 97 (23) (2010).

[82] U. Fischer, R. Gomeringer, M. Heinzler, R. Kilgus, F. Näher, S. Oesterle, H. Paetzold, A. Stephan, Tabellenbuch Metall, 45th ed., Europa Lehrmittel, Haan-Gruiten, 2011.

[83] R. Abel, Schneidkeramik in der Guss - Stahlbearbeitung, Expert Verlag, Grafenau 1/Wurtt, 1982.

[84] Hompage:http://www.saarstahl.com/fileadmin/saarstahl_extranet/images/04_produkte/walzstahlsorten/deutsch/1191_1201_C45E_C45R.pdf, Stand 29.05.2015.

[85] W. Seidel, F. Hahn, Eisen-Kohlenstoff-Legierungen, in: W. Seidel, F. Hahn (Eds.), Werkstofftechnik, Carl Hanser Verlag GmbH & Co. KG, 2014, pp. 91-107,.

[86] P. Miranzo, M.I. Osendi, E. Garcia, Fernandes, A. J. S., V.A. Silva, F.M. Costa, R.F. Silva, Thermal conductivity enhancement in cutting tools by chemical vapor deposition diamond coating, 12th European Conference on Diamond, Diamond- Like Materials, Carbon Nanotubes, Nitrides & Silicon Carbide 11 (3-6) (2002) 703-707.

[87] Z.Z. Fang, M.C. Koopman, H. Wang, 1.04 - Cemented Tungsten Carbide Hard metal-An Introduction, in: V.K. Sarin (Ed.), Comprehensive Hard Materials, Elsevier, Oxford, 2014, pp. 123-137.

[88] T. Teppernegg, T. Kluensner, C. Kremsner, C. Tritremmel, S. Puchegger, C. Czettl, S. Masoner, R. Pippan, R. Ebner, High Temperature Mechanical Properties of WC-Co Hard Metals, International Journal of Refractory Metals and Hard Materials 56 (2015) 139-144.

[89] R. Kieffer, F. Benesovsky, Hartmetalle, Springer Vienna, 1965.

[90] J. Ferreira, M.P. Amaral, F.V. Antunes, J. Costa, A study on the mechanical behaviour of WC/Co hard metals, International Journal of Refractory Metals and Hard Materials 27 (1) (2009) 1-8.

[91] G.D. Blumenthal, The Effect of Temperature on the Elastic Moduli of Cemented Tungsten Carbide, 1968.

[92] H.G. Schmid, D. Mari, W. Benoit, C. Bonjour, The mechanical behaviour of cemented carbides at high temperatures, Material Science and Engineering: A 105-106, (2) (1988) 343-351.

[93] G. Östberg, K. Buss, M. Christensen, S. Nogren, H.-O. Andrén, D. Mari, G. Wahnström, I. Reineck, Mechanisms of plastic deformation of WC-Co and Ti(C,N)-WC-Co, Science of hard materials, Part II, in: Selected papers from the 8th International Conference on the Science of Hard Materials 24 (1-2) (2006) 135-144.

[94] Y. V. Milman, S. Luyckx, I.T. Northrop, Influence of temperature, grain size and cobalt content on the hardness of WC-Co alloys, International Journal of Refractory Metals and Hard Materials 17 (1-3) (1999) 39-44.

[95] Y. Torres, M. Anglada, L. Llanes, Fatigue mechanics of WC-Co cemented carbides, Science of Hard Materials, in: Selected Papters of the 7th International Conference on the Science of Hard Materials 19 (4-6) (2001) 341-348.

[96] J.S. August, H.S. Kalish, The Effect of Composition on the Fracture Toughness of Hard Materials, in: Proceedings on the 10th Plansee Seminar 1981: Trends in Refractory Metals, Hard Metals and Special Materials and Their technology, Reutte, 1981, pp. 743-760

[97] N. Ingelstrom, H. Nordberg, The fracture toughness of cemented tungsten carbides, Engineering Fracture Mechanics 6 (3) (1974) 597-607.

[98] R. Warren, B. Johannesson, The Fracture Toughness of Hard metals, Sintered Metal- Ceramic Composites (1984) 365-375.

[99] B. Johannesson, R. Warren, Subcritical crack growth and plastic deformation in the fracture of hard metals, Materials Science and Engineering: A 105–106, (2) (1988) 353-361.

[100] M. Tkadletz, C. Mitterer, N. Schalk, Internal Communication: Material input data of Ti-Al-Ta-N coating for simulation model, Leoben, 2015.

[101] F.W. Bach, T. Duda, Moderne Beschichtungsverfahren, Wiley-VCH, Weinheim, 2000.

11 Appendix

Publication I

Spatial Correlation of Tensile Residual Stress and Thermal Fatigue Damage in Coated Cemented Carbide Milling Inserts

T. Teppernegg[1], T. Klünsner[1], C. Tritremmel[1], C. Czettl[2], J. Keckes[3], T. Wroblewski[4], R. Ebner[1], R. Pippan[5]

[1] Materials Center Leoben Forschung GmbH, Roseggerstraße 12, 8700 Leoben, Austria

[2] CERATIZIT Austria GmbH, Metallwerk-Plansee-Straße 71, 6600 Reutte, Austria

[3] Department of Materials Physics, Montanuniversität Leoben, Jahnstraße 12, 8700 Leoben, Austria

[4] DESY, HASYLAB, Notkestraße 85, 22607 Hamburg, Germany

[5] Erich Schmid Institute of Materials Science, Austrian Academy of Sciences, Jahnstrasse 12, 8700 Leoben, Austria

Abstract

Thermo-mechanical fatigue induced by interrupted tool-workpiece contact and wear are the main damage mechanisms in coated cemented carbide milling inserts. This study examines a damage mechanism in milling inserts by local correlation of the emergence of tensile residual stress and damage in form of cracks. The studied milling tools that cut 42CrMo4 steel in normalized state were made of fine-grained WC - 8 wt.% Co coated with arc evaporated TiAlN-based. To focus on early stages of damage, the inserts performed a defined number of contacts with the workpiece. The development of residual stresses was studied in the WC phase as a function of the number of contacts. Their position along the cutting edge was examined via synchrotron X-ray diffraction with high lateral resolution. In order to document the degree of damage present at various stages of tool life, selected milling inserts were prepared by focused ion beam milling and investigated by scanning electron microscopy. The location of the first observed significant tensile residual stresses was compared with the position of the most pronounced thermal fatigue crack at the end of service life. The position of tensile residual stresses in an insert with 1000 tool-workpiece

contacts corresponds well with the position of thermal fatigue cracks in milling inserts at the end of service life.

Keywords : WC-Co cemented carbide, residual stress, damage, synchrotron, milling

Introduction

In milling processes, high cyclic contact pressures and chip sliding velocities arise [1] accompanied by alternating temperature loads [2-5]. These loads act locally on the tool edge causing wear [1] and possibly also local plastic deformation [4] that triggers the buildup of tensile residual stresses upon cooling. Combcracks, that are the most prominent form of thermal fatigue cracks in milling inserts, exhibit a growth plane normal to the cutting edge [2,4]. Opitz et al. expected that the direction of tensile residual stresses that lead to the formation of these cracks are oriented in a direction parallel to the cutting edge [4].
Kirchlechner et al. investigated the emergence of residual stresses, induced by thermal shock on coated steel specimens, with high lateral resolution using synchrotron X-ray diffraction [6]. The used method allowed for a position resolved measurement of residual stresses in polycrystalline materials [11]. This would be the ideal method to study position-resolved correlation of the emergence of tensile residual stresses and combcracks in milling inserts.
Ekemar et al. indicate that the site of crack initiation is located at the hottest point on the surface of the rake face behind the cutting edge [7]. Moreover, the combcracks grow from their site of nucleation towards the cutting edge [4, 8-9]. The number of thermal cycles needed for crack initiation is not well-known. On the one hand, only one thermal cycle was needed to create a crack density of $2x10^{11}$ microscopic cracks per m² in thermo-shock experiments with uncoated cemented carbide [10]. On the other hand, first macroscopic combcracks were found in uncoated milling inserts after 200 cutting cycles by stereo microscopy [4].There qualitatively understanding of the evolution of residual stress and damage in milling tools is based on guesses.
The present paper investigates the early development of residual stress and damage in milling inserts.

Experimental details

The studied milling inserts were made of WC - 8 wt.% Co with an average WC grain size of 1 µm and were coated with TiAlN-based deposited by cathodic arc evaporation with a thickness of 8 µm. The inserts exhibit dimensions of 6.35 x 11.4 x 10 mm³ and chamfered cutting edges. 42CrMo4 steel in normalized state with an upper yield strength of 400 N/mm² was used as workpiece material. Face milling tests were carried out as illustrated in Fig. 1 using a type EX-CELL-O XB406 miller with a spindle power of 57 kW.

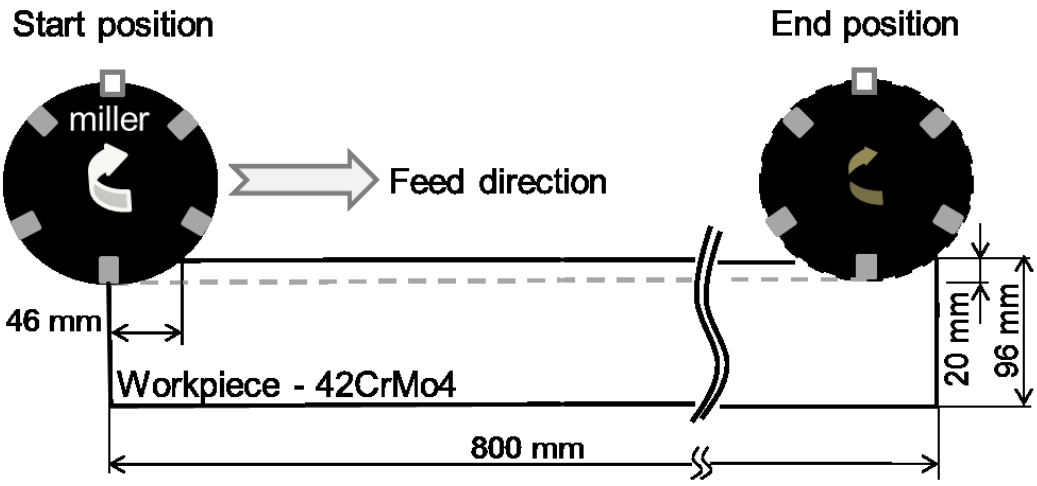

Fig.1: Scheme of machining test setup

The tool holder with a diameter of 125 mm and holding capacity for six inserts machined a workpiece with the dimensions of 800 x 96 x 200 mm^3. All performed machining tests were carried out without water or air cooling in a synchronous milling arrangement. Only one of the six milling inserts actually did cut to maximize the length of constant cutting conditions at a limited size of the workpiece (see white rectangle in miller symbol in Fig. 1). To ensure a constant contact length of each tool-workpiece contact, a distance of 46 mm was removed by a dummy tool at the beginning and the end of each cut segment (cf. “start position” and “end position” in Fig. 1). Thus, 1900 tool-workpiece contacts with constant cutting conditions were performed within one segment length. Milling tests with higher numbers of tool-workpiece contacts (>1900) required the movement of the miller to the start position for it to cut a further segment. The machining experiments were stopped after two, ten, 100, 500, 1000, 1900, 9400 and 15000 tool-workpiece contacts. For example, 15000 tool-workpiece contacts correspond to eight cut segments in the current testing setup. The top view of the milling insert with 1000 tool-workpiece contacts is shown in Fig. 2.

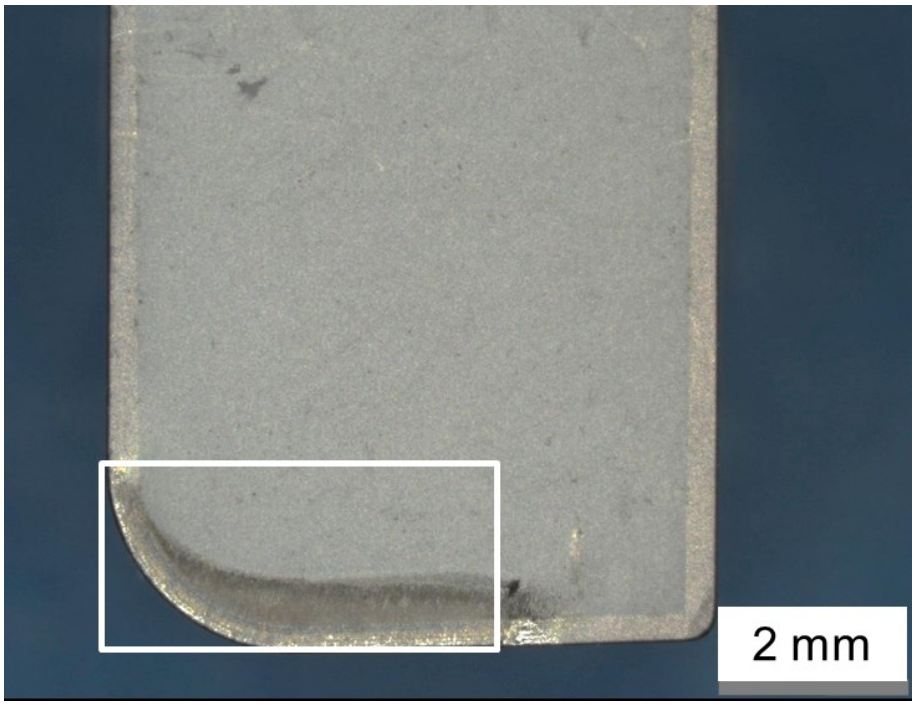

Fig.2: Top view of used milling insert after 1000 tool-workpiece contacts under constant cutting conditions. White margin indicates area of residual stress mapping (see Fig. 3).

The cutting parameters of the discussed test setup are shown in Tab. I. To document the extent and location of damage in form of cracks at the end of service life (about 40000 tool-workpiece contacts), a milling insert was tested under similar conditions as described in Tab. I. Feed rate and cut segment length were changed from 0.4 mm to 0.5 mm per tooth and 800 mm to 96 mm, respectively. To reduce the required testing efforts, beginning and end sections of cut segments were also milled with the investigated insert.

Tab. I: Cutting parameters of used machining test setup

Machining parameters		
Speed of rotation	[rev. / min]	560
Feed rate	[mm / tooth]	0.4
Cutting depth	[mm]	4
Contact length	[mm]	51.4
Cutting speed	[m / min]	220

Residual stresses in selected inserts were characterized at the G3 beamline of the Hasylab synchrotron source in Hamburg using a 4-circle diffractometer and monochromatic synchrotron X-rays with an energy of 10 keV. The position resolved measurements of residual stress were performed using the MAXIM system [11] applying the side inclination

method [12]. The residual stresses were determined in the tungsten carbide phase of the hard metal substrate in a region of about 5 µm below the interface between coating and WC-Co substrate. Please note that the uncertainty associated with the residual stress measurements is in the order of magnitude of the determined values and is influenced by two factors. On the one hand, the diffraction intensity is strongly affected by the number of illuminated WC grains. On the other hand the lateral resolution of the measurement is diminished due to the necessary distortion correction procedure resulting in a lateral resolution of 100 µm².

Surface topography of the rake faces was investigated by scanning electron microscopy (SEM, Zeiss Auriga). Selected milling inserts at 1000 and 15000 tool-workpiece contacts as well as at end of service life were prepared with a focused ion beam (FIB, Orsay Physics Cobra Z-05) to document the presence or absence of combcracks at a certain stage of insert life.

Results and Discussion

Residual stresses in selected milling inserts with zero, two, ten and 1000 tool-workpiece contacts were characterized in a position-resolved manner within a rectangular area indicated in Fig. 2. The corresponding two-dimensional distribution of the residual stress component oriented parallel to the rectangle's longer side is presented in Fig. 3. Dark and light shades of grays represent compressive and tensile residual stresses respectively.

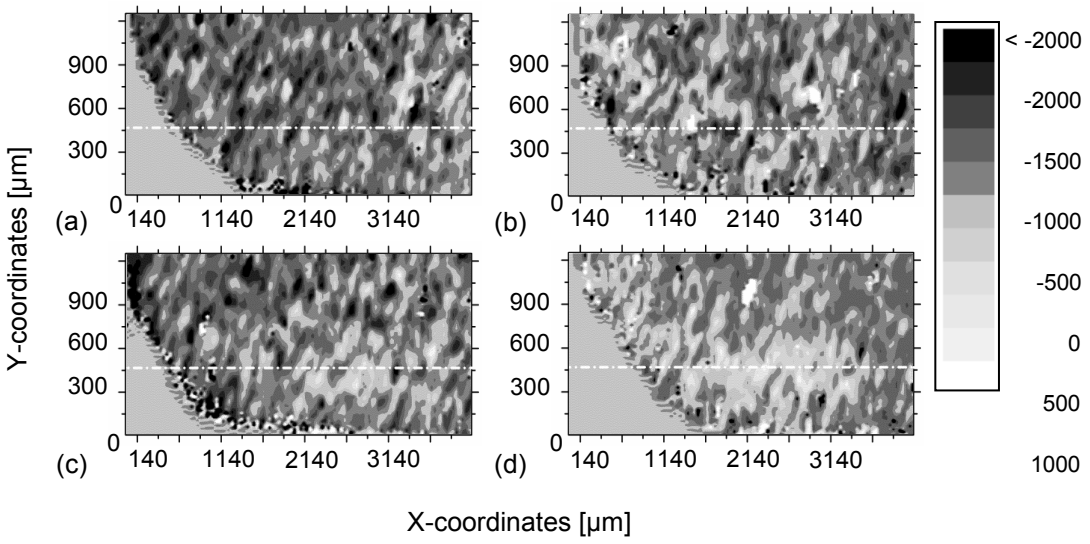

Fig.3: Position resolved maps of residual stress in x-direction in milling inserts with (a) 0, (b) 2, (c) 10 and (d) 1000 tool-workpiece contacts. The lower boundaries of the stress maps correspond to the straight portions of the cutting edges of the inserts. Please mind that x- and y- coordinates scale differently.

In the virgin milling insert predominantly compressive residual stresses were observed (see Fig. 3(a)). As seen in Fig. 3(b) and 3(c), the residual stress state of milling inserts with two and ten cuts showed a slight tendency towards tensile stresses as indicated by the increased fraction of light gray areas. However, after 1000 tool-workpiece contacts significant tensile residual stresses have developed in x-direction in an area of approximately 0.3 mm x 1.5 mm as indicated by the high fraction of light grey regions in Fig. 3(d). The center of significant tensile residual stress buildup is located about 0.4 mm from the straight portion of the cutting edge. Local variations of residual stress in x-direction along the dashed lines indicated in Fig. 3 are presented in Fig. 4.

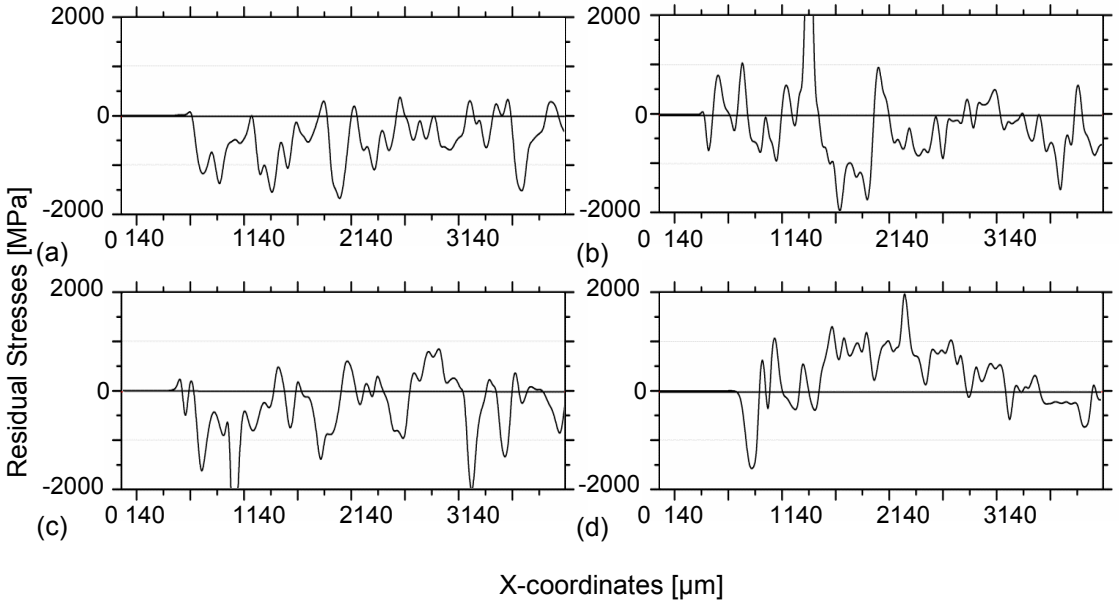

Fig.4: Profiles of residual stress in x-direction obtained from horizontal sections of residual stress maps in milling inserts as indicated by dashed lines in Fig. 3: (a) 0, (b) 2, (c) 10 and (d) 1000 tool-workpiece contacts

As can be seen in Fig. 4(a), the residual stresses in the virgin insert are mainly compressive. This finding corresponds with results of neutron diffraction experiments from literature with uncoated cemented carbide specimens [13,14]. There are no significant changes in the observed residual stress state in specimens with two and ten tool-workpiece contacts respectively. The determined residual stress values are still mainly compressive (cf. Fig. 4(b) and 4(c)). However, significant tensile residual stresses of about 1000 MPa were observed in the specimen with 1000 tool-workpiece contacts on a length of scale of about 1.5 mm (see Fig. 4(d)). Please note that the uncertainty associated with the measured value is about 900 MPa. The present results indicate that under the investigated cutting conditions more than ten tool-workpiece contacts are required to build up significant tensile residual stresses on the rake face of the inserts.

To document the present state of damage, surface topography of the rake faces of milling inserts at zero, 1000, 15000 tool-workpiece contacts and at end of service life (about 40000 tool-workpiece contacts) were investigated by SEM (see Fig. 5).

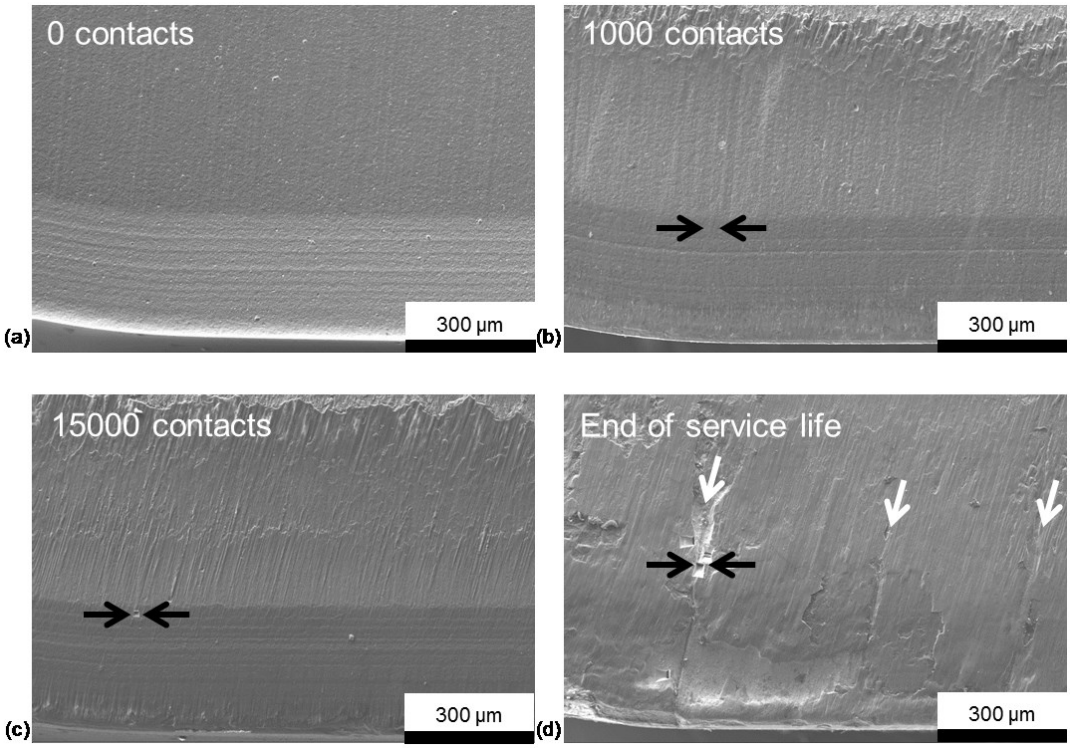

Fig. 5: SEM micrographs showing surface topography of the rake faces of milling inserts at (a) zero, (b) 1000, (c) 15000 tool-workpiece contacts and (d) end of service life (about 40000 tool-workpiece contacts). Black arrows in (b), (c) and (d) indicate areas of detailed SEM / FIB investigations shown in Fig. 6. White arrows in (d) indicate positions of combcracks at end of service life.

As can be seen in Fig. 5(a) to 5(c) the milling inserts with zero, 1000 and 15000 tool-workpiece contacts do not show any cracks on the surface. The contact between tool and workpiece during cutting induces adhesive and abrasive wear up to approximately one millimeter from the cutting edge (see Fig. 5(b) to 5(d)). The milling insert at end of service life shows combcracks indicated by white arrows in Fig. 5(d). The position of the most pronounced combcrack, indicated by the leftmost of the white arrows in Fig. 5(d), corresponds with the position of the highest tensile residual stress found in the milling insert after 1000 tool-workpiece contacts (compare Fig. 3(d) and Fig. 4(d). Typical crater wear marks [2] with complete coating removal were observed near the cutting edge of the insert at end of service life.

Detailed investigations of the tool surface including some FIB cuts are summarized in Fig. 6. Figure 6(a), 6(c) and 6(e) show SEM images of the rake faces of milling inserts after 1000, 15000 tool-workpiece contacts and at end of service life; the white lines in the figures

indicate the positions of cross sections prepared by FIB cuts that are shown in Fig. 6(b), 6(d) and 6(f). The positions of the mentioned FIB cross sections were chosen within the area of tensile residual stress buildup in the insert with 1000 tool-workpiece contacts shown in Fig. 3(d). To produce a smooth FIB cut, a platinum layer was deposited prior FIB cutting. This platinum layer appears as a bright film on top of the darker hard coating on the cemented carbide substrate. In the analyzed milling inserts with up to 15000 tool-workpiece contacts no macroscopic cracks were observed, neither in the coating nor in the cemented carbide substrate (e.g. see Fig. 6(a) to 6(d)). The inhomogeneity in Fig. 6(b) was found to be not a crack but a pore around a droplet in the arc-evaporated TiAlN-based coating. Such droplets are typical for coatings deposited by means of arc evaporation coating processes [15]. The most pronounced combcrack in the tool at end of service life is shown in detail in Fig. 6(e) and 6(f). The cross section of the crack shows that both crack flanks and edges are shattered and that the crack itself is partially filled up with chip material and tungsten carbide fragments. The end of the crack is not visible and consequently the crack is deeper than 15 µm. Cracks appear also in the hard coating.

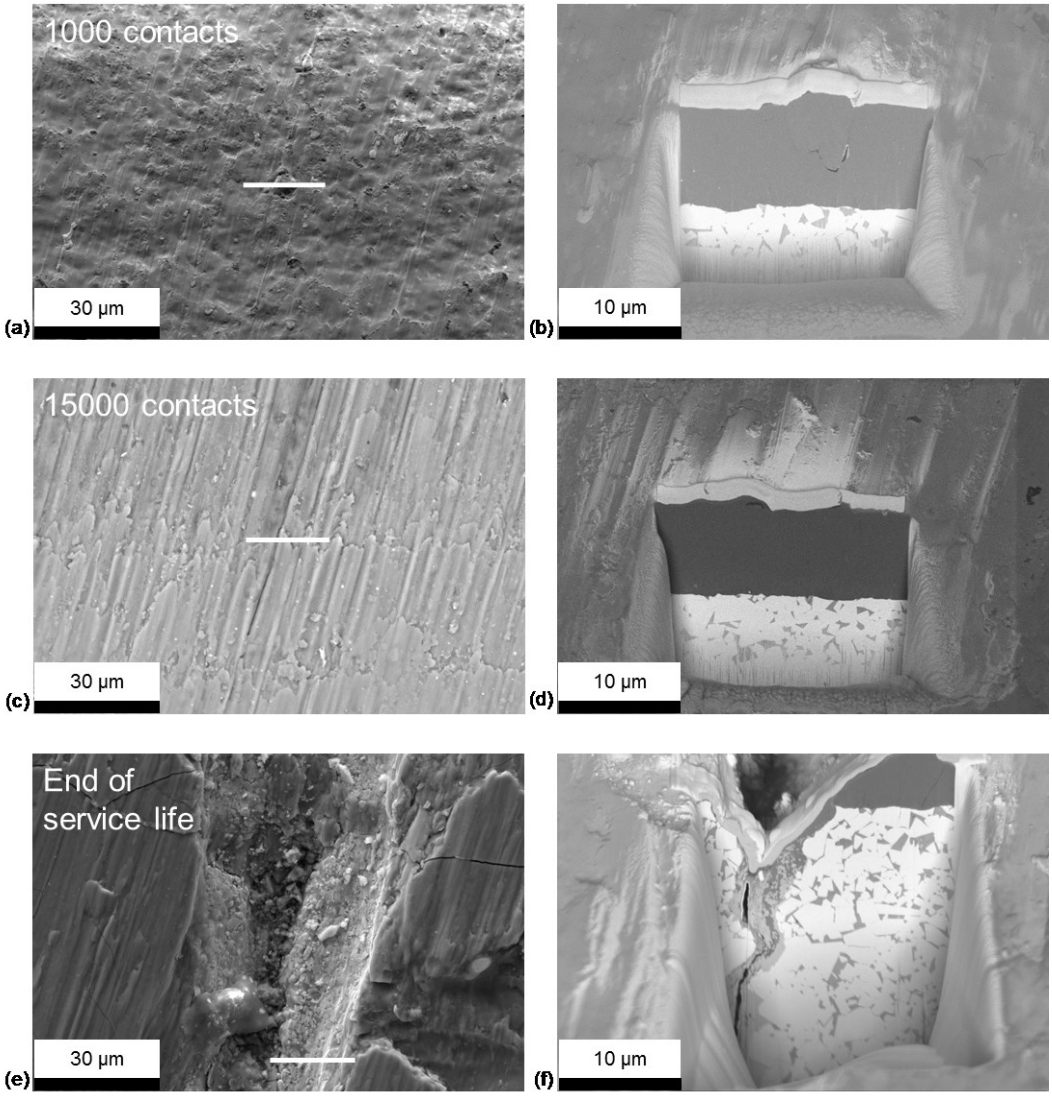

Fig. 6: SEM micrographs showing surface topography of rake faces of milling inserts after (a) 1000 and (c) 15000 tool-workpiece contacts, (e) end of service life (about 40000 tool-workpiece contacts) – white lines in figures on the left indicate positions of FIB cuts. FIB cross sections of tools at (b) 1000 and (d) 15000 tool-workpiece contacts and (f) end of service life. Bright top layers on top of cross sections are protective platinum layers.

The presented results indicate that under the investigated cutting conditions more than 15000 tool-workpiece contacts are needed to create combcracks detectable by SEM.

Summary and Conclusions

The residual stress state in cemented carbide milling inserts coated with TiAlN-based was successfully characterized via synchrotron X-ray diffraction with high lateral resolution. In milling inserts with zero, two and ten tool-workpiece contacts residual stresses were found to be mainly compressive. The rake face of a milling insert with 1000 tool-workpiece contacts showed significant tensile residual stresses of about 1000 MPa in a region as large

as 0.3 mm x 1.5 mm close to the cutting edge. The maximum values were observed at a distance of about 0.4 mm away from straight part of the cutting edge. No pronounced combcracks were found in milling inserts with up to 15000 tool-workpiece contacts in detailed SEM investigations including cross sections prepared by FIB, neither in the cemented carbide substrate nor the hard coating. The position of the area of significant tensile residual stress buildup in the milling insert with 1000 tool-workpiece contacts corresponds well with the location of the most pronounced combcrack in a milling insert at end of service life.

Acknowledgement

Financial support by the Austrian Federal Government (in particular from the Bundesministerium für Verkehr, Innovation und Technologie and the Bundesministerium für Wirtschaft, Familie und Jugend) and the Styrian Provincial Government, represented by Österreichische Forschungsförderungsgesellschaft mbH and by Steirische Wirtschaftsförderungsgesellschaft mbH, within the research activities of the K2 Competence Centre on "Integrated Research in Materials, Processing and Product Engineering", operated by the Materials Center Leoben Forschungs GmbH in the framework of the Austrian COMET Competence Centre Programme, is gratefully acknowledged.

References

1. V.P. Astakhov , Tribology of Metal Cutting, Tribology and Interface Engineering Series No. 52, Elsevier, (2006)
2. W. Schedler, Hartmetall für den Praktiker, Plansee Tizit, VDI- Verlag GmbH, (1988)
3. M. Lagerquist, Powder Metallurgy 18, 71-87, (1975)
4. H. Opitz, W. Lehewald, Forschungsberichte des Landes Nordrhein- Westfalen, Nr. 1146, Westdeutscher Verlag, Köln und Opladen (1963)
5. E.M. Trent, P.K. Wright, Metal Cutting, fourth edition, Butterworth/Heinemann, Oxford (2000)
6. C. Kirchlechner, K.J. Martinschitz, R. Daniel, C. Mitterer, J. Donges, A. Rothkirch, M. Klaus,
   C. Genzel, J. Keckes, Scripta Materialia 62, 774-777, (2010)
7. C.S.G. Ekemar, S.A.O. Iggström, G.K.A. Hedén, Material for Metal Cutting, Proc. Conf. of BIRSA, Scarborough, pp.133-142, (1970),
8. A.C.A. Melo, J.C.G. Milan, M.B. da Silva, Á.R. Machado, Journal of the Brazilian Society of Mechanical Sciences & Engineering 28 [3], 269-277, (2006)
9. P.K. Philip, Wear 47, 45-60, (1978)
10. S. Ishihara, H. Shibata, T. Goshima, A.J. McEvily, Scripta Materialia 52, 559-563, (2005)

11. T. Wroblewski, O. Clauß, H.A. Crostack, A. Ertel, F. Fandrich, Ch. Genzel, K. Hradil, W. Ternes, E. Woldt, Nuclear Instruments and Methods in Physics Research A 428, 570-582, (1999)
12. Ch. Genzel, C. Stock, W. Reimers, Material Science and Engineering A 372, 28-43, (2004)
13. D. Mari, A.D. Krawitz, J.W. Richardson, W. Benoit, Material. Science and Engineering A 209,
    197-205,(1996)
14. M. Bartosik, R. Daniel, Z. Zhang, M. Deluca, W. Ecker, M. Stefenelli, M. Klaus, C. Genzel, C. Mitterer, J. Keckes, Surface and Coating Technology 206, 4502-4510, (2012)
15. B. Rother, J. Vetter, Plasmabeschichtungsverfahren und Hartstoffschichten, Deutscher Verlag für Grundstoffindustrie, Leipzig, (1992)
16. K.W. Mertz, H.A. Jehn, Praxishandbuch moderner Beschichtungen, Fachbuchverlag Leipzig, Leipzig, (2001)

Publication II

Residual Stress and Damage in Coated Hard Metal Milling Inserts

T. Teppernegg[1], T. Klünsner[1], P. Angerer[1], C. Tritremmel[1], C. Czettl[2], J. Keckes[3], R. Pippan[4], R. Ebner[1]

[1] Materials Center Leoben Forschung GmbH, Roseggerstraße 12, 8700 Leoben, Austria

[2] CERATIZIT Austria GmbH, Metallwerk-Plansee-Straße 71, 6600 Reutte, Austria

[3] Department of Materials Physics, Montanuniversität Leoben, Jahnstraße 12, 8700 Leoben, Austria

[4] Erich Schmid Institute of Materials Science, Austrian Academy of Sciences, Jahnstrasse 12, 8700 Leoben, Austria

Abstract

Wear and thermo-mechanical fatigue induced by interrupted tool-workpiece contact are the main damage mechanisms in coated hard metal milling inserts. Depending on the magnitudes of thermal and mechanical loads, one damage mechanism may be dominant and determine tool lifetime. In the present work a milling test was applied with specific conditions in which wear acts as the dominant damage mechanism and no combcracks appeared on the inserts. The evolution of residual stress in milling inserts and wear damage at several stages of tool life was investigated. All studied milling tools were made of fine-grained WC - 8 wt.% Co coated with an arc-evaporated TiAlN based film and they cut normalized 42CrMo4 steel material. The damage state of selected milling inserts was investigated by means of focused ion beam milling and scanning electron microscopy. A significant buildup of tensile residual stress was detected via synchrotron X-ray diffraction in a used milling insert at a very early stage of application. This buildup occurs in an area of about 0.3 mm x 1.5 mm close to the cutting edge. A special preparation technique enables the measurement of residual stresses in this small region of interest by in-house X-ray diffraction facilities to shed light on the evolution of residual stresses in milling inserts in their complete tool life. The deduced values of tensile residual stress in a used insert measured by synchrotron techniques as well as by in-house X-ray measurements are comparable.

Introduction

In milling processes, the main damage mechanisms are wear and thermal fatigue [1],[2]. Thermal fatigue is characterized by combcracks, which appear with crack planes perpendicular to the cutting edge [3],[4]. The tool lifetime of milling inserts may be determined by mainly one of the mentioned damage mechanism, e.g. wear damage, or of a combination of both. Which of the two is dominant is determined by the respective cutting conditions [3],[4]. Wear damage is induced generally by two main mechanisms: One is adhesive wear, in which workpiece material sticks to the tool's rake face during cutting and the other mechanism is abrasive wear, where particles of the coating move over the rake face [3],[5]. Abrasive wear kinetics is highly increased when debris in form of hard metal and coating fragments are introduced by the shattering of exposed surface features such as combcrack flakes [2].

Combcrack creation requires a sufficiently high temperature difference between heating upon cutting and cooling upon idle time [2],[5]. The use of liquid cooling agents in milling leads to thermal shocks acting in the milling tools and therefore fosters the creation of combcracks [7]. Combcrack formation in milling insert can be suppressed by lowering the temperature amplitudes acting at the tool edge, e.g. by heating the inserts [2]. Both, the cyclic thermal loads caused by frictional heating in the tool-chip interface and plastic deformation during cutting, are localized close to the cutting edge to initiate the nucleation and the growth of combcracks [2]. Local plastic deformation, which appears in a small area close to the cutting edge, is introduced mainly by thermal stress amplitudes induced by frictional heating. The combination of high cutting forces and high temperature surpass the flow stress of a tool material. Upon cooling, these loads then trigger the buildup of tensile residual stress in the cutting edge of milling inserts. Cyclic mechanical loads in form of cyclic contact pressure between chip and tool may also introduce local plastic deformation close to the cutting edge [8].

Kirchlechner et al. investigated the emergence of residual stress induced by cyclic thermal shocks in coated steel disc with position resolved high lateral resolution using synchrotron X-ray diffraction [9],[10]. In earlier work, significant tensile residual stress buildup was found on the rake face of a used milling insert in a region of approximately 0.3 x 1.6 mm² [6], which is indicated in Fig.1 by a black frame. The center of this region of interest (ROI) was located about 0.4 mm from the cutting edge. Tensile residual stresses were determined in a used milling insert in a direction parallel to the straight part of the cutting edge and were found to exhibit a value of about 1000 MPa (see Fig.1).

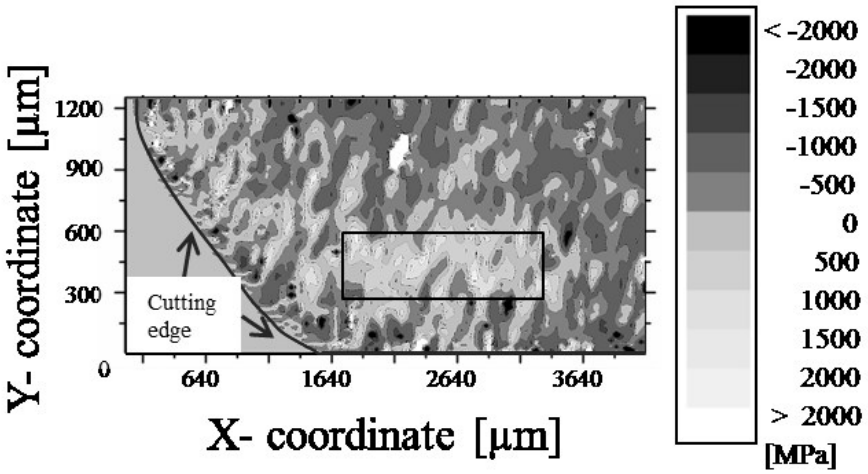

Fig.1: Map of residual stress acting in horizontal direction in the WC phase on the rake face of a used milling insert with 1,000 tool-workpiece contacts. The black frame indicates the area with significant tensile residual stress buildup [6].

The evolution of residual stress and damage was investigated only in the very early stages of tool life [6]. The further evolution of residual stress and damage in milling tools in later stages of application is currently not described in the open literature.

The present paper investigates the development of residual stress in milling inserts in later stages of tool life via X-ray diffraction (XRD) using a special covering method. Additionally, the damage state of selected milling inserts was documented.

Experimental

The studied milling inserts were made of WC - 8 wt.% Co hard metal and exhibited an average WC grain size of 1 µm. Furthermore, all inserts were coated with a TiAlN-based film deposited by cathodic arc evaporation with a thickness of 8 µm. The insert dimensions were 6.35 x 11.4 x 10 mm³, cutting edges were chamfered. Face milling tests were carried out using a test setup as described in more detail in [6] (see Fig.2). The same workpiece material as applied in [6] was used, being a 42CrMo4 steel in a normalized state with an upper yield strength of 400 N/mm².

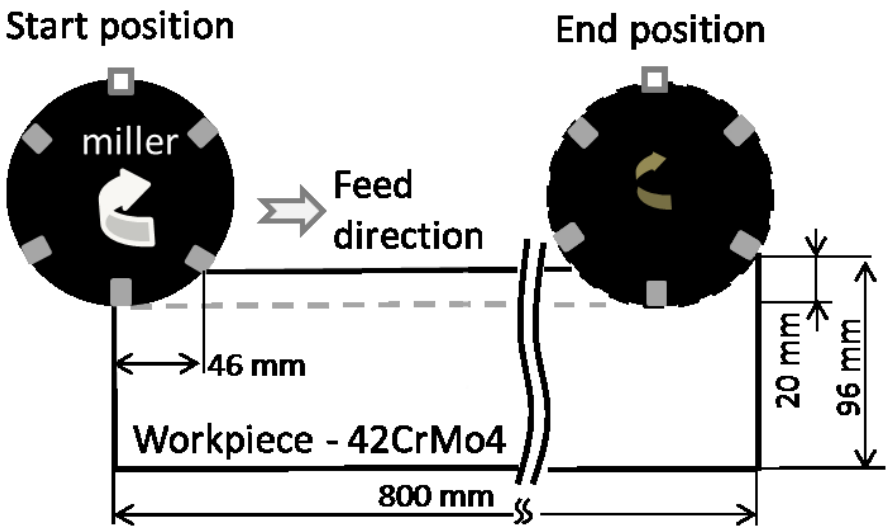

Fig.2: Scheme of one cut segment in the applied milling test setup, as also used in [6].

All performed machining tests were carried out without lubricant or air cooling. A single edge synchronous milling arrangement was applied, which means that only one insert actually did cut (see white rectangles in Fig. 2). The used cutting speed was 220 m/min, the feed rate was 0.4 mm/tooth, and the depth of cut was 4 mm. To ensure a constant length of each tool-workpiece contact, in the present paper also referred to as “cut”, a distance of 46 mm was removed by a dummy tool at the beginning and the end of each cut segment (cf. “start position” and “end position” in Fig.2). In this arrangement 1,900 tool-workpiece contacts with constant cutting conditions were performed within one cut segment length. Milling tests with a higher number of cuts required the movement of the milling tool to the start position to cut a new segment. For example a specimen that cuts 3 800 times removes two segments. In earlier work [6], the machining experiments were stopped after 10 and 1,000 cuts, respectively. In the present work, tests were done with 50, 500, 5,600, 9,600, 13,100, 17,700, 23,400, 26,200 and 37,400 cuts (end of lifetime).

The residual stress state in the region of interest (ROI) was determined in the direction parallel to the straight portion of the cutting edge in the tungsten carbide phase of the hard metal substrate in the same manner as described in [11]. The information was acquired in a depth region ranging from the interface between coating and WC-Co substrate and about 5 µm below this interface. The residual stress states of all milling inserts were measured via in-house XRD facility as reported in [11].

As previously described in [11], areas outside of the ROI on the milling inserts’ rake faces (black frame in Fig.3 a) were covered manually with a thin brass foil, see Fig.3 b). Brass was chosen as cover material to avoid the overlap of diffraction peaks from the cover material and the peak used for the determination of residual stress in the WC phase.

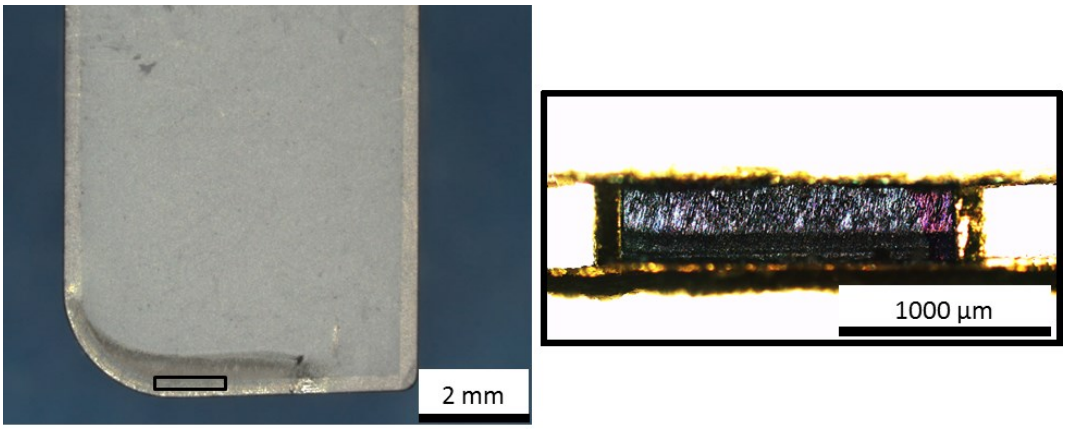

Fig.3: a) Top view of the rake face of used milling insert [6]. Rectangle frame indicates the detail shown in b): Top view of the rake face at the cutting edge of the milling insert, where area outside of the region of interest (ROI) is covered by brass foil [11]. Approximate ROI dimensions 1600 µm x 300 µm.

XRD measurements were conducted with a D8 Discover diffractometer (Bruker AXS, Germany) in parallel beam geometry (40 kV, 35 mA, Cu Kα radiation). The diffractometer was equipped with a Sol-X energy dispersive detector, an open (90°) Eulerian cradle and a polycarpellary collimator. The same diffraction maximum (2 1 1) of the hexagonal WC phase [12] at 2θ angel of 117.3° was selected as in our previous work [11] for the stress determination. The measured stress component was parallel to the straight portion of the cutting edge of the milling insert. It is favourable to choose a diffraction geometry with incident and diffracted beam orientated parallel to the long axis of the uncovered ROI to minimize any shadowing of the ROI by the covering brass foil. Otherwise, the measurement error, induced by the high amount of shadowed surface fraction, is increased. The effect would be larger at tilted samples ($\psi > 0$). Consequently, the ω-method was selected for the determination of the stress component [13]. Here, the measured stress vector lies in the plane spanned by incident and diffracted beam and is parallel to the sample surface, while the sample rotation axis ω is perpendicular to incident and diffracted beam and parallel to the sample surface. For the stress determination, the diffraction intensity was recorded in a 2θ diffraction angle range from 114.6 - 119.1° and sample tilt angles $\psi = \omega$ up to 35° as in earlier work [11]. For the evaluation of the diffraction angles of the measured peaks, the TOPAS 4.2 software [14] by Bruker AXS, Germany, was used. For each sample the residual stress component parallel to the sample surface and parallel to the straight portion of the cutting edge was then deduced from the slope determined by linear regression in the $\sin^2\psi$ plot according to the formalism described in [13]. No stress components perpendicular to the sample surface were taken in consideration.

The rake and flank face surface topography was investigated by scanning electron microscopy (SEM, Zeiss Auriga Crossbeam field emission gun). Furthermore, the chemical composition of the surface was investigated by energy dispersive spectroscopy (EDX). Selected milling inserts with 1,000 and 17,800 cuts as well as at end of service life (37,400 cuts) were prepared by means of focused ion beam technique (FIB) to visualize the damage state after application.

Results and Discussion

The evolution of residual stress in the ROI with increasing number of tool-workpiece contacts determined with the laboratory X-ray source and the cover-technique described above is presented in Fig.4. The ROI in the virgin milling insert showed compressive residual stress of -850 ± 270 MPa. This finding corresponds well with results from synchrotron residual stress measurements in [6] and results of neutron diffraction experiments with uncoated hard metal specimens in [15]. In the early stages of use the residual stresses in the WC phase changes dramatically within the ROI. After 10 cuts the compressive residual stresses were reduced to approximately -140 ± 120 MPa and already after 500 cuts tensile residual stresses of about 300 ± 80 MPa were observed. The highest tensile residual stresses of approximately 930 ± 230 MPa were found in a specimen with 1,000 cuts. This value corresponds well with the value of about 1000 MPa found in exactly the same specimen by synchrotron X-ray diffraction [6]. After about 10,000 tool-workpiece contacts the tensile residual stress is decreased to a plateau value of about 500 MPa until the end of tool lifetime.

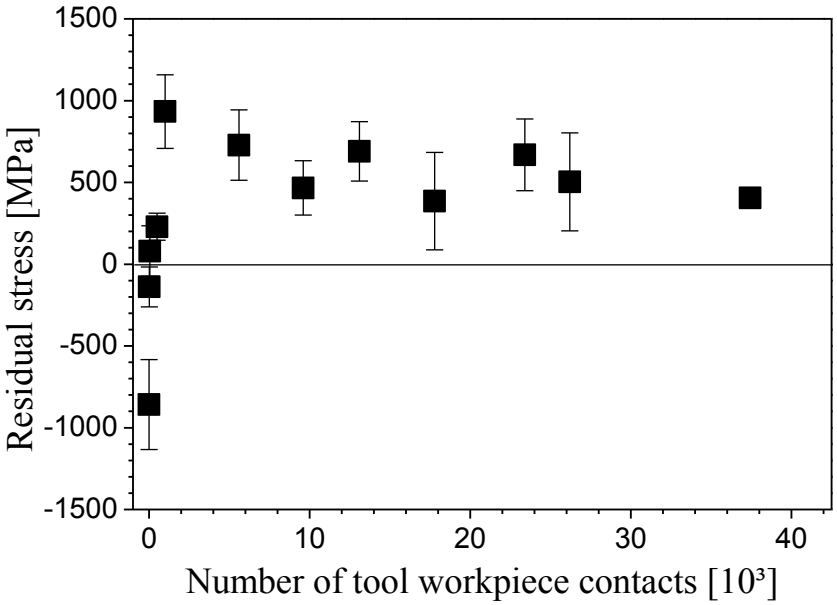

Fig.4: Residual stress data plotted as function of the number of tool-workpiece contacts: the data were determined locally in a small region of interest (ROI) in a cutting insert as defined by a "cover method" [11].

To document the surface topography and damage state at the rake faces of selected milling inserts with 1,000, 17,500 and at the end of lifetime after about 37,400 cuts were investigated by SEM, see Fig.5 a)-c). Small grey coloured frames in these overview images indicate the positions of surface images with higher magnification located at the upper edge of the chamfer as shown in Fig.5 d)-f). Fig.5 g)-i) show FIB cross sections with their respective positions indicated by lines in Fig.5 d)-f). To produce a smooth FIB cut, a platinum layer was deposited on the specimens prior to FIB cutting. This platinum layer appears as a bright film on top of the dark grey workpiece material or on the grey coloured hard coating on the cemented carbide substrate in Fig.5 g), h) and i).

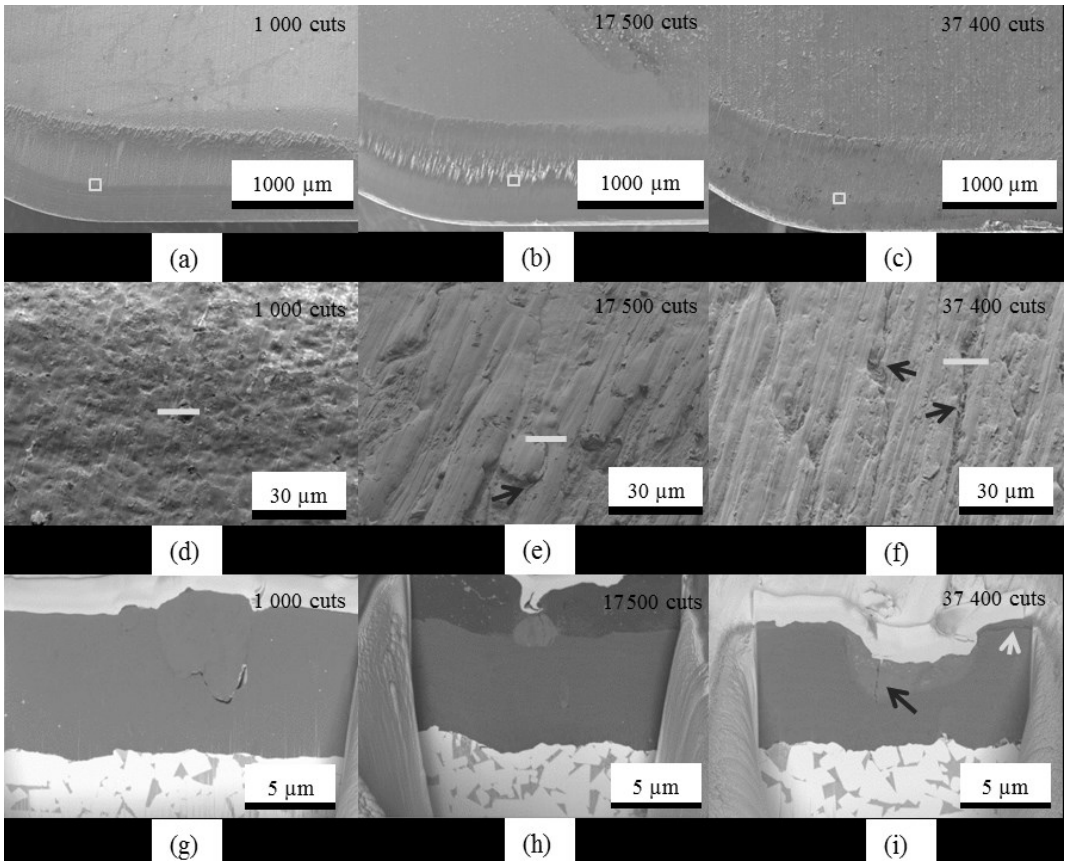

Fig. 5: SEM micrographs showing the surface topography of the rake faces of milling inserts after different numbers of tool workpiece contacts i.e. cuts. Black frames in a), b) and c) indicate the positions of d), e) and f) surface topography images with higher magnification. Lines in d), e) and f) indicate the positions of FIB cross sections shown in g), h) and i). Bright top layers on top of cross sections represent protective platinum layers.

The milling tests were stopped after 37,400 cuts because flank wear reached a critical magnitude. Fig.6 shows the increase of cutting edge wear within tool life. A continued use of the worn tool after 37,400 cuts would increase the risk of complete fracture of the insert. The presented results indicate that at the investigated cutting conditions abrasive and adhesive wear is the dominant damage mechanism.

Adhesive wear marks and abrasive wear, which look like grooves, were found in milling inserts with more than 1,000 tool workpiece contacts, e.g. see Fig.5 e), f), h) and i). In the Fig.5 h) the groove was in the adhered workpiece layer and in Fig. i) it was in the coating, respectively. Width of the grooves tends to increase with increasing number of cuts, see FIB cross sections in Fig.5 h) and i).

During cutting application this adhered workpiece layer seems to be removed and re-created. After 17,500 cuts the milling insert exhibited a workpiece layer thickness of about 4 µm (see in Fig.5 h)) whereas the milling insert at the end of lifetime had a much lower thickness, see grey coloured arrow in Fig.5 i). Additionally, workpiece material also

completely filled up the grooves, as seen in the FIB cross sections in Fig.5 i). Along of these filled groves, cracks were found normal to the cutting edge, see black arrows in Fig.5 e) and f). The crack growth started from the surface and was stopped when the crack reached the workpiece material/coating interface, documented in the FIB cross sections as black arrow in Fig.5 i). Nordin et al. [16] also found this kind of wear damage in form of grooves on their milling inserts using austenitic steel as workpiece material.

Fig.6 shows SEM flank face surface of the milling inserts with 1,000, 17,500 cuts and end of lifetime. During application the coating at the cutting edge is removed. Without the protection of the coating wear damage is strongly increased. At the end of lifetime the coating on the tool's flank face is removed up to a distance of about 100 µm from the cutting edge, see Fig.6 c). The limiting factor regarding lifetime in the current test setup was that the whole cutting edge was disintegrated.

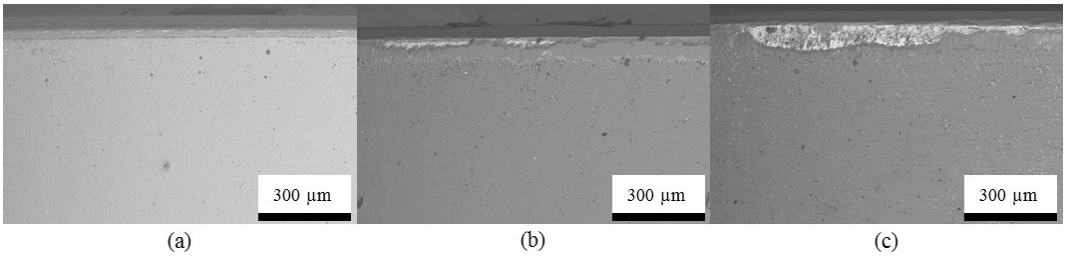

Fig.6: SEM images of the flank face of used inserts after a) 1,000, b) 17,500 cuts and c) end of lifetime (37,400 cuts).

In this test setup, neither macroscopic nor microscopic combcracks were observed in the coating or WC-Co substrate. This result is not typical for milling experiments, mainly documented in the literature. In most milling tests performed in the past, combcracks or "thermal" cracks were always observed, independent of the important cutting parameters feed rate, cutting speed and depth of cut [2],[17],[18]. For a certain test setup Bathia et al. described a combination of process parameters under which no tool failure induced by combcracks occurred due to subcritical thermal or mechanical tool loading [4]. For this situation to occur, the feed rate and the cutting speed had to be lower than 0.1 mm/revolution and 1.5 m/s, respectively. In the current paper and in earlier work [6] a feed rate of 0.4 mm/revolution and a cutting speed of 220 m/min (3.6 m/s) were applied. Despite of the use of higher feed rate and cutting speed, wear damage and not combcrack formation limited the tool lifetime. The parameter intervals for the described process field of tool failure by cracks were also dependent on the radius of the cutting edge. A milling insert with enlarged cutting edge radius widened the process parameter field in which wear before fracture occurs [4].

In milling experiments in the past uncoated cutting tools were tested and investigated [2],[3],[18]. The combined use of protective hard coatings along with chamfered cutting

edges, which reduces the sharpness of the edge, seems to enlarge the process parameter field of no tool failure induced by cracks effectively. Therefore, in the experiments wear damage dominated the tool lifetime.

Summary and Conclusions

The evolution of residual stress in an area of 0.3 x 1.6 mm close to the cutting edge of coated hard metal milling inserts over the complete tool life was successfully documented via X-ray diffraction with a special covering technique. The residual stress values determined in a virgin insert and an insert with 1,000 tool-workpiece contacts measured by in-house facilities were comparable with the corresponding values found by synchrotron facilities in earlier work. A virgin insert exhibits compressive residual stresses, already after 500 tool-workpiece contacts the compressive residual stresses were completely removed and tensile residual stresses of about 300 ± 80 MPa were observed. The highest tensile residual stresses of approximately 930 ± 230 MPa were found in a specimen with 1,000 tool-workpiece contacts. With increasing number of tool-workpiece contacts the tensile residual stress slightly decreases and at end of lifetime the insert exhibits tensile residual stress of about 400 MPa.
The lifetime in the current test setup is determined by wear damage. No pronounced combcracks were found in detailed SEM investigations including FIB cuts, neither in the coating nor in substrate material.

Acknowledgements

We thank Bernhard Sartory for his valuable technical assistance concerning the SEM investigations.
Financial support by Austrian Federal Government (in particular from Bundesministerium für Verkehr, Innovation und Technologie and Bundesministerium für Wirtschaft, Familie und Jugend) represented by Österreichische Forschungsförderungsgesellschaft mbH and the Styrian and the Tyrolean Provincial Government, represented by Steirische Wirtschaftsförderungsgesellschaft mbH and Standortagentur Tirol, within the framework of the COMET Funding Programme is gratefully acknowledged.

References

[1] V.P. Astakhov , Tribology of Metal Cutting, Tribology and Interface Engineering Series No. 52, 2006, Elsevier, London.

[2] H. Opitz, W. Lehewald, Untersuchungen über den Einsatz von Hartmetallen beim Fräsen, Forschungsberichte des Landes Nordrhein- Westfalen, Nr. 1146, 1963, Westdeutscher Verlag, Köln und Opladen.

[3] P.C. Pandey, S.M. Bhatia, H.S. Shan, “Thermo-Mechanical Failure of Cemented Carbide Tools in Intermittent Cutting“, Annals of the CIRP, 1979, vol. 28, pp.13-17.

[4] S.M. Bathia, P.C. Pandey, H.S. Shan, “Failure of Cemented Carbide Tools in Intermittent Cutting”, Precis. Eng., 1979, vol. 1, Issue 3, pp. 148-152.

[5] W. Schedler, Hartmetall für den Praktiker, Plansee Tizit, 1988, VDI, Düsseldorf.

[6] T. Teppernegg, T. Klünsner, C. Tritremmel, C. Czettl, J. Keckes, T. Wroblewski, R. Ebner, R. Pippan, “Spatial Correlation of Tensile Residual Stress and Thermal Fatigue Damage in Coated Cemented Carbide Milling Inserts”, Proceedings of the 18th Plansee Seminar, Reutte, 2013.

[7] A.C.A. Melo, J.C.G. Milan, M.B. da Silva, Á.R. Machado, “Some Observations on Wear and Damages in Cemented Carbide Tools”, J. Braz. Soc. Mech. Sci., 2006, vol. 28, pp. 269-277.

[8] I. Yellowley, G. Barrow, “The Influence of Thermal Cycling on Tool Life in Peripheral Milling”, Int. J. Mach. Tool D. R., 1976, vol. 16, Issue 1, pp. 1-12.

[9] C. Kirchlechner, K.J. Martinschitz, R. Daniel, C. Mitterer, J. Donges, A. Rothkirch, M. Klaus, C. Genzel, J. Keckes, “X-ray diffraction analysis of three-dimensional residual stress fields reveals origins of thermal fatigue in uncoated and coated steel”, Scripta Mater., 2010, vol. 62, pp. 774-777

[10] T. Wroblewski, O. Clauß, H.A. Crostack, A. Ertel, F. Fandrich, Ch. Genzel, K. Hradil, W. Ternes, E. Woldt, “A new difractometer for materials science and imaging at HASYLAB beamline G3”, Nucl. Instrum. Meth. A, 1999, vol. 428, pp. 570-582.

[11] T. Teppernegg, T. Klünsner, C. Tritremmel, P. Angerer, C. Czettl, J. Keckes, R. Ebner, R. Pippan, “Evolution of Residual Stress and Damage in Coated Hard Metal Milling Inserts over the Complete Tool Life”, Int. J. Refract. Met. H., 2014, submitted.

[12] ICDD Database Powder Diffraction File #00-051-0939.

[13] U. Welzel, J. Ligot, P. Lamparter, A.C. Vermeulen, E.J. Mittemeijer, “Stress Analysis of Polycrystalline Thin Films and Surface Regions by X-ray Diffraction”, J. Appl. Crystallogr., 2005, vol. 38, pp. 1-29.

[14] Bruker AXS, TOPAS V4. “General profile and structure analysis software for powder diffraction data”, 2005, Karlsruhe.

[15] D. Mari, A.D. Krawitz, J.W. Richardson, W. Benoit, “Residual stress in WC-Co measured by neutron diffraction”. Mat. Sc.i Eng. A-Struct., 1996, vol. 209, pp. 197-205.

[16] M. Nordin, R. Sundström, T.I. Selinder, S. Hogmark, “Wear and failure mechanisms of multilayered PVD TiN/TaN coated tools when milling austenitic stainless steel”, Surf. Coat. Tech., 2000, vol. 133-134, pp. 240-246.

[17] M. Lagerquist, “A Study of the Thermal Fatigue Crack Propagation in WC-Co Cemented Carbide”, Powder Metall., 1975, vol. 18, pp. 71-87.

[18] C.S.G. Ekemar, S.A.O. Iggström, G.K.A. Hedén, “Influence of some Metallurgical Parameters of Cemented Carbide on the Sensitivity to Thermal Fatigue Cracking at Cutting Edges”, Material for Metal Cutting, Proc. Conf. of BIRSA, Scarborough, 1970, pp. 133-142.

Publication III

Evolution of Residual Stress and Damage in Coated Hard Metal Milling Inserts Over the Complete Tool Life

T. Teppernegg[1], T. Klünsner[1], P. Angerer[1], C. Tritremmel[1], C. Czettl[2], J. Keckes[3], R. Ebner[1], R. Pippan[4]

[1] Materials Center Leoben Forschung GmbH, Roseggerstraße 12, 8700 Leoben, Austria

[2] CERATIZIT Austria GmbH, Metallwerk-Plansee-Straße 71, 6600 Reutte, Austria

[3] Department of Materials Physics, Montanuniversität Leoben, Jahnstraße 12, 8700 Leoben, Austria

[4] Erich Schmid Institute of Materials Science, Austrian Academy of Sciences, Jahnstrasse 12, 8700 Leoben, Austria

Abstract

In coated hard metal milling inserts the main damage mechanisms are thermal fatigue induced by interrupted tool-workpiece contact and wear. Dependent on the magnitudes of thermal and mechanical loads in two applied test setups, either wear or thermal fatigue in form of combcracks is induced. The evolution of residual stress and damage in the used milling inserts was documented over their complete lifetime. In a region of interest on the tool rake face a significant buildup of tensile residual stress was observed via a synchrotron based technique. A special preparation technique enabled position resolved measurements in this area by in-house X-ray diffraction facilities to study the evolution of residual stress over the entire tool lifetime. The onset of cracking was observed to happen in this region of interest by means of focused ion beam milling and scanning electron microscopy. The residual stress levels observed are comparable in used inserts at early stages of application, independent of the different cutting conditions and the applied characterization technique. At the end of tool life wear damage dominated inserts showed tensile residual stress, whereas thermal fatigue as the dominant damage mechanism resulted in compressive residual stresses.

Keywords: WC-Co; thermal fatigue; wear; X-ray diffraction; residual stress; milling tools

Introduction

The dominant damage mechanisms in milling processes are wear and thermal fatigue [1], the later induces characteristic cracks, that will be referred to as combcracks throughout this paper. Wear damage is generally induced by two mechanisms: One is adhesive wear, in which workpiece material sticks to the tool's rake and flank face during cutting and the other one is abrasive wear, where material is removed from the tool surface [2], [3]. Abrasive wear kinetics are highly increased when debris in form of hard metal and coating fragments are introduced by the shattering of exposed surface features such as combcrack flanks [1].

Combcracks appear in cutting tools after a certain number of load cycles with propagation planes perpendicular to the cutting edge of a milling insert. Some authors postulated that the temperature difference between heating upon cutting and cooling upon the idle period in a cutting cycle is the key factor influencing damage [1], [5]. They assumed that the cyclic thermo-shock fosters combcrack formation. During idle time, when high cooling rates are effective, tensile residual stresses are created upon surface material contraction [1], [5]. Opitz et al. [1] expected that these residual stresses are oriented parallel to the cutting edge and foster crack growth. Yellowley et al. [6] determined plastic deformation during cutting which is localized close to the cutting edge - this initiates nucleation and growth of combcracks [2]. Local plastic deformation at the tool edge is introduced by thermal stress amplitudes induced by frictional heating [6]. A combination of these thermal stresses and the sufficiently high load stresses can surpass the flow stress of a tool material at the present temperature. Upon cooling, these loads can trigger the buildup of tensile residual stress in the cutting edge of milling inserts. Cyclic mechanical loads in form of cyclic contact pressure between chip and tool may also introduce local plastic deformation close to the cutting edge [6]. Bathia et al. [7] described a combination of process parameters under which no tool failure induced by combcracks occurs in intermittent turning of mild steel plates due to subcritical thermal or mechanical tool loading. For this situation to occur, the feed rate and the cutting speed have to be lower than 0.1 mm/revolution and 1.5 m/s, respectively. The parameter intervals for the described process field of tool failure caused by cracks are also dependent on the radius of the tool's cutting edge. A milling insert with large cutting edge radius widens the process parameter field in which wear rather than fracture determines tool life [7].

Cyclic thermal shocks in coated steel discs and the resulting residual stresses were investigated by Kirchlechner et al. [8]. The position resolved measurements with high lateral resolution were enabled by using synchrotron based X-ray diffraction [9]. Teppernegg et al. [4] found a significant tensile residual stress buildup on the rake face of a used milling insert in a region of approximately 0.3 x 1.6 mm². In Fig. 64 the surface of milling insert's rake face

is shown. The dashed frame indicates the area of the position resolved residual stress measurements and the black frame represent the position of the mentioned region of tensile residual stress build up. This region will be referred to as region of interest (ROI). The center of this ROI was located about 0.4 mm from the cutting edge [4]. In previous work, tensile residual stress with a value of about 1000 MPa was detected in the WC phase of a used milling insert in a direction parallel to the horizontal and straight part of the cutting edge (see Fig.1) [4].

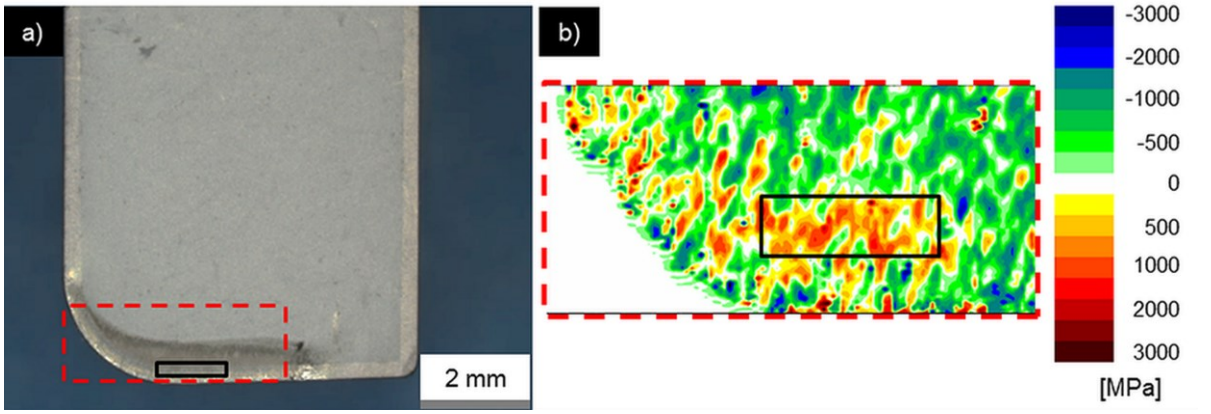

Fig. 64: Results of stress measurements via synchrotron X-ray radiation taken from [4]. Top view of the rake face of a used milling insert with 1000 tool-workpiece contacts. Dashed frame in a) indicates the area of residual stress measurement shown in b) that represents a position resolved map of residual stress acting in horizontal direction in the WC phase. Solid frame in b) indicates the area with detected significant tensile residual stress buildup [4]. For the interpretation of the stress colored scale bar we refer the reader to the online version of this article.

Currently, no data on the evolution of residual stresses in milling tools during the complete tool life is available in the open literature. In the present work, the evolution of residual stress in used milling inserts is compared during the complete tool life for two different test setups. In addition, the resulting damage states are compared. In one setup the main influence on tool lifetime is combcrack formation, in the other one wear damage is dominant. The results shall illustrate the interaction of residual stress and damage for the investigated milling test setup.

Experimental

Fig. 2 shows two different test setups for the milling experiments. In Fig.2a test setup A is shown, Fig.2b illustrates test setup B, also used in [4] and [10]. The following test setup parameters were the same in both test setups.

- Milling inserts geometry
- Single edge synchronous milling arrangement
- Cut workpiece material
- Cutting speed of 220 m/min
- Depth of cut of 4 mm
- No use of cooling agents such as lubricants or cold air
- Milling tool holder referred to as “miller” in Fig.2 with a diameter of 125 mm

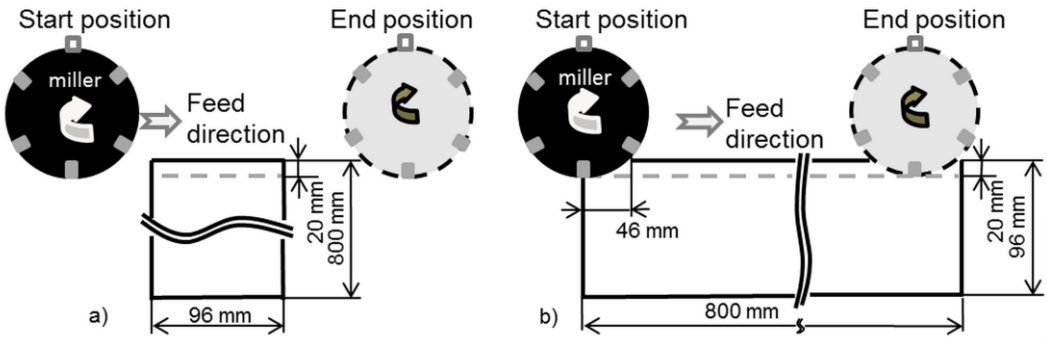

Fig. 2: Scheme of applied milling test setups with different cut segment lengths and feed rates of a) 96 mm and 0.5 mm/tooth referred to as test setup A and b) 800 mm and 0.4 mm/tooth referred to as test setup B [4], [10]. Only one of six cutting inserts in tool-workpiece contact.

All investigated milling inserts were made of WC - 8 wt.% Co hard metal with an average WC grain size of 1 µm. They were coated with a TiAlN-based film having a thickness of 8 µm, deposited by cathodic arc evaporation. The insert dimensions were 6.35 x 11.4 x 10 mm³, cutting edges were chamfered. The workpiece material was a 42CrMo4 steel in a normalized state with an upper yield strength of 400 N/mm², workpiece dimensions were 800 x 96 x 200 mm³. The milling tests in test setup A were stopped after accumulates tool-workpiece contact length (aTWCL) of 2.5, 36, 407.8, 611.7 m and at end of lifetime after 2 854.7 m. In test setup B the machining experiments were stopped after 10, 50, 500, 1000, 5 600, 9 600, 13 100, 17 700, 23 400, 26 200 and 37 400 tool-workpiece contacts. This corresponds to aTWCLs of 0.51, 2.57, 25.72, 51.44, 288.06, 493.82, 673.86, 910.49, 1 203.7, 1 347.73 and 1 923.86 m, more details regarding test setup B are given in [10].

The differences between test setup A and B are the start and end positions of the milling tool (see Fig.2), the cut segment length, and the feed rate per tooth. The cut segment length in test setup A was 96 mm and the applied feed rate was 0.5 mm/tooth. In test setup B the cut segment length of 800 mm and a feed rate of 0.4 mm/tooth were used. Due to the differences in the start and end position of the milling tool, the milling inserts in test setup A experienced non-constant tool-workpiece contact lengths at the beginning and at the end of

each cut segment. With increasing number of contacts, the tool-workpiece contact length (TWCL) increased from 0.47 mm at the first cut within one cut segment length to 51.44 mm after 92 cuts. Until TWCL reaches a constant value of 51.44 mm after 92 cuts, the insert aTWCL of 2.5 m under non-constant cutting conditions. The milling inserts used in test setup B cut the entire cut segment lengths under constant cutting conditions with constant TWCL because the beginning and the end of the segment are removed by a dummy tool.

The residual stress state in the ROI (see Fig.1a) was determined in the direction parallel to the straight portion of the cutting edge in the WC phase of the hard metal. The values of residual stress were acquired in a depth region ranging from the interface between coating and WC-Co substrate and ~ 5 µm below this interface. The residual stress states of all milling inserts were measured by a D8 Discover X-ray diffractometer (Bruker AXS, Germany) in parallel beam geometry (40 kV, 35 mA, Cu Kα radiation). The diffractometer was equipped with a Sol-X energy dispersive detector, an open (90°) Eulerian cradle and a polycapillary collimator. The areas outside of the ROI were covered with a brass foil, see Fig.3. The diffraction maximum (211) of the hexagonal WC phase at 117.3° 2θ was selected for the subsequent stress determination [11]. Brass was chosen as a cover material to avoid the overlap of the diffraction peak (211) originating from the WC phase in the sample and the cover material.

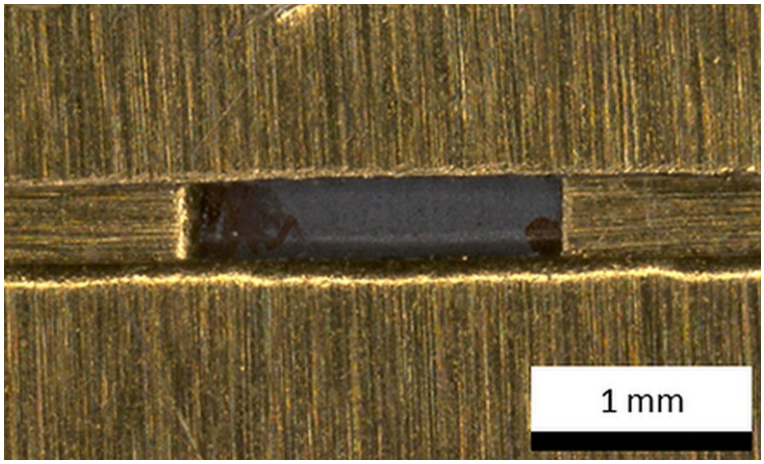

Fig.3: Stereomicroscopic image of a milling insert's rake face prepared for residual stress measurement in the region of interest (ROI). The rectangular area in the center of the image represents the ROI, the other areas correspond to areas outside of the ROI covered by a brass foil.

Preliminary experiments showed that for the determination of the stress component parallel to the straight portion of the milling insert's cutting edge it is favourable to choose a diffraction geometry with incident and diffracted beam parallel to this direction. These beams penetrate the WC phase parallel to the long axis of the uncovered ROI to minimize shadowing effects caused by the covering brass foil. Otherwise, the shadowed fraction of the

rectangular ROI with a long axis a and a short axis b would be larger by a factor of five at the same incidence angle θ if symmetric incident and diffracted beam are assumed and no sample tilt is considered (ψ = 0). The effect would be larger at tilted samples (ψ > 0). Consequently, for the determination of the stress component parallel to the straight portion of the cutting edge, the ω-method was selected [12]. For the stress determination, diffraction intensity was recorded in a diffraction angle range 2θ from 114.6 to 119.1° and sample tilt angle ψ up to 35°. For the determination of the diffraction angle of the measured peaks the TOPAS 4.2 Software [13] by Bruker AXS, Germany, was used. In each sample the residual stress component parallel to the sample surface and parallel to the straight portion of the cutting edge was then deduced from the slope determined by linear regression in the $\sin^2\psi$ plot according to the formalism described in [14].

The rake face surface topography was investigated by scanning electron microscopy (SEM, crossbeam field emission gun, Zeiss Auriga). The chemical composition of the surface was investigated by X-ray spectroscopy (EDX) with an EDAX Apollo 40+ detector. Cross sections of selected milling inserts of test setup A with aTWCLs of about 407.8, 611.7 and 2854.7 m (end of lifetime) were prepared by means of the focused ion beam technique (FIB, Orsay Physics Cobra Z-05 FIB extension) to document the damage state after application.

Results and Discussion

Residual stress evolution

The evolution of residual stress over the complete tool life of milling inserts tested by test setup A and B is illustrated in Fig.4. Compressive residual stresses of 850 ± 270 MPa were found in the ROI of the virgin milling insert. These results correspond well with the synchrotron residual stress measurements with values of about -600 MPa in the ROI as presented in [4] and the results with values of -500 MPa in neutron diffraction experiments of uncoated hard metal specimens given in [15]. They are comparable due to a similar penetration depth of the synchrotron and the X-ray diffraction experiments. The use of 10 keV accelerating voltage in the synchrotron measurements results in a penetration depth of about 1.3 µm in the substrate. In the laboratory diffractometer an X-ray wavelength of 1.54 Å (corresponding to an energy of 8 keV) was used, which corresponds to a penetration depth of about 1.7 µm. The data refer to the mean penetration depth up to which a fraction of (e - 1) / e = 63 % of the incident radiation is absorbed. Furthermore, the variation of the absorption coefficient in the WC phase as a function of the applied wavelength as well as the incident angle in each specific diffraction experimental setting have been taken into consideration [16].

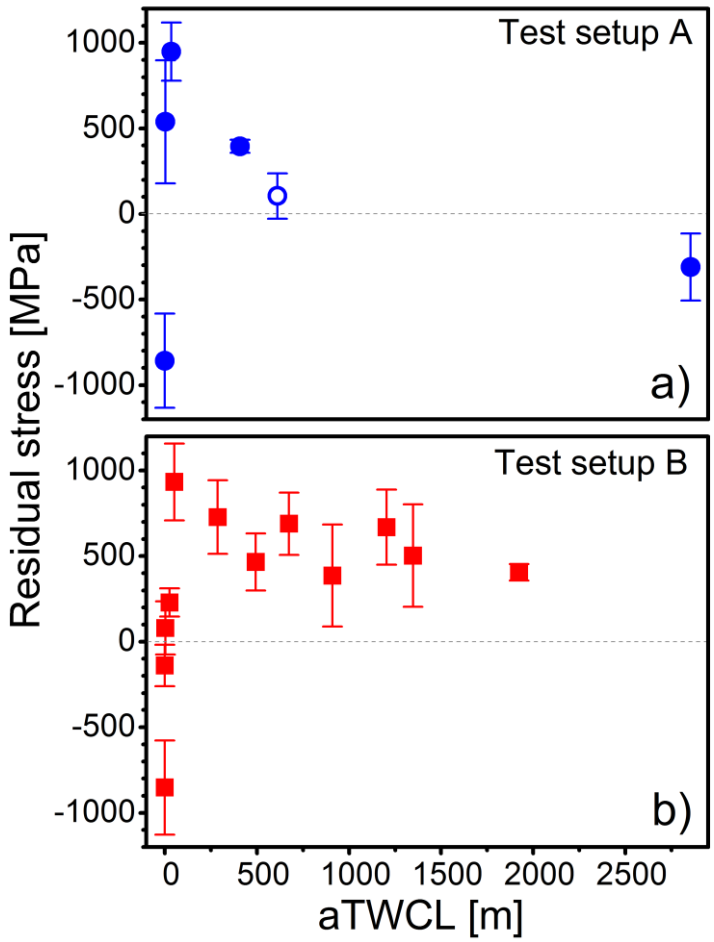

Fig. 4: Residual stress determined on the rake faces of milling inserts tested in a) test setup A and b) test setup B [10] plotted as a function of accumulated tool-workpiece contact length (aTWCL). Open circle in a) represents specimen with first observed combcrack. The data were determined locally in a small region of interest (ROI) close to the cutting edge by a "cover method" involving X-ray diffraction with a laboratory X-ray source as described in the experimental section.

At very early stages of application, the residual stress evolution in the milling inserts is comparable for both test setups. The detected compressive residual stresses in the virgin insert are reduced after a few meters of aTWCL in both test setups. The insert tested in test setup A, with 2.4 m of aTWCL already showed tensile residual stresses of 540 ± 360 MPa (see Fig.4a). After 1000 tool-workpiece contacts, which correspond to an aTWCL of 36 m in test setup A and 51.4 m in test setup B, the highest tensile residual stresses of about 930 ± 230 MPa and 950 ± 170 MPa [10] were found. Both measured values correspond well with the results of synchrotron measurements published in [4]. Until about 500 m of aTWCL the residual stresses are comparable in inserts tested in both test setups. After 611 m of aTWCL, the first combcrack appears in the ROI of an insert tested in test setup A (see open circle in Fig.4a). The tensile residual stresses found in this specimen decrease significantly to about 100 MPa from a plateau value of about 500 MPa, found in inserts of comparable aTWCL in

test setup B. At the end of lifetime, the residual stress state in the inserts tested in the two test setups is considerably different. Compressive residual stresses of 310 ± 190 MPa were observed in inserts tested in test setup A, in which thermal fatigue dominantly determines lifetime. In contrast, a plateau of tensile residual stresses of about 500 MPa is present until the end of lifetime in the inserts from test setup B, in which wear damage dominates (details in [10]. The absence of a significant drop in the detected tensile residual stresses in Fig.4b) indicates the absence of combcracks in inserts in the late phase of tool life.

When combcracks form on milling insert surfaces, tensile residual stresses relax around their crack flanks and reduce the driving force for nucleation and growth of new cracks in their vicinity [17]. Therefore, combrack density reaches a constant value after a certain number of load cycles [5]. This saturation value and the number of cuts after which it is reached are influenced by the cutting parameters [18].

Damage state

To document surface topography and damage state of the rake faces of selected milling inserts SEM images were acquired from inserts tested in test setup A with an aTWCL of 407.8, 611.7 and 2 854.7 m. The corresponding SEM images are illustrated in Fig.5a-c. Additionally, Fig.5a shows the surface topography of an insert close to its end of lifetime with an aTWCL of 1923.86 m tested in test setup B. Black arrows in these overview images indicate the positions of FIB cross sections, placed within the ROI at the position of the most prominent combcrack, illustrated in Fig.5b. This position coincides with the position of the significant buildup of tensile residual stress, documented in [4]. A platinum layer was deposited on the specimens prior to FIB cutting to produce smooth FIB cross sections. This platinum layer appears as a bright film on top of the darker workpiece material and hard coating.

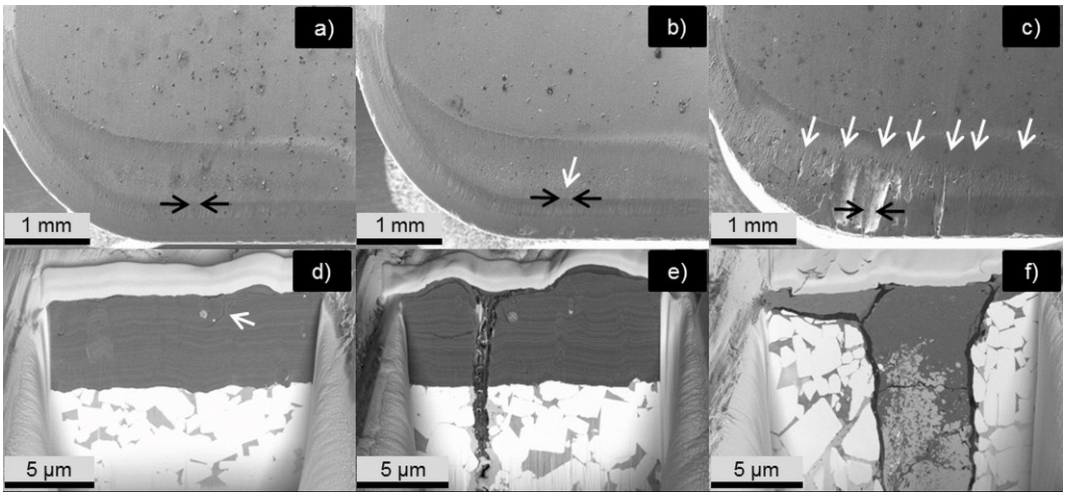

Fig.5: SEM micrographs showing the surface topography of the rake faces of milling inserts tested in test setup A after different accumulated tool-workpiece contact lengths of a) 407.8, b) 611.7 and c) 2854.7 m. Black arrows in a), b) and c) indicate the positions of FIB cross sections shown in d), e) and f). White arrows mark b) and c) the positions of combcracks, d) a crack close to a metallic droplet typical for arced PVD coatings. Bright layers on top of cross sections represent protective platinum layers.

At early stages of application wear dominates the damage of the milling inserts. The FIB cross section of the insert with an aTWCL of 407.8 m shows cracks close to a droplet, marked by a white arrow in Fig.5d. Droplets are micrometre-sized coating defects and are typical for arc evaporated coatings [19]. The cracks which appear around droplets were most likely created upon tool loading. Tkadletz et al. [20] found a similar damage pattern in an arc evaporated TiAlTaN coating after a ball on disc test. The first combcrack appeared in an insert with an aTWCL of 611.7 m, see white arrow in Fig.5b and e. Upon its discovery the combcrack had already penetrated coating and hard metal substrate. Its width was about 1 µm at the surface and its length greater than 15 µm, see FIB cross section in Fig.5e. With increasing aTWCL the number of combcracks increased and at the end of lifetime the insert showed seven combcracks, illustrated in Fig.5c. Additionally, the coating was partially removed from the surface in an area of about 500 x 500 µm² (see Fig.5c) and cracks with growth planes parallel to the cutting edge were found. By the application of EDX in the FIB cross section seen in Fig.5f, the dark layer above the hard metal substrate was identified as workpiece material. EDX measurements showed that the combcrack itself was filled with workpiece material and tungsten carbide fragments. Both crack flanks and edges were shattered. The crack opening measured at the surface was approximately 6 µm.

In contrast, the insert tested in test setup B showed no combcracks at its end of lifetime, see Fig.6 [10]. Adhesive and abrasive wear dominates the tool lifetime, details described in [10]. Wear grooves were detected at the rake face surface that were filled with workpiece

material, see Fig.6b. Within this workpiece material in the wear groove, small cracks were observed, which started at the surface and stopped at the workpiece material/coating interface, detailed described in [10].

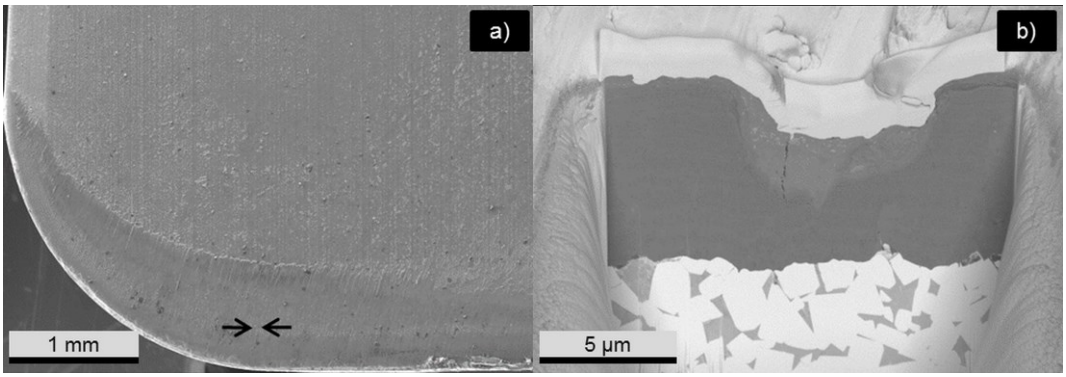

Fig.6: SEM micrographs showing the surface topography of the rake face of an insert at end of lifetime tested in test setup B [10]. Black arrows in a) indicate the position of a FIB cross section shown in b). Bright layer on top of dark coating material represents protective platinum layer.

Even though the cutting parameters applied in test setup B were more severe than in cutting applications in which wear was the dominant damage mechanism [7], wear rather than thermal fatigue determines tool lifetime. This situation is only described for moderate cutting parameters [7] or for reduced acting temperature amplitudes achieved by heating the used inserts during application [1]. Many authors describe damage situations comparable to the one observed in test setup A, independent from the cutting parameters feed rate, cutting speed and cutting depth [1],[5],[18]. The parameter intervals for the described process parameter field of tool failure due to cracking are also dependent on the radius of the cutting edge [7]. A large cutting edge radius widens the process parameter field in which wear before fracture occurs [7] and influences the tool tip loading situation [21]. In contrast to the test setup described in [7], test setup B includes coated cutting inserts with chamfered cutting edges. As to be expected, blunting and chamfering of the cutting edge seem to enlarge the process parameter field in which tool failure is induced rather by wear instead of combcracks.

Temperature amplitudes acting in milling processes are crucial to the nucleation and propagation of combcracks [1]. The thermal shock that occurs when the milling tool moves from the segment end to start position within about 3 s is more severe than in the short idle periods of 96 ms between tool-workpiece contacts within a cut segment. In test setup A the milling tool moved about 300 times between segment end and start position, in test setup B only 20 times. The exact thermal load situation of the tool including heating and cooling rates and amplitudes is currently under investigation via finite element simulation studies.

Conclusions

The aim of the present work is to illustrate the evolution of residual stress and damage in coated hard metal milling inserts over their complete lifetime for two different setups of a milling application. In earlier work information on the location of a significant buildup of tensile residual stress on the tool's rake face was acquired using synchrotron facilities. A special cover method facilitates the position resolved residual stress measurement in the area of interest via X-ray diffraction using in-house X-ray sources.

In their virgin state milling inserts exhibit a compressive residual stress state. Already after 1000 tool-workpiece contacts tensile residual stresses of about 1000 MPa are observed in inserts from both investigated test setups. In one of the two setups thermal fatigue loads triggered the formation of combcracks that dominantly determined tool lifetime. Upon the appearance of the first combcrack the detected tensile residual stresses decreased significantly. Detailed SEM investigations including FIB cuts revealed that with increasing accumulated tool-workpiece contact length the number and the opening of combcracks increased. In contrast, tool life in the second test setup was determined by wear damage and a plateau of tensile residual stress was present until the end of lifetime. The measured residual stress values at early stages of application were comparable with corresponding values found by synchrotron facilities in earlier work.

The current investigation indicates that the amplitudes of thermal loads and the magnitude of thermal shocks have a major influence of the evolution of residual stress and damage in coated hard metal milling inserts.

Acknowledgements

We thank Uwe Ossberger for fruitful discussions.

Financial support by Austrian Federal Government (in particular from Bundesministerium für Verkehr, Innovation und Technologie and Bundesministerium für Wirtschaft, Familie und Jugend) represented by Österreichische Forschungsförderungsgesellschaft mbH and the Styrian and the Tyrolean Provincial Government, represented by Steirische Wirtschaftsförderungsgesellschaft mbH and Standortagentur Tirol, within the framework of the COMET Funding Programme is gratefully acknowledged.

References

[1] Opitz H, Lehewald W. Untersuchungen über den Einsatz von Hartmetallen beim Fräsen. Forschungsberichte des Landes Nordrhein-Westfalen Nr. 1146. Köln und Opladen: Westdeutscher Verlag; 1963.

[2] Pandey PC, Bhatia SM, Shan HS. Thermo-Mechanical Failure of Cemented Carbide Tools in Intermittent Cutting. CIRP Annals 1979; 28: 13-17.

[3] Schedler W. Hartmetall für den Praktiker. Düsseldorf: Plansee Tizit VDI; 1988.

[4] Teppernegg T, Klünsner T, Tritremmel C, Czettl C, Keckes J, Wroblewski T, Ebner R, Pippan R. Spatial Correlation of Tensile Residual Stress and Thermal Fatigue Damage in Coated Cemented Carbide Milling Inserts. Reutte: Conference proceedings of the 18th Plansee Seminar; 2013. HM 47.

[5] Ekemar CSG, Iggström SAO, Hedén GKA. Influence of some Metallurgical Parameters of Cemented Carbide on the Sensitivity to Thermal Fatigue Cracking at Cutting Edges. Material for Metal Cutting. Scarborough: Conference proceedings of BIRSA; 1970. 133-142.

[6] Yellowley I, Barrow G. The Influence of Thermal Cycling on Tool Life in Peripheral Milling. Int J Mach Tool D R 1976; 16 Issue 1: 1-12. doi:10.1016/0020-7357(76)90009-3.

[7] Bathia SM, Pandey PC, Shan HS. Failure of Cemented Carbide Tools in Intermittent Cutting. Precis Eng 1979; 1 Issue 3: 148-152. doi:10.1016/0141-6359(79)90041-2.

[8] Kirchlechner C, Martinschitz KJ, Daniel R, Mitterer C, Donges J, Rothkirch A, Klaus M, Genzel C, Keckes J. X-ray diffraction analysis of three-dimensional residual stress fields reveals origins of thermal fatigue in uncoated and coated steel. Scripta Mater 2010; 62: 774-777. doi:10.1016/j.scriptamat.2010.02.006.

[9] Wroblewski T, Clauß O, Crostack HA, Ertel A, Fandrich F, Genzel Ch, Hradil K, Ternes W, Woldt E. A new difractometer for materials science and imaging at HASYLAB beamline G3. Nucl Instrum Meth A 1999; 428: 570-582. doi:10.1016/S0168-9002(99)00144-8.

[10] Teppernegg T, Klünsner T, Tritremmel C, Angerer P, Czettl C, Keckes J, Ebner R, Pippan R. Residual Stress and Damage in Coated Hardmetal Milling Inserts. Orlando: Conference proceedings - Tungsten, Refractory & Hardmaterials VIII; 2014.

[11] ICDD Database Powder Diffraction File #00-051-0939

[12] Welzel U, Ligot J, Lamparter P, Vermeulen AC, Mittemeijer EJ. Stress Analysis of Polycrystalline Thin Films and Surface Regions by X-ray Diffraction. J Appl Crystallogr 2005; 38: 1-29. doi:10.1107/S0021889804029516.

[13] Bruker AXS. TOPAS V4. General profile and structure analysis software for powder diffraction data. Karlsruhe: 2005.

[14] Spieß L, Schwarzer R, Behnken H, Teichert G. Moderne Röntgenbeugung. Wiesbaden: Teubner; 2005

[15] Mari D, Krawitz AD, Richardson JW, Benoit W. Residual stress in WC-Co measured by neutron diffraction. Mat Sci Eng A-Struct 1996; 209: 197-205. doi:10.1016/0921-5093(95)10147-0.

[16] Angerer P, Strobl S. Equi-Penetration Grazing Incidence X-Ray Diffraction Method (EP-GIXD) – Stress Depth Profiling of Ground Silicon Nitride. Acta Mater. (accepted)

[17] Raninger P, Ecker W, Antretter T, Leindl M, Ebner R. Interaction of heat checks in aluminum pressure casting dies and their effect on fatigue life. Key Eng Mat 2012; 488-489: 626-629. doi: 10.4028/www.scientific.net/KEM.488-489.626.

[18] Lagerquist M. A Study of the Thermal Fatigue Crack Propagation in WC-Co Cemented Carbide. Powder Metall 1975; 18: 71-87.

[19] Rother B, Vetter J, Plasmabeschichtungsverfahren und Hartstoffschichten. Leipzig: Deutscher Verlag für Grundstoffindustrie; 1992

[20] Tkadletz M, Mitterer C, Sartory B, Letofsky-Papst I, Czettl C, Michotte C. The effect of droplets in arc evaporated TiAlTaN hard coatings on the wear behaviour. Surf Coat Tech. 2014; doi:10.1016/j.surfcoat.2014.01.010.

[21] Bouzakis K D, Michailidis N, Vidakis N, Efstathiou K, Leyendecker T, Erkens G, Wenke R, Fuss H G. Optimization of the cutting edge radius of PVD coated inserts in milling considering film fatigue failure mechanism. Surf Coat Tech 2000; 133-134: 501-507. doi:10.1016/S0257-8972(00)00971-3.

Publication IV

Residual Stress and Damage in Post - Treated Coated Milling inserts

T. Teppernegg[1], T. Klünsner[1], C. Tritremmel[1], P. Angerer[1], C. Czettl[2], R. Ebner[1]

[1] Materials Center Leoben Forschung GmbH, Roseggerstraße 12, A-8700 Leoben, Austria
[2] CERATIZIT Austria GmbH, Metallwerk-Plansee-Straße 71, A-6600 Reutte, Austria

Abstract

Post-treatment of coated hardmetal milling tools can enhance their application properties. Local plastic deformation during cutting can lead to tensile residual stress build-up close to the cutting edge where damage in form of comb cracks can be triggered. This work examines the influence of post-treatment with different durations on the emergence of residual stress and its influence on tool life. The residual stress state was determined with high lateral resolution in the WC phase of differently post-treated inserts in the virgin state and after 1000 cuts via an in-house X-ray diffraction method. To document their damage state the milling inserts were investigated by scanning electron microscopy.

Introduction

In milling processes there are two main damage mechanisms influencing tool lifetime, which are wear and thermal fatigue [1]. The characteristic cracks that form show propagation planes perpendicular to the cutting edge and will be referred to as comb cracks throughout this paper [2]. Their nucleation requires a sufficiently high temperature difference between heating upon cutting and cooling upon idle time [3]. The use of cooling lubricants aggravates thermal shocks acting in the milling tools and therefore fosters comb crack formation, whereas the use of heated inserts does supress comb crack initiation [3]. A combination of thermal stresses induced by frictional heating [4] and mechanical loads in form of cyclic contact pressure between chip and tool surface can surpass the flow strength of the tool material at the cutting edge temperature [5]. This leads to local plastic deformation close to the cutting edge, which in turn triggers a tensile residual stress buildup in the cutting edge [5]. Opitz et al. expected that the direction of these tensile residual stresses induced in cutting processes are oriented in a direction parallel to the cutting edge [3]. These tensile residual stresses were detected experimentally, localized in an area of about 0.3 x 1.6 mm² on the rake face of a used milling insert [6], which is hence referred to as region of interest (ROI) and is illustrated in Fig.1a). The residual stress measurements performed with high

lateral resolution in the WC phase were done via a synchrotron based X-ray diffraction technique [7]. The black frame in Fig.1a) represents the position of the mentioned ROI [6]. The residual stresses parallel to the cutting edge in used milling inserts during their complete tool life in this ROI were determined via a cover method in earlier work, see Fig.1b) [8]. After 36 m of accumulated tool-workpiece contact length (aTWCL) a peak in tensile residual stress of about 1000 MPa was found [8].

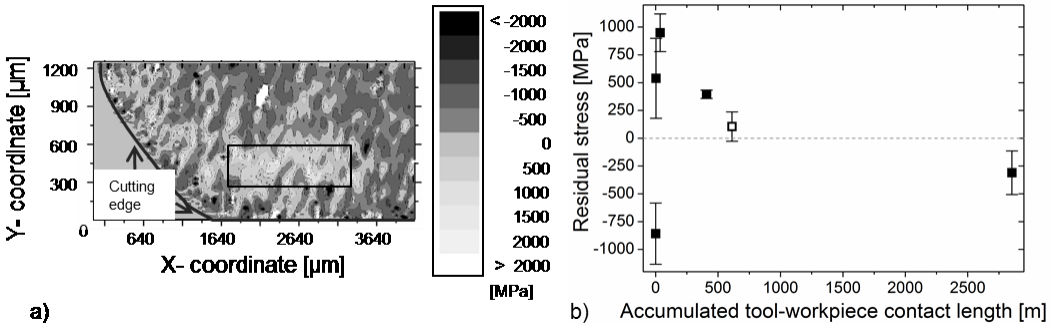

Fig.1: a) Position resolved residual stress map with high lateral resolution of the rake face of a used milling insert with 1000 tool-workpiece contacts. Black frame in a) indicates area with significant tensile residual stress buildup referred to as region of interest (ROI) [6], b) residual stress evolution of used milling inserts over their complete lifetime [8].

Blasting processes as post-treatment for coated hardmetal cutting inserts can induce compressive residual stresses in e.g. CVD (chemical vapor deposition) coatings and the WC phase of the hardmetal substrate [9]. These compressive residual stresses lead to increased tool lifetime [9]. Currently, no data on the influence of different post-treatment parameters on the residual stress evolution in used milling inserts is available in the open literature.

Experimental

Fig.2 illustrates the single edge synchronous face milling arrangement, in which inserts with dimensions of 6.35 x 11.4 x 10 mm³, having a chamfered cutting edge, were tested. The milling tests were carried out in the same way as described in more detail in [8]. The inserts were made of WC - 8 wt.% Co hardmetal with an average WC grain size of 1 µm. All investigated inserts were coated with a TiAlN-based film with a thickness of 8 µm deposited by arc evaporation.

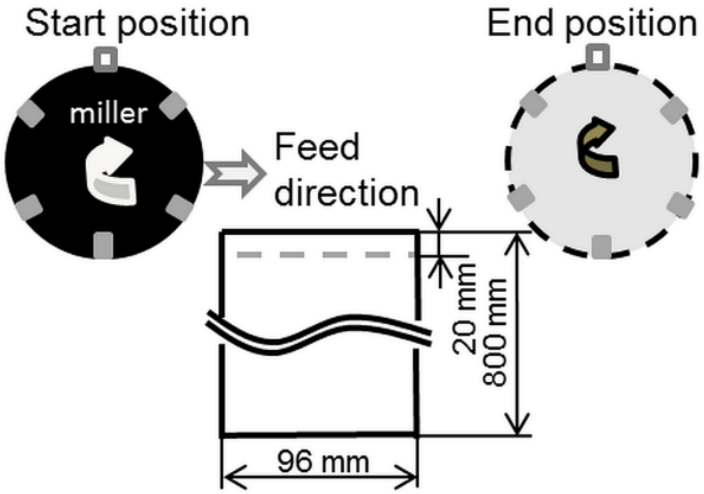

Fig.2: Scheme of applied milling test setup, as also used in [8].

The investigated milling inserts were post-treated via a dry blasting process. An injector blasting plant was applied using spherical particles composed of zirconia, silica and alumina with grain sizes ranging from 125 µm to 250 µm. The applied blasting pressure was 3 bar. Three different blasting times were chosen. After 168, 252 and 336 seconds the blasting process was stopped.

A 42CrMo4 steel in normalized state with an upper yield strength of 400 N/mm² and dimensions of 800 x 96 x 200 mm³ was used as workpiece material. The performed experiments were carried out without lubricant or cold air cooling. The cutting speed was 220 m/min, the milling tool holder referred to as “miller” exhibited a diameter of 125 mm and the applied feed rate was 0.5 mm per tooth. At the beginning and the end of one cut segment length of 96 mm the tool-workpiece contact length is not constant. With increasing number of contacts, the tool-workpiece contact length (TWCL) increased from 0.47 mm at the first cut within one cut segment length to 51.44 mm after 92 cuts. Until TWCL reaches a constant value of 51.44 mm after 92 cuts, the insert’s accumulated tool-workpiece contact length (aTWCL) was 2.5 m under non-constant cutting conditions at each beginning and end of a cut segment length. The milling tests were stopped after an aTWCL of 36.00, 407.81, 815.60, 1631.25, 1631.28, 2039.10, 2446.90 m and at end of lifetime.

The residual stress state was determined in the tungsten carbide phase within the ROI in inserts in a virgin state (value of aTWCL = zero) and after 36 m of aTWCL. The investigated direction of residual stress was parallel to the straight portion of the cutting edge, more details described in [8]. In addition, the residual stress state of a non-blasted virgin insert was determined to be compared with results from blasted inserts. The information on residual stress was acquired via a D8 Discover X-ray diffractometer (Bruker AXS, Germany) in parallel beam geometry (40 kV, 35mA, Cu Kα radiation) in a depth region ranging from the

interface between coating and WC-Co substrate and approximately 1.7 µm below this interface. The areas outside of the ROI were covered by brass foil to collect information on the residual stress state from the ROI only, see Fig.3.

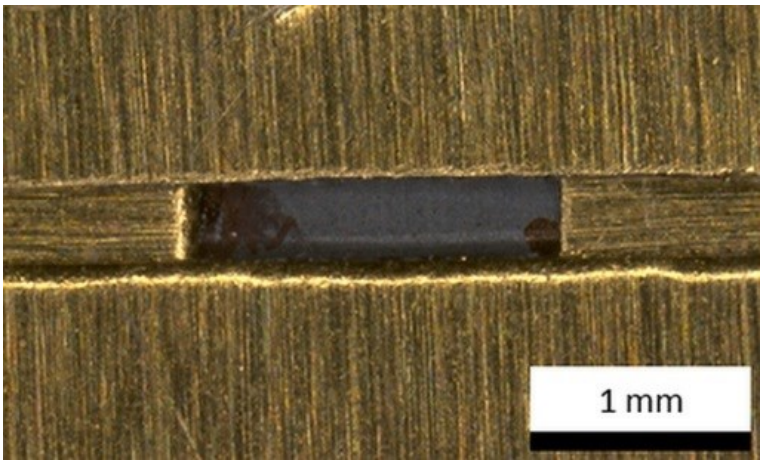

Fig.3: Rake face of used milling insert - areas outside of ROI are covered by brass foil [8].

The (211) diffraction peak of the hexagonal WC phase at 117.3° 2θ was selected for the subsequent stress determination [10] and therefore brass was chosen as cover material to avoid the overlap of the peak. The ω-method [11] was applied for stress determination; the diffraction intensity was recorded in a diffraction angle 2θ range from 114.6 to 119.1° and sample tilt angle ψ up to 35°. In each sample the residual stress component parallel to the sample surface and parallel to the straight portion of the cutting edge was then deduced from the slope determined by linear regression in the $\sin^2\psi$ plot according to the formalism described by Welzel in [12]. No stress components perpendicular to the sample surface were considered. The rake and flank face surface topography of all used milling inserts was investigated by scanning electron microscopy (SEM, Zeiss Auriga with Crossbeam field emission gun).

Results and discussion:

Residual stress measurements

The residual stress state of inserts with aTWCL values of zero (virgin) and 36 m are illustrated as a function of dry blasting time in Fig.4. The residual stress state of an insert after coating deposition without blasting post-treatment is included in Fig.4.

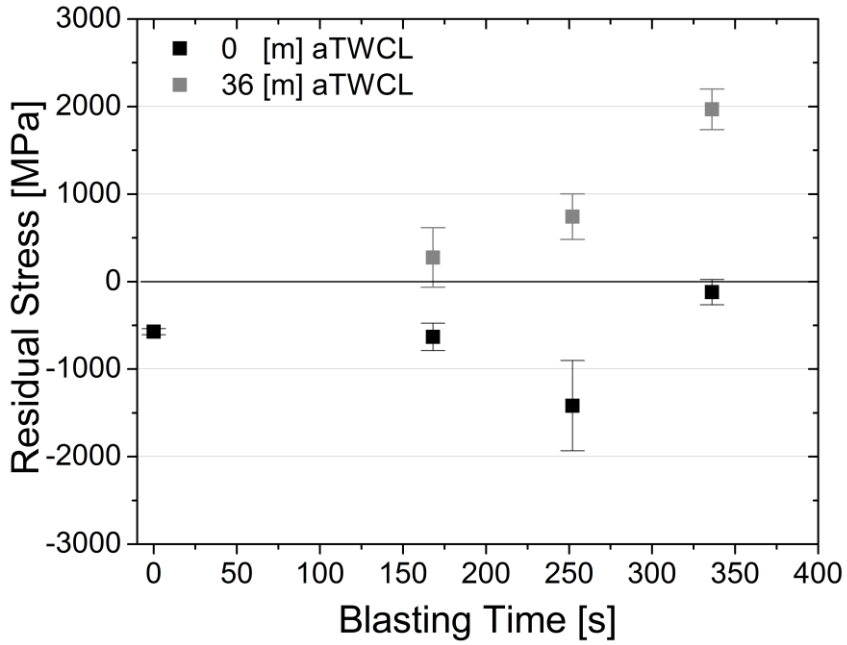

Fig.4: Residual stress data plotted as function of dry blasting time: Black squares indicate the residual stress values measured in the ROI of inserts after post-treatment without any tool-workpiece contacts. Grey squares represent results from used inserts with 36 m of accumulated tool-workpiece contact length (aTWCL).

After coating deposition and before post-treatment via blasting the WC phase in the ROI exhibits compressive residual stresses of about -570 MPa. All inserts with blasting times greater than zero in the virgin state show compressive residual stresses. The observed values of residual stress have no clear relation with the dry blasting time: A value of residual stress of -600 MPa being very similar to the one from the non-blasted insert was observed in the virgin insert with the lowest dry blasting time of 168 s. After 252 s of dry blasting, the observed compressive residual stress reaches a value of about -1000 MPa. The insert with 336 s of dry blasting time exhibits a compressive residual stress value of about -130 MPa.

After 36 m of aTWCL all inserts show a change in their residual stress state - all specimens exhibit tensile residual stresses. This tendency was also observed in earlier work [8], compare Fig.1b). With increasing blasting time the determined tensile residual stresses in the inserts increase from 300 MPa to 1900 MPa. It seems that short blasting times decelerate the build-up of tensile residual stresses after a certain number of tool-workpiece contacts compared to longer blasting times.

Damage state

Fig.5 shows the number of comb cracks observed in the SEM as function of aTWCL. The first comb crack was visible in all inserts after 407 m of aTWCL independent of blasting time. In

inserts which were blasted for 252 s and 336 s, the number of comb cracks increased with increasing aTWCL. In contrast, the insert with the lowest blasting time developed its second comb crack only after 815 m aTWCL.

The blasting duration had no significant influence on the lifetime. All inserts reached their end of lifetime after 2446 m aTWCL. At end of lifetime, the insert which was blasted for 168 s had seven comb cracks. The insert, which was blasted for 252 s, did exhibit five comb cracks and the insert, which was blasted for 336 s, possessed six comb cracks at the end of lifetime.

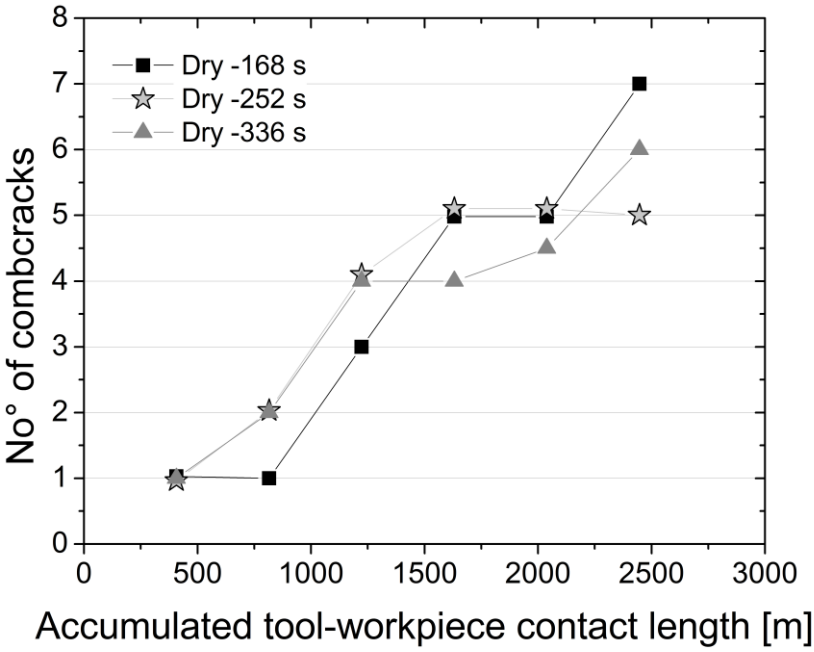

Fig.5: Detected number of comb cracks as function of the accumulated tool-workpiece contact length (aTWCL). The different symbols indicate the inserts with different dry blasting time.

A SEM surface micrograph of a milling insert blasted for 168 s is shown in Fig.6 with the positions of comb cracks indicated by white arrows. In industrial practice, the end of lifetime is defined not by the comb cracks but the appearance of a kind of crack that runs parallel to the cutting edge. It connects several comb cracks and therefore it increases the danger of cutting edge breakage significantly. The position of this crack is indicated by black arrows in Fig.6. This kind of crack appears very close to the end of lifetime and is induced by pure mechanical fatigue as documented by its observation also in heated cutting inserts by other authors [3].

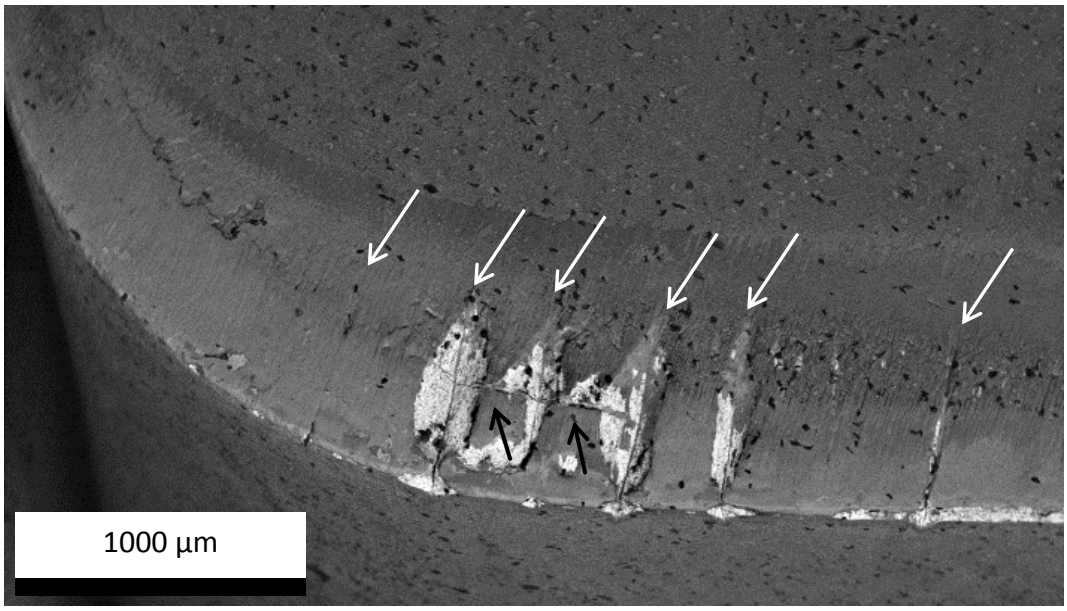

Fig.6: SEM surface micrograph of a milling insert's rake face with a dry blasting time of 168 s at its end of lifetime. White arrows indicate the positions of comb cracks. Black arrows indicate a crack that runs parallel to the cutting edge connecting three comb cracks. The appearance of this kind of crack determines the end of lifetime because of the increased danger of breakage of the insert.

Conclusions and Outlook

The residual stress state in hardmetal milling inserts coated with TiAlN-based films was successfully characterized via an in-house X-ray diffraction technique including a special covering method for enhanced lateral resolution. Inserts which were post-treated via dry blasting with different blasting time were investigated in the virgin state and after milling of 36 m of accumulated tool-workpiece contact length (aTWCL). The inserts in the virgin state exhibit compressive residual stress values from -130 MPa to -1000 MPa. No clear relation was found between the value of residual stress in the inserts after deposition and dry blasting and the applied dry blasting time. After the use of the inserts for 36 m of aTWCL all inserts showed tensile residual stresses with values between 300 MPa and 1900 MPa. All inserts reached their end of lifetime after 2446 m of aTWCL.

The blasting time had no significant influence on the evolution of tensile residual stresses after 36 m of aTWCL, the creation of comb cracks and consequently on end of lifetime. The influence of the variation of blasting pressure on the residual stress state in hard coating and hardmetal substrate may be significant to tool lifetime and deserves attention in future research activities.

Acknowledgements:

Financial support by the Austrian Federal Government (in particular from Bundesministerium für Verkehr, Innovation und Technologie and Bundesministerium für Wirtschaft, Familie und Jugend) represented by Österreichische Forschungsförderungsgesellschaft mbH and the Styrian and the Tyrolean Provincial Government, represented by Steirische Wirtschaftsförderungsgesellschaft mbH and Standortagentur Tirol, within the framework of the COMET Funding Programme is gratefully acknowledged.

References:

[1] W. Schedler, „Hartmetall für den Praktiker, Plansee Tizit“, VDI, Düsseldorf, (1988)

[2] C.S.G. Ekemar, S.A.O. Iggström, G.K.A. Hedén, “Influence of some Metallurgical Parameters of Cemented Carbide on the Sensitivity to Thermal Fatigue Cracking at Cutting Edges”, Material for Metal Cutting, Proc. Conf. of BIRSA, Scarborough, pp. 133-142, (1970)

[3] H. Opitz, W. Lehewald, „Untersuchungen über den Einsatz von Hartmetallen beim Fräsen“, Forschungsberichte des Landes Nordrhein-Westfalen, Nr. 1146, Westdeutscher Verlag, Köln und Opladen, (1963)

[4] V.P. Astakhov, “Tribology of Metal Cutting”, Tribology and Interface Engineering Series No. 52, Elsevier, London, (2006)

[5] I. Yellowley, G. Barrow, “The Influence of Thermal Cycling on Tool Life in Peripheral Milling”, Int. J. Mach. Tool D. R., vol. 16, Issue 1, pp. 1-12, (1976)

[6] T. Teppernegg, T. Klünsner, C. Tritremmel, C. Czettl, J. Keckes, T. Wroblewski, R. Ebner, R. Pippan, “Spatial Correlation of Tensile Residual Stress and Thermal Fatigue Damage in Coated Cemented Carbide Milling Inserts”, Proceedings of the 18th Plansee Seminar, Reutte, HM47, (2013)

[7] T. Wroblewski, O. Clauß, H.A. Crostack, A. Ertel, F. Fandrich, Ch. Genzel, K. Hradil, W. Ternes, E. Woldt, “A new difractometer for materials science and imaging at HASYLAB beamline G3”, Nucl. Instrum. Meth. A, vol. 428, pp. 570-582, (1999)

[8] T. Teppernegg, T. Klünsner, C. Tritremmel, P. Angerer, C. Czettl, J. Keckes, R. Ebner, R. Pippan, “Evolution of Residual Stress and Damage in Coated Hard Metal Milling Inserts over the Complete Tool Life”, Int. J. Refract. Met. Hard Mater., (2014), submitted.

[9] H. van den Berg, H. Westphal, M. Schneeweiss, M. Dietz, S. Köhler, J. Glühmann, U. Gieland, „Wie die Eigenspannungen den Verschleiß beeinflussen“, Werkstatt und Betrieb, , vol. 138, Nr. 12, pp. 50-54, (2005)

[10] ICDD Database Powder Diffraction File #00-051-0939.

[11] Spieß L, Schwarzer R, Behnken H, Teichert G. „Moderne Röntgenbeugung“, Teubner, Wiesbaden, (2005)

[12] U. Welzel, J. Ligot, P. Lamparter, A.C. Vermeulen, E.J. Mittemeijer, “Stress Analysis of Polycrystalline Thin Films and Surface Regions by X-ray Diffraction”, J. Appl. Crystallogr., vol. 38, pp. 1-29, (2005)

Publication V

Evolution of Residual Stress in Ti-Al-Ta-N Coatings on Hard Metal Milling Inserts

T. Teppernegg[1], P. Angerer[1], T. Klünsner[1], C. Tritremmel[1], C. Czettl[2]

[1] Materials Center Leoben Forschung GmbH, Roseggerstraße 12, 8700 Leoben, Austria
[2] CERATIZIT Austria GmbH, Metallwerk-Plansee-Straße 71, 6600 Reutte, Austria

Abstract

Coated WC-Co hard metal milling inserts applied in milling application show thermal fatigue induced by interrupted tool-workpiece contact and wear as the two main damage mechanisms. Depending on the magnitudes of thermal and mechanical loads, either wear or thermal fatigue in form of combcracks may be dominant and determine the insert's lifetime. The present work illustrates the evolution of residual stress in an arc-evaporated Ti-Al-Ta-N coating for two different milling test setups, in one of which wear acted as the dominant damage mechanism. In the other test setup thermal fatigue fostered the formation of combcracks. Earlier work revealed a location on the tool's rake face, referred to as region of interest, with a significant buildup of tensile residual stresses in the WC phase of the substrate using synchrotron facilities. The residual stress state in the coating was determined in this region of interest by a cover method on the tools' rake faces after a defined number of cuts by X-ray diffraction using in-house facilities. In the wear dominated test setup, compressive residual stresses remained present until the end of tool life in coatings. Tensile residual stresses were found in coatings on inserts in which thermal fatigue was dominant.

Keywords: Ti-Al-N; thermal fatigue; wear; X-ray diffraction; residual stress; elastic constants; milling tools

Introduction

Thermal fatigue and wear are the dominant damage mechanisms in milling application [1]. The former one induces characteristic cracks (see Fig.1), which are commonly referred to as combcracks. Wear damage is usually initiated with adhesive wear, in which workpiece material sticks to the insert's rake and flank face during application [2], and abrasive wear at the tool surface [3]. The kinetics of abrasive wear is increased when debris in form of coating

and hard metal fragments are produced by the crushing of surface asperities such as combcrack flanks [1].

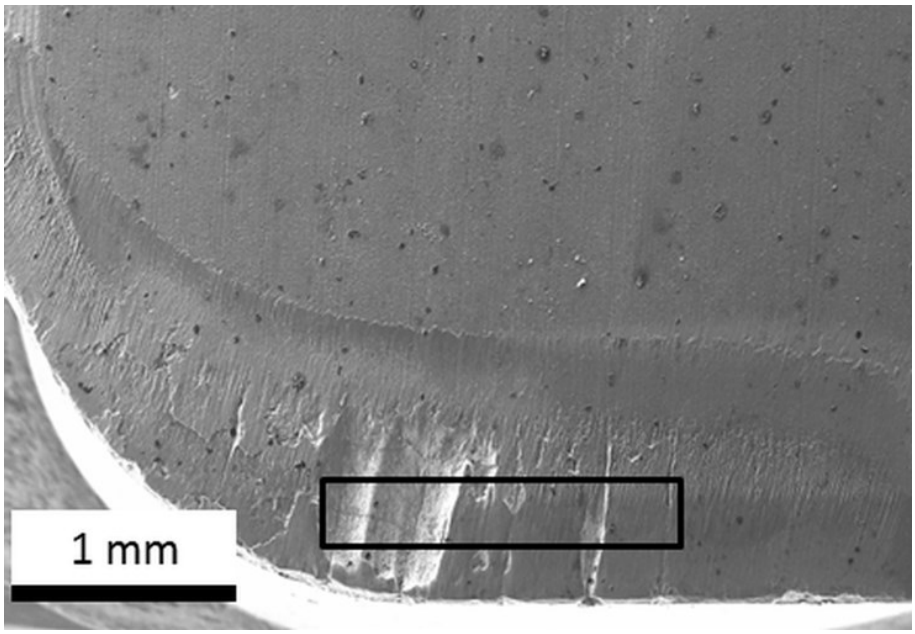

Fig.1: Scanning electron microscopy micrograph of a milling insert's rake face at the end of lifetime. The black rectangle indicates the position of the region of interest (ROI) in which significant tensile residual stress build-up was observed in the WC phase [10].

After a certain number of tool-workpiece contacts, combcracks appear with propagation planes perpendicular to the cutting edge (see Fig.1). In the literature, some authors postulated that temperature differences between heating upon cutting and cooling upon the idle period in a cutting cycle are the key factor to combcrack initiation [1], [3], [4]. The recurrent thermo-shock with high cooling rates during idle time which induce periodic surface material shrinkage fosters tensile residual stress creation [1], [4]. Opitz et al. expected that the direction of tensile residual stresses is oriented parallel to the cutting edge that leads to the formation of combcracks [1]. The use of cooling agents leads to intensive thermo-shock acting in milling inserts, which fosters combcrack creation [5]. Milling with heated inserts suppresses the crack propagation by lowering the temperature differences at tool edges [1].

Yellowley et al. expected plastic deformation during cutting that is localized close to the cutting edge [6]. This local plastic deformation is introduced by thermal stress amplitudes, induced by frictional heating [7], which initiate the nucleation and growth of combcracks [2], [7]. At the present cutting temperature a combination of thermal stresses and sufficiently high load stresses can exceed the flow stress of a tool material and provoke the buildup of tensile residual stress close to the cutting edge upon cooling. Plastic deformation close to

the cutting edge may also be introduced by cyclic mechanical load in form of cyclic contact pressure between chip and insert [6].

Teppernegg et al. detected a significant tensile residual stress build-up in the WC phase on the rake face of a used milling insert in a region of approximately 0.3 × 1.6 mm² [8] (see black rectangle in Fig.1) via position resolved synchrotron X-ray diffraction with high lateral resolution [9]. Positon resolved residual stress measurements in the WC phase using laboratory X-ray sources and a special cover method did yield results similar to the ones from synchrotron measurements in this region of interest [10]. Details regarding the two compared test setups are described elsewhere [10]. At early stages of application, the residual stresses in the milling inserts are similar for both test setups: At the virgin state the residual stress state is compressive but within 1000 tool-workpiece contacts (also "cuts") it changed to a tensile state. Upon the appearance of the first combcrack the detected tensile residual stresses decreased significantly in the WC phase in inserts, in which thermal fatigue was dominant, whereas tensile residual stresses remained constant until the end of lifetime in the wear dominated test setup [10].

Nowadays, hard coatings are used to enhance the wear and thermal fatigue resistance of milling inserts. Currently, no data on the evolution of residual stress in milling insert's coatings during a tool's lifetime is available in the open literature. In the present work, the evolution of residual stresses in the coating of used milling inserts is compared for two different test setups. The influence of the chemical composition of the coating on the elastic constants such as Young's modulus E, Poisson ratio □ and X-ray elastic constant $1/2\, s_2$ in dependence of the crystallographic plane is discussed. These results shall illustrate the interaction of residual stresses with the observed damage states in [10] and [11] of the investigated milling inserts.

Experimental

The coating investigated within this work was deposited on a 8 wt.% Co WC-Co hard metal milling insert (6.4 × 11.4 × 10.0 mm³) with an average WC grain size of 1 µm. An industrial scale cathodic arc evaporation system (Oerlikon Balzers RCS) was applied for deposition of a Ti-Al-Ta-N coating with a thickness of 8 µm. All milling inserts did exhibit a chamfered cutting edge and cut a block (800 × 96 × 200 mm³) of 42CrMo4 steel in a normalized state with an upper yield strength of 400 N/mm².

The used milling test setups A and B are presented in Fig.2a) and Fig.2b), respectively.

Details on machining parameters are described in [10] for both test setups. The same milling insert geometry and steel workpiece material were used in both test setups. All tests were

done in a single edge synchronous milling arrangement without cooling agents such as liquid lubricants or cold air. To foster thermal fatigue damage in test setup A, the cut segment length was reduced to 96 mm and a different start and end position compared to test setup B were chosen [10].

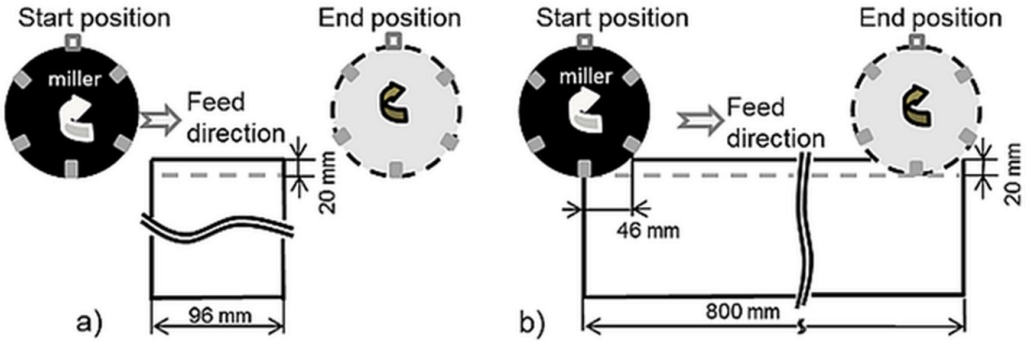

Fig.2: Scheme of single edged milling arrangements with different cut segment length of a) 96 mm referred to as test setup A [10] and b) 800 mm referred to as test setup B [8], [11].

The start and end position in test setup A lead to non-constant tool-workpiece contact length (TWCL) at the beginning and the end of each cut segment. With increasing number of cuts, the TWCL increased from 0.47 mm at the first contact within one cut segment length to 51.44 mm after 92 cuts. The insert cuts an accumulated tool-workpiece contact length (aTWCL) of 2.50 m under non-constant cutting conditions. After 92 cuts the TWCL remains constant at 51.44 mm for 100 cuts to become non-constant again for another 92 cuts at the end of the cut segment. The milling inserts in test setup B experienced constant TWCL throughout a cut segment because the beginning and the end of the cut segments are removed by a dummy tool. The milling experiments in test setup A were stopped after an aTWCL of 36.0, 407.8 and 611.7 m and at end of lifetime. After 611.7 m of aTWCL the first combcrack appeared. In the insert at end of lifetime the determination of the residual stresses in the coating was not possible because of delamination of the coating within the region of interest (ROI), see Fig.1 [10].

In test setup B the milling tests were stopped after an aTWCL of 51.4 m, 493.8 m and at end of lifetime at 1923.8 m. No combcracks were observed in the insert at end of lifetime that was determined by flank wear.

The residual stress state in the ROI (1.6×0.3 mm²) (see Fig.3) was determined in the direction parallel to the straight portion of the cutting edge (see Fig.1) in the cubic TiN phase of the coating.

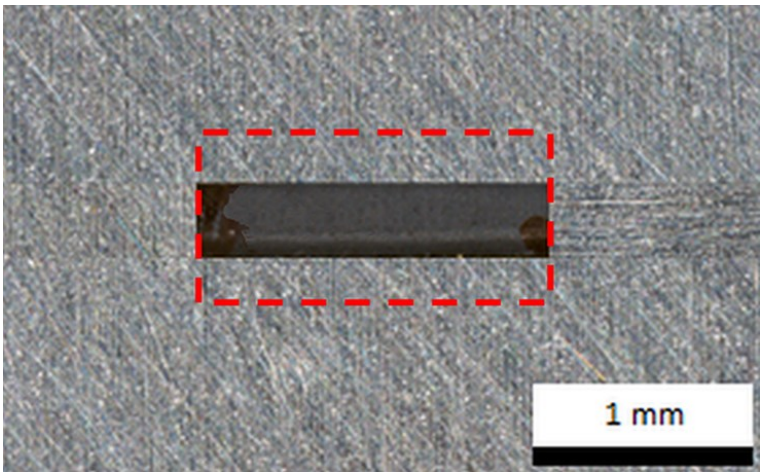

Fig.3 Light optical microscopy image of the rake face of one of the investigated milling insert, which is prepared for position resolved X-ray diffraction in the region of interest (ROI, 1.6 × 0.3 mm²). Areas outside of this region were covered by a lead foil, which is fixed by a double faced-adhesive tape. Red dashed rectangle indicates size and position of an enlarged ROI described in the text (1.6 × 0.6 mm²).

The residual stress was determined with a mean penetration depth of about 4 µm. This depth results from the actual diffraction geometry and the chosen radiation wavelength. In one specimen with an aTWCL of 407.8 m, which corresponds to 4000 cuts at constant TWCL, under test setup A conditions, one additional measurement was done in a vertically enlarged ROI with unchanged horizontal position (1.6 × 0.6 mm²), see red dashed rectangle in Fig. 3. This served to assure the lateral localization of the residual stresses in the coating in analogy to the residual stresses in the WC phase as determined in earlier work via synchrotron X-ray diffraction [8].

The residual stress states of all milling inserts were determined by a D8 Discover X-ray diffractometer (Bruker AXS, Germany) in parallel beam geometry (40 kV, 40 mA, Cr Kα radiation). All measurements were done using a Sol-X energy dispersive detector, an open (90°) Eulerian cradle and a polycapillary collimator. The areas outside of the ROI were covered with a lead foil, which was fixed by a double-faced adhesive tape, see Fig.3. The diffraction maximum (100) of the cubic TiN phase at a diffraction angle 2θ of 66.8° was selected for the subsequent stress determination [12]. Lead was selected as a proper cover material for regions outside of the ROI to avoid any overlap of the diffraction peak originating from the TiN phase in the coating and the cover material. The stress component parallel to the straight portion of the milling insert's cutting edge was determined. Corresponding stress determination experiments in the WC phase as described in [8] and [10] showed that it is favourable to select a diffraction geometry with incident and diffracted beam orientated parallel to this direction to minimize shadowing effects caused by the covering lead foil. This effect would be enlarged at tilted samples ($\psi \neq 0$) as well as if a

rectangular shaped ROI with a large aspect ratio is considered. Consequently, the ω-method [13] was selected for the determination of the stress component parallel to the straight portion of the cutting edge. The diffraction intensity was recorded in a diffraction angle range 2ϑ from 64.2° to 69.0° and a sample tilt angle ψ up to 20.0°. For the background correction a diffractogram of a lead foil sample was determined with the same measurement parameters as the actual stress measurements. For each diffraction angle 2ϑ and for each tilt angle ψ the observed diffraction intensity I_{sample} was corrected according to the relation $I_{corr}(\vartheta, \psi) = I_{sample}(\vartheta, \psi) - I_{Pb}(\vartheta, \psi)$. The subsequent data reduction was performed using the corrected diffraction intensity. The diffraction angles of the measured diffraction maxima were then determined by TOPAS 4.2 software (Bruker AXS, Germany) [14]. For each sample the residual stress component parallel to the surface and parallel to the straight portion of the cutting edge was then deduced from the slope determined by linear regression in the $\sin^2\psi$-plot according to the formalism described in [15].

Results and discussions

The residual stress is calculated according to the modified fundamental relation (see Eq. 1) given e.g. in [15] from the regression in a diagram strain vs. $sin^2\psi$ in which only the stress component parallel to the cutting edge was considered.

$$\varepsilon(\psi) = \frac{1+\nu}{E} \cdot \sigma \cdot sin^2\psi + \frac{1}{E} \cdot [-2 \cdot \nu \cdot \sigma] \quad (1)$$

The slope $\sigma \times (1 + \nu) / E$ in such a diagram can then be interpreted as the residual stress in units of the reciprocal X-ray elastic constant $E / (1 + \nu)$. For now, a quantitative discussion of the XRD results will refer to this parameter due to uncertainties in the elastic constants of the coating material, which depend on its exact chemical composition and on its possible anisotropy (texture).

The evolution of residual stresses in the Ti-Al-Ta-N coating as a function of aTWCL is shown in Fig.4. In test setup A, in which combcracks are the dominant damage form, the residual stresses until the first appearance of a combcrack after milling 611.7 m aTWCL are illustrated in Fig.4a). The residual stress evolution during the complete tool life in specimens tested in the wear dominated test setup is shown in Fig.4b). The open circle Fig.4a) indicates a result from the enlarged ROI explained before.

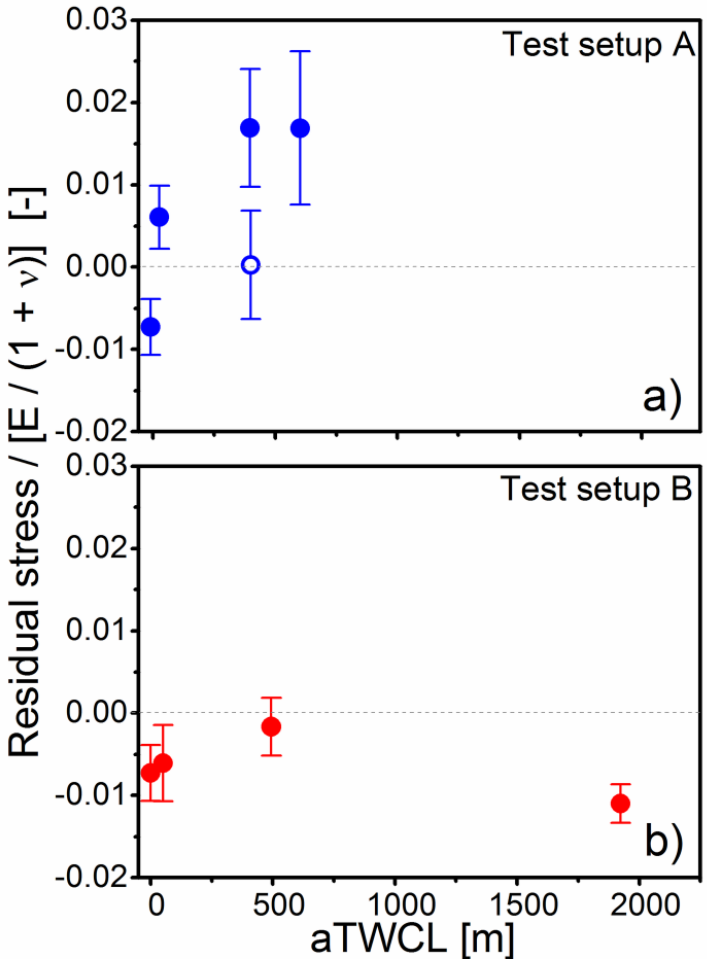

Fig.4: Residual stress determined in a Ti-Al-Ta-N coating on the rake face of milling inserts tested in a) test setup A and b) test setup B. All results were determined locally closed to the cutting edge in region of interest with dimension of 1.6 × 0.3 mm² (closed symbols). The open circle in a) indicates residual stress data of an enlarged ROI of about 1.6 × 0.6 mm² (see Fig.3).

Compressive residual stresses of about $-7.2 \times 10^{-3} \times E / (1 + \nu)$ were found in the virgin specimen. In test setup B the residual stresses remained in compression in a range from -1.6×10^{-3} to $-11.0 \times 10^{-3} \times E / (1 + \nu)$ throughout the whole tool lifetime. In test setup A the residual stress state changed within a few meters of aTWCL - after 1000 cuts, which correspond to 36 m of aTWCL, tensile residual stresses of about $6.1 \times 10^{-3} \times E / (1 + \nu)$ were determined. In a specimen with 407.8 m of aTWCL the tensile residual stresses were observed to have increased to about $16.9 \times 10^{-3} \times E / (1 + \nu)$. Also the specimen which contained the first observed combcrack, the residual stress state was found to be in tension. These tensile residual stresses were shown to be localized in lateral vertical direction in the ROI (0.3 × 1.6 mm, see Fig.3) by comparing results from it and the enlarged ROI (0.6 × 1.6 mm) in one and the same specimen: Residual stress determined in the enlarged ROI showed a value close to zero (see open circle in Fig.4a)). This result is interpreted as an averaging of tensile and compressive residual stresses inside and outside of the ROI, as

revealed to be present in the WC phase via position resolved residual stress measurements using synchrotron radiation (see in [8]).

In the WC phase the evolution of the residual stresses is similar at early stages of application independent from the investigated test setup [10]. In the coating the evolution of residual stresses was different and was dependent on the used test setup. Today it is not completely understood, in which region of the substrate-coating composite combracks nucleate. In test setup B, in which wear damage was dominant and no combcracks were observed [11], the compressive residual stresses in the coating may have prevented combcrack formation. In test setup A, the coating (see Fig.4a)) and the WC phase [10] did exhibit tensile residual stresses which possibly promoted the nucleation and growth of combcracks.

In contrast to the evolution of residual stress observed in the WC-Co substrate in test setup A 0, the tensile residual stresses in the coating did not decrease when the first combcrack appeared. In the WC phase the found tensile residual stresses decreased and at end of lifetime the residual stress state was compressive [10]. Tkadletz et al. found cracks around droplets, being inhomogeneities found in arc evaporated coatings [16], induced by shear stresses after ball on disc tests 0. In both test setups, arising cutting forces may foster the introduction of this kind of cracks. However, if they are present in the coating, their orientation, density and/or distance to one another [18] did not lead to the reduction of the observed residual stresses to zero (see Fig.4).

In the present work the influence of the Al content in the cubic $Ti_{1-x}Al_xN$ phase on the elastic constants Young's modulus E, Poisson ratio ν and the X-ray elastic constant $1/2\ s_2 = (1 + \nu) / E$ was closely inspected. All their values given in Fig. 5 are based on the tensor of elastic constants as calculated by first principle density-functional theory and experimentally verified by Tasnádi et al. [19]. Calculated in accordance with the models of Voigt [20] and Reuss [21] for the crystallographic directions [100] and [111] in the cubic phase they display a clear dependence on the crystal's Al content.

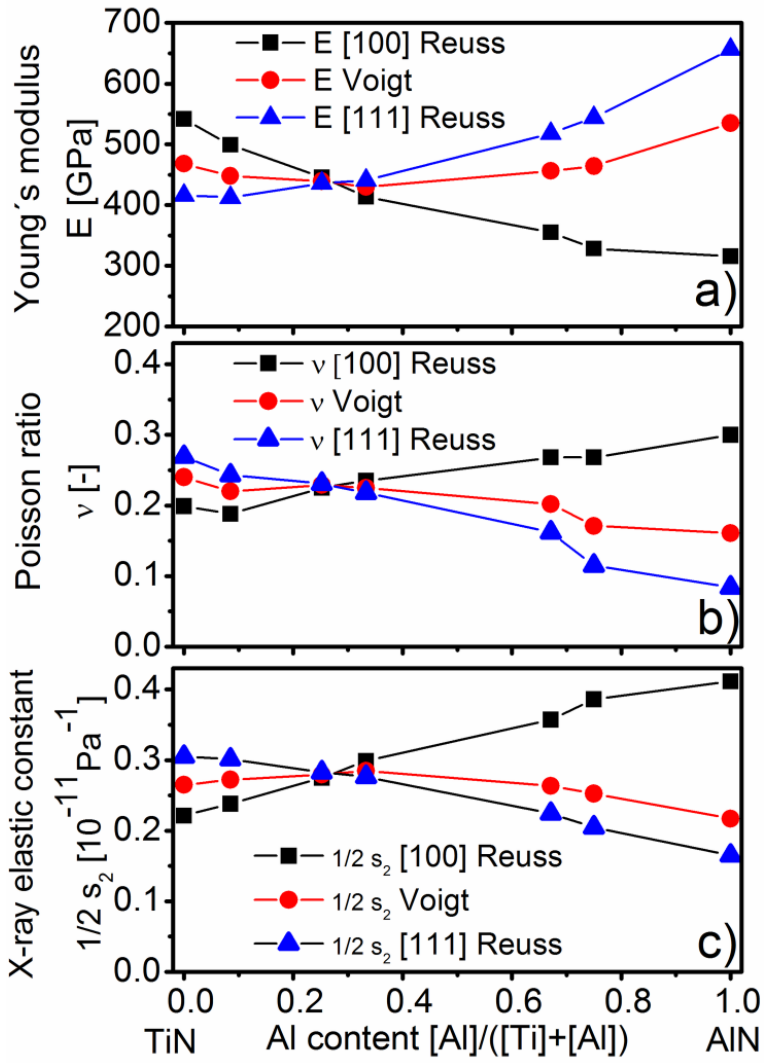

Fig.5: Elastic constants plotted as function of the Al content in a cubic $Ti_{1-x}Al_xN$ phase as recalculated from [19]: a) Young's modulus, b) Poisson ratio, and c) X-ray elastic constant. The values of the elastic constants refer to different crystallographic directions in the cubic cell (Miller indices are given).

As displayed in Fig.5a) the Young's modulus calculated according to Reuss' model decreases and increases with rising Al content in the [100] and [111] direction, respectively. Young's modulus derived by the Voigt model increases with the Al content (see Fig.5a)). The Poisson ratio decreases with increasing Al content using the Reuss' model for the [111] direction and the Voigt model, and increases, when the [100] direction is evaluated applying the Reuss model (Fig.5b)). The X-ray elastic constants $1/2\ s_2 = (1 + \nu) / E$ in [100] direction according to Reuss´ model rise with increasing aluminium content whereas the corresponding values in [111] direction and the ones calculated using the Voigt model decrease (see Fig.5c)).

An example shall illustrate the relevance of the performed evaluation: The compressive residual stresses in the virgin milling insert can be numerically calculated based on the different elastic constants influenced by the coating's Al content (cf. Fig.5). In the

crystallographic [100] direction these residual stresses vary from -3.2 to -2.0 GPa, calculated using the Reuss' model with elastic constants of TiN and $Ti_{0.33}Al_{0.66}N$, respectively. The difference of residual stresses calculated using the Voigt model with elastic constants of TiN and $Ti_{0.33}Al_{0.66}N$ is negligible - the values varied between -2.7 and -2.8 GPa, respectively. Calculations of residual stresses using Reuss elastic constants for the crystallographic [111] direction yield values from -2.4 GPa for TiN to 3.3 GPa for $Ti_{0.33}Al_{0.66}N$.

The actual elastic and X-ray constants of the Ti-Al-Ta-N coating can be influenced by structural and chemical inhomogeneity, e.g., preferred grain growth directions, grain orientation and droplets originating from the arc deposition process, as well as a variable Ta content. These topics deserve attention in future research activities.

Conclusions

The aim of the present work is to show the evolution of residual stresses in an arc evaporated Ti-Al-Ta-N coating deposited on hard metal milling inserts during tool lifetime for two different milling test setups. Earlier work revealed a location on the tool's rake face referred to as region of interest (ROI), with a significant buildup of tensile residual stresses in the WC phase using synchrotron facilities. A special cover method facilitated the position resolved determination of residual stress in the ROI (1.6 × 0.3 mm²) via X-ray diffraction using in-house X-ray sources. This cover method involved the use of lead foil to cover areas outside of the ROI. In the virgin coating compressive residual stresses were detected. In the first analysed test setup, in which mainly wear damage limited the tool lifetime, the residual stresses in the coating remained in a compressive state until end of lifetime. In the second investigated test setup, in which thermal fatigue triggered the formation of combcracks, tensile residual stresses were observed in the coating already after 1000 tool-workpiece contacts. These stresses increased with increasing number of cuts and remained in tension when the first combcrack appeared. The tensile residual stress values provided in this work were expressed in units of the reciprocal X-ray elastic constant $E / (1 + \nu)$ due to certain uncertainties in the elastic constants of the coating material, which depend on its exact chemical composition and on its possible anisotropy (texture).

Since it is not completely understood, in which region of the substrate-coating composite combcracks nucleate, further efforts in this field are necessary. Also, the influence of alloying elements on crystallographic elastic constants deserves attention in future research activities.

Acknowledgments:

We thank Christian Mitterer and Jozef Keckes for fruitful discussions concerning the residual stress determination.

Financial support by Austrian Federal Government (in particular from Bundesministerium für Verkehr, Innovation und Technologie and Bundesministerium für Wirtschaft, Familie und Jugend) represented by Österreichische Forschungsförderungsgesellschaft mbH (837900) and the Styrian and the Tyrolean Provincial Government (1000032317), represented by Steirische Wirtschaftsförderungsgesellschaft mbH and Standortagentur Tirol , within the framework of the COMET Funding Programme is gratefully acknowledged.

References:

[1] Opitz H, Lehewald W. Untersuchungen über den Einsatz von Hartmetallen beim Fräsen. Forschungsberichte des Landes Nordrhein-Westfalen Nr. 1146. Köln und Opladen: Westdeutscher Verlag; 1963.

[2] Pandey PC, Bhatia SM, Shan HS. Thermo-Mechanical Failure of Cemented Carbide Tools in Intermittent Cutting. CIRP Annals 1979; 28: 13-17.

[3] Schedler W. Hartmetall für den Praktiker. Düsseldorf: Plansee Tizit VDI; 1988.

[4] Ekemar CSG, Iggström SAO, Hedén GKA. Influence of some Metallurgical Parameters of Cemented Carbide on the Sensitivity to Thermal Fatigue Cracking at Cutting Edges. Material for Metal Cutting. Scarborough: Conference proceedings of BIRSA; 1970. 133-142.

[5] Melo ACA, Milan JCG, da Silva MB, Machado AR. Some Observations on Wear and Damages in Cemented Carbide Tools. J Braz Soc Mech Sci 2006; 28: 269-277. doi:10.1590/S1678-58782006000300004.

[6] Yellowley I, Barrow G. The Influence of Thermal Cycling on Tool Life in Peripheral Milling. Int J Mach Tool D R 1976; 16 Issue 1: 1-12. doi:10.1016/0020-7357(76)90009-3.

[7] Bathia SM, Pandey PC, Shan HS. Failure of Cemented Carbide Tools in Intermittent Cutting. Precis Eng 1979; 1 Issue 3: 148-152. doi:10.1016/0141-6359(79)90041-2.

[8] Teppernegg T, Klünsner T, Tritremmel C, Czettl C, Keckes J, Wroblewski T, Ebner R, Pippan R. Spatial Correlation of Tensile Residual Stress and Thermal Fatigue Damage in Coated Cemented Carbide Milling Inserts. Reutte: Conference proceedings of the 18th Plansee Seminar; 2013.

[9] Wroblewski T, Clauß O, Crostack HA, Ertel A, Fandrich F, Genzel Ch, Hradil K, Ternes W, Woldt E. A new difractometer for materials science and imaging at HASYLAB beamline G3. Nucl Instrum Meth A 1999; 428: 570-582. doi:10.1016/S0168-9002(99)00144-8.

[10] Teppernegg T, Klünsner T, Angerer P, Tritremmel C, Czettl C, Keckes J, Ebner R, Pippan R. Evolution of Residual Stress and Damage in Coated Hard Metal Milling Inserts Over the Complete Tool Life. Int J Refract Met H 2014; 47: 80-85. doi: 10.1016/j.ijrmhm.2014.07.005.

[11] Teppernegg T, Klünsner T, Tritremmel C, Angerer P, Czettl C, Keckes J, Ebner R, Pippan R. Residual Stress and Damage in Coated Hardmetal Milling Inserts. Orlando: Conference proceedings - Tungsten, Refractory & Hardmaterials VIII; 2014.

[12] ICDD Database Powder Diffraction File #00-051-0939.

[13] Welzel U, Ligot J, Lamparter P, Vermeulen AC, Mittemeijer EJ. Stress Analysis of Polycrystalline Thin Films and Surface Regions by X-ray Diffraction. J Appl Crystallogr 2005; 38: 1-29. doi:10.1107/S0021889804029516.

[14] Bruker AXS. TOPAS V4. General profile and structure analysis software for powder diffraction data. Karlsruhe: 2005.

[15] Spieß L, Schwarzer R, Behnken H, Teichert G. Moderne Röntgenbeugung. Wiesbaden: Teubner; 2005.

[16] D.M. Mattox. Handbook of Physical Vapor Deposition (PVD) Processing, 2nd ed. Oxford: Elsevier Science; 2010.

[17] Tkadletz M, Mitterer C, Sartory B, Letofsky-Papst I, Czettl C, Michotte C. The effect of droplets in arc evaporated TiAlTaN hard coatings on the wear behaviour. Surf Coat Tech 2014; 257: 95-101. doi:10.1016/j.surfcoat.2014.01.010.

[18] Raninger P, Ecker W, Antretter T, Leindl M, Ebner R. Interaction of heat checks in aluminum pressure casting dies and their effect on fatigue life. Key Eng Mater 2012; 488–489:626–9. doi:10.4028/www.scientific.net/KEM.488-489.626.

[19] Tasnádi F, Abrikosov I A, Rogström L, Almer J, Johansson M P, Odén M. Significant elastic anisotropy in $Ti_{1-x}Al_xN$ alloys. Appl Phys Lett 2010; 97: 231902-231902-3. doi:10.1063/1.3524502.

[20] Voigt W. Lehrbuch der Kristallphysik. Leipzig: Teubner; 1910.

[21] Reuss A. Berechnung der Fließgrenze von Mischkristallen auf Grund der Plastizitätsbedingung für Einkristalle. Z Angew Math Mech 1929; 9: 49-58. doi:10.1002/zamm.19290090104

Publication VI

High Temperature Mechanical Properties of WC-Co Hard Metals

T. Teppernegg[1], T. Klünsner[1], C. Kremsner[1], C. Tritremmel[1], C. Czettl[2], S. Puchegger[3], S. Marsoner[1], R. Pippan[4], R. Ebner[1]

[1] Materials Center Leoben Forschung GmbH, Roseggerstrasse 12, 8700 Leoben, Austria

[2] CERATIZIT Austria GmbH, Metallwerk-Plansee-Straße 71, 6600 Reutte, Austria

[3] Center for Nanostructure Research, University of Vienna, Boltzmanngasse 5, 1090 Vienna, Austria

[4] Erich Schmid Institute of Materials Science, Austrian Academy of Sciences, Jahnstrasse 12, 8700 Leoben, Austria

Abstract

Understanding of the load situation and consequently the lifetime of cutting tools made of WC-Co hard metal requires quantitative data for thermo-mechanical properties. For the elevated temperatures present in application, these data are currently rather rare. The present work does discuss elastic material properties up to 1100 °C and compressive yield strength up to 900 °C, both as a function of Co content. The fracture toughness was determined as a function of the WC grain size and Co content up to 800 °C. Young's modulus and yield strength decrease with increasing temperature. A significant rise in fracture toughness was observed at 800 °C with increasing Co content and decreasing WC grain size. A possible reason for this increase is an increase in the plastic zone size at elevated temperatures.

Keywords: WC-Co hard metal, elastic properties, yield strength, fracture toughness, high temperature properties, CTOD

Introduction

WC-Co hard metal (HM) is the preferred material for wear components and cutting tools in metal machining since the 1920s [1]. Especially cutting inserts have to endure high mechanical and thermal loads during application. These loads depend on the tool geometry, the cutting parameters (cutting speed, feed rate etc.), the use or absence of lubricants and the workpiece material being machined [1].

The finite element (FE) method is a powerful tool for advanced tool design via simulation of the cutting process including the estimation of mechanical and thermal tool loads [2]. The realistic simulation of strains and stresses in the WC-Co substrate during cutting and their effects on lifetime requires detailed knowledge of the mechanical properties, in particular Young's modulus E and shear modulus G, Poisson's ratio v, yield strength $R_{p0.2}$, fatigue strength and fracture toughness K_{IC}. Also the thermo-physical properties are necessary to develop adequate material models for FE simulation [3]. For 25 °C, i.e. room temperature (RT) most of the relevant data [4] are available in the literature but for higher temperatures they are rare. There is some information available on high temperature K_{IC} [5],[6],[7] and yield strength determined by three point bending [8] and four point bending [6], respectively. Si Mohand et al. determined E of a single HM grade up to 1000 °C using a four point bending test setup [6]. A systematic investigation on the influence of Co content and WC grain size on the mechanical properties of hard metals as a function of temperature is not documented in literature. The focus of this work is to provide missing data on E, G, v, $R_{p0.2}$ and K_{IC} at elevated temperatures.

Experimental

A range of mechanical properties of six hard metal grades shown in Fig. 1 was investigated as a function of temperature: Four HM grades, denoted A, B, C and D, are varied in Co content at a similar average WC grain size. Two additional grades, being E and F, have the same Co content as C but vary in WC grain size. All investigated HM grades contained 2 wt.% of a mixture of titanium-, tantalum- and niobium-carbides.

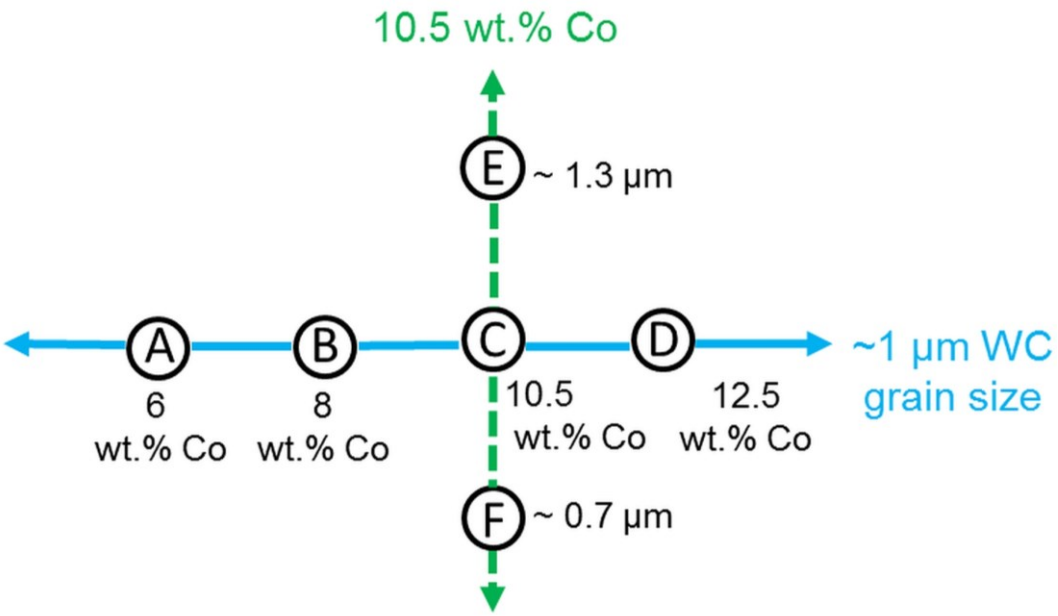

Fig.1: Overview of the investigated hard metal (HM) grades. A variation of Co content at a constant average WC grain size includes HM grades A, B, C and D whereas HM grades E and F have different average WC grain size at a constant Co content.

All HM grades were produced via a powder metallurgical route and sintered at a temperature of about 1400 ± 50 °C. The Young's- and shear modulus were determined in a vacuum furnace via a resonant beam technique, using rectangular bar specimens with dimensions of 45×4×3 mm³. At each temperature step, a spectrum (resonance intensity as a function of the frequency) is measured, from which the eigenfrequencies of the bar can be acquired. The difference between the calculated eigenfrequencies and the measured eigenfrequencies is then minimized using the elastic constants as variables of the fit [9]. The Poisson's ratio was determined indirectly according to Eq.1 [10]. The Young's moduli were determined from RT to 1100 °C, the shear moduli and Poisson's ratios only up to 700 °C, because the higher eigenfrequencies necessary to fit them could not be determined reliably above 700 °C.

$$\nu = \frac{E}{2 \times G} - 1 \tag{1}$$

WC-Co hard metals exhibit elevated levels of flow stress and limited ductility. Therefore, the determination of their compressive yield strength $R_{p0.2}$ requires special measures in terms of the applied specimen geometry to assure a high resistance to buckling under compressive loading and a small sample diameter to limit the forces necessary for testing, for further details see [11]. The used specimen geometry represents a compromise between the mentioned requirements. It exhibits a non-constant cross section with a minimum diameter

of 5.5 mm (see Fig. 2). It was used for the HM grades A, C and D in static uniaxial tests under compression loading conditions using a servo-hydraulic testing machine (Instron 8803).

Fig.2: Specimen for uniaxial compression tests.

The experiments were carried out from RT to 900 °C under ambient atmosphere, the heating was performed inductively. Strain measurements were done contactlessly via a laser extensometer (P - 2S- 50 / 400 Hz, Fiedler Optoelectronic GmbH) within a gauge length of 8 mm. The attained strain values required correction since they represent a mean stress-strain response of different specimen diameters. The correction was performed by means of a finite element model with the specimen's geometry, with its Young's modulus and the experimentally attained load-displacement curves as input parameters. All experiments were done at a strain rate of 5×10^{-3} s^{-1}. The compressive yield strength $R_{p0.2}$ was determined at a plastic strain of 0.2 % using the corrected stress-strain curves.

High temperature (HT) fracture toughness was determined by single edge notched bending (SENB) tests with testing condition associated with the standard ASTM E399 [12] with the notch refined by a razor blade. Presented values represent results from three rectangular bar specimens for the HM grades A, D, E and F. Error bars are derived from standard deviation of the attained values. The specimen dimensions were 36×7×4 mm³ (L×W×B), the distance between the two outer supports was 32 mm. The fatigue crack was introduced via cyclic compression at a stress ratio R of 10 with a stepwise increase of the applied stress intensity factor range ΔK until a fatigue crack was detected. The lengths of the fatigue cracks ranged between 30 µm and 100 µm. The experiments were done using a spindle drive testing facility. Tests at RT and 300 °C were performed under ambient atmosphere, for tests at temperatures from 500 up to 800 °C vacuum conditions were chosen to avoid oxidation of crack flanks. Surface topography of the fracture surfaces attained in the SENB experiments was studied by scanning electron microscopy (SEM, crossbeam field emission gun, Zeiss Auriga). The average roughness R_a of areas as large as 25×30 µm² on the fracture surface located close to the transition zone to the fatigue pre-crack fracture surface was determined for the HM grades A, D, E and F from SEM micrographs using the software package Alicona

MEX. A cross section of a fracture surface of HM E tested at 800 °C was prepared by means of focused ion beam milling (FIB, Orsay Physics Cobra Z- 05 FIB extension).

Results and Discussion

Young's modulus

The Young's modulus *E* is shown as a function of temperature for HM grades with a variation in Co content in Fig. 3a) and in WC grain size in b), respectively.

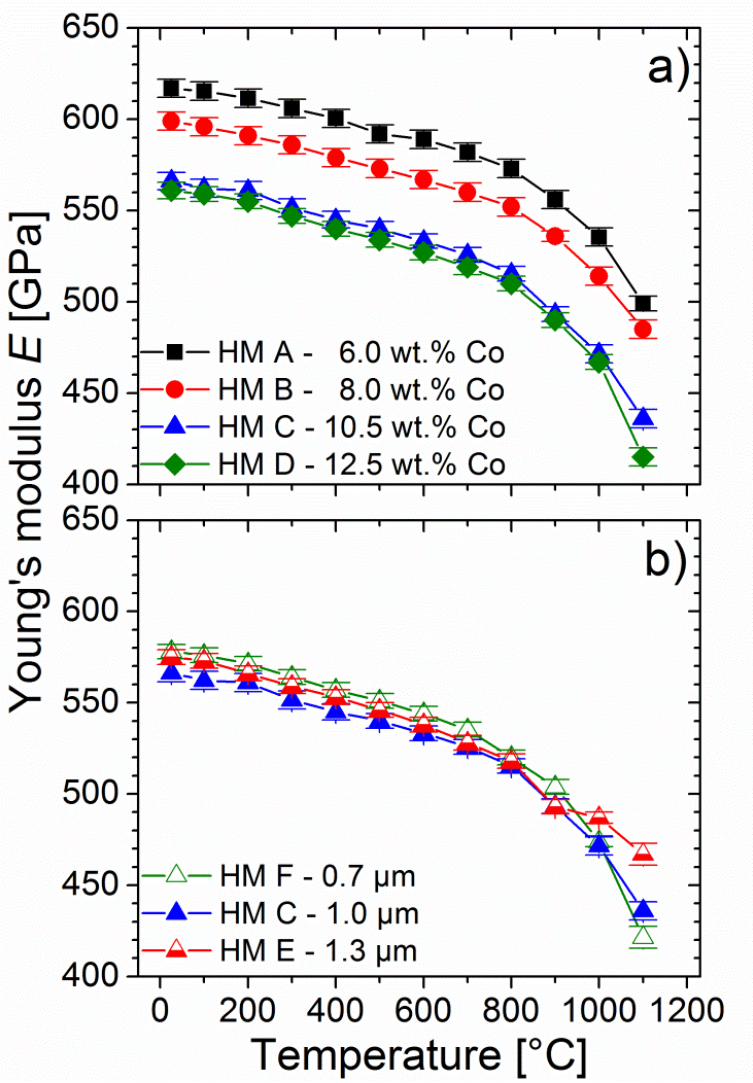

Fig.3: Young's modulus *E* as function of temperature in dependence on a) Co content (see Fig. 1) and b) average WC grain size (see Fig. 1).

At RT *E* depends solely on the Co content as it decreases with increasing Co content, see Fig. 3a), whereas it is independent of the WC grain size, see Fig. 3b). The observed values of *E* are in good agreement with results found for RT by Doi et al. who also compared their values with results from rules of mixture [13]. Doi et al. were the first to describe a decrease of *E*

with increasing Co content and its independence of the WC grain size at RT [13]. As shown in Fig. 3, *E* decreases steadily with increasing temperature showing a pronounced drop above 800 °C. Mohand et al. determined *E* for a HM grade with 6 wt.% Co and a mean WC grain size of 2 µm via a high-temperature four point bending test setup [6]. They assumed only linear elastic material behaviour when calculating it from load-displacement data [6]. At 800 and 1000 °C this HM grade did show *E* values of 361 ± 30 GPa and 193 ± 20 GPa, respectively [6]. Their values are significantly lower than those observed in the current work. This is most likely due to the neglection of significant plastification of the specimen surface in bending experiments at elevated temperatures at which the yield strength is significantly reduced compared to RT.

Shear modulus

The dependence of the shear modulus *G* on temperature for the HM grades with a variation in Co content is shown in Fig. 4a) and with a variation in WC grain size in Fig. 4b).

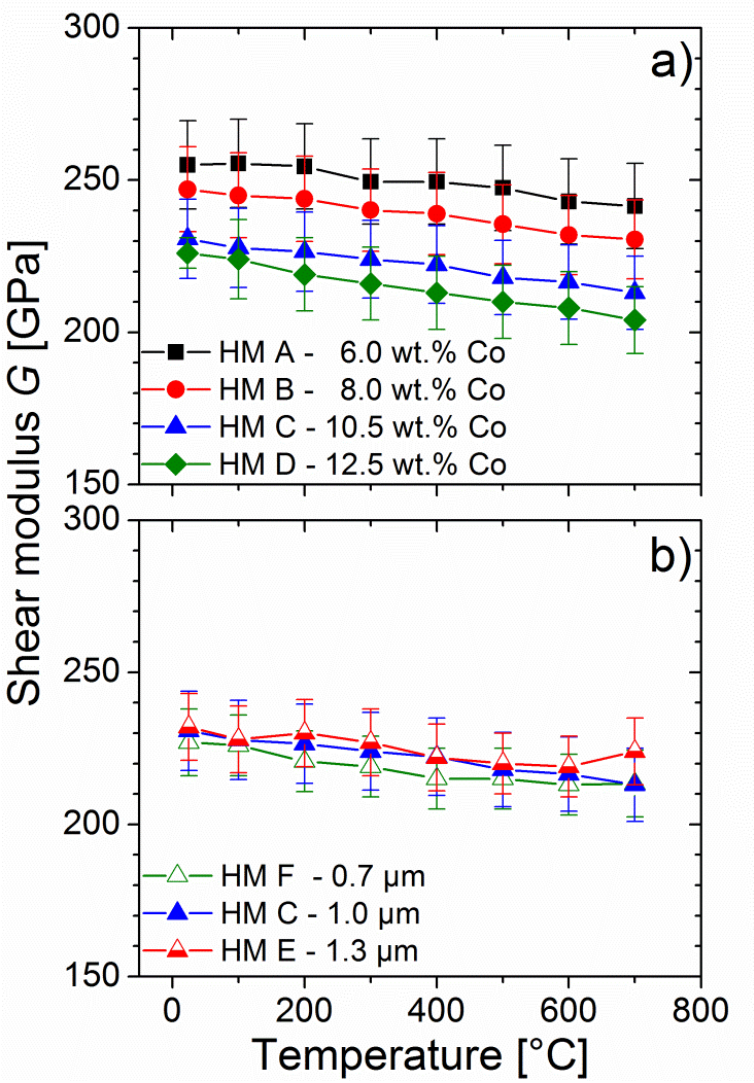

Fig.4: Shear modulus *G* as function of temperature in dependence on a) Co content and b) average WC grain size.

In the investigated temperature interval *G* is not significantly influenced by the WC grain size and it decreases only slightly with increasing Co content. This corresponds well with findings described in [13]. At RT the measured G values correspond well with literature findings [4].

Poisson's ratio

The Poisson's ratio ν as function of temperature is illustrated in Fig. 5.

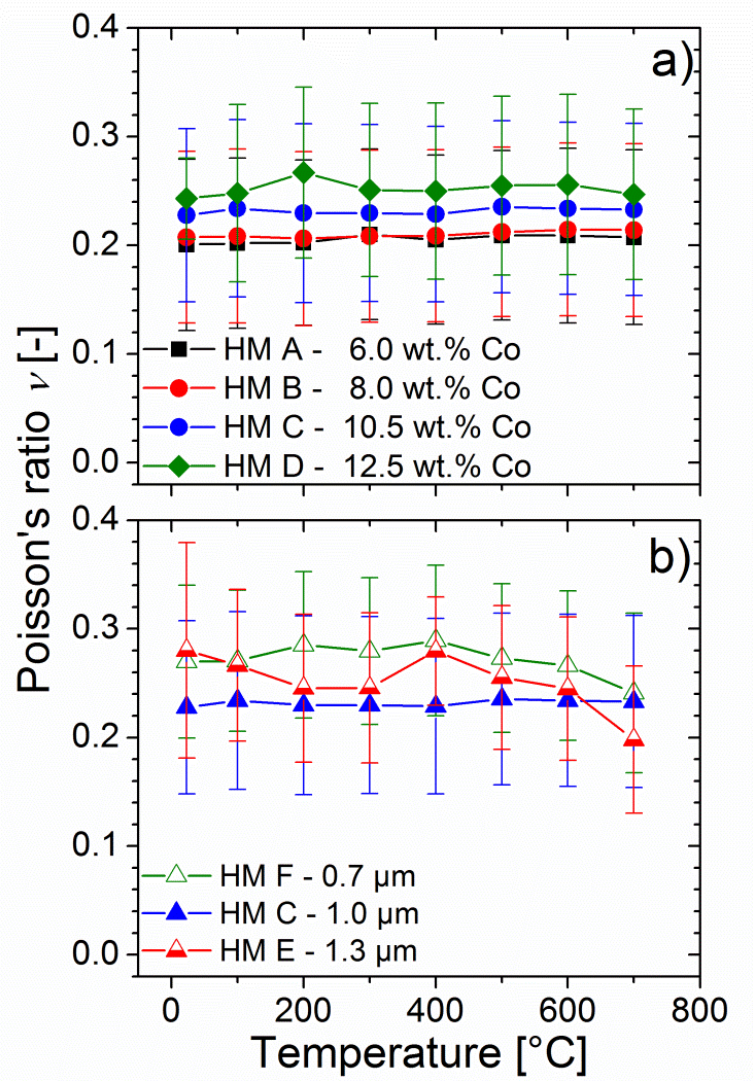

Fig.5: Poisson's ratio ν as function of temperature in dependence on a) Co content and b) average WC grain size.

The values of ν are influenced neither by the Co content nor the WC grain size, nor the temperature in the investigated parameter interval. All RT values of the investigated HM grades are in a range from 0.198 to 0.280, which corresponds well with literature [4],[13].

Flow behaviour

Stress-strain curves for the selected HM grades A, C and D attained under compressive loading are presented from RT up to 900 °C in Fig. 6. The tests were stopped without specimen fracture at 2 % compressive strain to avoid buckling.

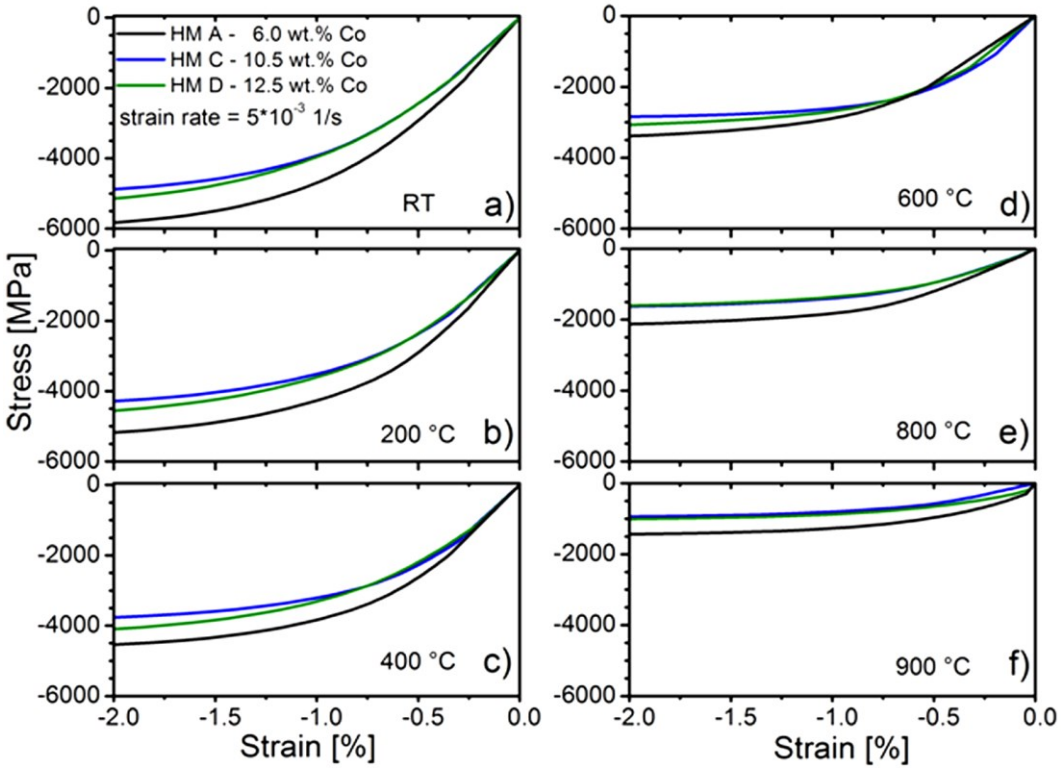

Fig.6: Stress-strain curves attained under compressive loading for the HM grades A, C and D at a) room temperature (RT), b) 200 °C, c) 400 °C, d) 600 °C, e) 800 °C and f) 900 °C.

In the investigated temperature range the compressive yield strength decreases with increasing Co content as observed at RT by Klünsner et al. [14]. The differences in yield strength between HM grades with 6 to 12.5 wt.% Co observed in the current work decrease with increasing temperature. Co content differences ≤ 2 wt.% do not lead to significant differences in flow behaviour, see Fig. 7. All HM grades show remarkable strain hardening that decreases with increasing temperature, see Fig. 6. At RT the compressive yield strength $R_{p0.2}$ ranges from 4400 to 3800 MPa, at 900 °C from 750 to 620 MPa (see Fig. 7).

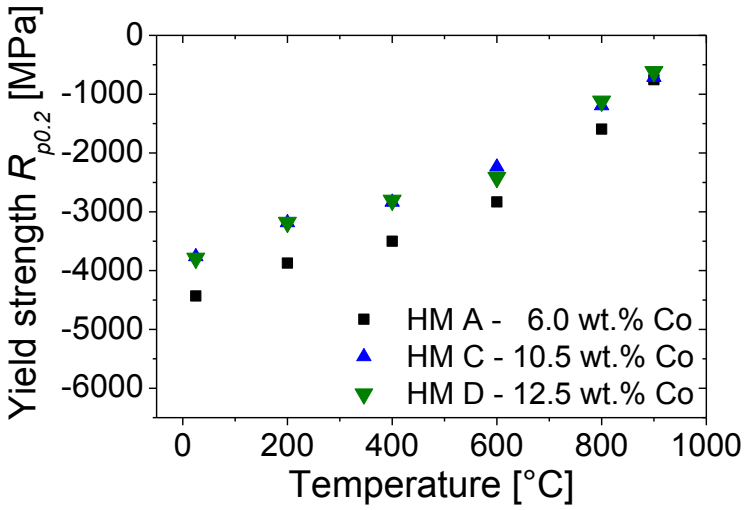

Fig.7: Compressive yield strength $R_{p0.2}$ of selected HM grades A, C and D as function of temperature.

These results are comparable with stress-strain curves determined at elevated temperature via 3 point bending tests at a strain value of 0.5 % [8]. At 1000 °C the flow behaviour of a HM grade with 11 wt.% Co [8] is similar to the one of HM grades C and D at 900 °C determined in the current work. Milmann et al. investigated the HT hardness of WC-Co which decreases with increasing temperature down to a value of 50 % of the RT hardness at 800 °C [15]. Analogously to the evolution of HT hardness also the yield strength $R_{p0.2}$ decreases with increasing temperature, see Fig. 7. At RT the respective values of HM grades A and D are comparable to literature values being -4850 and -3560 MPa for HM grades with respective Co content of 6 and 12 wt.% and a similar respective average WC grain size [11]. At 900 °C the HM grades A, C and D exhibit only about 15 % of their RT yield strength. At RT the HM A with the lowest Co content of 6 wt.% shows a significantly higher $R_{p0.2}$ than HM grades with higher binder content.

Fracture toughness

The fracture toughness K_{IC} as a function of temperature for the HM grades with varied Co content is given in Fig. 8a), and varied WC grain size in Fig. 8b).

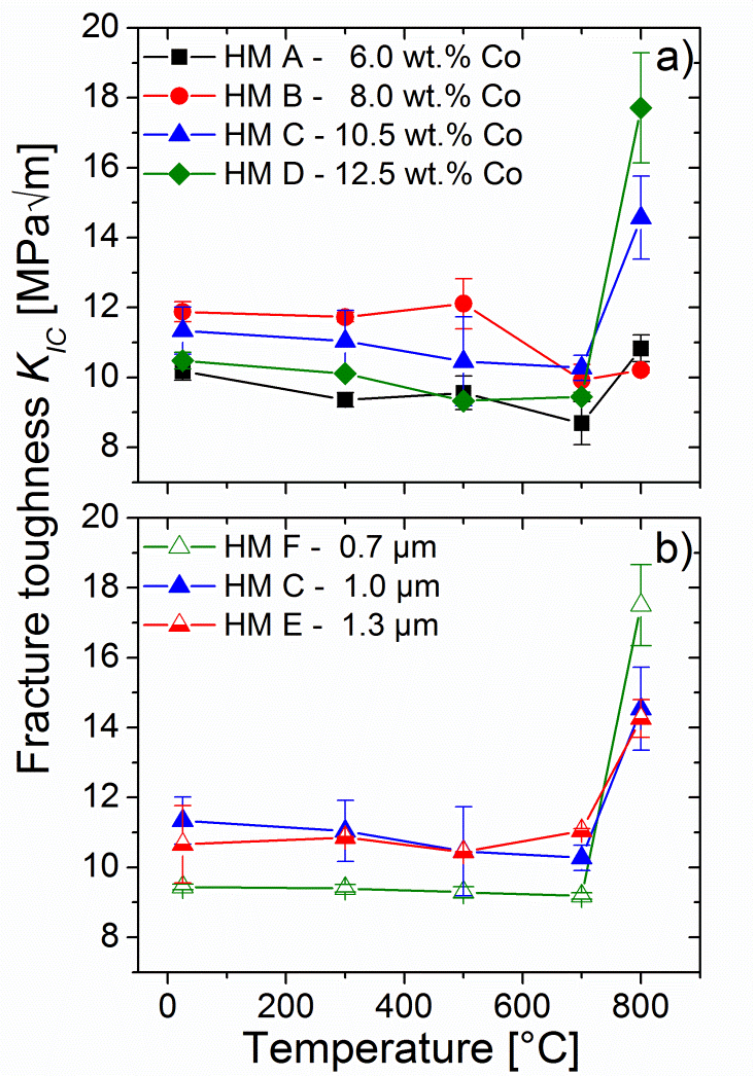

Fig.8: Fracture toughness K_{IC} as function of temperature in dependence on a) Co content and b) average WC grain size.

K_{IC} of the mentioned grades ranges from 8.7 to 12.1 MPa√m remaining almost constant between RT and 700 °C. This behavior is comparable with findings from literature [5], [6], [7] Some authors indicated that at RT an increase of K_{IC} was induced by an increase in Co content but their investigated HM grades did not exhibit a constant mean WC grain size [5],[16].

Above 700 °C the Co content has a significant influence on K_{IC}, see Fig. 8a). At 800 °C HM grades C and D exhibit K_{IC} values of about 17.7 and 14.6 MPa√m, respectively, which are well above the plateau observed at lower temperatures. K_{IC} of HM grades A and B, obtained at 800 °C, remains within the plateau. For HM grades very similar to HM A, other authors also detected a rise in K_{IC} with increasing temperature [5], [16]. At 800 °C the HM F with the smallest mean WC grain size exhibits the highest K_{IC} of about 17.5 MPa√m. HM grades C and E with coarser mean WC grain size possess K_{IC} values of about 14.5 and 14.3 MPa√m, see Fig.

8b). The trend towards increasing K_{IC} with decreasing WC grain size is comparable with findings from literature, in which two HM grades with the same Co content and mean WC grain sizes of one and two micrometers were compared [5].

The crack tip opening displacement *CTOD* gives information on how much the crack has to be opened to trigger propagation. There is a relation between the size of the plastic zone r_p located in front of the crack tip, calculated according to Irwin (see Eq. 3 - plain strain) the $R_{p0.2}$ and the K_{IC} value [17].

$$r_p = \frac{1}{\pi} \times \left(\frac{K_{IC}}{R_{p0.2}}\right)^2 \tag{3}$$

The stresses acting in the SENB tests were much lower than $R_{p0.2,}$ (see Fig. 7) therefore Eq. 4 can be used for calculation of *CTOD* requiring Young's Modulus, yield strength and fracture toughness (see Eq. 4) [18]. $R_{p0.2}$ values necessary at 300, 500 and 700 °C for the calculation of *CTOD* were interpolated between values given in Fig. 7.

$$CTOD = \frac{K_{IC}^2}{E \times R_{p0.2}} \tag{4}$$

The *CTOD* values and the plastic zone sizes of HM grades A, C and D are illustrated in Fig. 9 for the investigated temperature range.

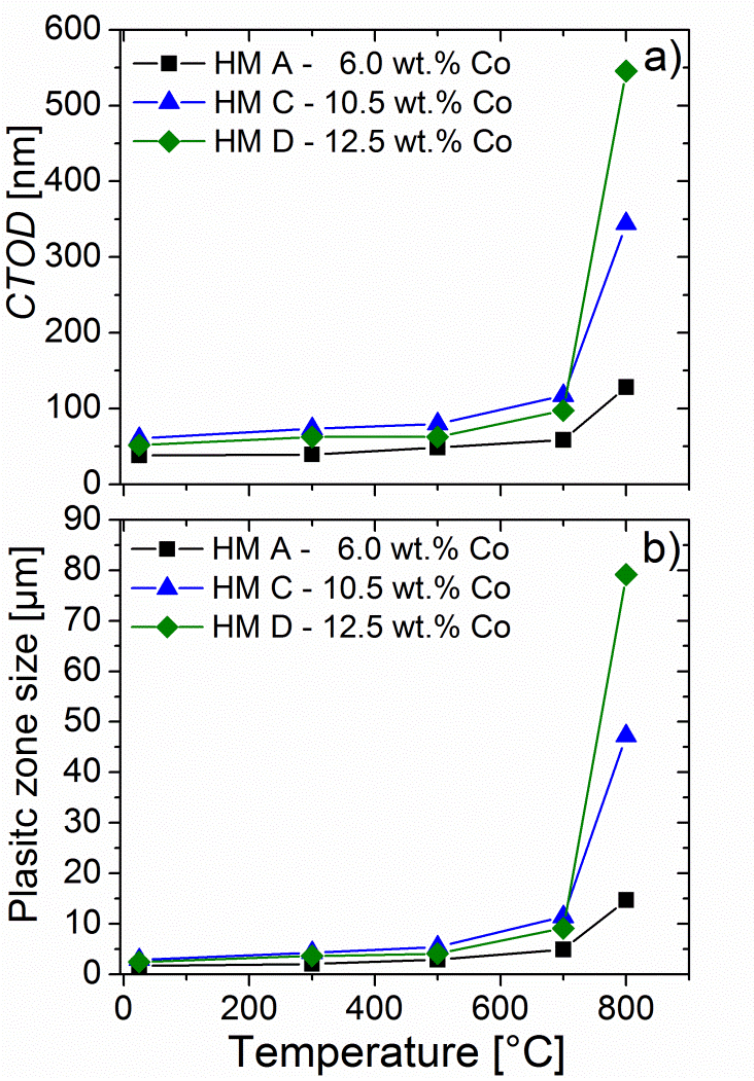

Fig.9: a) Crack tip opening displacement *CTOD* and b) plastic zone size of selected HM grades A, C and D as a function of temperature.

They remain almost constant for all HM grades up to 500 °C, whereas at 800 °C both r_p and *CTOD* are significantly increased for HM grades C and D, respectively. The rise of r_p and *CTOD* of HM A is far less pronounced. From RT to 500 °C r_p is similar or somewhat larger than the WC grain size for all HM grades. Above 700 °C, *CTOD* approaches respective values close to and r_p values well above the average WC grain size.

The morphology of fracture surfaces produced in SENB tests was documented via SEM for all HM grades, e.g. for HM E tested at RT, see Fig. 10a), and at 800 °C, see Fig. 10b). The positions of the SEM micrographs were regions of unstable crack propagation i.e. overload fracture close to the fatigue pre-crack necessary for K_{IC} determination (Fig. 11a)). White arrows in Fig. 10b) and black circles in a FIB cross section in Fig. 10c) indicate rounded Co features observed on the fracture surfaces.

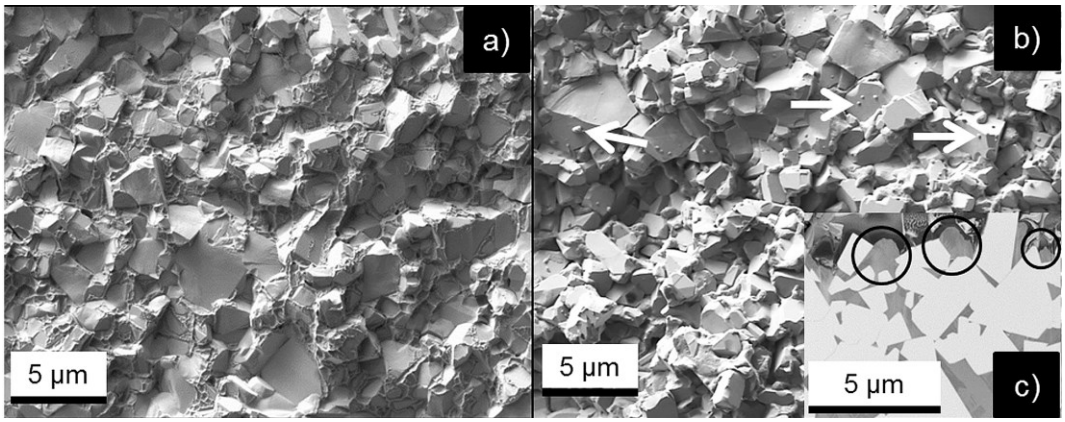

Fig.10: SEM micrograph of fracture surface of HM E from SENB after testing at a) room temperature and b) 800 °C; c) FIB cross section of fracture surface shown in b). White arrows in b) and black circles in c) indicate rounded structures of the Co binder.

These round structures cannot be observed on the RT fracture surface where a dimple shape of the Co phase prevails that is characteristic for instable crack propagation in WC-Co hard metals at RT [19], see Fig. 10a). The transformation from dimples to round shapes is most likely driven by the enhanced surface diffusion and reduction of surface energy during annealing of the fracture surface after testing when elevated temperatures act over a relatively long period of time. A similar behaviour is known e.g. for pearlitic steels, in which cementite lamellas transform into globular ones [20]. This hypothesis is supported by the fact that fracture surfaces formed at RT that underwent an additional annealing treatment with the same temperature-time history as SENB specimens tested at 800 °C show the same Co binder morphology.

The dashed line in Fig. 11 indicates the transition between zones of fatigue crack propagation and instable crack propagation; the black arrows show the crack propagation direction.

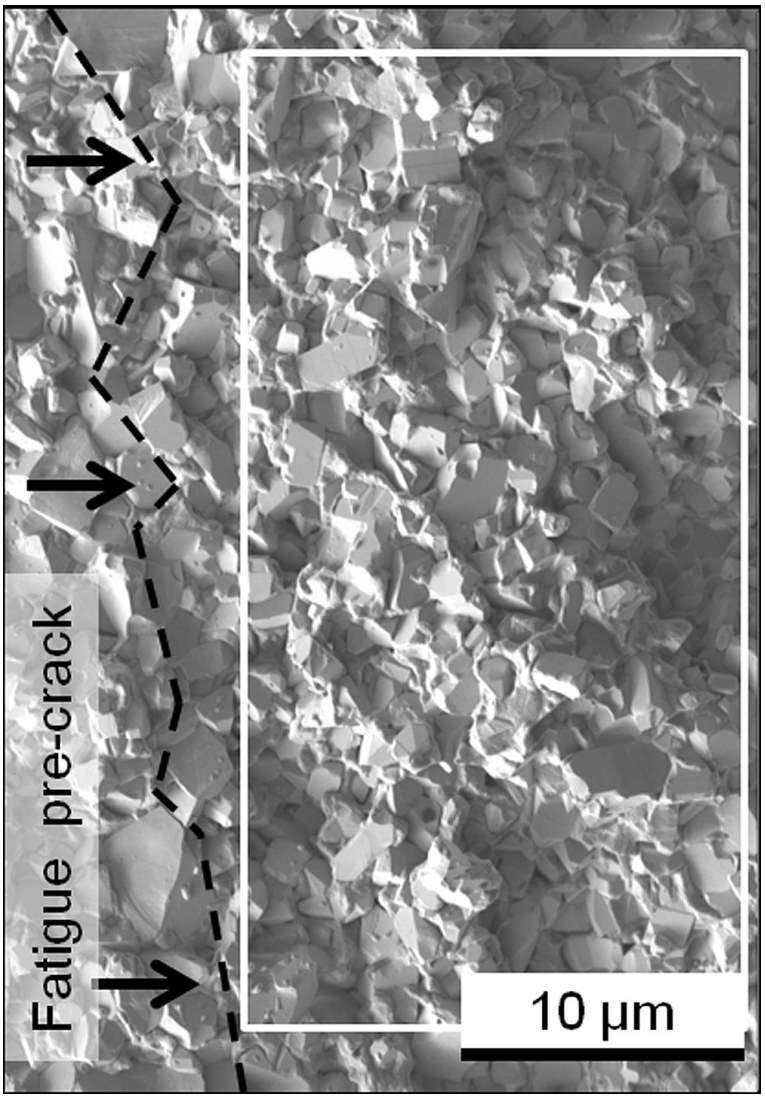

Fig.11: SEM micrograph of fracture surface of HM E. The dashed line indicates the transition between the fatigue pre-crack and instable crack propagation.

The white rectangle in Fig. 11 indicates the area of roughness evaluation in terms of R_a. The respective roughness values are documented in Fig. 12.

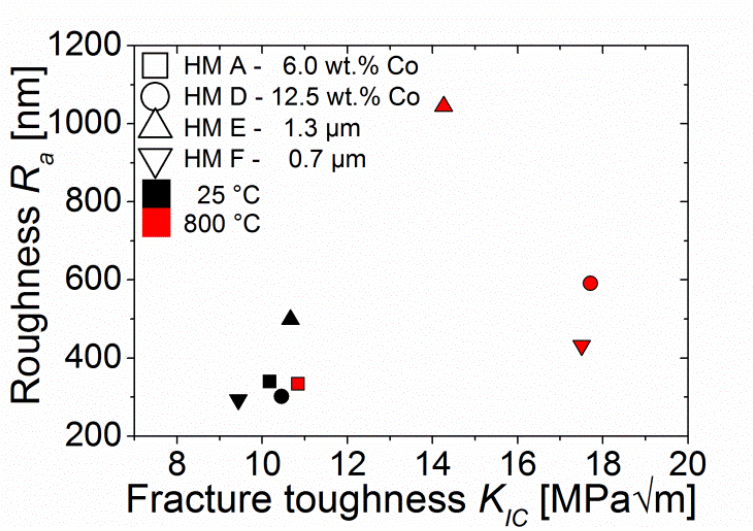

Fig.12: Average roughness in terms of R_a of fracture surfaces from SENB specimens tested at RT and 800 °C as function of determined fracture toughness K_{IC} for selected HM grades A, D, E and F.

At RT the R_a values observed for HM grades A, D and F are similar; HM E did exhibit the highest value. R_a values observed on fracture surfaces obtained at 800°C rise compared to the RT values for all HM grades except HM A with the lowest Co content. Note that this increase of fracture surface roughness is connected with a rise of K_{IC} (c.f. Fig. 8). A possible explanation for this observed correlation is the lowered yield strength at elevated temperatures and the therefore increased plastically deformed volume in front of the crack tip. The plastic zone at 800°C is significantly larger than at RT and also larger than the average WC grain size. Also *CTOD*, that scales with an elevated level of strain concentrated in the crack tip's very vicinity, does rise significantly above 700 °C. These changes may have significantly altered the distribution of the fracture path along the principally possible ones within the WC-Co microstructure described in the literature for RT conditions [21]: along a) WC-WC interfaces, b) WC-Co interfaces, c) within the Co binder and d) near the WC- binder interface. The clarification to what extent this occurred was not within the scope of the current work and calls for further research.

Conclusions

Within this work material properties such as Young's and shear modulus, Poisson's ratio, yield strength, fracture toughness are determined as a function of temperature for WC-Co hard metals with a systematic variation in Co content and WC grain size. Young's and shear modulus decrease with increasing temperature and Co content. Poisson's ratio is not influenced by temperature, Co content and WC grain size. Yield strength decreases with increasing temperature and increasing Co content. From room temperature to 700 °C there is no pronounced influence of Co content and WC grain size on fracture toughness within the

investigated parameter range. At 800 °C all investigated hard metal grades with a Co content higher than 8 wt.% showed a significant increase in fracture toughness. Average fracture surface roughness increased with increasing testing temperature for these grades. A potential explanation for this observation is an altered crack path along the principally possible ones within the WC-Co microstructure triggered by an increase of plastically deformed volume around the crack tip at elevated temperatures.

Acknowledgments

We thank Uwe Ossberger for fruitful discussions concerning the FE simulation for the strain correction. In equal measure we want to thank Peter Kutlesa and Kevin Tobisch for their support concerning HT fracture toughness and stress-strain curve determination.

Financial support by Austrian Federal Government (in particular from Bundesministerium für Verkehr, Innovation und Technologie and Bundesministerium für Wirtschaft, Familie und Jugend) represented by Österreichische Forschungsförderungsgesellschaft mbH and the Styrian and the Tyrolean Provincial Government, represented by Steirische Wirtschaftsförderungsgesellschaft mbH and Standortagentur Tirol, within the framework of the COMET Funding Programme is gratefully acknowledged.

References

[1] Schedler W. Hartmetall für den Praktiker. Düsseldorf: Plansee Tizit VDI; 1988.

[2] Strenkowski JS, Carroll JT. A finite element model of orthogonal metal cutting. J Manuf Sci E-T Asme 1985; 107 Issue 4: 349-54. doi:10.1115/1.3186008.

[3] Astakhov VP. Tribology of Metal Cutting. Oxford: Elsevier; 2006.

[4] Brooks KJA. World Directory and Handbook of Hardmetals and Hard Materials. 6th ed. Great Britian: International Carbide Data; 1996.

[5] Warren R, Johannesson B. The Fracture Toughness of Hardmetals. Sintered Metal Ceramic Composites. New Delhi: Conference Proceedings of the 3rd International School; 1984. 365-75.

[6] Mohand HS, Fantozzi G, Orange G, Dubois J. Comportement mécanique à haute temperature des carbures cementes WC-Co. Rev Int Hautes Temp 1982; 19: 311-23.

[7] Ferreira JAM, Pina Amaral MA, Antunes FV, Costa JDM. A study on the mechanical behaviour of WC/Co hardmetals. Int J Refract Met H 2009; 27: 1-8. doi:10.1016/j.ijrmhm.2008.01.013.

[8] Schmid HG, Mari D, Benoit W. The Mechanical Behaviour of Cemented Carbides at High Temperature. Mat Sci Eng A-Struct 1988; 105/106: 343-51. doi:10.1016/00255416(88)90716-1.

[9] Lins W, Kaindl G, Peterlik H, Kromp K. A novel resonant beam technique to determine the elastic moduli in dependence on orientation and temperature up to 2000 °C. Rev Sci Instrum 1999; 70 Issue 7: 3052-8. doi:10.1063/1.1149867.

[10] Gottstein G. Physikalische Grundlagen der Materialkunde. 3rd ed. Berlin Heidelberg: Springer; 2007.

[11] Klünsner T, Marsoner S, Ebner R, Glaetzle J, Pueschel A, Pippan R. Influence of Microstructure on Stress-Strain Behaviour of WC-Co Hard Metals in Static and Cyclic Loading. Reutte: Conference proceedings of the 17th Plansee Seminar; 2009. AT10/1-10.

[12] ASTM E399. Standard Test Method for Linear-Elastic Plane-Strain Fracture Toughness K_{IC} of Metallic Materials. West Conshohocken: ASTM International. doi:10.1520/E0399.

[13] Doi H, Fujiwara Y, Miyake K, Oosawa Y. A Systematic Investigation of Elastic Moduli of WC-Co Alloys. Metall Mater Trans B 1970; 1: 1417-1425. doi:10.1007/BF02900264.

[14] Klünsner T, Marsoner S, Ebner R, Pippan R, Glätzle J, Püschel A. Effect of microstructure on fatigue properties of WC-Co hard metals. Procedia Eng 2010; 2: 2001-10. doi:10.1016/j.proeng.2010.03.215.

[15] Milman YV, Luyckx S, Northrop IT. Influence of temperature, grain size and cobalt content on the hardness of WC-Co alloys. Int J Refract Met H 1999; 17 Issue 1-3: 39-44. doi:10.1016/S0263-4368(98)00038-9

[16] Johannesson B, Warren R. Subcritical Crack Growth and Plastic Deformation in the Fracture of Hard Metals. Mat Sci Eng A-Struct 1988; 105/106: 353-61. doi:10.1016/0025-5416(88)90717-3.

[17] Anderson TL. Fracture Mechanics. Fundamentals and Applications. 3rd ed. Boca Raton: Taylor & Francis Group; 2005.

[18] Zhu XK, Joyce JA. Review of fracture toughness (G, K, J, CTOD, CTOA) testing and standardization. Eng Fract Mech 2012; 85: 1-46. doi:10.1016/j.engfracmech.2012.02.001.

[19] Erling G, Kursawe S, Luyckx S, Sockel HG. Stable and unstable fracture surface features in WC-Co. J Mater Sci Lett 2000; 19: 437-8.

[20] Seidl WW, Hahn F. Werkstofftechnik Werkstoffe - Eigenschaften Prüfung – Anwendungen. 10th ed. München: Hansen; 2014.

[21] Sigl LS, Exner HE. Experimental study of the mechanics of fracture in WC-Co alloys. Metall Trans A 1987; 18A: 1299-308.